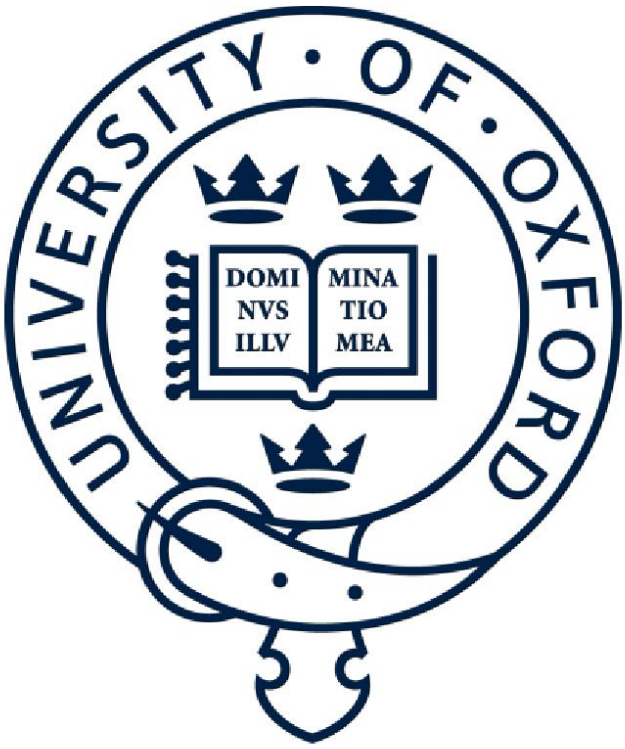
THE IRRADIATION RESISTANCE OF OXIDE DISPERSION STRENGTHENED STEELS



CHRISTOPHER BURROWS

UNIVERSITY OF OXFORD

SUPERVISOR: PROF STEVE ROBERTS CO SUPERVISOR: DR PAUL BAGOT

Acknowledgements

I would like to thank my supervisors Professor Steve Roberts and Dr Paul Bagot for supporting me throughout my work at Oxford both in the laboratory and with useful discussions in meetings and over coffee on Friday mornings.

I would like to thanks all those who collaborated with me in the course of my research. Special thanks must go to Mike Gorley without whom I would have had no material to work with. Karl Dawson, Judy Kim and Chris Hardie all provided invaluable support which is acknowledged and referenced in the text. Additional thanks must go to Sergio Lozano Perez and Ceri Williams for their help with training and their patience in the many discussions we had over the course of my research.

I would like to thank the staff at the Surrey Ion Beam Centre for their help in conducting the ion implantations sometimes at short notice and at unsociable hours!

Finally I would like to thanks all my colleagues and friends at Oxford for making my time here so enjoyable, my parents for everything they have done in the course of my rather long stretch in higher education and my partner Hannah for her support, kindness and forbearance.

Preface

This thesis is an account of the work undertaken by the author in the Department of Materials at the University of Oxford between October 2010 and January 2014. The work was completed under the supervision of Professor Steve Roberts and Dr Paul Bagot and was jointly funded by Rolls Royce PLC and the Engineering and Physical Sciences Research Council (EPSRC). No part of this thesis has previously been submitted for a degree at this or any other university. Where the work of other authors is included it is referenced and acknowledged in the text. A list of references has been given at the end of this thesis.

Abstract

Reduced activation oxide dispersion strengthened (ODS) steels are candidate alloys for use in fusion reactor systems and are fabricated by mechanically alloying yttrium oxide to a reduced activation ferritic steel powder. The product is consolidated at high temperature by hot isostatic pressing (HIP), producing a dispersion of nanometre sized oxide particles throughout the ferritic microstructure. These particles have been shown to both improve the high temperature mechanical properties of the alloy and provide trapping sites for helium gas.

The use of these particles to sequester helium is of particular significance in the development of a structural ODS steel for fusion reactor systems. A fusion power reactor, based on the ITER design, is expected to produce over 2000 appm transmutant helium in any steel components exposed to the core neutron flux. At these gas concentrations, conventional steels undergo severe swelling and embrittlement, motivating the development of materials capable of managing helium accumulation.

This thesis investigates the use of the oxide particle dispersion in sequestering helium introduced by ion implantation. An initial characterisation of a model Fe-14Cr-0.25Y_2O_3 (wt%) system was completed using high resolution transmission electron microscopy (HRTEM) and atom probe tomography (APT). This demonstrated the efficacy of the production methods and the gas trapping capabilities of the oxide particles via argon gas, introduced during the mechanical alloying process.

The subsequent consolidation of a full set of Fe-14Cr-3W-0.2Ti-0.25Y_2O_3 (wt%) ODS alloys at 1150^{o}C, 1050 ^{o}C and 950 ^{o}C produced a systematic variation in the density of the particle dispersion. The characterisation of these materials using APT provided an insight into the consistent $Y_2Ti_3O_5$ particle chemistry found in each consolidation, and identified a stoichiometric shift from $Y_2Ti_3O_5$ to $YTiO_2$ following short term annealing periods at 1000^{o}C. Though further work is required, this shift is thought to be

consistent with a thermodynamically mediated transition of the metastable clusters to stable oxide particles.

Following implantation with 2000 appm helium and examination under TEM, the helium bubble and particle densities were found to be closely correlated thus providing evidence for an association between the particles and the gas bubbles. Controlling the helium bubble density via the particle dispersion demonstrates the potential use of processing temperature in controlling how helium accumulates in an implanted ODS microstructure.

The effects of both bubble and particle densities on mechanical properties were investigated further using nanoindentation methods. Significant local variation in the hardness of the ODS steels was found to result from the bimodal grain size distribution of the material. By using only those measurements taken from large grained regions of the ODS, the grain refinement and particle hardening effects could be deconvolved and used to quantify particle hardening using a dispersed barrier model.

The significant hardening effects with helium addition observed in the reference alloys were found to be almost entirely absent from the ODS systems, though anomalous softening in the 950^{o}C consolidation indicated a potentially unexpected interaction between the bubble and particle populations. A possible explanation for this anomaly and a proposal for further work to establish its origin is discussed.

Contents

1 Literature Review 9
1.1 Introduction 9
1.2 The Physical Causes and Consequences of Irradiation Damage 11
1.2.1 Neutron Scattering Cascade and Defect Production 11
1.2.2 Defect Accumulation and Transport 12
1.3 The Consequences of Irradiation Damage 19
1.4 Engineering Radiation Resistance 20
1.5 The Development of Irradiation Resistant Alloys 21
1.5.1 Reduced Activation Ferritic Martensitic Steels 21
1.5.2 Simulating The Irradiation Environment 24
1.6 Oxide Dispersion Strengthened Alloys 27
1.6.1 Introduction 27
1.6.2 Fabrication Methods and Processing Variables 29
1.6.3 Properties and Structure of the Oxide Dispersions 33
1.6.4 Mechanical Properties of Oxide Dispersion Strengthened Alloys 47
1.6.5 Thermal and Irradiation stability of Oxide Dispersion Strengthened Alloys 52
1.6.6 Helium Management Capability of Oxide Dispersion Strengthened Steels 55
1.7 Conclusions and Proposed Work 63
2 Experimental Methods 65
2.1 Ion Implantation 65
2.1.1 Sample Preparation and Mounting 65
2.1.2 SRIM Calculation 66
2.2 Atom Probe Tomography 67
2.2.1 Principle of Operation 67
2.2.2 Sample Preparation 69
2.2.3 Selecting the Analysis Conditions 71
2.2.4 Mass Spectra 72
2.2.5 3D Reconstruction 76
2.2.6 Data Analysis Techniques 78
2.3 Transmission Electron Microscopy 80
2.3.1 Disk Sample Preparation Method 81
2.3.2 Lift Out Sample Preparation Method 81
2.3.3 Fresnel Contrast Microscopy 82

2.3.4 Energy Filtered Transmission Electron Microscopy 83
2.4 Nanoindentation 84
2.4.1 Principle of Operation 84
2.4.2 Data Analysis 85
2.4.3 Continuous Stiffness Measurement 87
2.4.4 Pile Up and Sink In 87
2.5 Electron Backscattered Diffraction 88
3 Production and Characterisation of a Model ODS Alloy 89
3.1 Summary 89
3.2 Alloy Production 89
3.2.1 Powder Metallurgy 90
3.2.2 Mechanical Alloying 91
3.2.3 Consolidation 92
3.3 Characterisation 93
3.3.1 TEM 93
3.3.2 STEM 94
3.3.3 Spatially Resolved EDX 95
3.3.4 APT 97
3.4 Discussion 101
3.4.1 Particle Characterisation Using Complementary TEM/APT Techniques 101
3.4.2 Vessel Composition and Powder Contamination 103
3.4.3 Argon Trapping at Particle Boundaries 103
3.5 Summary 104
4 Characterisation of a YWT ODS System Processed Using Systematically Varying Consolidation Conditions 105
4.1 Summary 105
4.2 Materials and Methods 106
4.3 TEM Characterisation 108
4.4 APT Characterisation 112
4.4.1 Solute Selection 112
4.4.2 D_{max} and N_{min} Selection 114
4.4.3 L Selection 121
4.4.4 Matrix Correction 121
4.4.5 Particle Number Density Variation with Consolidation Temperature 122
4.4.6 Alloy Chemistry Variation with Consolidation Temperature 124

4.4.7 Particle Chemistry Variation with Consolidation Temperature 126
4.4.8 Titanium-Manganese Precipitates 128
4.4.9 Grain Boundary Analysis 134
4.4.10 Thermal Stability 137
4.5 Discussion 142
5 Helium Implantation of a YWT ODS System with Varying Oxide Particle Number Densities 149
5.1 Summary 149
5.2 Helium Implantation 150
5.3 Data Analysis and Image Processing 153
5.4 Bubble Densities 158
5.4.1 Experimental Control – Implanted and Unimplanted Samples 158
5.4.2 Implanted Alloys 158
5.5 Discussion 162
6 Micromechanical Response To Helium Implantation 166
6.1 Summary 166
6.2 Hardness Measurements 168
6.3 Hardness and Microstructure in Oxide Dispersion Strengthening Alloys 170
6.3.1 SEM Characterisation 173
6.3.2 EBSD Characterisation 175
6.4 Discussion 180
7 Conclusions and Future Work 184
7.1 Characterisation of a YWT ODS System Under Systematically Varying Consolidation Conditions 184
7.1.1 Conclusions 184
7.1.2 Future Work 185
7.2 Helium Implantation of a YWT ODS System with Varying Oxide Particle Number Densities 185
7.2.1 Conclusions 186
7.2.2 Future Work 186
7.3 Micromechanical Response To Helium Implantation 187
7.3.1 Conclusions 187
7.3.2 Future Work 188
8 Appendix A 189
9 Appendix B 190

1 Literature Review

1.1 Introduction

The pressures of climate change and energy security have renewed global interest in advanced nuclear power concepts and their potential for meeting our ever growing energy needs, whilst also reducing our carbon emissions and reliance on non-renewable fossil fuels [1]. However, the safety and economic viability of both Generation IV fission and future fusion power plants depend on the development of new materials capable of enduring the intensely hostile operating conditions likely to be seen in service [2].

For the plasma facing components (PFC) and blanket structures of prototype fusion reactors these conditions include; operating temperatures above 500^{o}C, cyclical stresses, ion sputtering and intense 14MeV neutron fluxes capable of inflicting end of life atomic displacement damage of up to 200dpa (displacements per atom). Under such a bombardment, vacancies and self-interstitial (SIA) defects build up, changing the microstructure and chemistry of an alloy by defect clustering, transmutation, solute segregation, radiation induced precipitation and void formation. [3]

In steels the displacement damage undergoes a variety of interactions with the hydrogen and helium transmutant gas products of (n,α) nuclear reactions. The steady accumulation of insoluble helium at 10appm/dpa (atomic parts per million) poses particular problems, including bubbling, void development and grain boundary embrittlement, all of which compound the problems caused by displacement defects [3][4].

A wide variety of neutron induced transmutations cause radionuclides to build up in materials, changing their composition and limiting the alloying elements available for use in plasma facing components to those few which do not form harmful long term transmutation products [5]. These include Fe, Cr, W, V, Ta, Y and C. In steels W, V and Ta are sometimes substituted for Mo, Nb and Ni in an effort to suppress alloy contamination and reduce the waste burden on decommissioning. [6]

In steels the combined effects of displacement damage and transmutant gas build-up severely degrade the material properties and the reliability of components in service by a number of mechanisms, most of which show some temperature dependence. Hardening and embrittlement generally occur below about 0.35 of the melting temperature T_m which could potentially cause vessel fracture on shut down and cooling [7].

A complete loss of uniform tensile strain ductility and unpredictable volumetric swelling from $0.3T_m$ accompanies creep from $0.45T_m$ above doses of about 10dpa. Under the application of cyclical stresses these effects could permanently deform components, compromising plasma critical reactor geometries and complicating maintenance and repair [7].

When these effects act in combination with fracture toughness reductions, segregation or precipitation-induced phase instabilities and helium bubble accumulation at grain boundaries, the challenges become considerable. Materials are needed with capabilities beyond those presently available to nuclear engineers, with a superior mix of mechanical, physical and radiological properties that are stable under prolonged exposure to the core environment.

The following survey will review the recent progress made in fulfilling these demands using reduced activation oxide dispersion strengthened steels (ODS) (sometimes called nanostructured ferritic alloys). These have shown particular promise for managing transmutation gases at high temperatures and are a leading candidate material for structural applications in prospective fusion reactor systems.

We begin by discussing the physical causes and consequences of radiation damage and the fundamentals of engineering radiation resistance. The development of resistant alloys using reactor relevant radiation experiments follows, before we make a detailed study of the published material concerned with the gas sequestering capabilities of the oxide particles and their performance under irradiation.

1.2 The Physical Causes and Consequences of Irradiation Damage

A comprehensive mathematical treatment of radiation effects on materials would go far beyond the scope of this survey of irradiation resistance in ODS steels. G. S. Was provides an in-depth text on the fundamentals of radiation damage in [8]. A summary of the essential phenomena are presented here to set the stage for a further discussion of irradiation resistance in ferritic alloys.

1.2.1 Neutron Scattering Cascade and Defect Production

Energetic neutrons entering a crystal lattice collide with atoms, setting off a collision cascade shown schematically in Figure 1.1. Each collision generates a primary recoiling atom (PRA) which in turn sets off further collisions through the lattice. The displacement of atoms from their lattice sites produces a high local density of vacancies and self-interstitial (SIA) defects. These often form clusters and complexes with alloy solutes in a variety of configurations [8].

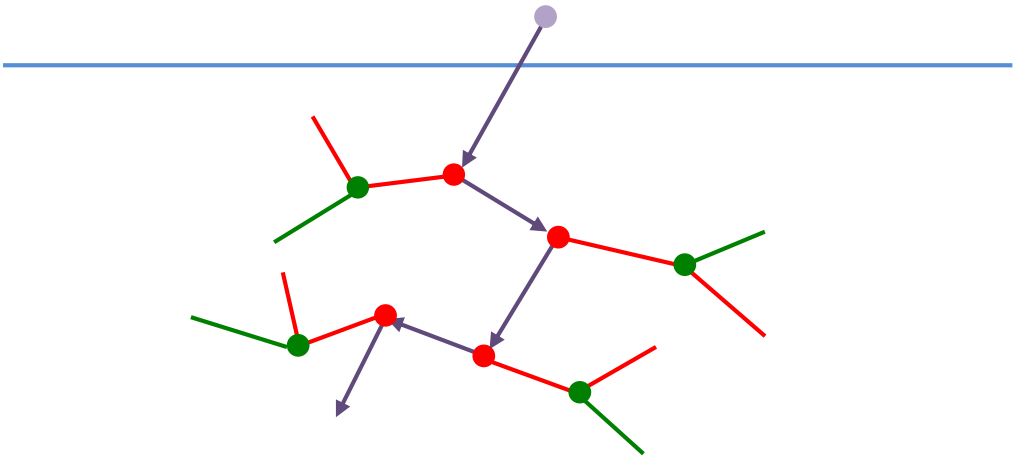


Figure 1.1 A collision cascade caused by the incident neutron (purple) which generates primary recoiling atoms (red) which in turn generate branching cascades (green)

Most vacancies and SIAs are short lived and recombine in the cascade, but above $0.3T_m$ about one third escape and diffuse through the lattice with significant implications for the microstructure. The defect production rate depends on the neutron energy spectrum and the flux, variables which need to be considered in any attempt to simulate reactor relevant irradiation conditions [8].

An incident neutron flux also causes nuclear transmutation in the target alloy producing both hydrogen and helium via the (n,p) and (n,α) reactions in iron. Hydrogen diffuses sufficiently rapidly such that it soon reaches equilibrium with the environment but helium accumulates at a rate typically presented in terms of appm/dpa [14]. In iron 14MeV fusion neutrons produce helium at 10 appm/dpa, about one order of magnitude above that of the fast fission neutron spectrum [9].

1.2.2 Defect Accumulation and Transport

Figure 1.2 shows the various fates awaiting those displacement defects that diffuse away from the recoil cascade. These include vacancy-SIA recombination (both in the matrix and at trapping sites) and annihilation and accumulation at sinks. Figure 1.2 presents the basic components of a kinetic theory treatment of radiation effects developed by Mansur [10] which shows how the rate of defect annihilation and accumulation at sinks for interstitials R_i and vacancies R_v varies in terms of the defect diffusion coefficient $D_{i/v}$ the atomic defect fraction $C_{i/v}$ and the total defect sink strength $Z_{i/v}$.

Equation 1.1 $$R_{i/v} = D_{i/v} C_{i/v} Z_{i/v}$$

These sinks could be dislocations, precipitates, grain boundaries, unstable voids or stable bubbles. The sink strength for bubbles, voids and precipitates may be found from the diffusion equations formulated by Mansur [10] approximated to spherical sinks. The approximation shown in Equation 1.2 includes the sink radius r_s and the number density N_s.

Equation 1.2 $$Z_s = 4\pi r_s N_s$$

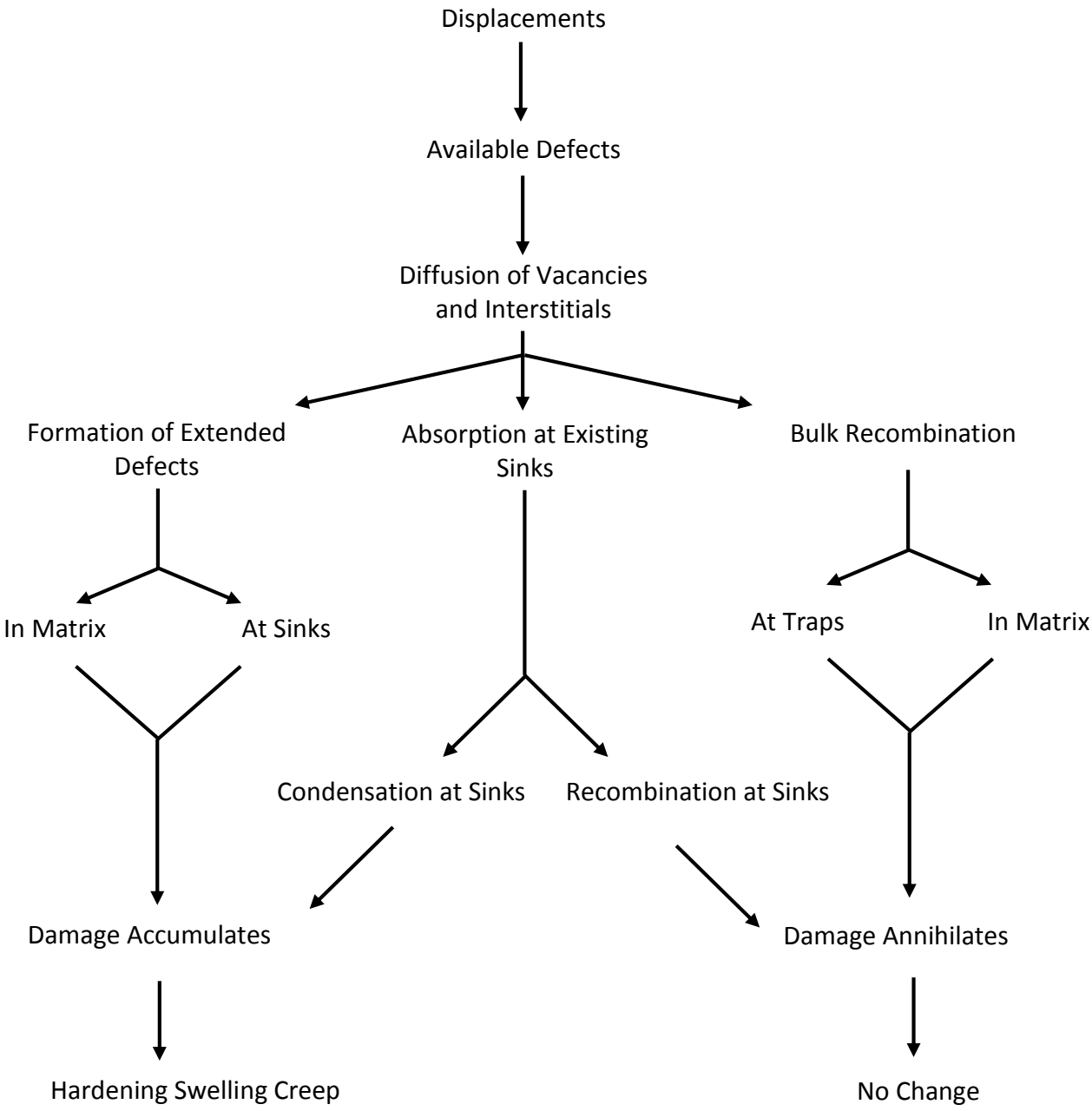


Figure 1.2 Summary of the main conceptual elements in the development of radiation defects from the initial displacement [10].

By substituting the volume fraction f_s for the number density N_s in Equation 1.2 the sink strength of a spherical precipitate particle can be estimated. Equation 1.3 indicates that a high volume fraction of small particles should boost the rate of defect accumulation and annihilation at such sinks.

Equation 1.3 $$Z_s = \frac{3f_s}{r_s^2}$$

For dislocations the sink strength may be approximated to the dislocation density with a bias factor introduced for SIAs which preferentially annihilate at dislocations. Stress fields shift the bias factor for different directions of applied stress, promoting irradiation creep with a minimal temperature dependence and a net vacancy flux causing void swelling and shifts in solute concentrations [10].

Transmutant helium accumulation compounds these problems. Bubble formation at precipitate interfaces and dislocations promotes void swelling and embrittlement [3]. At grain boundaries the combined influence of applied stress and helium concentrations of even one part per million promote cavitation and cracking, reducing creep rupture times and high temperature ductility [11] [12].

Odette and Stoller have completed in-depth studies of helium effects in nuclear steels combining experimental observations [13] [14] and simplified models of bubble development [15] [16] using the kinetic treatment developed by Mansur which is presented below in Equation 1.4 to Equation 1.11 [10].

Subject to a vacancy flux $Z_v^c D_v C_v$, an interstitial flux $Z_i^c D_i C_i$, and a vacancy emission $Z_v^c D_v C_v^c$, a helium bubble of radius r_c swells according to Equation 1.4. Substituting for the equilibrium vacancy concentration C_v^e and the pressure P using Equation 1.5 and Equation 1.6 a spherical bubble stabilized by m helium atoms swells depending on a compressibility factor z, the free surface energy γ, the vacancy volume Ω_v, and the temperature T according to Equation 1.7 [10][15].

Equation 1.4
$$\frac{dr_c}{dt} = \left[Z_v^c D_v C_v - Z_i^c D_i C_i - Z_v^c D_v C_v^c\right]\frac{1}{r_c}$$

Equation 1.5
$$C_v^c = C_v^e \exp\left[\frac{\Omega_v}{kT}\left(\frac{2\gamma}{r_c} - P\right)\right]$$

Equation 1.6
$$P = \frac{3zmkT}{4\pi r_c}$$

Equation 1.7
$$\frac{dr_c}{dt} = \left[Z_v^c D_v C_v - Z_i^c D_i C_i - Z_v^c D_v C_v^e \exp\left[\frac{\Omega_v}{kT}\left(\frac{2\gamma}{r_c} - \frac{3zmkT}{4\pi r_c}\right)\right]\right]\frac{1}{r_c}$$

Schematic plots of Equation 1.7 are shown in Figure 1.3. Each curve corresponds to a different helium content m, or vacancy supersaturation S, as presented in Equation 1.8. Solutions for case (ii) when r_b and r_v converge, provide the critical helium content m^* and the critical bubble radius r_b^* at the bubble to void conversion point. Equation 1.9 and Equation 1.10 show the parametric dependencies of these quantities. Over typical reactor operating temperatures the critical helium content varies from 10^2 atoms per bubble at 300°C to 10^7 atoms per bubble at 700°C, with a corresponding change in the critical radius from 0.5nm to about 100nm [15]. Modifying these parameters by tuning the microstructure would provide some measure of control over bubble development and the vacancy flux required to incubate unstable voids [15].

(i) At a subcritical helium content the bubble is unable to sustain a net vacancy absorption and shrinks back to r_b.

(ii) The critical bubble to void conversions occurs when r_b and r_v converge to r_b^* at some critical helium content m^*. Voids swell continuously by vacancy absorption.

(iii) At a supercritical helium content or high vacancy supersaturation, no physical solutions to Equation 1.7 are possible.

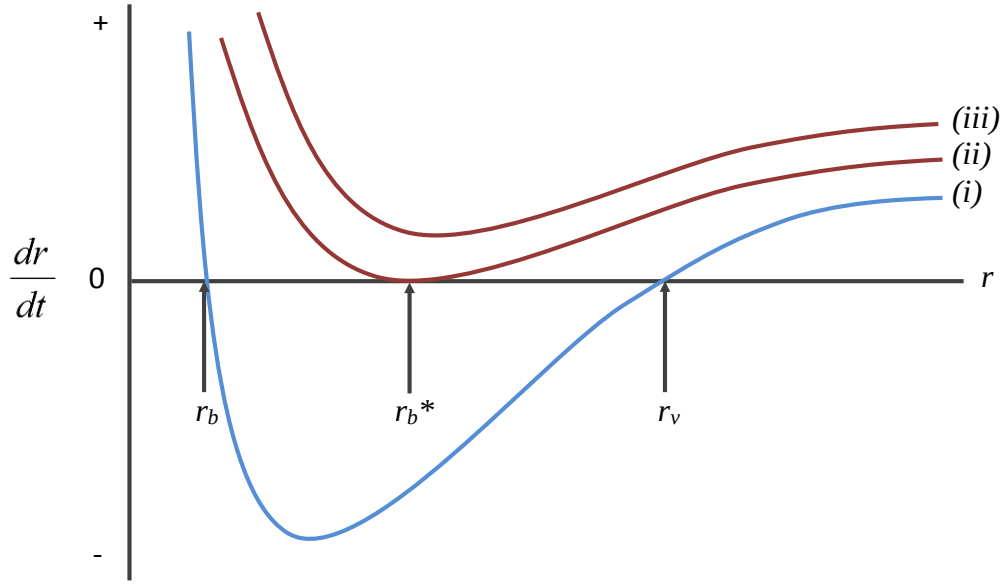


Figure 1.3 Bubble development plotted schematically through the threshold for bubble to void conversion at some critical helium content [17]

Equation 1.8 $$S = \frac{Z_v^c D_v C_v - Z_i^c D_i C_i}{D_v C_v^e}$$

Equation 1.9 $$m^* = \frac{32}{27}\left(\frac{4\pi}{3}\right)\left(\frac{\gamma}{kt}\right)^3\left(\frac{\Omega}{\ln S}\right)^2$$

Equation 1.10 $$r^* = \frac{4\pi\gamma}{3kT\ln S}$$

Stoller admits that the use of an ideal gas approximation in the substitution made for pressure from Equation 1.6 introduces significant deviations from the limited amount of experimental data that was available for high pressure helium at the time of publication in 1985. However, the parametric relationships shown in Equation 1.8 and Equation 1.9 prove useful in modelling the bubble to void conversion [15]. Odette uses the concept of a critical helium content *m** to interpret the characteristic bimodal size distribution of bubble populations observed in the TEM and suggests a simple relationship between bubble number density N_b, helium content *m* and the critical atomic displacement damage *dpa** necessary to drive void formation [14].

Equation 1.11 $$dpa^* = 10^6 \Omega m^* N_b$$

When plotted in Figure 1.4, Equation 1.11 shows the incubation dose *dpa** reaching 400 dpa for a bubble density of 5×10^{22} at 500°C below which void swelling would be completely suppressed. The relationship shows the capacity for even modest bubble populations to delay the evolution of unstable voids, turning helium bubbles from a potential problem into a useful method for protecting the microstructure [17].

Expanding on the simple model outlined in Figure 1.3, Stoller introduces a hard sphere equation of state developed by Brierley and MacInnes to replace the ideal gas assumption, in an attempt to more closely approximate experimental data [15] [18]. Presented in Equation 1.12 and Equation 1.13 the hard sphere model sets the sphere diameter *d* using an interatomic potential chosen to give a reasonable temperature dependence in *d* at the pressures of interest.

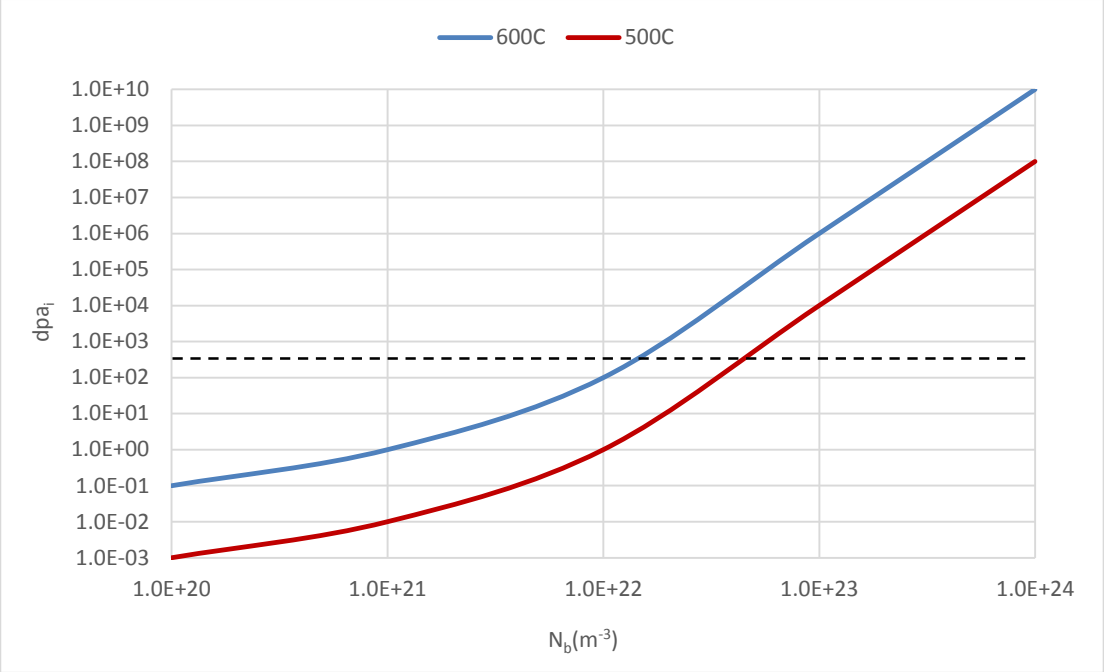


Figure 1.4 A modest number density N_b of 1nm helium bubbles boosts the incubation dose to 400 dpa (dashed line) [17]

Equation 1.12 $$\frac{PV}{mkT} = \frac{1 + y + y^2 + y^3}{(1-y)^3}$$

Equation 1.13 $$y = \frac{\pi m d^3}{6V}$$

Finding good agreement with the helium compression data recorded by Bridgeman, Brierley and MacInnes [18] settled upon a modified Buckingham potential for their model, which Stoller used to develop a correction for the values of m^* and r^* predicted using Equation 1.6 [15]. However, Bridgeman's early data differ considerably from the more recent measurements made by Mills, Liebenberg and Bronson [19]. Derived from 670 sets of PVT data in the 2 to 20 kbar range, Mills, Liebenberg and Bronson developed the empirical equation of state presented in Equation 1.14. When compared in a comprehensive survey by Donnelly [20], use of the Buckingham potential in the hard sphere model produces a much less convincing result (assuming the modern data are more reliable than Bridgeman's).

$$V = (22.575 + 0.0064655T - 7.2645T^{-\frac{1}{2}})P^{-\frac{1}{3}}$$

Equation 1.14

$$+ (-12.483 - 0.024549T)P^{-\frac{2}{3}}$$

$$+ (1.0596 + 0.10604T - 19.641T^{-\frac{1}{2}} + 189.84T^{-1})P^{-1}$$

Although a closer fit to Mills, Liebenberg and Bronson [19] can be obtained using a Leonard Jones potential, Donnelly suggests a more satisfactory result would incorporate a density dependence into the hard sphere diameter. He discusses the various soft sphere models from Young [21], Trinkhaus [22] and Wolfer [23] and presents these alongside Equation 1.14 in Figure 1.5 [20]. Good agreement between Mills, Liebenberg and Bronson and the soft sphere models, (particularly at high pressures) leads Donnelly to recommend the use of Equation 1.14 in all pressure to density conversions for helium filled bubbles.

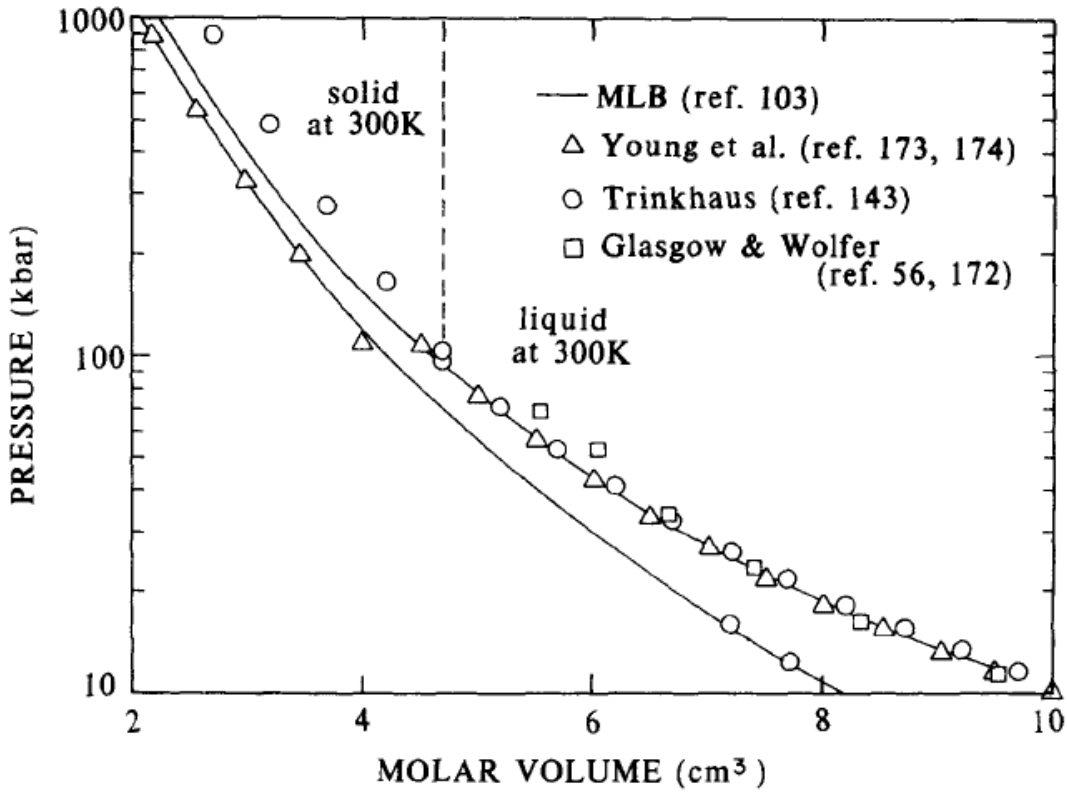


Figure 1.5 High pressure PV isotherms for helium at 300K plotted from MLB with the predictions from Young, Trinkhaus and Wolfer [20]

1.3 The Consequences of Irradiation Damage

The defects associated with neutron radiation exposure, discussed in Section 1.2, impair the mechanical properties of reactor components in a number of different ways. The most serious constitute a risk to the safe operation of reactor systems and would necessitate impractically frequent maintenance and component replacement. Odette presents a summary of the most severe [14]:

i. Low temperature hardening caused by dislocations, precipitation and bubbling.
ii. High temperature softening and loss of creep rupture strength caused by helium.
iii. Loss of fracture toughness through grain boundary embrittlement.
iv. Loss of uniform strain ductility through reduced strain hardening.
v. Volumetric swelling caused by bubble/void formation and growth.
vi. Low temperature irradiation creep and creep cavity formation.
vii. Intergranular stress corrosion cracking caused by solute segregation and hardening.
viii. Unpredictable segregation and precipitation induced microstructural instabilities.

All of these problems need to be considered in the development of structural alloys but some feature more than others depending on the susceptibility of particular alloy systems. An appreciation for the basic kinetic framework outlined by Mansur and its further development and application by Stoller and others, enables those weaknesses to be mitigated to some extent via a degree of microstructural engineering in candidate alloys[10].

1.4 Engineering Radiation Resistance

Composition, processing and thermo-mechanical treatments offer opportunities to build resistance into a microstructure from the initial cascade onwards. Having eliminated transmutation prone elements (especially Ni) from a candidate alloy, any approach to microstructural engineering should attempt to exploit relationships between the various sinks to control the fate of defects [24].

Dislocations are a major defect sink and dense, stable dislocation networks suppress both the vacancy $Z_v^c D_v C_v$ and interstitial flux $Z_i^c D_i C_i$ impinging on the microstructure. Sink strength imbalances can be used to compensate for the net vacancy flux produced by the dislocation bias for interstitial absorption but BCC alloys are usually preferred for the smaller bias factor compared to FCC systems [14]. FCC austenitic steels also suffer particularly severe void swelling leading to the present focus on BCC ferritic and martensitic systems [13] [25].

Stable dislocation networks provide sites for helium bubble formation. Dense dislocation networks can support substantial populations of subcritical bubbles which provide another defect sink and boost the incubation dose needed to cause unstable void swelling [14]. At high temperatures these benefits are lost to bubble coalescence potentially assisted by pipe diffusion through the dislocation network. A trade-off between the benefits afforded by high temperature facilitated self-diffusion and those offered by stable helium containment is therefore inevitable [14].

The higher self-diffusion coefficients of BCC alloys help to mitigate the conflict to some extent. Nevertheless, at proposed reactor operating temperatures, thermally mobilized helium poses a major risk to the integrity of grain boundaries unless effective trapping sites can be introduced into the matrix. These would need to be stable at both high temperatures and high neutron fluxes but could potentially exhibit far higher sink strengths than typical dislocation networks at much greater densities [14].

In summary the irradiation resistance of a candidate BCC alloy formulated from low activation elements may be delivered via high dislocation densities and a dispersion of stable gas trapping sites of sufficient number to confine the helium to a population of small high pressure bubbles. These trapping sites, if provided by matrix precipitates would have the added benefit of pinning dislocations and boosting creep strength.

The implementation of these criteria for resistance in developmental alloys produced the first generations of reduced activation ferritic martensitic steels and their oxide dispersion reinforced counterparts. A brief discussion of the development of these materials and the techniques used to assess their relative merits will provide a useful introduction to the broader analysis of the now expansive body of literature concerning ODS alloys and their irradiation and gas management capabilities.

1.5 The Development of Irradiation Resistant Alloys

1.5.1 Reduced Activation Ferritic Martensitic Steels

The present generation of fast breeder and light water reactors makes use of austenitic stainless steels for fuel cladding and core structural components. Although capable of successfully sustaining 150 dpa in some high burn-up scenarios, the propensity for swelling always imposes limits on their performance [26]. Attempts to suppress swelling have seen titanium and silicon added to austenitic steels in an effort to produce the sink dominated microstructures capable of trapping helium and promoting defect recombination at fine scale precipitates [27].

These efforts show some success in delaying the onset of swelling up to 135 dpa in fast breeder reactors but the operational conditions of plasma facing components in a fusion reactor and the susceptibility of austenitic steels to helium embrittlement are likely to prevent their use. Comprehensive surveys of the problems associated with these materials and the present reliance on ferritic and martensitic (FM) alloys is available in [28] [29] and [30].

The BCC lattice and low dislocation bias of FM steels provide greater resistance to both swelling and embrittlement. For comparison, a typical austenitic steel swells by 1% when subjected to 10 dpa at 575K. A ferritic steel would need to receive 100dpa to undergo a comparable volume change [3]. High self-diffusion coefficients, sink strengths and submicron lath structures all contribute to the irradiation resistance of FM steels which have consequently become a major area of research and development [31].

9 - 12% Cr FM steels have been successfully used in fission plants up to 145 dpa at temperatures from 400°C to 600°C with no indications of embrittlement or severe volume changes [26]. Hardening and embrittlement do occur below 400°C making operating temperature a key point of concern for FM alloys [26]. More recently Baluc confined a survey of FM candidates to four principal reduced activation ferritic martensitic (RAFM) alloys which are listed below with their compositions [32].

	Elemental Composition (wt%)								
	Fe	**Cr**	**W**	**Mn**	**V**	**Si**	**C**	**Ta**	**N**
F82H	BAL	7.46	1.96	0.21	0.15	0.10	0.09	0.023	0.006
JLF	BAL	9.0	2.0	0.45	0.25	0.2	0.1	0.07	0.05
Eurofer 97	BAL	8.9	1.1	0.47	0.2	-	0.11	0.14	-
CLAM	BAL	8.98	1.55	0.4	0.21	-	0.11	0.15	-

Table 1.1 RAFM alloy compositions (wt%) [32]

All of these alloys face an operating temperature problem. Below 400°C in the displacement damage regime, irradiation causes hardening and embrittlement, including a loss of ductility, fracture toughness and a much higher ductile-to-brittle transition temperature (DBTT). Figure 1.6 shows the shift in DBTT with neutron irradiation at 300°C (up to a maximum dose of 2.5 dpa) for a variety of RAFM materials, including Eurofer (-70°C to 0 °C) and F82H (-60°C to -10°C) [32] [36]. The significant reductions in ductility observed in these alloys following irradiation are likely to severely restrict their deployment as structural materials, particularly in the breeding blanket and other areas likely to be subject to high neutron fluxes below the core operating temperature.

Although the high dose databases are limited, above 400°C all the candidate materials demonstrate a robust performance up to 550°C when tensile strength collapses followed closely by creep strength from 600°C. RAFM alloys are thus confined to an operational window between 400°C and 550°C [32]. As with the ductility losses observed at lower temperatures this upper temperature limit imposes itself on present fusion power plant designs, all of which use RAFM materials in their plasma facing components or breeding blanket modules to some extent [33] [34] [35].

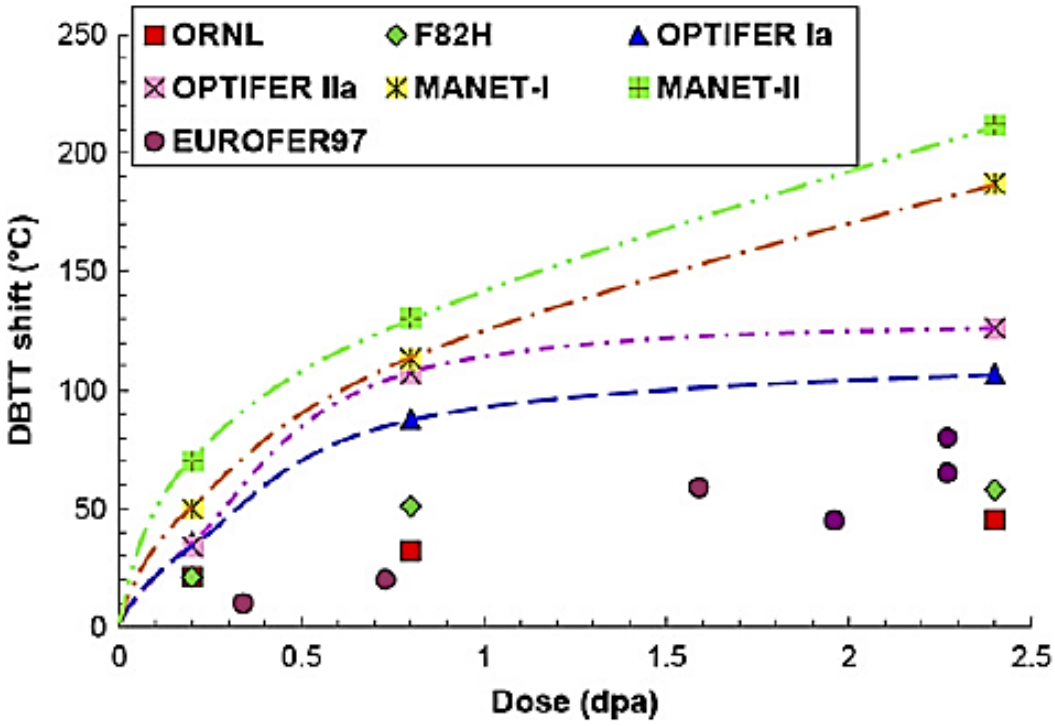


Figure 1.6 Shift in DBTT with neutron dose at 300°C for a selection of RAFM alloys. [36]

Demands for materials capable of operating up to 700°C to boost plant efficiency and ease plasma containment are driving much of the present development work. Klueh demonstrated a microalloyed 9% Cr tempered martensitic steel with acceptable creep characteristics in the 700°C range using themo-mechanical treatments to form dispersions of nanoscale carbonitride precipitates [37] [38]. But even with these improvements, RAFM steels have yet to demonstrate the necessary microstructural and mechanical stability at the doses and helium concentrations anticipated in end of life fusion reactor scenarios. Efforts to simulate those scenarios are now a major component of the materials development effort.

1.5.2 Simulating The Irradiation Environment

Table 1.2 compares the irradiation environments found in a variety of nuclear facilities including a DEMO type fusion reactor and the International Fusion Materials Irradiation Facility (IFMIF) [39]. Both are yet to be constructed and at present there are no facilities capable of producing a neutron spectrum to match the anticipated first wall conditions.

Defect production (in steels)	Fusion neutrons (3-4 GW reactor first wall conditions)	Fission neutrons (BOR 60 reactor)	High energy protons (590 MeV proton accelerator)	IFMIF (high flux test module)
Damage Rate (dpa per year)	20-30	20	10	20-50
Helium (appm per dpa)	10-15	<1	130	10-12
Hydrogen (appm per dpa)	40-50	<10	800	40-50

Table 1.2 Defect production in steels for various facilities [3]

In the absence of a good fusion analogue for materials testing, other more available radiation sources have to be pressed into service. Since each differs in one or more ways from the actual conditions of interest, establishing good data correlation becomes essential [40]. Fast fission reactors offer one approach capable of delivering up to 40 dpa per year but suffer from such low transmutation rates that samples need to be doped with Ni or B to compensate for the low neutron energies and boost helium production [41].

In an effort to avoid the introduction of helium breeding dopant elements, Yamamoto et al explored the possibility of using α emitting isotopes deposited onto samples to implant helium under neutron flux [42]. Figure 1.7 outlines the basic concept of an implanter foil geometry which may be modified to supply fusion relevant helium/dpa ratios and dpa rates for a given neutron spectrum.

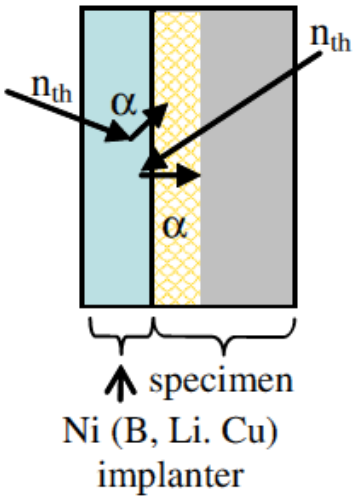


Figure 1.7 Ni implanter foil deposited onto a sample forming a helium implanted layer under neutron flux. Thicknesses vary from 1.0 to 4.0µm [42]

In the likely event of a fast test reactor being unavailable for use there are a variety of accelerator based neutron sources including; deuteron beams with tritiated targets, neutral beams with plasma targets, deuteron beams with lithium targets and spallation sources. Some of these methods make good fusion surrogates and the present design of IFMIF makes use of a flowing lithium target for a 40MeV deuteron beam [40]. However major technical challenges need to be overcome if accelerators like these are to be continuously operated over the necessary time scales [40].

In practice neutron irradiation experiments are difficult to undertake because of the handling problem which limits experimental techniques to those easily performed in a hot cell. When combined with the issue of reactor access these difficulties have motivated the use of charged particle accelerators to inflict displacement damage and implant helium in candidate alloys.

Ion beams can deliver very high dose rates and are capable of delivering end of life doses to materials in a matter of hours. Although simpler and less costly there are two major difficulties to contend with. The elastic cross section of heavy ions confines displacement damage to a layer a few microns from the irradiated surface. Focused ion beams are needed to access the implanted layer and the associated micromechanical assessment techniques introduce scaling issues and size effects some of which are discussed in Section 1.6.4 [43].

The approximation of a neutron flux using heavy ions to cause damage and helium ions to simulate transmutation raises the question of how to satisfactorily compare the one with the other. One approach is to simply consider the incident self-ions to function as the primary recoil atom (PRA) produced by a neutron collision [8].

The PRA spectrum determines the amount of energy received by the target lattice and may be related to the total damage in the material. Different PRA spectra cause different types of damage and samples irradiated to the same dpa may suffer from a variety of different defects. Matching the PRA spectrum to the anticipated neutron flux and comparing the damage morphologies from different irradiations enables ions to be substituted for neutrons with some confidence [43].

The role of the injected interstitials, dose rate dependencies, the exact circumstances of dual implantations and beam heating all need consideration but ultimately the speed and ease of ion irradiation make it far easier to iterate conditions and assess computational models [8]. These principles are extended in gas implantation studies using argon and neon models of the transmutant helium, in an attempt to simplify the subsequent detection and analysis of the accumulated gas [44] [46].

Comparisons of helium and neon implantations in nickel conducted by Marochov in 1988 demonstrated that neon makes a good surrogate for helium provided local gas concentrations are controlled in the implantation process. Being a heavier atom, neon enables both displacement damage and gas to be delivered to a target in one implantation [44]. Zhang applied these findings in an embrittlement study of RAFM and ODS alloys at high neon doses [45].

Both Zhang and Klimenkov exploited heavier gas surrogates to enable energy dispersive x-ray (EDX) characterization of bubble populations, a technique incapable of detecting light elements like helium. Klimenkov used the Kα line from argon incorporated into the microstructure during manufacturing to determine approximate bubble pressures from x-ray signal intensities, obviating the need for a separate gas implantation process [46]. The findings from these studies, particularly those using trapped argon gas are discussed in more detail in Section 3.4.3.

1.6 Oxide Dispersion Strengthened Alloys

1.6.1 Introduction

Oxide dispersion strengthened steels build on the properties of RAFM steels by supporting all the microstructural components necessary for irradiation resistance. These include a dense dispersion of nanometre scale gas trapping sites that protect grain boundaries, suppress swelling and potentially boost creep strength enabling operation at temperatures beyond the displacement damage regime.

These trapping sites are formed from yttrium oxide based nanoparticles precipitated from solid solution during a hot consolidation process first developed by J. J. Fisher for the International Nickel Company in 1978 [47]. The compositions of four early alloy systems are shown in Table 1.3.

	Elemental Compositions (wt%)						
	Fe	**Cr**	**W**	**Al**	**Ti**	**Mo**	**Y_2O_3**
MA956	BAL	20	-	5	-	-	0.5
MA957	BAL	14	-	-	0.9	0.3	0.25
PM2000	BAL	20	-	5.5	0.5	-	0.5
12YWT	BAL	12	2.5	-	0.4	-	0.25

Table 1.3 Developmental ODS compositions (wt%)

Early commercial materials fabricated by the Fisher method included the aluminium containing ODS alloys MA 956 and PM2000, both of which suffered from coarse microstructures dominated by Y-Al-O complex oxide particles [50]. By contrast aluminium free variants like MA 957 supported a fine dispersion of Y-Ti-O complex oxide particles and demonstrated the considerable improvement in tensile properties shown in Figure 1.8. [48] [49] [50].

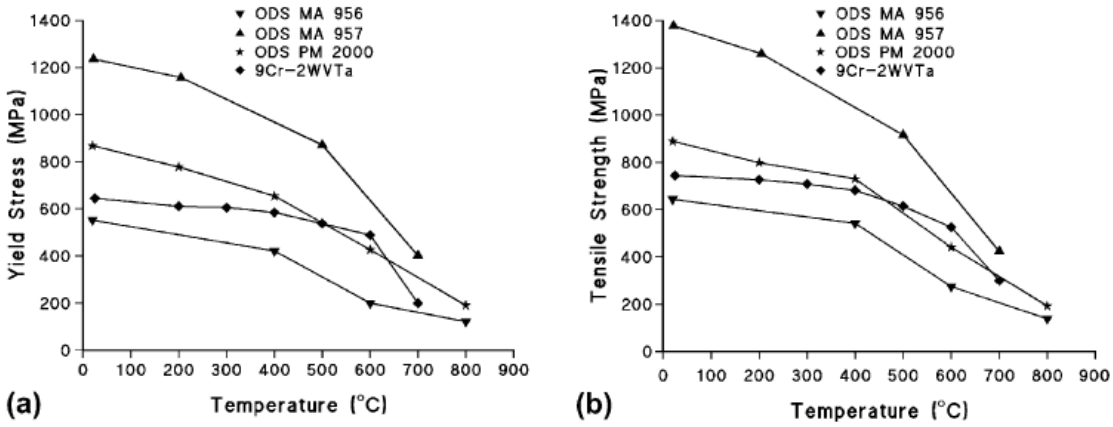


Figure 1.8 Comparison of tensile properties for the MA 956 and PM2000 (Y-Al-O ODS systems) MA 957 (Y-Ti-O ODS system) and a conventional 9Cr reduced activation steel (a) Yield stress (b) Tensile strength [50]

Figure 1.8 shows the loss of tensile performance with temperature for all the ODS steels, although MA 957 demonstrates considerably improved tensile properties up to 700°C [49]. These improvements are generally attributed to the denser particle dispersion that forms in titanium containing systems. The general trend in both tensile and creep rupture properties as shown in Figure 1.9 supports the present reliance by most developmental alloys on some variant of the yttrium-tungsten-titanium (YWT) formulation and the dense dispersion of fine Y-Ti-O precipitates it yields.

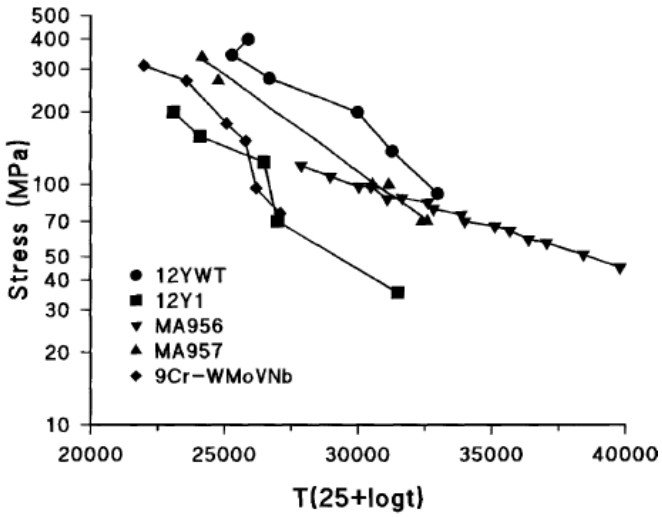


Figure 1.9 Rupture stress comparison of the commercial (MA 956 MA 957) and experimental (12YWT 12Y) ODS alloys using the Larson Miller Parameter (T = temp t = time) [50]

In the following sections the fabrication processes and compositional parameters used by various research groups to produce ODS materials are surveyed and the characteristics and formation mechanisms of the oxide nanoclusters are discussed. Mechanical properties are briefly considered before the closing sections review the unprecedented irradiation stability and gas management properties of the ODS microstructure.

1.6.2 Fabrication Methods and Processing Variables

Although it is beyond the scope of this review to make a full discussion of the immense body of work completed on ODS fabrication, the methods by which these materials are produced directly determine their microstructural development and thus their irradiation properties, through a variety of different variables. Unfortunately discussions of these variables are often frustrated by the presence of commercial vendors in the powder processing industry who consider such information to be commercially sensitive.

Figure 1.10 shows a schematic of the basic ODS production process. Elemental or pre-alloyed powders are mechanically alloyed by ball milling with powdered yttrium oxide. The yttrium oxide dissolves in the iron chromium matrix in a process which may be monitored by x-ray diffraction (XRD) and EDX [51]. The milled powder needs to be degassed and canned in a mild steel vessel for hot consolidation which may be by hot isostatic pressing (HIP) or extrusion. Thermo-mechanical treatments usually follow consolidation and vary depending on the uses of the completed product [52] [53].

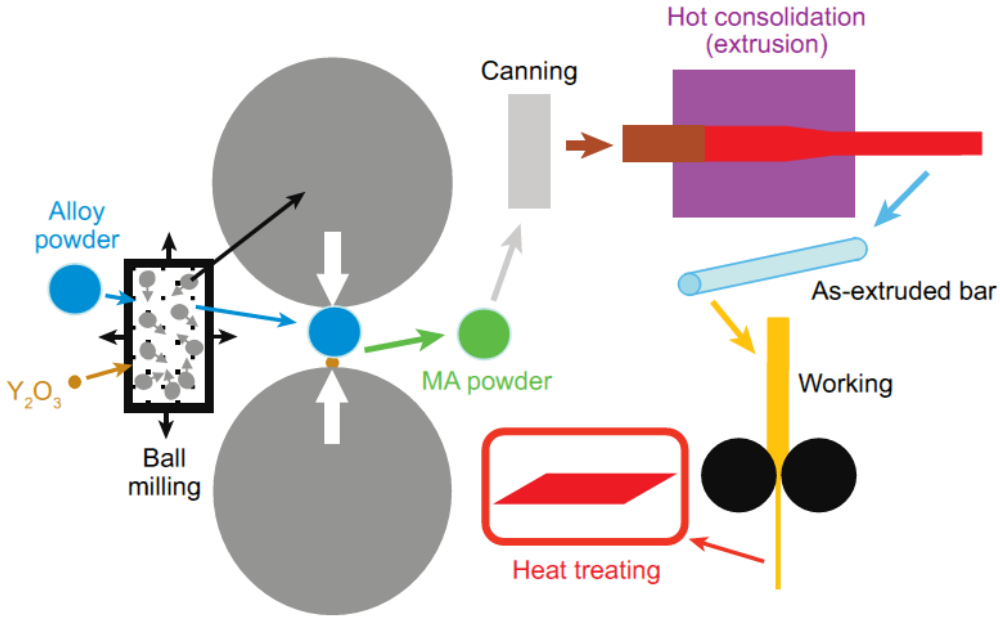


Figure 1.10 Schematic of the ODS fabrication process showing mechanical alloying and consolidation by extrusion followed by thermo-mechanical heat treatments [14].

The variables at each step in the process flow need to be considered to understand the relationship of process conditions to the development of a radiation tolerant microstructure. Typical compositions follow the YWT pattern discussed above, with Cr 9 - 14 wt%, Ti 0.2 - 1.0 wt%, W 1 - 3 wt% and Y_2O_3 0.25 - 0.5 wt% [14]. Each component fulfils a role in the alloy. Corrosion and oxidation resistance relies on the Cr content of the matrix, for which the W provides solid solution strengthening while Y, Ti and O cluster together to form the dispersion strengthening and gas trapping sites [14].

The mechanical alloying process involves continuous welding and fracturing of the powder particles under the impact of steel milling balls in a rotating vessel. These are made from a hard material often similar in composition to the powder to reduce contamination. The milling occurs in an inert atmosphere over the course of tens of hours, typically at speed of between 200 and 400 rpm. The process reduces the mixture of brittle ceramic and ductile metal to a powdered alloy ready for consolidation [54].

The 10µm to 20µm powder grains are saturated with yttrium, oxygen, vacancies and dislocations. The susceptibility to contamination by atmospheric gases and eroded

milling vessel material may be countered by shorter milling periods and lower speeds but all milling variables and their dependencies need to be considered. Suryanarayana provides a comprehensive survey of milling technologies and parameters for reference in [55] and [56]. The milling systems and variables chosen for the production of alloys used in the following experimental sections are discussed in Section 3.2.

The material development programs directed by Ukai for breeder reactor cladding directly demonstrated the impact of milling variables on the irradiation performance of consolidated material [57]. Ukai sampled material milled in both helium and argon subjected to various consolidation processes and heat treatments, which along with other post processing methods are discussed below.

Milled powders are usually vacuum degassed and canned prior to consolidation by either hot isostatic pressing or extrusion at 1000°C to 1200°C. The thermal effects of consolidation can be simulated by annealing in the same temperature range, an approach validated by Alinger using neutron scattering data taken from annealed and consolidated samples of a 14YWT alloy presented in Figure 1.11.

The curves show the neutron scattering cross section varying with scattering vector and provide an indication of both particle size r and number density N_d as indicated on Figure 1.11. The steadily changing shape of the curves suggest a modest particle coarsening effect with processing temperature but significantly the annealed and consolidated curves lie on top of one another, supporting the subsequent use of annealing to study the effects of consolidation on the particle dispersion [58].

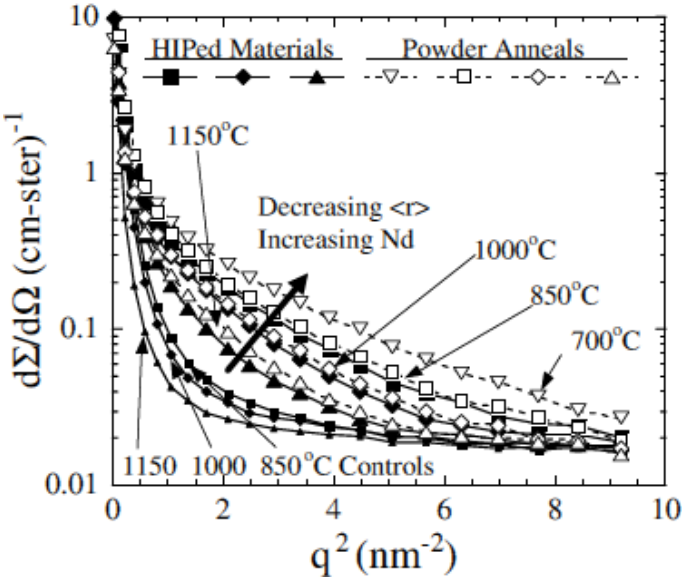


Figure 1.11 Variation of neutron scattering cross-section with scattering vector showing the effect of consolidation / annealing temperature on cluster formation in a 14YWT ODS alloy. [58]

The method of consolidation directly influences grain structure, forming elongated textured grains in extruded material. A 10:1 length to width ratio commonly appears in extruded pipe material, producing a low toughness orientation for crack propagation and reducing hoop creep strength by up to 50% compared to the axial direction [14]. Post extrusion thermo-mechanical treatments are used to mitigate these problems and enable the grain morphology to be controlled. Ukai placed particular emphasis on the use of these treatments in the manufacture of fast reactor fuel cladding from 9 - 11Cr martensitic ODS alloys and provides a summary of the considerable body of work completed for these materials in [59] and [60].

Use of the austenite to martensite phase change in martensitic and ferritic martensitic steels, developed in Europe and Japan, helps to limit grain anisotropy for pipe and plate applications but the formation of coarse oxide phases in the martensite weakens these materials. Optimum values for process parameters are able to mitigate these problems but in general oxide and carbide particles form in both martensitic and ferritic ODS alloys. Although usually tolerable these phases can both suppress Y-Ti-O clustering and cause embrittlement [59][60].

In general the selection of process parameters and alloy constituents needs to account for the potential formation of a variety of phases which may evolve in service at high temperatures and under neutron irradiation to yield a host of microstructural defects. A successful fabrication is widely regarded as delivering a material composed of sub-micron equiaxed grains, containing a dense dispersion of Y-Ti-O nanoclusters. The character of these clusters forms the core area of current ODS development [61].

However, the prevailing trend towards combining the particle dispersion with a fine grained microstructure likely originates in the unsubstantiated attribution of any large grained regions in an ODS microstructure to the uneven distribution of particle forming elements during mechanical alloying. This assumption is shown to be mistaken in Section 3.3.1 and the deconvolution of the microstructural and particle hardening mechanisms demonstrated in Section 6.4 calls the present assumptions regarding the benefits of a fine grained alloy into question.

1.6.3 Properties and Structure of the Oxide Dispersions

Transmission electron microscopy (TEM) and atom probe tomography (APT) studies by Miller and Hoelzer identified 5nm to 20nm yttrium-oxygen clusters in consolidated MA 957 [49]. The micrographs and atom maps produced in these studies and shown in Figure 1.12 support earlier studies by Ukai and Larson on titanium-oxygen clustering and demonstrate the significant refinement of the particle dispersion with the addition of titanium [62][63]. A variety of complementary techniques including TEM and APT have been used to characterise both the particles and the nature of the particle formation process.

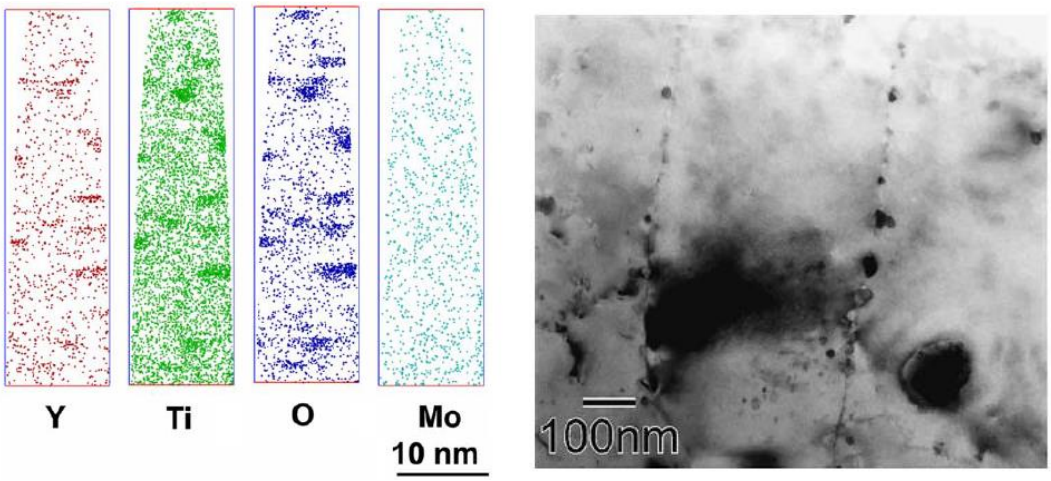


Figure 1.12 Y-Ti-O Clusters in MA 957 (a) APT maps of Y Ti O and Mo (b) TEM micrograph showing clusters segregated to a grain boundary [49]

Alinger largely relied on small angle neutron scattering (SANS) to characterise particle populations, including measurements of the average radius *r,* number density *N* and volume fraction *f* [58] [64]. Although difficult to interpret, data sets like those shown in Figure 1.11 enabled both the determination of r = 1.3nm, $N = 6.6\times10^{23}m^{-3}$ and f = 0.65% for MA 957 and implied cluster stoichiometries of $Y_2Ti_2O_7$ and Y_2TiO_5 [60].

These findings were consistent with TEM studies of MA 957 and in general SANS and TEM data collected from YWT alloys match closely [66]. By contrast APT data from YWT systems has differed appreciably from TEM and SANS [49], showing metal to oxygen ratios of 1:1 and Ti to Y ratios of 1:3 suggesting that the particles are either metastable phases or possibly incoherent precipitate precursors [65].

Odette expressed concerns with the interpretation of APT data [66] and considers the pyrochlore $Y_2Ti_2O_7$ structure to be a well-established feature of the 2nm particles commonly found in YWT alloys, substantiated by extensive HRTEM and SANS studies [66]. However the interpretation of SANS data requires extensive prior knowledge of the system under study and therefore the apparent agreement between SANS and TEM may simply be the result of using TEM observations to undertake this interpretation.

The particular interpretive difficulties in APT occur at the interface between the oxide particles and the surrounding alloy. Differences in the field evaporation conditions between the iron and the ceramic cause a preferential evaporation of the oxide particle. The electric field distortions produced by the uneven evaporation warp the flight trajectories of the surrounding material on field ionisation. This artificially mixes ions from the surrounding alloy into the particle during detection producing chemo-spatial artefacts in the reconstruction [61].

The effect of these trajectory aberrations are discussed by Marquis in a comparison of MA 957 and ODS Eurofer 97. Several small 2.0 to 3.0 nm yttrium rich clusters are shown in the atom maps presented in Figure 1.13 alongside averaged one dimensional concentration profiles taken through the clusters along the evaporation direction. The solute (yttrium and titanium) enriched regions seen beneath these clusters are identified by Marquis as indicative of an aberrated reconstruction of a core-shell structure produced when the core solute atoms preferentially evaporate [67].

Figure 1.14 presents further evidence for these effects showing yttrium, titanium and oxygen rich cores surrounded by chromium shells in particles between 8.0 and 10.0 nm in size. Since these features are larger than the aberration length scales, the distortions present in the smaller particles are absent from Figure 1.14. Consequently the core-shell structure here is easily spotted in both the atom maps and the concentration profiles [67].

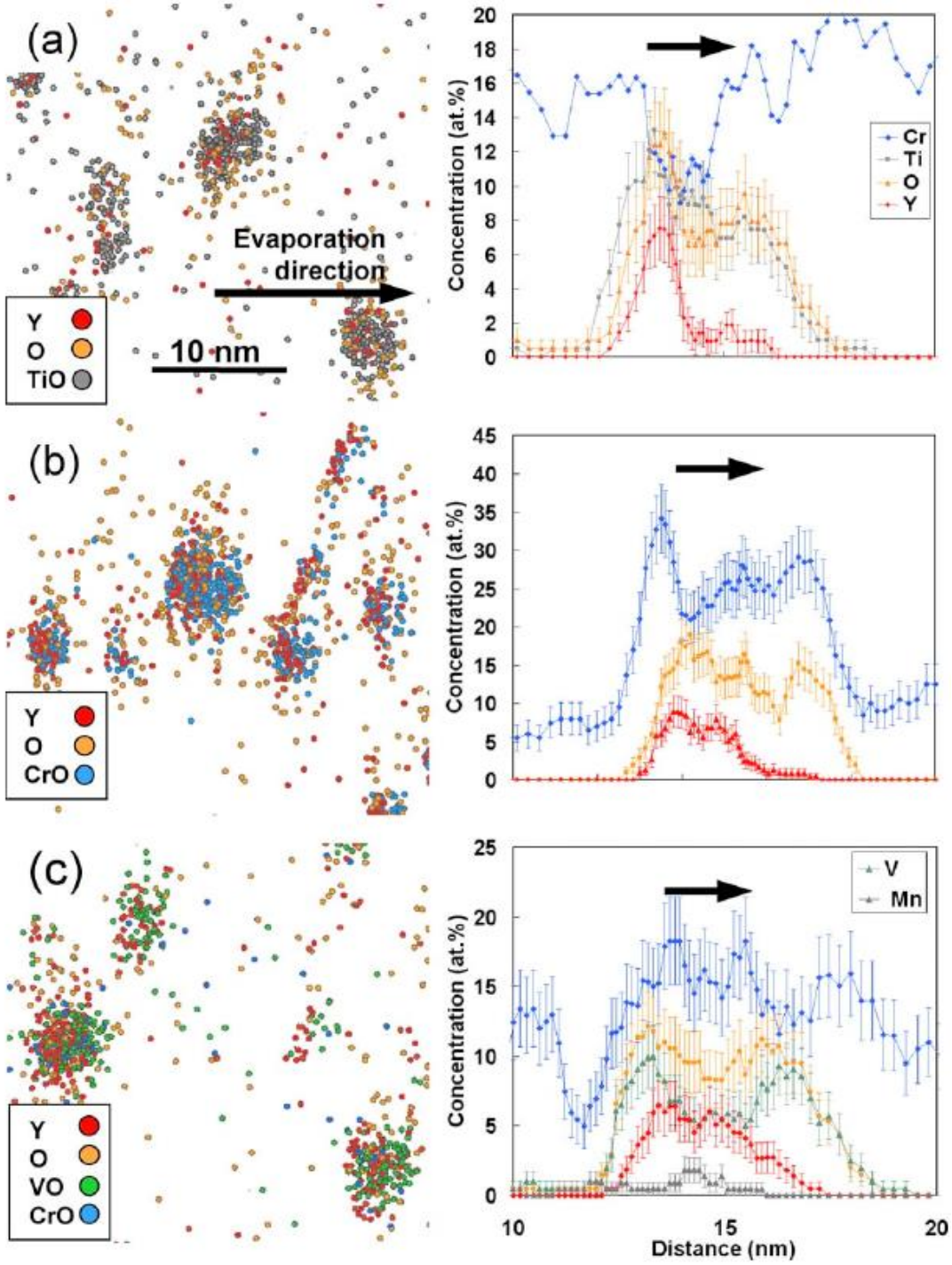


Figure 1.13 APT reconstructions of the smaller clusters and concentration profiles along the evaporation direction showing the distorted YTiO core and Cr shell [67]

(a) MA 957 (b) ODS Fe - 12Cr (c) ODS Eurofer 97

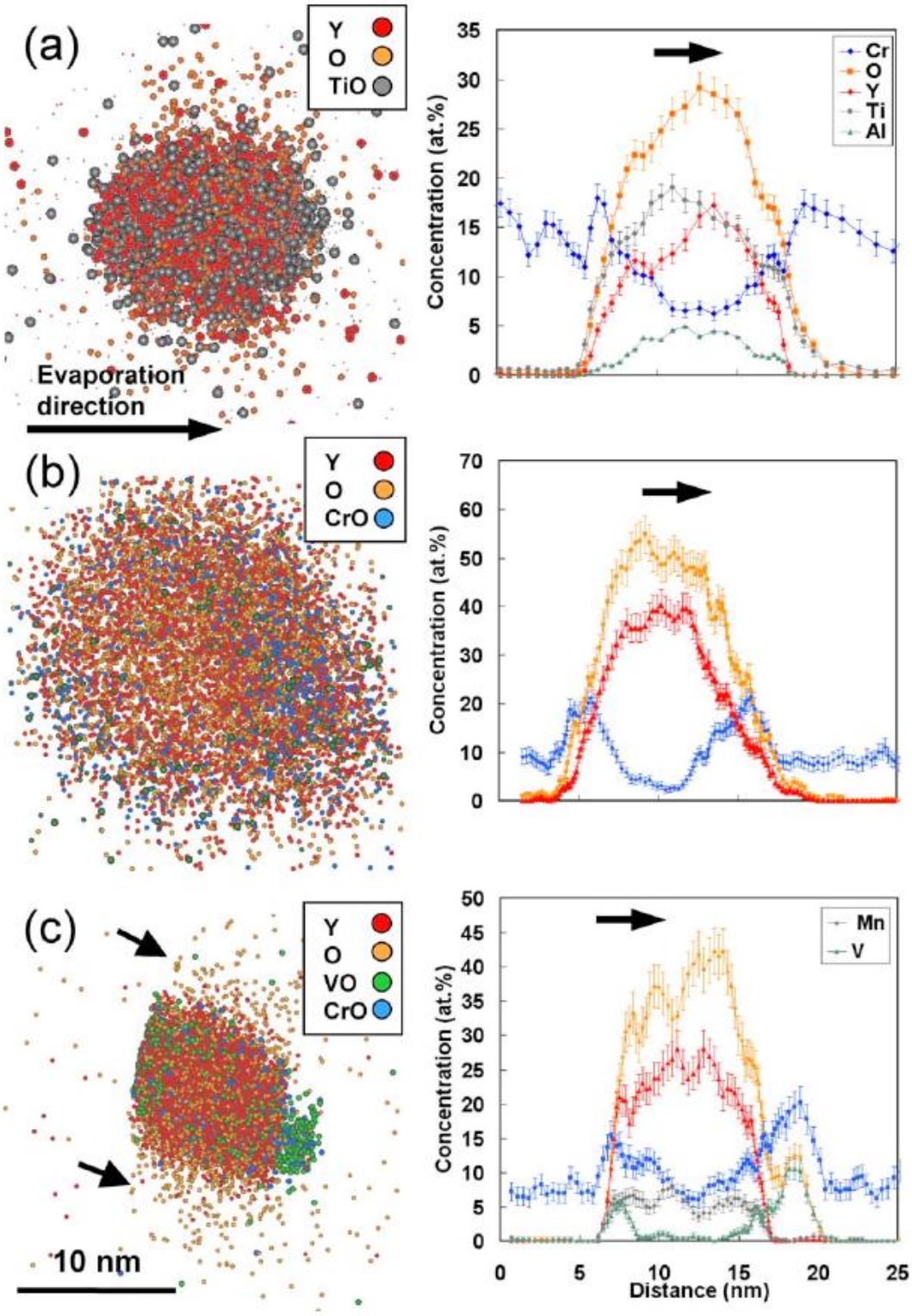


Figure 1.14 APT reconstructions of the larger clusters and concentration profiles along the evaporation direction showing the YTiO core and Cr shell [67]

(a) MA 957 (b) ODS Fe - 12Cr (c) ODS Eurofer 97

Hatzoglou [68] similarly makes use of an analysis along the evaporation direction to see the chromium shell by exploiting those occasions when an oxide particle is exposed to a uniform electric field. These occur just before the particle begins to field evaporate and at the moment when evaporation ends. At these points the material surrounding the particle ionises in a uniform field, experiencing minimal aberration as shown in Figure 1.15. This successfully resolves the chromium enrichment in these regions. To date reproducing the artefact computationally and formulating a possible correction has proven difficult.

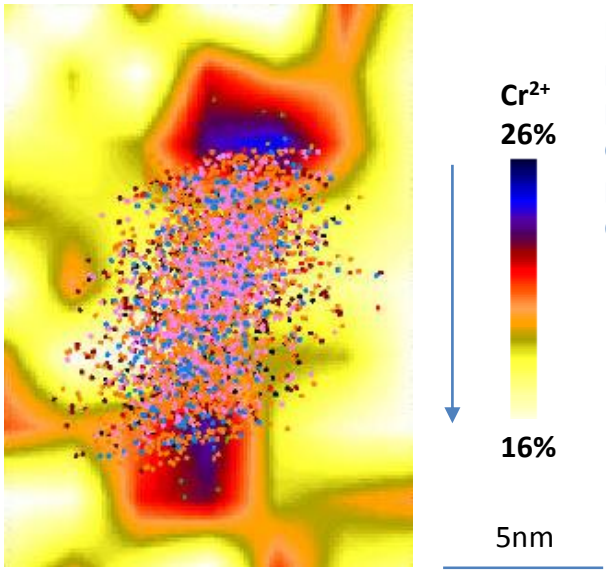


Figure 1.15 Chromium concentration profile around an yttrium oxide particle showing the evidence of a chromium shell above and below the particle. Note the arrow indicated the direction of evaporation [68]

Though a known artefact, the aberration problems discussed in [67] and [68] continue to influence the interpretation of APT data. Rogozhkin et al used the BOR-60 research reactor to irradiate ODS Eurofer 97 samples to 32 dpa at 330°C in 2011. These were run in a hot cell adapted atom probe and the data compared to unirradiated material. 1.0 to 3.0nm clusters enriched in Y, O, Mn and Cr but depleted in V by the irradiation process were identified and discussed but these conclusions are undermined by references to the abundance of matrix element in the clusters, which Rogozhkin considers to be evidence for their essentially diffuse nature [69].

Rogozhkin admits the statistical limitations of the small data sets obtained from the irradiated material but Marquis specifically considers the presence of matrix atoms in the nanoclusters to be an aberration artefact, deliberately subtracting matrix concentrations of Fe and Cr from the data set prior to cluster characterization [67]. No

aberration correction methods are discussed in either [67] or [69] and the application of the recently developed lattice rectification methods presented by Moody et al would seem premature for materials of such complexity [70].

Instead Marquis recommends complementary TEM observations be conducted of the particle structure allowing ions identified in an APT dataset to be correctly partitioned to the shell or the core upon reconstruction [67]. Resolving these structures in the TEM requires a high resolution capability with combined chemical analysis and some confidence in HREM interpretation to overcome the potential difficulties associated with magnetic samples and subnanometre features.

Williams and Marquis made progress in combining TEM and APT to study the same region of a sample of ODS Eurofer 97 at low resolution [71]. Figure 1.16 shows both the bright field micrograph of an electropolished atom probe tip and the corresponding region reconstructed in the atom probe. A grain boundary and a dispersion of nanoclusters are evident but the TEM micrograph lacks the necessary resolution to confirm the concentration profiles shown in Figure 1.17 which appear to indicate core-shell segregation patterns in the solute elements [71].

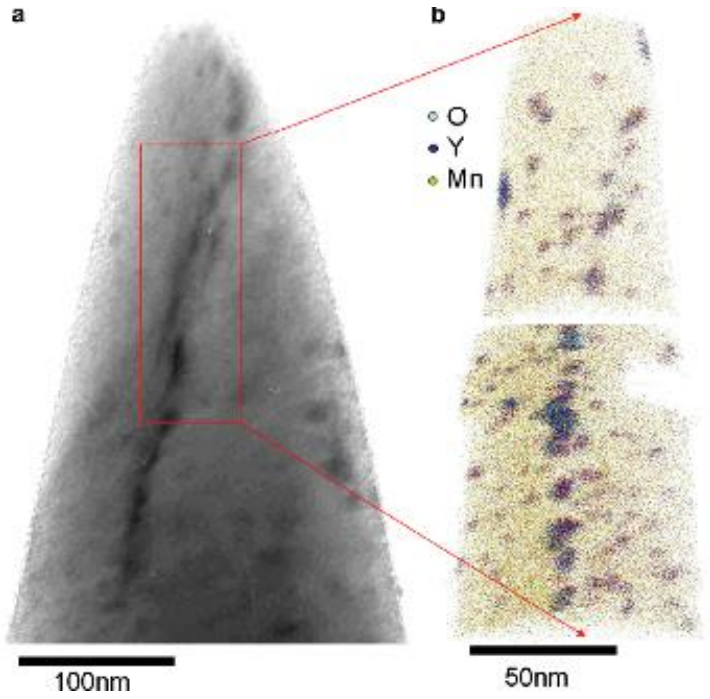


Figure 1.16 ODS Eurofer 97 atom probe sample (a) Bright field TEM micrograph showing a grain boundary (b) Atom probe reconstruction showing the same boundary in O, Y and Mn [71].

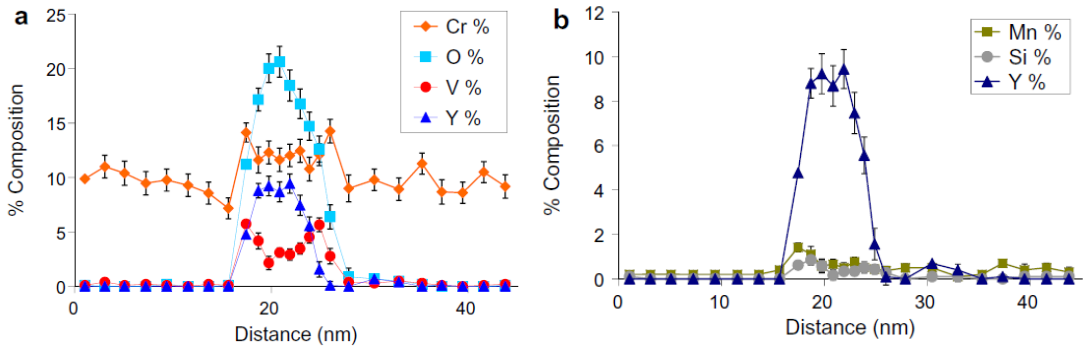


Figure 1.17 1D APT concentration profiles taken in the evaporation direction through a nanocluster showing the solute shell and YO core of the particle [71].

Based on the data presented in Figure 1.17 various particle formation routes are discussed by Williams [71]. The concentration profiles like those shown in Figure 1.17(a) suggest a solute segregation process, building a shell around a particle core precipitated from the solid solution. Alternatively if vanadium and chromium play the role assigned to titanium in the particle formation routes proposed by Oka, shell formation could directly assist particle nucleation and growth by lowering interfacial energies [72].

Both of these routes are considered by Williams, but the difficulty in reliably interpreting the reconstructed data prevent firm conclusions being made. A more comprehensive study of the particle formation process at each stage of alloy fabrication builds upon the data presented in [71] using an Fe-14Cr-2W-0.3Ti (wt%) system alloyed to either $0.3Y_2O_3$ or $0.5Fe_2Y$ (wt%) [73]. The reconstruction problems are addressed via a robust cluster selection method developed in [74] and a systematic study of the field evaporation process in bulk Y_2O_3, $Y_2Ti_2O_7$ and Y_2TiO_5 [61] [75].

Satisfied by the stoichiometric compositions measured in the bulk ceramic, Williams finds no reason to believe that the particle compositions measured by APT are erroneous [73]. It is suggested that although thermodynamically more favourable, the $Y_2Ti_2O_7$ structure may only develop in alloys exposed to high temperature thermo-mechanical treatments, like those used by Ribis and de Carlan in their characterisation of $Y_2Ti_2O_7$ particles by HREM (discussed more extensively in Section 4) [73] [76].

Both the Y_2O_3 and Fe_2Y alloys studied by Williams, show particle formation beginning in the mechanical alloying stage and continuing during degassing at 800^{o}C (a much higher temperature than is typically used) before consolidation at 1150^{o}C. Under these conditions, in a low oxygen environment, Williams suggests that the competing thermodynamic and kinetic driving forces in the YWT system favour the defective rock salt oxide structure first proposed by Hirata [77]. The vacancy content of a rock salt particle conveniently allows it to accommodate a variety of different stoichiometries and metal to oxygen ratios, including those commonly reported in APT.

Williams rules out the possibility of controlling particle size and composition using thermal treatments, attributing variations in the particle character from the initial formation during degassing, through consolidation and annealing, to a coarsening process mediated by the formation of large grain boundary oxides from the same solute pool. Given these conclusions, the use of such a high degas temperature becomes questionable, since as Williams notes, the powder undergoes consolidation effectively inoculated by particle nuclei that have developed during the degassing stage of manufacturing [73].

Following a 4 hour consolidation at 1150^{o}C, the Y:Ti:O ratios in the particles shift appreciably from 1:4:10 at degassing to 1:2:3 at consolidation, potentially indicating a significant change in chemistry and structure [73]. Williams considers the roles played by the constituent elements in this change in the context of their relationship to oxygen but no further discussion of their partitioning to a core shell structure or its potential role in particle formation is made [73].

Further work on the core shell structure by Alinger [58] Miller [65] and Klimenkov [78] offers some insight into distribution of titanium in YWT alloys and vanadium in ODS Eurofer. Klimenkov makes use of scanning transmission electron microscopy (STEM), energy dispersive x-ray spectroscopy (EDX) and electron energy loss spectroscopy (EELS) to capture the core shell structure [78]. Cr-V shells and Y-O cores, like those seen in the APT data, emerge in the spatially resolved EDX maps of two ODS Eurofer nanoclusters shown in Figure 1.18. The intensity profiles of EELS and EDX line scans shown in Figure 1.19 enable the rough proportions of the core and shell to be inferred.

The chromium depletion at the particle boundary seen in Figure 1.19(d) leads Klimenkov to suggest that the shell must form on cooling when Cr diffusion rates are low enough for a depleted region to persist in the consolidated alloy. No references are provided but the possibility of particle formation during mechanical alloying is ruled out on the basis of TEM studies conducted on powder particles. Mn and V are assumed to play a part in the particle formation process based upon their potential to fulfil the role assigned to titanium by Ukai [79] and Oka [72].

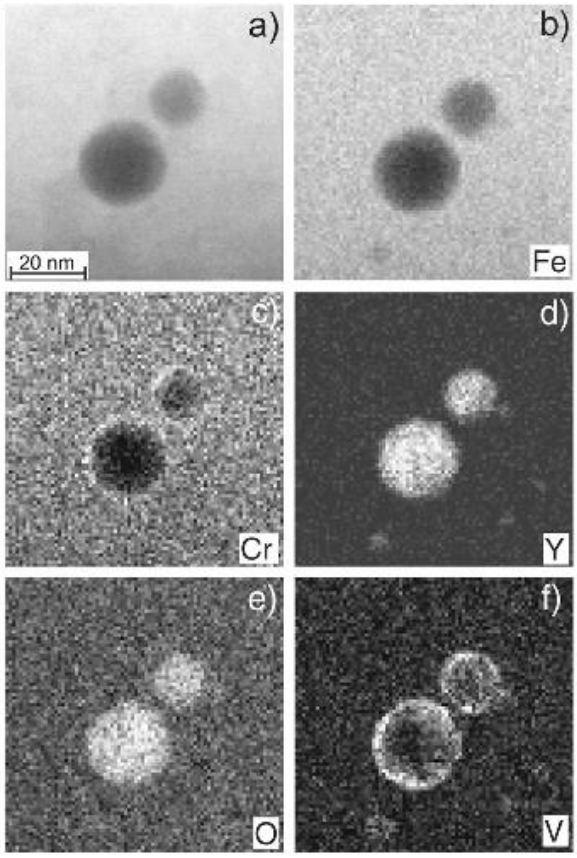


Figure 1.18 EDX mapping of two ODS Eurofer 97 nanoclusters showing segregation of chromium and vanadium to the shell and yttrium and oxygen to the core [78].

(a) HAADF micrograph

(b) Fe - Kα

(c) Cr - Kα

(d)Y - L

(e) O - K

(f) V - Kα

Figures 1.18 and 1.19 demonstrate the capability of analytical microscopy in characterising the particles and the potential for EELS and EDX studies to directly support APT. However, the data presented in Figures 1.18 and 1.19 are taken using a 1nm STEM probe from 10nm to 20nm particles. Since precipitates of these sizes are mostly free from trajectory aberrations when analysed in the atom probe they are less in need of supplementary characterisation to substantiate the reconstruction. Unfortunately in 2 and 3nm particle populations where complimentary techniques would be most beneficial, STEM probes of the nanometre order lack the necessary resolution, requiring the use of alternative techniques.

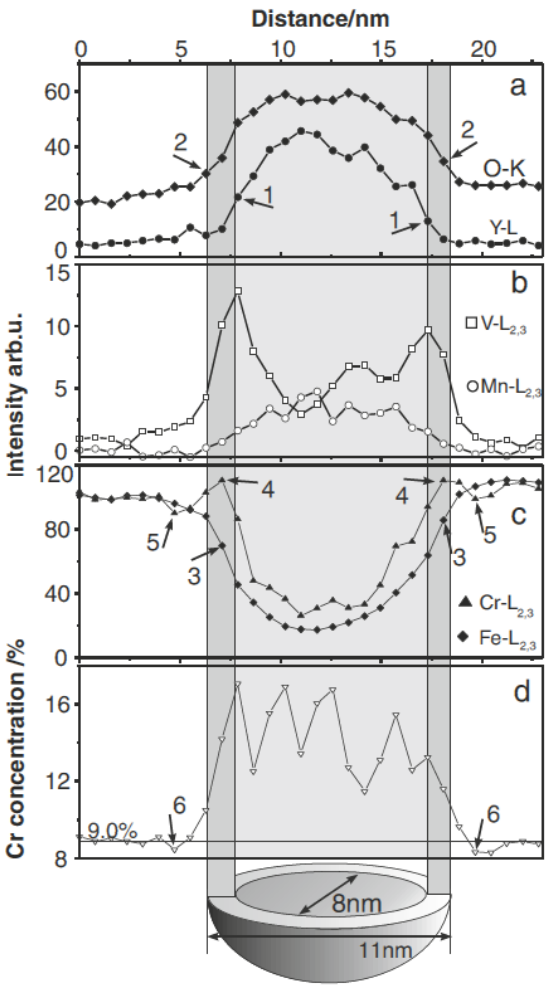


Figure 1.19 Intensity profiles for EDX and EELS line scans taken through nanoclusters showing segregation of the constituent elements to the core and shell regions [78].

(a) O - K and Y - L

(b) V - L and Mn - L

(c) Cr - L and Fe - L

(d) Cr content

Hsiung [80] and Lozano-Perez [81] both attempt to characterise particles like those shown in Figure 1.13 at the subnanometre scale. Each takes a different approach but both capture a core shell structure present in particles of the nanometre order. Hsiung applies HRTEM methods to a Fe-16Cr-4.5Al-0.3Ti-2W-0.37Y_2O_3 (wt%) ODS alloy capturing the micrographs presented in Figure 1.20. These show monoclinic $Y_4Al_2O_9$ oxides embedded in what appear to be amorphous shells surrounding both the small particles like those in Figure 1.20 and larger particles of 20nm or more [80].

The material used in Hsiung's HRTEM study received a basic thermo-mechanical treatment at 1050°C for 1 hour following consolidation. A subsequent study of thermal stability subjected samples to a 900°C anneal for 168 hours and found that the particles lost their amorphous shell. This is indicative of a metastable structure susceptible to equilibrating under prolonged exposure to high temperatures [80].

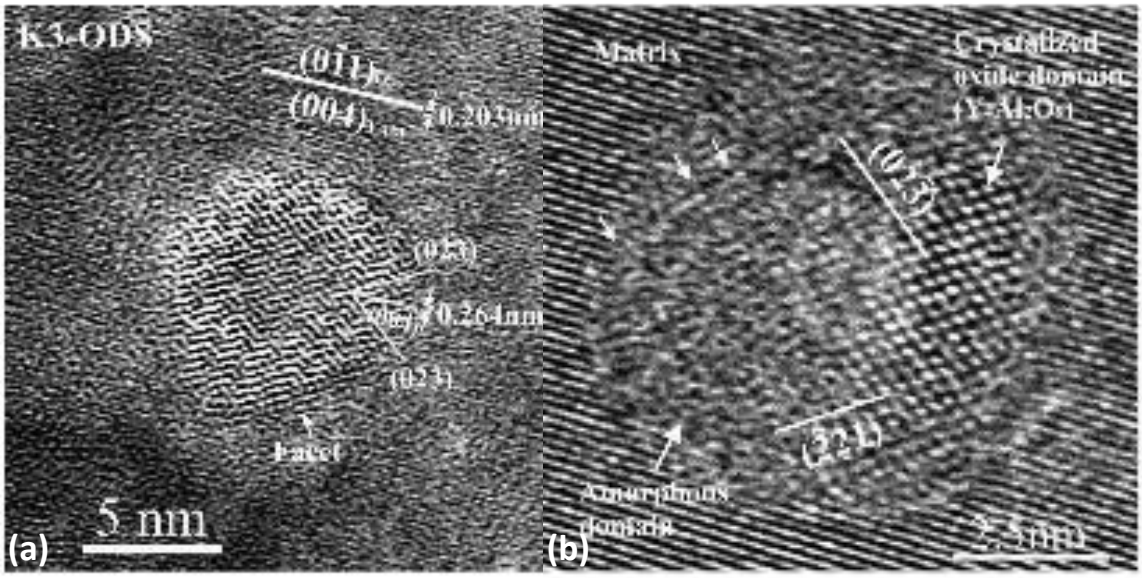


Figure 1.20 HRTEM micrographs of small nanoclusters with orientation relationships determined by FFT methods [80]

(a) Faceted interface and amorphous shell

(b) $Y_4Al_2O_9$ crystal embedded in an amorphous oxide region.

Based on this controversial interpretation, that ignores the other potentially artificial origins of these amorphous shell-like features, Hsiung proposes the three stage particle formation mechanism shown in Figure 1.21. The Y_2O_3 powder particles are fragmented and become amorphous in the milling process. These amorphous agglomerates recrystallize under consolidation, rejecting solute atoms from the core region to a shell. The core and shell composition therefore depend on the alloy components with YAlO cores present in Al based ODS systems and YTiO cores produced by titanium based alloys [80].

The mechanism implies a simple relationship between particle size and shell thickness. Larger particles necessarily need to move more solute and thus build thicker shells, provided the rate of solute rejection to the shell exceeds the rate of diffusion into the matrix [80]. The competing effects of these two processes could be a cause for the shifts in SANS parameters noted by Alinger in alloys subjected to different processing temperature profiles [64].

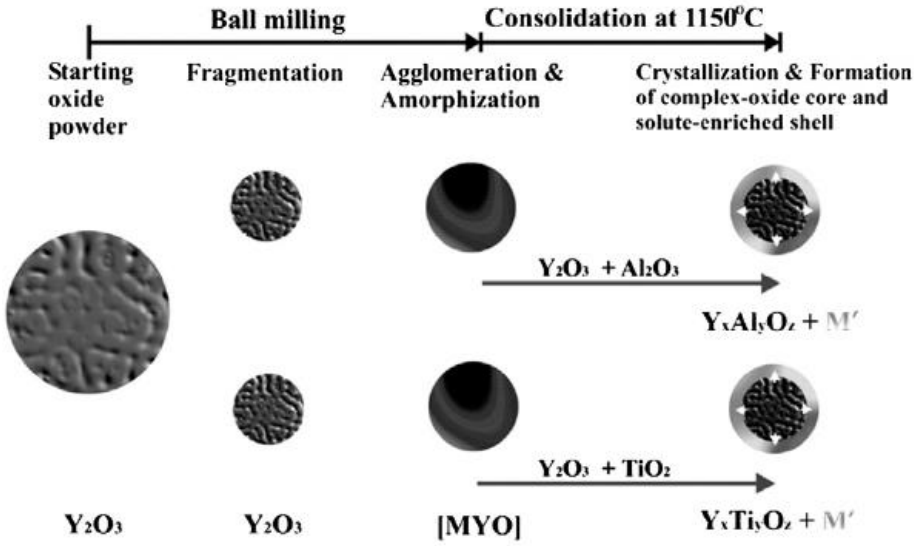


Figure 1.21 Schematic of the three stage mechanism of particle formation proposed by Hsiung [80]

(i) Fragmentation of Y_2O_3 powder

(ii) Fragments become amorphous and agglomerate in the matrix material

(iii) Crystallization of the amorphous oxide core and rejection of solute atoms to shell region.

Slow heating in the powder annealing studies presented in [64] triggered precipitation at temperatures approaching 650°C in 14YWT alloys. If these low temperatures protect the nascent nanoclusters from diffusion, their shell character could be quite different from those processed at more conventional temperatures, typically 1150°C. Regrettably SANS provides no information on particle structure but the use of temperature profiling to control particle character is potentially significant in developing optimum manufacturing methods for these alloys [14] [64].

Lozano-Perez' study of a model 12-Cr ODS alloy used energy filtered transmission electron microscopy (EFTEM) combined with multivariate statistical analysis (MSA) techniques to image subnanometre oxide particles [81]. Like EELS, EFTEM makes use of characteristic core shell electron energy losses to produce compositional maps of a TEM sample. The techniques differ in the manner of data capture. STEM-EELS instrumentation operates in a spatially serial manner while EFTEM captures data in

parallel. Both techniques suffer from similar statistical limitations and benefit from computational post processing [82].

The potential for EFTEM to be a complementary TEM technique for APT and SANS led Certain to combine APT and EFTEM in the characterisation of 9 and 14Cr YWT ODS steels in [83] and [84]. Certain discusses the difficulties encountered by Bentley and Hoelzer who found their attempt to build on SANS studies of a 12 Cr ODS with bright field TEM confounded by surface oxide films which limited their minimum feature size to 6nm [85].

Using an LaB_6 equipped Philips CM30, 2nm features were successfully identified in elemental maps made using the jump ratio technique like those shown in Figure 1.22 [83]. This technique is easy to apply and simply divides an image recorded at the iron absorption peak with one recorded immediately prior to the peak. However, the identification of a substantial particle population below 2nm in size using the atom probe demonstrates the potentially misleading nature of any characterisation based solely upon TEM if a subnanometre resolution cannot be reached reliably, leading Certain to recommend always combining both techniques in future work.

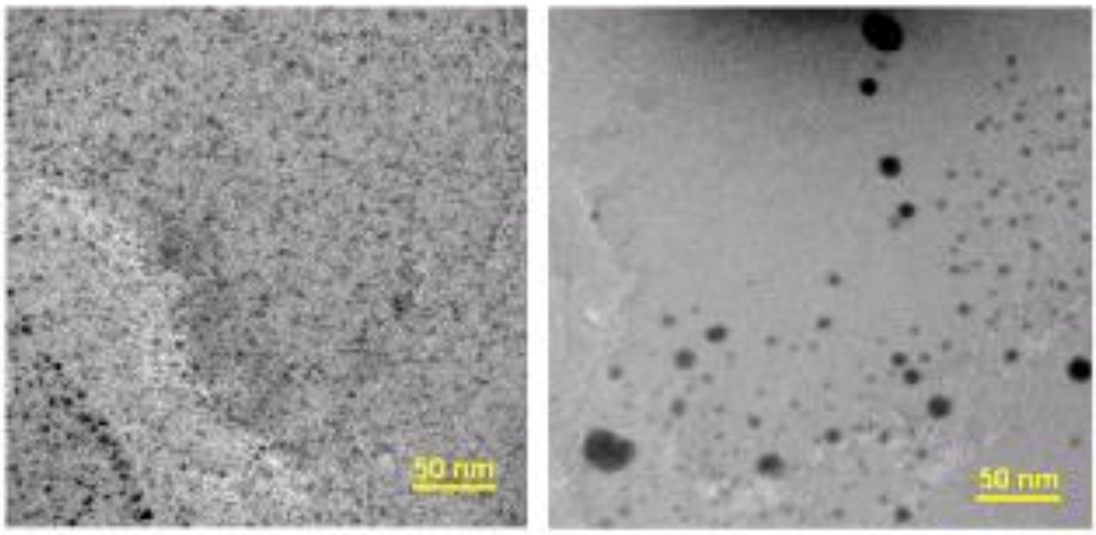
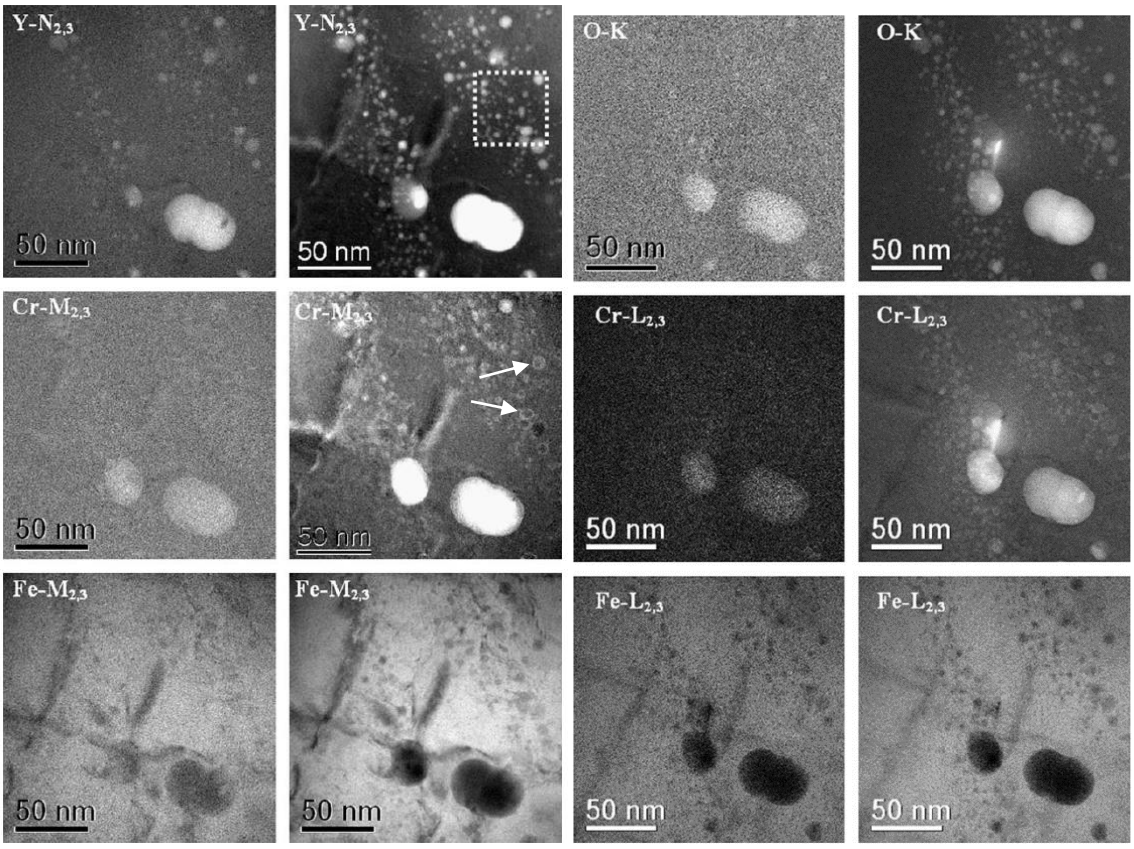


Figure 1.22 Fe M jump ratio micrographs showing the differences in nanocluster distribution from area to area [83].

In an attempt to make EFTEM and APT directly comparable at these scales Lozano-Perez made a characterisation of a simplified Fe-12Cr-0.4Y_2O_3 alloy using a double aberration corrected instrument with improved high tension stability. To compensate

for magnetic interference from the sample the optics were realigned for each new sample area. These were chosen to keep the material thickness below 100nm in each case but even with these precautions noise in the raw data was found to obscure features below 1.0nm in size [81].

Figure 1.23 compares the raw and MSA processed data for both the core shell energy loss and outer shell low energy loss datasets. Although the smallest features are only apparent in the low loss maps the boosted signal to noise ratio delivered by the MSA enables subnanometre particles to be captured in the data. Lozano-Perez concludes that the presence of a Cr rich shell throughout the particle population may even pose a local corrosion risk to the matrix [81].



(a) **(b)**

Figure 1.23 EFTEM maps from a 12Cr - 0.4Y_2O_3 ODS system [81]

(a) Low loss EFTEM elemental maps from raw data (left column) and MSA post processed data (right column). Cr shells are visible around the smaller particles in the low loss Cr map as indicated.

(b) Core loss EFTEM elemental maps from raw data (left column) and MSA post processed data (right column)

1.6.4 Mechanical Properties of Oxide Dispersion Strengthened Alloys

The static and creep strengths of ODS alloys are derived from a fine grain structure, a pinned dislocation network and the dense dispersion of nanofeatures. The long established commercial alloys (particularly MA 957) have been studied extensively and are often used to baseline the mechanical properties of newer alloys or to demonstrate the effects of new processing methods. Figure 1.24 compares the temperature dependent yield stress for a number of MA 957 variants included by Salston and Odette in a comprehensive database of MA 957 properties [86].

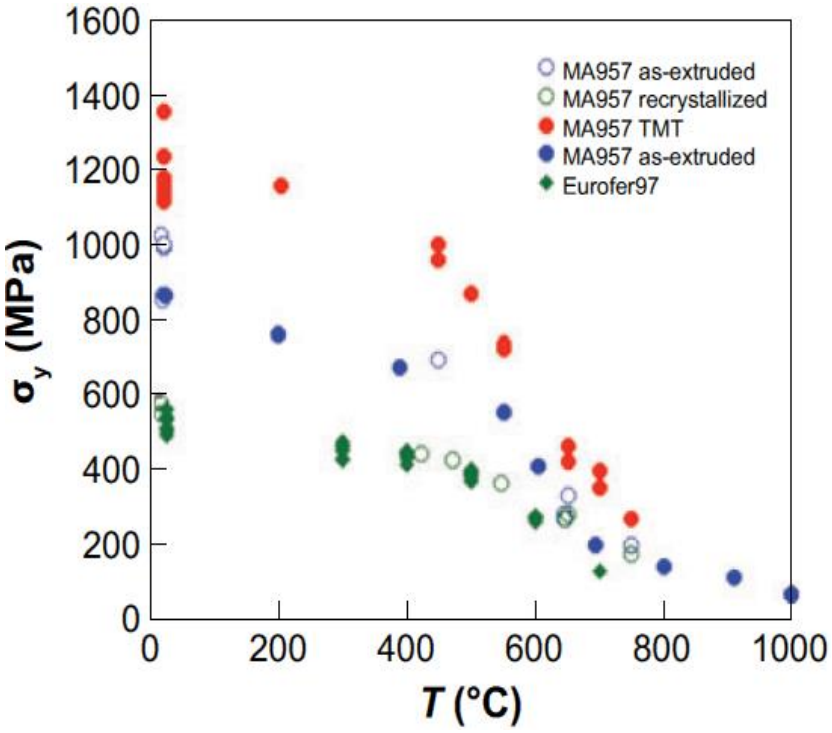


Figure 1.24 Comparison of the temperature dependent yield stress of MA 957 subjected to different thermo-mechanical treatment and a Eurofer RAFM steel [14][86]

The plot demonstrates the impact thermo-mechanical treatments can have on the mechanical performance of an ODS alloy and the comparative weakness of RAFM steels. The strongest alloys are invariably YWT based and become stronger at lower consolidation temperatures [14]. Hoelzer and Bentley demonstrate the boost to temperature dependent yield stress provided by 850°C consolidation for a 14YWT alloy from ambient to 800°C, at which the difference in yield strength between 1175°C and 850°C consolidations of the same alloy exceeds 200MPa. Their data suggest the denser dispersion of nanoclusters formed at lower temperatures is responsible for the additional strengthening effect and observe a concomitant reduction in ductility [87].

Typically ODS alloys show reasonable ductility comparable to tempered martensitic steels. Uniform elongation strains of 2% to 20% and total elongation strains of 5% to 30% are common with a minimum at an intermediate temperature between about 300^{o}C and 700^{o}C [86][88]. However, for all compositions, anisotropy plays a major role in the performance of extruded materials and needs to be taken into account when data are presented [14].

The effects of anisotropy on creep strength were briefly touched on when discussing fabrication methods in Section 1.6.2 but in general high strength ODS materials have high creep rupture strengths and creep onset stresses. Thermo-mechanical treatments may be used to compensate for anisotropic creep behaviour in MA 957 demonstrating that both the nanofeature population and the grain and dislocation structures play a role in creep performance [86] [87] [88].

Fracture toughness shows a dependence on microstructural texture, the orientation of a particular crack system to that texture, and in the case of MA 957, on oxide inclusions elongated by the extrusion process [14]. Modification of carbide and oxide inclusion morphology by thermo-mechanical treatment improves Charpy transition temperatures by up to 100^{o}C and the wholesale reduction in the number of carbides and oxides delivers both high strength and high toughness in the equiaxed microstructures produced by HIPing [89].

In summary, with post consolidation thermo-mechanical treatments, ODS alloys can support yield strengths in excess of 1400MPa combined with moderate toughness improvements above DBTTs between -80 ^{o}C and -40^{o}C [14]. These properties are produced by a combination of a dense nanocluster population and its interaction with the dislocation network and grain structure. Although anisotropy causes directional variations, creep properties are generally good and a combination of processing variables and heat treatments provide opportunities for toughness improvements.

Studying the effects of irradiation on these properties can prove challenging. Though easy to apply and interpret, the conventional mechanical tests used in mechanical

characterisations like those presented in [86] [87] [88] need large volumes of material. The residual activity following neutron irradiation of these samples would confine them to hot cells and complicate handling. Ion implantation alleviates these concerns but produce layers of irradiated material only a few microns deep.

These problems motivated the application of micromechanical techniques capable of accessing the mechanical behaviours of ion implanted layers and neutron irradiated volumes small enough to remove the need for remote handling. A variety of techniques applied to both neutron and ion irradiated ODS and RAFM alloys are outlined by Pouchon [90] and Hosemann [91]. These include nanoindentation and micro pillar compression, the latter implemented using a FIB system.

Nanoindentation is an efficient method for measuring the mechanical properties of thin films including modulus, hardness and creep response but the technique suffers from a number of potential problems. The complex stress state around the indenter tip gives rise to an indentation size effect which increases the apparent hardness of the material as the indent size decreases. Indentation size effects were identified by Hardie in iron chromium alloys in both the irradiated and unirradiated condition [92].

The limited volumes of irradiated material produced when these samples were self-ion implanted frustrated efforts to quantify the size effect in the irradiated alloy [92] but Hardie suggests that the defect dispersion generated by the irradiation could supress the size effect. If so the particle dispersion in an ODS alloy might perform a similar function.

Takayama makes use of the model developed by Nix and Gao [93] to account for the indentation size effect in single and dual ion implanted F82H steels [94]. The model predicts a bulk hardness H_0 for both the unimplanted alloy and the implanted layer up to a 300nm indentation depth h. As shown in Figure 1.25 beyond about 500nm the hardness returns to the value predicted for the unirradiated samples as the plastic zone around the indenter tip moves into the unimplanted material below the implanted layer.

Pile-up around the indentation further complicates measurement and features prominently in a major review of the technique completed by Oliver and Pharr [95]. The accumulation of material around the indent changes the contact area between the indenter tip and the material in an unpredictable way artificially increasing both the measured hardness and modulus. Investigation of a suspect indent site by SEM or AFM allows the area function to be corrected if significant pile-up occurs [95].

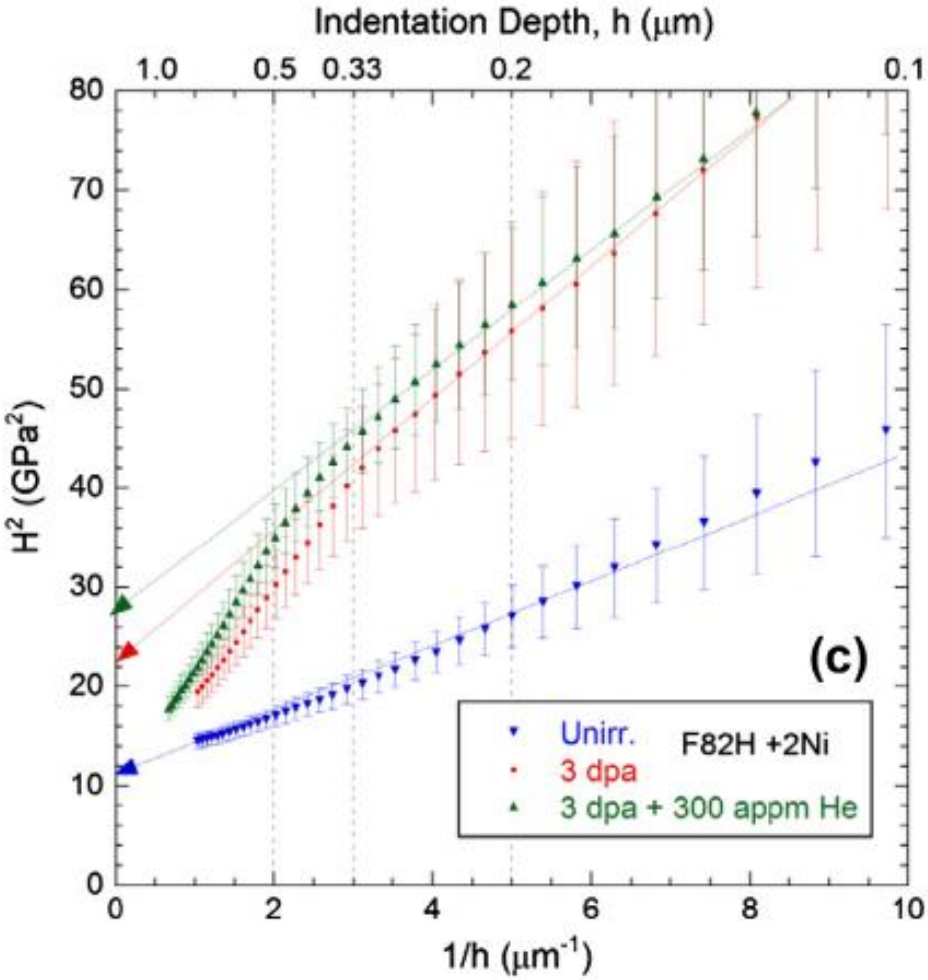


Figure 1.25 Nix and Gao plots of hardness H varying with depth h for implanted and unimplanted F82H showing the shoulder around 300nm where the indenter begins to sample the softer substrate below the implanted layer [94].

Micromechanical testing methods overcome some of the limitations associated with indentation. Offering considerable flexibility in design and implementation, initial experiments used a FIB system to prepare micropillar compression specimens for testing in a nanoindenter using a flat punch. Shin applied the technique in a 15YWT

ODS system using two pillar geometries shown in Figure 1.26 and characterised the deformed microstructure using TEM foils lifted from the compressed pillars [96].

Shin found good agreement between the microcompression measurements and the bulk yield stress measured using tensile specimens. No size effects were present in the stress strain response, even in pillars 1.0m wide, while TEM micrographs show a highly pinned dislocation network. This lead Shin to conclude that the particles define the characteristic length scale in the microstructure and dominate all other effects in the pillars as Hardie supposed [96].

The limitations of the technique are not discussed by Shin but substrate compliance and imperfect FIB milling are both potential sources of uncertainty in micropillar experiments. These have motivated efforts to devise more elaborate methods designed to produce simpler stress states subject to fewer uncertainties, including micro-cantilever bend tests used at various scales to investigated grain boundary fracture and single crystal plasticity. None of these techniques have yet produced published data for ODS alloys but are potentially powerful new methods for investigating the mechanical properties of irradiated materials.

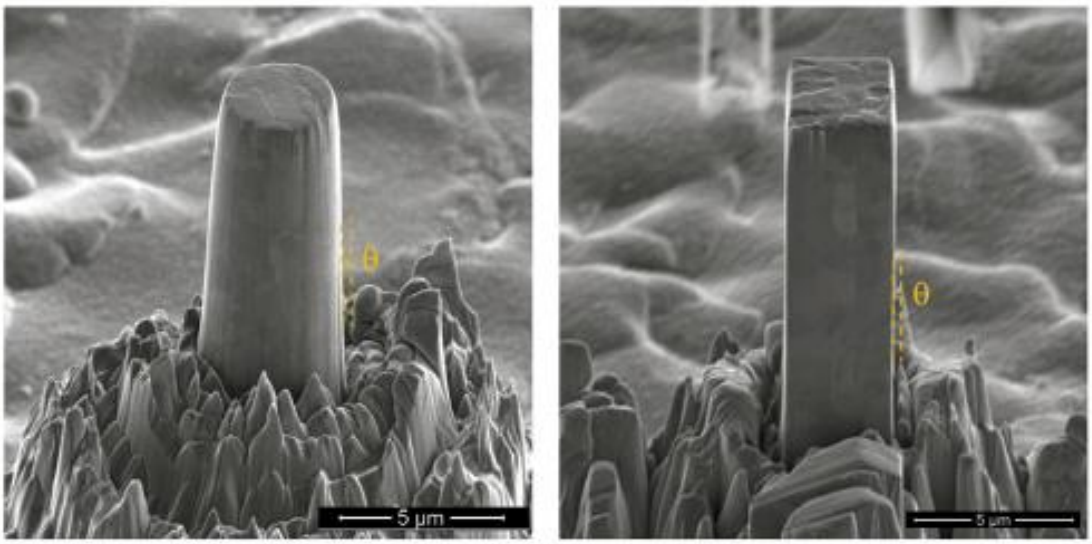


Figure 1.26 Circular and square micropillar pillars used in compression testing of irradiated Fe-15Cr-2W-0.2Ti-0.35Y_2O_3 [96]

1.6.5 Thermal and Irradiation stability of Oxide Dispersion Strengthened Alloys

Thermal stability studies on a variety of ODS alloys were completed by Miller using APT and by Odette using TEM and SANS. Miller refers to a number of high temperature creep and thermo-mechanical processing experiments which find 2 - 4nm YTiO clusters present in samples of YWT alloys for all the studied conditions up to 14500 hours at 800^{o}C, demonstrating the remarkable stability of the particles [49] [65] [97].

Odette and Alinger note the continued stability of the grain and dislocation structure in MA 957 up to 1000^{o}C at 3000 hours [98]. Above 900^{o}C moderate coarsening of the nanoclusters occurs accompanied by porosity and a 3% drop in microhardness. This is possibly attributable to chromium depletion during vacuum annealing. Though no direct evidence for this yet exists in ODS alloys, the significance of chromium evaporation during annealing is considered in Section 4.4.10 [99].

Microhardness continues to drop over 8000 hours at 1000^{o}C. Above 1200^{o}C the microstructure coarsens considerably. Some longer term studies are yet to report but Odette considers YWT based alloys to be essentially stable below 850^{o}C but warns of their vulnerability to α' precipitation at low temperatures and high chromium contents [100] [98].

Yamashita reports the continued stability of the dislocation and grain structure in MA 957 under neutron irradiation up to 100 dpa at 700^{o}C, accompanied by a modest reduction in the number density of nanoclusters [101]. These findings are consistent with ion irradiation studies by Kasada, which found no changes in samples of Fe - 19Cr - 0.3W - 0.3Ti - 0.35Y_2O_3 wt% and Fe - 19Cr - 2W - 4Al - 0.3Ti - 0.35Y_2O_3 wt% irradiated with 6.4MeV Fe ions up to 150 dpa at 700^{o}C [102].

In a series of neutron and ion irradiations, Certain provides evidence for dynamic particle stability, combining EFTEM and APT to show particle dissolution in a Fe-14Cr-3W-0.4Ti-0.25Y_2O_3 wt% alloy over a -75 to 600^{o}C temperature range from 5 dpa [83] [84]. At 100 dpa the EFTEM maps in Figure 1.27 show complete particle dissolution. At service temperatures the microstructure appears unchanged from the unirradiated condition showing a dense particle population that Certain believes continuously recovers from dissolution via the diffusion of ejected solutes back to the particles.

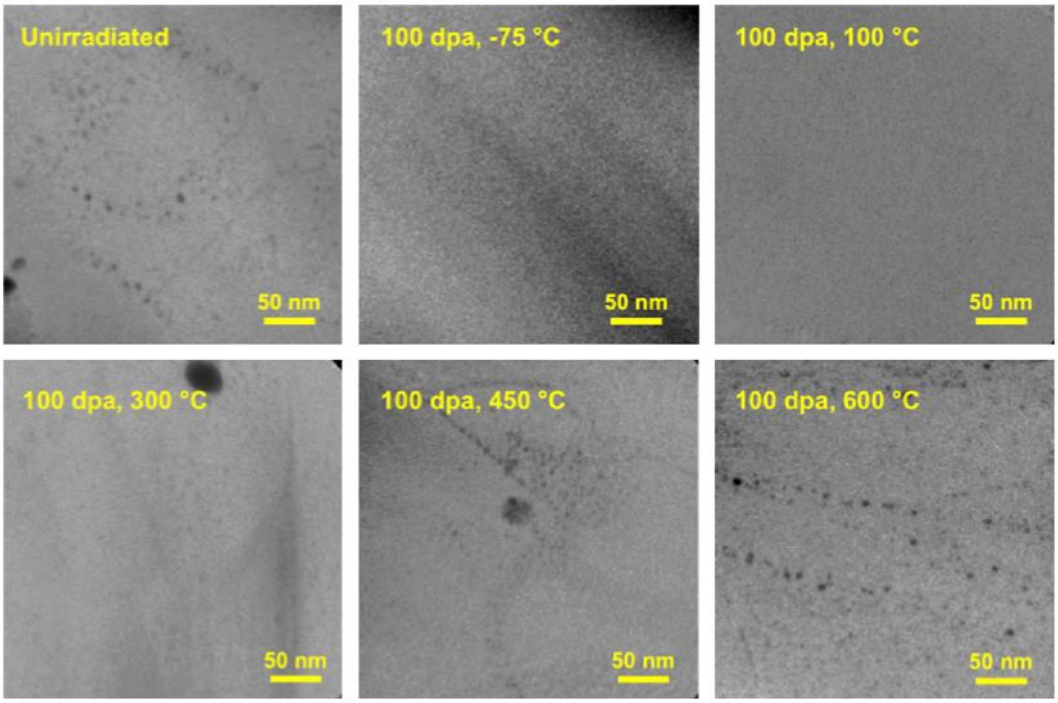


Figure 1.27 Fe-M Jump ratio images from samples of 14YWT irradiated at -75°C 100°C, 300°C, 450°C and 600°C showing dynamic particle stability at 100 dpa [84]

Provided the irradiation takes place at a sufficiently high temperature to facilitate this process, the particle dispersion should remain stable even at very high doses. The dose and temperature dependencies of particle dissolution are likely to vary with alloy composition and particle structure. Monnet observes particle dissolution between 400°C and 580°C in neutron irradiated specimens and reproduces the effect using both ion and electron irradiations but notices the development of smaller particles around larger oxides in the neutron irradiated material [103].

Monnet attributes the presence of these particle halos to the thermal cycle experienced by the neutron irradiated samples in the reactor pile. Certain found no halo structures in any of the samples studied in [84]. Given the unconventional alloy compositions used in [103] and the prevalence of large oxides in the microstructure the particle halos may be an anomalous product of the experimental conditions.

Below 500°C modest swelling does occur in neutron irradiated ODS steels [16]. Although the sink density of their microstructure helps to supress void formation,

Monnet reports voiding associated with the oxide particles in all of the neutron irradiated samples below 500^{o}C [42]. Voids develop under both electron and neutron irradiation in the 400 ^{o}C to 500 ^{o}C range and recovered regions of the microstructure lacking the typical sink density of an ODS were demonstrated to be particularly vulnerable to void swelling in both MA 956 and MA957 [104] [105].

Irradiation hardening effects are similarly confined to temperatures below 550^{o}C reflecting the behaviour of conventional RAFM steels [106]. In general ductility losses accompany hardening and swelling reducing both uniform and total elongation. A comparison of MA 957 and RAFM steel completed by Alamo used the BOR-60 and OSIRIS research reactors to irradiate samples at between 300^{o}C and 325^{o}C to 42 dpa. Ductility losses in the F82H, JLF-1 and Eurofer RAFM steels were double those seen in the MA 957 [107].

MA 957 offers further improvements over RAFM alloys in irradiation creep studies especially at temperatures above 550^{o}C. Up to this threshold the precipitates in RAFM steels and the nanoclusters in ODS alloys both inhibit creep by blocking dislocation climb and glide. Above about 600^{o}C these precipitates succumb to thermal ageing effects and RAFM alloys lose their creep strength. The thermal stability of the nanoclusters discussed above prevents a similar collapse in ODS alloys preserving their creep properties and enabling higher reactor operating temperatures [108].

The thermal stability of ODS alloys enables their radiation tolerant microstructures to survive and function at higher temperatures but the addition of transmutant gases now needs to be considered. These are capable of accelerating the void incubation process potentially causing ODS alloys to swell in the manner of ordinary martensitic steels below 0.5Tm. Operating above 0.5Tm would help to suppress these effects but helium embrittlement would continue to be a problem unless the grain boundaries are appropriately protected by gas trapping sites [14].

1.6.6 Helium Management Capability of Oxide Dispersion Strengthened Steels

Under service conditions the helium content in the steel, plasma facing components of a fusion power reactor is expected to reach 2000appm with 200dpa associated displacement damage [14]. Precipitate interfaces, grain boundaries and dislocations provide nucleation sites for helium bubble formation which under a continuous vacancy flux are likely to swell and develop into unstable voids. The accumulation of helium along grain boundaries causes particular problems opening up creep cavities at high temperature. These can promote brittle intergranular fracture over transgranular modes at the low temperatures experienced during shut down and reconditioning [109] [110]. If the plasma facing materials are to function satisfactorily these microstructural vulnerabilities need to be addressed.

The formation and development of bubble populations depends on a number of variables including dose rate and irradiation temperature, but the presence of correlated displacement damage needs particular consideration when attempting to simulate a reactor environment in an accelerator [111]. Dual ion beam studies can successfully deliver both helium and displacement damage to samples and have provided compelling evidence for swelling suppression and bubble trapping in ODS steels. Nevertheless it must be remembered that the data these studies provide remains an imperfect approximation of reactor conditions [112].

Dual ion beam irradiation studies undertaken by Yutani, compared the response of the JLF - 1 RAFM alloy to the K3 Fe - 16Cr - 4.5Al ODS at 500^{o}C and 15appm/dpa [113]. Each sample received 60 dpa and 900 appm averaged over the implantation depth delivered by 6.4 MeV iron ions and 1.0 MeV helium ions. Yutani used the displacement damage profile predicted from SRIM calculations to calculate the swelling behaviour of the two materials at increasing levels of correlated damage up to a peak 150 dpa.

Figure 1.28 shows the relative stability of the ODS microstructure in the presence of helium at high levels of displacement damage compared to the RAFM alloy. Yutani attributes such remarkable swelling suppression to a dense population of gas trapping

sites capable of confining the helium to small bubbles and presents the comparison of bubble size and number density for each material shown in Figure 1.29. However, the measurements rely on the implantation profiles computed using the SRIM software in correlating displacement damage and swelling over 10nm length scales. Although the difference in bubble size between the ODS and JLF alloys is quite apparent, the data presented in Figures 1.28 and 1.29 is unreliable given the limitations of the SRIM software. These are discussed in more detail in Section 2.1.2.

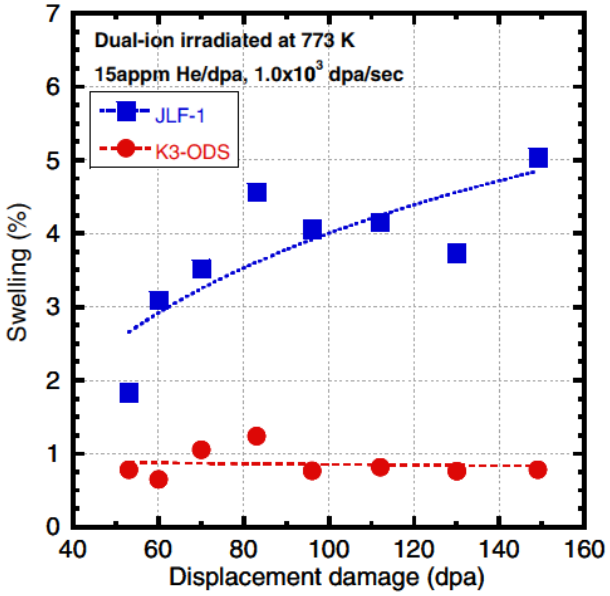


Figure 1.28 Swelling with dose for a 16Cr ODS and JLF-1 RAFM steel. The ODS shows remarkably invariant swelling at all doses. [113]

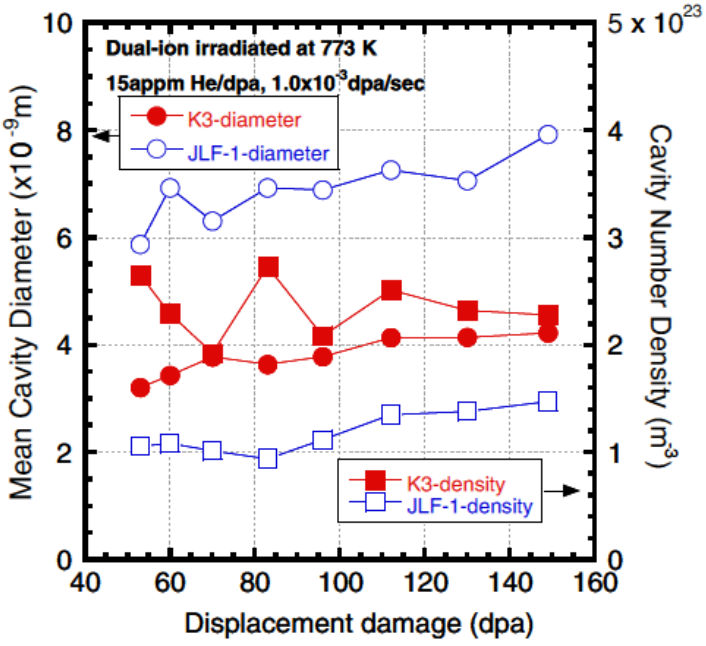


Figure 1.29 A comparison of bubble size and number density in a 16Cr ODS and JLF-1 RAFM steel. The ODS confines the gas to a denser population of smaller cavities consistent with the remarkable swelling resistance shown in Fig 23 [113]

Yutani easily identified measurable bubble populations in the implanted alloys but only a few larger oxide particles were recorded in the micrographs used to construct Figures 1.28 and 1.29. These were found to be associated with argon bubbles, likely trapped during the mechanical alloying process. Yutani nevertheless attributes the superior swelling behaviour of the ODS alloys to the particle dispersion, despite the apparently low particle densities visible in the surveyed regions of implanted samples [113].

Referring to prior SANS and APT studies conducted on the K3 ODS alloy, Yutani concludes that the majority of the oxide particles are simply below the resolution limit of the TEM. Kurtz, Yamamoto and Odette attempted to capture both particles and helium bubbles formed under neutron irradiation using a combination of Fresnel contrast in the TEM and EFTEM. Micrographs showing the results of these studies are presented in Figures 1.30, 1.31 and 1.32 for MA 957, Eurofer 97 and F82H [42] [114] [115] [116] [117].

The materials were irradiated in a reactor using prefabricated TEM samples prepared using NiAl α implanter layers as shown in Figure 1.7. $^{58}Ni(n_{th}\gamma)^{59}Ni(n_{th}\alpha)$ reactions in the NiAl layer uniformly implant the alloys with helium to depth of 5 - 8μm at fusion reactor helium/dpa ratios when exposed to neutron flux. Each sample received 9 dpa and 380 appm He at 500^{o}C.

EFTEM jump ratio maps and defocused bright field images were used to characterise the irradiated microstructures in each material. Yamamoto recorded an average particle size of 3.1nm in the implanted MA 957 and estimated the particle density to be 8×10^{23} m^{-3} . The average bubble size was found to be below 1.0nm and the average bubble density estimated to be approximately 3×10^{23} m^{-3} [14].

Based on the EFTEM and TEM data presented by Yamamoto, Odette reports that the bubbles are located primarily on the particle interfaces. He also supports the conclusions made by Yutani that the swelling resistance of ODS alloys stems from the

dense particle dispersion, which provides a thermally stable and irradiation tolerant sink for the transmutant helium [14] [116].

Bubbles are certainly seen at larger oxides in MA 957 like those shown in Figure 1.30 but no direct evidence for the close association between bubbles and small (<5.0nm) oxide particles is presented by Yamamoto. An apparent overlap between features in the EFTEM maps and TEM micrographs provides the sole basis for claiming an association between the two but the uncertainty in the spatial relationship between subnanometer features in different micrographs renders any conclusions regarding their association questionable.

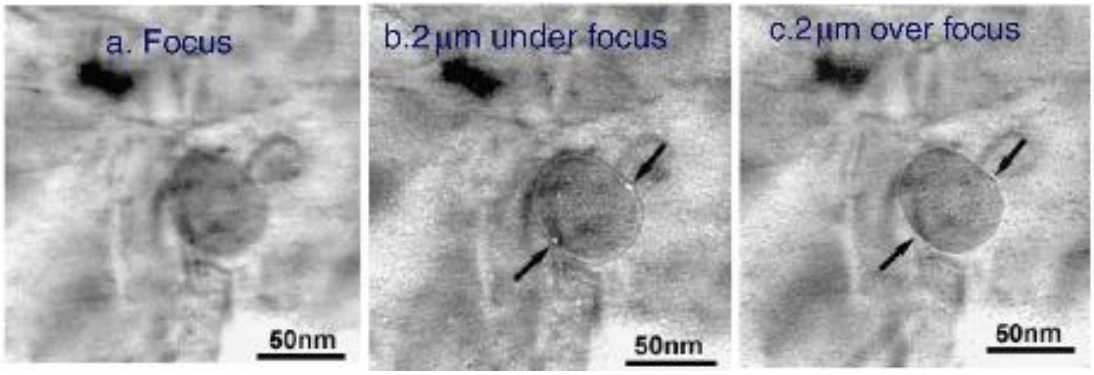


Figure 1.30 Through focus series of TEM micrographs of an oxide particle in a helium implanted region of MA 957. Notice helium bubbles on particle matrix interface as indicated by the arrows [42]

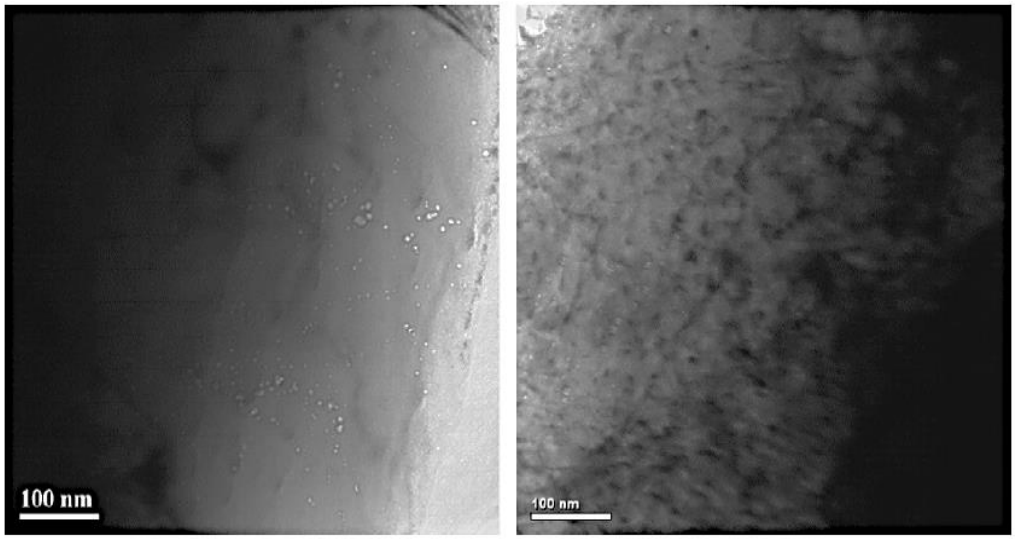


Figure 1.31 Bright field TEM micrograph of Eurofer 97 showing the bubble populations and dislocation structure [115]

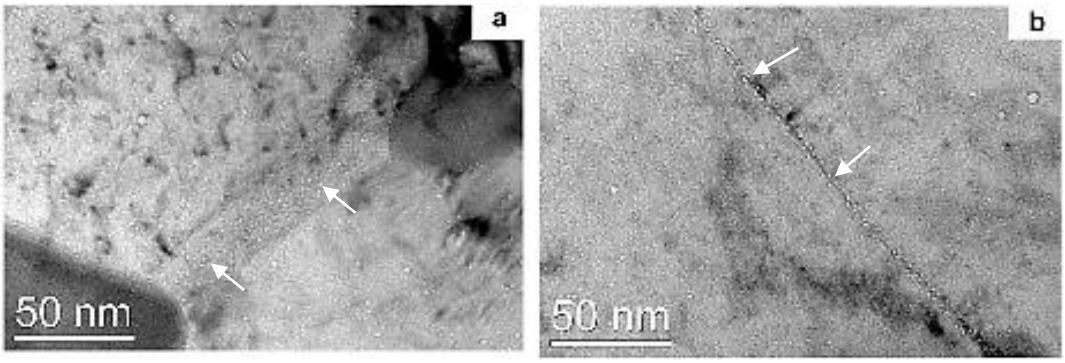


Figure 1.32 Bright field TEM micrographs of F82H showing cavity formation at grain boundaries as indicated[117]

The Eurofer 97 and F82H steels shown in Figures 1.31 and 1.32 contain bubbles with a larger average radius of 4.3nm at a lower density of 1.5×10^{22} m^{-3}, accompanied by large voids (>10nm) suggesting that bubble to void transitions are occurring in the manner outlined in Figure 1.3. In MA 957 the bubble density produces an average bubble separation of about 20nm; approximately four times the average particle separation distance. This indicates that the particle dispersion should be more than capable of sequestering helium and preventing its migration to grain boundaries.

Indeed given the apparent differences in bubble and particle densities, even weakly bound helium would be much more likely to cycle between particle interfaces before moving to a grain boundary [14] [115]. Once bound to a particle, bubbles should form excellent sinks for more helium, vacancies and self-interstitial atoms. Odette directly compares the bubble-laden grain boundaries in F82H and EUROFER 97 to the bubble-free boundaries in MA 957 in a set of micrographs shown in Figure 1.33.

Applying the high pressure equation of state developed by Stoller to the bubble fields shown in Figures 1.30 and 1.33, Yamamoto calculates the helium content of the MA 957 microstructure to be 130appm. This is about one third of the estimated dose received by the samples. In the F82H and Eurofer 97 samples the calculated helium content approaches the implanted quantity of 380 appm, leading Odette to suggest either helium loss from the sample or bubbles forming below the resolution limit of the TEM. Alternatively the hard sphere model may simply be inaccurate in these

circumstances justifying Donnelley's concerns regarding the use of Bridgeman's data in the model's development [14] [116].

If two thirds of the helium does occupy subnanometre bubbles, the actual bubble density could be comparable to that of the oxide particles. In an attempt to replicate the successful use of APT in characterising even the smallest oxide particles, Edmondson uses the technique to analyse a helium implanted 14YWT ODS steel. Here he takes the unusual step of using the 335KeV helium ions to inflict damage on the samples, delivering a peak dose of 30 dpa and implanting 100000 appm helium in the process [118] [119].

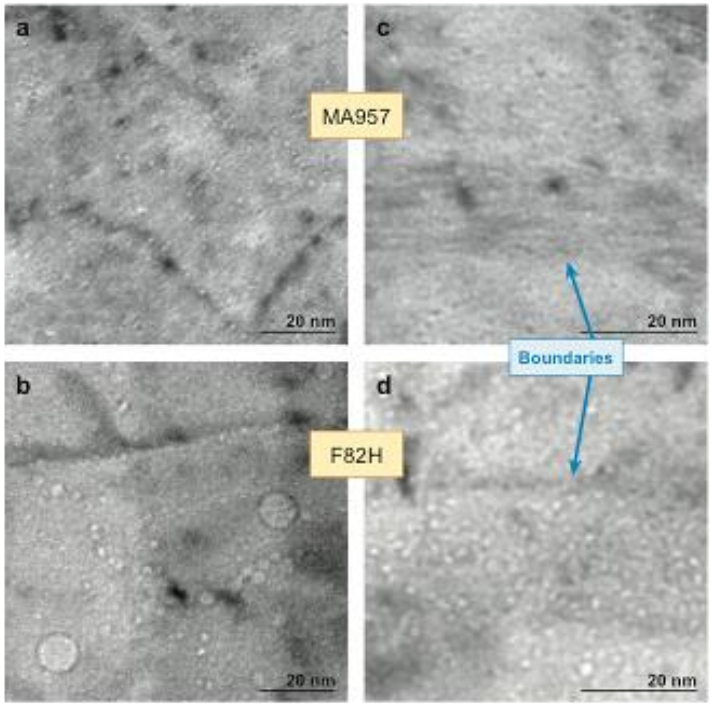


Figure 1.33 Comparison of helium implanted microstructures of MA 957 and F82H showing the denser population of smaller bubbles in MA 957 and bubble segregation to a grain boundary in F82H [14]

Edmondson's analysis of the APT data produced the set of isoconcentration and isodensity surfaces shown in Figure 1.34. These identify low density regions in pink and titanium rich particles in green. Edmondson attributes the local density reductions to the presence of helium bubbles noting the close relationship between the two features in Figure 1.34. These datasets apparently substantiate Odette's belief that a population of bubbles beneath the resolution limits of the TEM contain a significant portion of the implanted helium.

However, density variations can occur in APT datasets for a variety of reasons. Grain boundaries and precipitates can produce significant variations in density depending on the evaporation conditions, sample geometry and material properties. It seems highly likely that upon evaporation the bubbles identified in Figure 1.34 would suffer aberrations similar to those experienced by the oxide particles. In this case instead of a void appearing in the reconstruction local magnification effects would instead produce a region of greater density, as surrounding material was incorporated into the bubble [130].

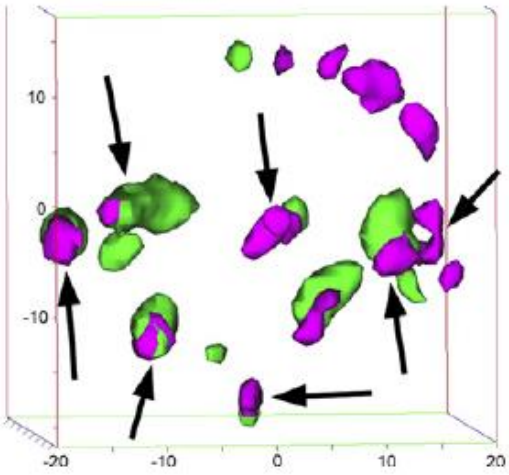
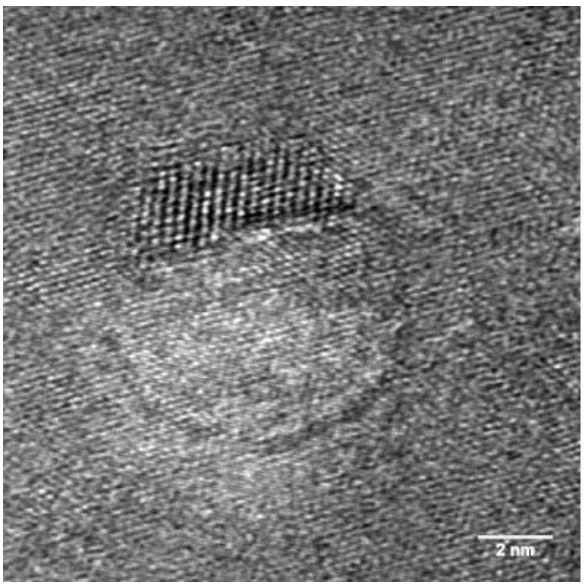


Figure 1.34 Pink isodensity surfaces outline helium bubbles and green isoconcentration surfaces show nanoclusters. Bubbles in direct contact with nanoclusters are identified by arrows [118]

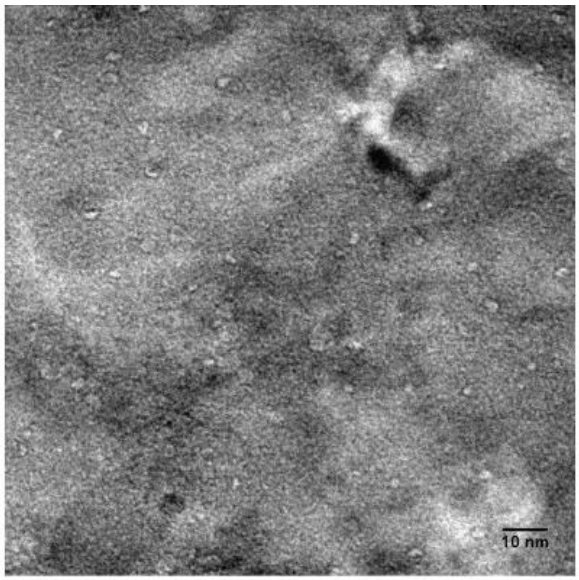
In any case APT provides no measure of the gas pressure in these bubbles and cannot provide an independent estimate of the helium content. Identifying the helium itself in samples run at very low temperature may be possible but the technique is likely to provoke controversy unless supported by TEM.

Recent HREM work by Ryazanov shown in Figure 1.35 provides direct evidence for helium trapping at nanometre scale particles in ODS Eurofer implanted with 1000appm helium at 300^{o}C and 500^{o}C [120]. At both temperatures bubbles form at the same density but are much larger at the higher temperature, making them easier to identify and allowing Ryazanov to successfully capture micrographs showing bubbles formed at 500^{o}C attached to the surface of 2.0 and 3.0nm particles in Figure 1.35 (a).

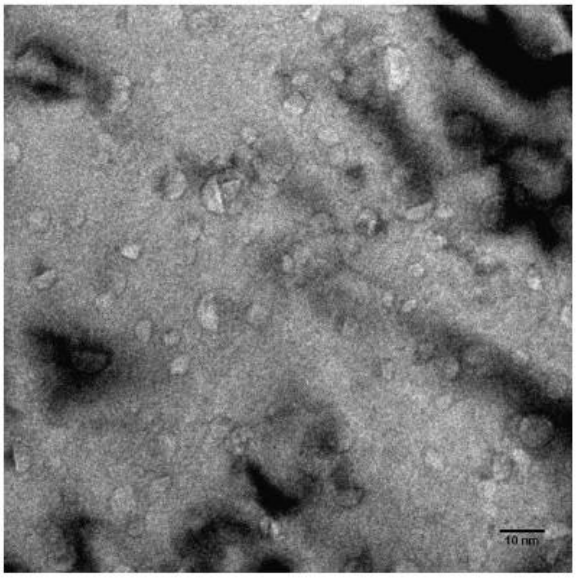
Together these experiments support the use of the particle population in YWT based ODS alloys to control accumulated helium gas. Studies like those undertaken by Henry [121] and Yamamoto [122] using spallation proton irradiation to 1600 to 1700 appm demonstrate both the risks helium embrittlement poses to RAFM alloys and crucially the potential for oxide dispersion strengthening to offer a measure of protection from such effects.



(a)



(b)



(c)

Figure 1.35 Helium bubbles in ODS Eurofer formed in 300°C and 500°C implantations [120]

(a) Under focus HR micrograph showing a bubble formed at 500°C at the surface of a 4nm oxide particle

(b) Bubble field produced during a 300°C implant

(c) Bubble field produced during a 500°C implant

1.7 Conclusions and Proposed Work

ODS alloys offer the improved irradiation resistance of a BCC reduced activation ferritic steel but demonstrate a number of further improvements which make them promising candidates for reactor applications including:

1. A dense populations of gas trapping sites at the oxide nanoparticles. These confine helium to high pressure nanometre scale bubbles suppressing swelling and protecting grain boundaries from embrittlement.
2. A thermally stable microstructure enabling reactor operation above 600^{o}C suppressing displacement damage and boosting plant efficiency.
3. Improved mechanical properties particularly tensile, creep and fatigue strengths. These are supported by a heavily pinned microstructure but are subject to considerable variation with processing conditions.

The anisotropy of extruded material is just one of a number of problems that need to be addressed before ODS alloys can be deployed in reactor environments. In some cases these can be mitigated in process parameter selection and thermo-mechanical treatment but more broadly the challenges outlined below highlight the need for a physical model of the alloy thermo-kinetics capable of predicting microstructural behaviour in processing, service and decommissioning.

1. Contamination in mechanical alloying from the alloying medium and the atmosphere causes batch to batch property variations.
2. Powder consolidation processes are costly compared to melt processing hampering commercial development.
3. Alloy inhomogeneity and carbide inclusions exacerbate the low fracture toughness particularly in anisotropic material.
4. Long term fatigue, creep and corrosion studies have yet to report for a number of candidate alloys.
5. The character and properties of the nanoclusters and the mechanics of the clustering process need to be understood.

6. Combinatorial studies for all production parameters and material properties in all conceivable service condition are simply impractical.

Given the complexities of these materials it becomes important to carefully select a parameter space for study and to control for all other variables as far as is practically possible. In service alloy performance will depend on a combination of environmental and material factors but fully combinatorial studies are beyond the scope of an individual research project.

Following an extended correspondence with G. R. Odette and others I proposed a study of the relationship between oxide particles and helium bubbles confined to a single alloy composition. Beginning by reproducing the variation of particle size and density with consolidation temperature reported by Alinger and Odette the effect of these variations on helium gas accumulation is studied with the hypothesis that there will be a correlation between particle and bubble number density.

By using APT instead of SANS new information on cluster chemistry and distribution during a systematic variation of the consolidation conditions becomes available for analysis in a controlled material. To provide the necessary confidence in the provenance of the materials to be used, all the powders were processed at Oxford by H. Zhang and M. Gorley under the conditions specified in Section 3.2 and consolidated using the hot isostatic pressing facilities at the University of Birmingham.

Helium implantation conditions were chosen to conform to prior work undertaken at the Surrey Ion Beam Centre and JANNUS facilities. Reference alloys containing no ceramic component were processed, consolidated and implanted alongside the ODS material to provide experimental controls for each stage of the analysis. The main experimental methods and details of alloy production are presented in Sections 2 and 3 respectively.

2 Experimental Methods

2.1 Ion Implantation

Helium ion implantations were conducted at the Surrey Ion Beam Centre using two electrostatic (Van De Graff) charge particle accelerators to deliver ions over multiple energies to produce a flat helium concentration profile from the sample surfaces to a depth of 3µm. The beam current and sample temperature were monitored during implantation and held constant to keep dose rate and thermal effects from influencing the outcome of the experiment.

2.1.1 Sample Preparation and Mounting

The consolidated alloys were cut into rectangular samples of approximately 1 x 10 x 10 mm using a cubic boron nitride blade and an ISOMET 4000 precision saw. The samples were ground flat using progressively finer silicon carbide paper before chemo-mechanical polishing with a 50nm colloidal silica suspension to produce a smooth surface free from significant mechanical deformation.

The samples were held in dovetailed steel rails fixed to a steel base plate as shown in Figure 2.1. The rail assembly provides a good thermal contact for the samples and a thermocouple attached to one of the dovetails records the temperature at the actual sample mounting position allowing the implantation temperature to be adjusted in response to beam heating. The ion beam is scanned over the aperture shown in Figure 2.1 with a 5.0mm spot size in a random pattern. Four Faraday cups surrounding the aperture continuously measure the beam current and allow the target to be irradiated to within 1% of the specified dose.

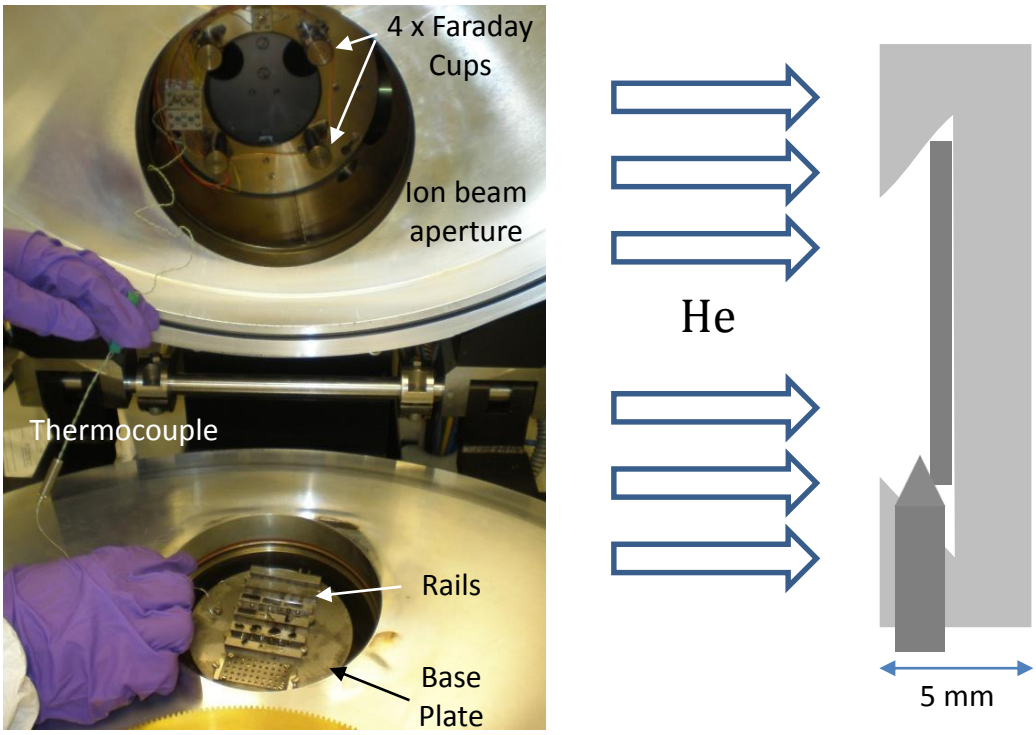


Figure 2.1

Base plate and rail assembly in the ion beam air lock undergoing thermocouple attachment. The beam aperture and the faraday cups are visible.

Section through rail dovetail showing a sample clamped in position by a grub screw.

2.1.2 SRIM Calculation

The ion energies and doses were selected using the 2008 edition of the SRIM (Stopping and Range of Ions in Matter) Monte Carlo code [123]. At each energy 5000 helium ion cascades were simulated in an iron target using a lattice displacement energy of 40eV [124]. The target composition can be usefully simplified to iron since chromium and iron have the same lattice displacement energy and comparable atomic densities. The energies used to conduct the implants in Section 5 are summarised in Table 5.1.

Full damage cascade calculations were used to simulate the implantation. These model every collision including those between recoiling and lattice iron atoms and record the number of iron vacancies, helium atoms and replacement collisions per angstrom thick layer of the target per incident ion. The sum of the replacement collisions and vacancies provides the number of displacements per incident ion. The

displacements per atom (DPA) in each angstrom thick layer are calculated from Equation 2.1 using the ion fluence ϕ, the number of displacements produced by an ion of the incident energy ν and the atomic density n, taking the interatomic spacing in BBC iron to be 2.48Å [125]. The helium content can be similarly calculated from the injected ion content.

Equation 2.1 $dpa = \frac{\phi v}{n}$

SRIM provides a useful approximation of the accumulated damage and helium content in a target material but the code make various simplifying assumptions. The calculations only model the ballistic phase of the cascade in an amorphous solid at 0K ignoring thermal effects and channelling behaviour. Fortunately a variety of techniques including secondary ion mass spectrometry (SIMS) and positron annihilation spectroscopy (PAS) have broadly substantiated SRIM calculations for iron chromium systems under helium and heavy ion bombardment [126] [127].

2.2 Atom Probe Tomography

Atom probe tomography couples controlled field evaporation and time of flight mass spectrometry to facilitate the three dimensional atomic characterisation of samples providing quantitative chemical and structural information about a material. The evolution of the instrument is covered extensively by Miller [128] but the basic principles of operation are summarised below.

2.2.1 Principle of Operation

Needle shaped samples having a radius of curvature at the tip of between 50nm and 100nm are fabricated by either electropolishing or FIB machining as outlined in Section 2.2.2. The sample is held in ultra-high vacuum and cooled to a temperature typically between 30K and 50K. A standing DC voltage is applied to the sample generating a high electric field at the tip. When the electric field becomes sufficiently

intense, atoms field ionise and accelerate away from the tip. Field evaporation is controlled by holding the voltage below the threshold for field ionisation and applying a voltage or laser pulse to the sample to trigger ionisation and ideally remove one atom from the tip at a time, though in practice multiple ionisations are not uncommon.

Recording the time of flight between the sample and the detector in a known field allows the mass of each ion to be computed and by assuming a simple flight trajectory the original location of the atom in the sample can be calculated based on the location of the ion impact at the detector surface. A schematic representation of the system implemented in a local electrode atom probe (LEAP) is shown in Figure 2.2.

The physics of the field ionisation process are still not fully understood but in simple thermodynamic terms an atom must move over a potential barrier to become an ion and escape from the sample surface. The laser pulsing method developed by Kellog and Tsong heats the sample providing the surface atoms with the necessary thermal energy to overcome the barrier to ionisation [129]. By using a thermal pulse rather than a field pulse to initiate ionisation, samples of lower conductivity can be analysed and the probability of sample facture is substantially reduced.

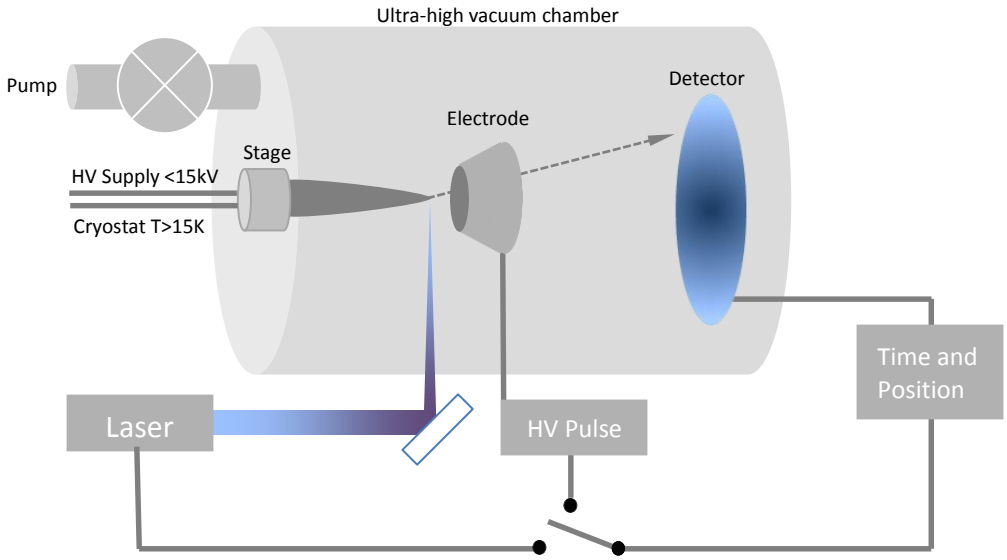


Figure 2.2 Schematic arrangement of a local electrode atom probe (LEAP) [128]

Although favoured in the analysis of a variety of materials including ODS alloys, the laser pulsing method introduces a variety of potential problems some of which are the subject of present controversies [130]. The laser illuminates the sample from one side and if misshapen or of low thermal conductivity, material may preferentially evaporate from the illuminated side. Poor heat dissipation, through either sample geometry or material characteristics, reduces mass resolution and facilitates atomic migration and rearrangement at the sample surface producing artefacts and promoting multiple ionisation evens [130].

The atom probe datasets presented in the following sections were recorded using a Cameca LEAP 3000 in laser mode. The use of a local electrode substantially reduces the voltage required to produce an electric field of sufficient strength, allowing higher pulse frequencies to be used at lower voltages. Both the mass resolution and data acquisition speed are improved provided the electrode is clean and stable during operation. Typical pulse frequencies lie between 50 kHz and 250 kHz but higher frequencies necessarily shorten the available detection window. At lower voltages the flight time for a heavy ion may be longer than that window, supressing the detection of heavy species and molecular ions.

Modern detector systems register about 37% of the incoming ions, all of which have the same probability of detection [130]. The detector consists of a stack of micro-channel plates to provide signal amplification and three delay line arrays capable of registering multiple ion impacts. The delay in signal propagation through the array provides the lateral coordinates for three dimensional reconstruction.

2.2.2 Sample Preparation

All sample preparation was performed using an electropolishing method in two stages. 0.5 x 0.5 x 20 mm matchsticks were prepared from bulk using a high speed saw and a cubic boron nitride blade. These were suspended in a layer of electrolyte made up from 25% perchloric acid 75% acetic acid and a DC voltage of up to 30V was applied continuously as shown in Figure 2.3.

Moving the matchstick through the electrolyte layer causes a neck to form before the two samples separate. The second stage shown in Figure 2.4 is performed under an optical microscope and allows the tip morphology to be more closely controlled. The voltage is applied manually and the sample moved through a 98% 2-butoxyethanol 2% perchloric acid electrolyte droplet suspended in a 2.0mm gold loop reducing the tip radius to below 100nm.

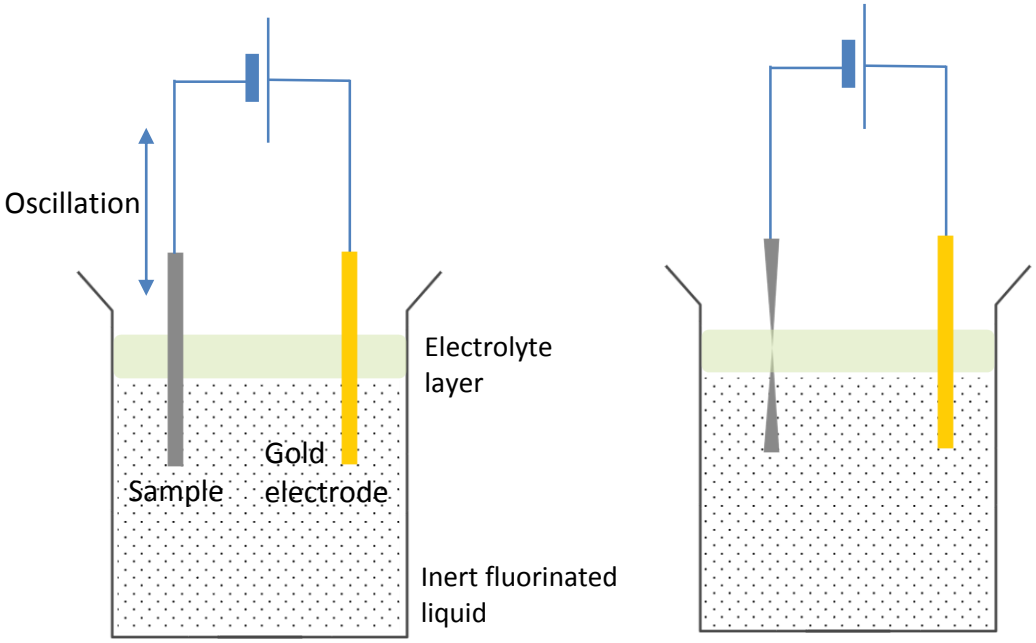


Figure 2.3 Schematic showing the first stage of electropolishing an APT sample

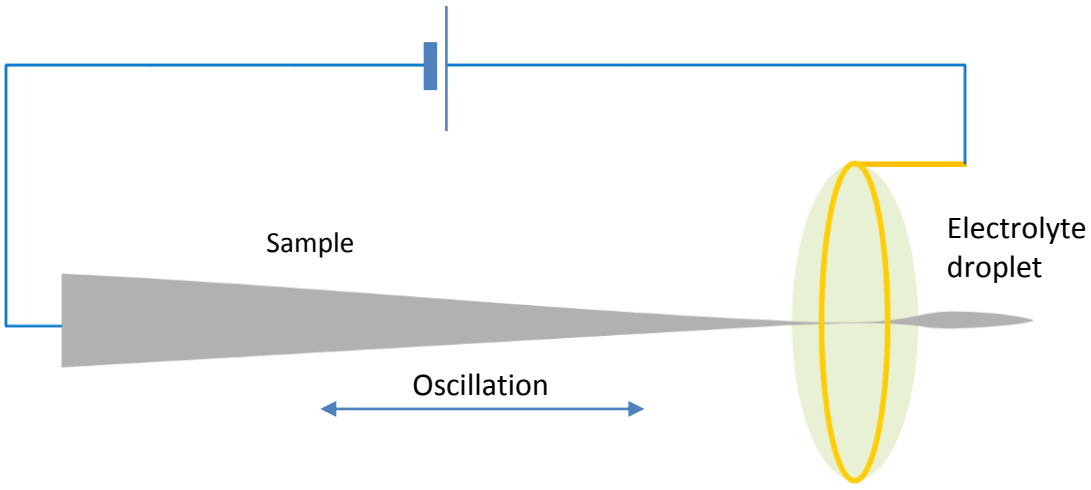


Figure 2.4 Schematic showing the second stage of electropolishing an APT sample

2.2.3 Selecting the Analysis Conditions

When polished and checked under an optical microscope, the samples are cleaned in methanol and pressed into copper crimp tubes. The samples are mounted in copper pucks perpendicular to the plane of the electrode and aligned inside the analysis chamber using the internal microscopes and positioning stage. When selecting the analysis conditions for a sample, an inevitable compromise between data quality and collection efficiency must be made as discussed below.

ODS alloys are commonly run in laser mode to improve the success rate over multiple runs and in some cases simply to conform to the practices of the community and enable more direct comparison between datasets. Voltage pulsing increases the likelihood of sample fracture and can contribute to the distortions experienced by samples containing multiple phases with different field evaporation conditions [61].

The spot size, pulse duration and wavelength of the laser are fixed but the pulse energy can be varied. At low energies field ionisation between pulses becomes more likely but at high energies multiple ionisation events occur more frequently, significantly complicating the mass spectrum [130]. Sample temperature and laser power both contribute to the thermal energy available for surface migration, though one may be used to compensate for the other if particular artefacts associated with thermally mobilised species are observed in the data.

A detailed analysis carried out by Williams, comparing the cluster compositions recorded in ODS samples run at pulse energies from 0.2nJ to 1.0nJ, found that the lower fields necessary for steady state evaporation at higher pulse energies reduced the measured iron content in the particles [61]. Assuming trajectory aberrations are entirely responsible for the iron content, Williams suggests that low field high pulse energy conditions may help to suppress the effect.

Unfortunately on instruments lacking adjustable wavelength lasers, these benefits must come at the expense of mass resolution and signal to noise ratio, which confined Williams to pulse energies between 0.2nJ and 0.4nJ at a base temperature of 30K to further reduce thermal effects [131] [61]. Following these conclusions all atom probe data presented in this thesis were taken using a 0.3nJ pulse energy. The base temperature was increased to 50K to further reduce fracturing and improve the yield of large datasets containing statistically significant numbers of oxide particles.

2.2.4 Mass Spectra

A labelled mass spectrum taken from a sample of the Fe-14Cr-0.2Ti-3W-0.25Y_2O_3 alloy processed at 1050^{o}C is shown in Figure 2.5. The spectrum is complex, containing various minor elements and molecular species, each having multiple isotopes. The relative quantities of alloying elements and the natural abundance of different isotopes assist in the identification of particular peaks, especially where peak overlap is suspected. For example, both titanium and tungsten and all their molecular ions are easily identified from the family of peaks formed by their major isotopes. If any have an anomalous height by comparison with the others it indicates that it may be convolved with peaks from another ion.

Deconvolution may be attempted in these cases by assigning some fraction of the counts in the anomalous peak to each ion based on the peaks recorded from their other isotopes. Unfortunately if the two ions have differing spatial distributions the reconstruction can become misleading. TiO^{2+} is a good example, having an easily identifiable pattern of one major and four minor isotopes as shown in Figure 2.6. The major isotope ^{48}Ti and the O_2^+ ion overlap at 32 producing an artificially large peak in the TiO^{2+} pattern. Part of the peak can be assigned to TiO in proportion to the minor TiO peaks with the remainder being identified as O_2; but as noted, the deconvolution cannot account for any difference in the spatial distribution of the two species.

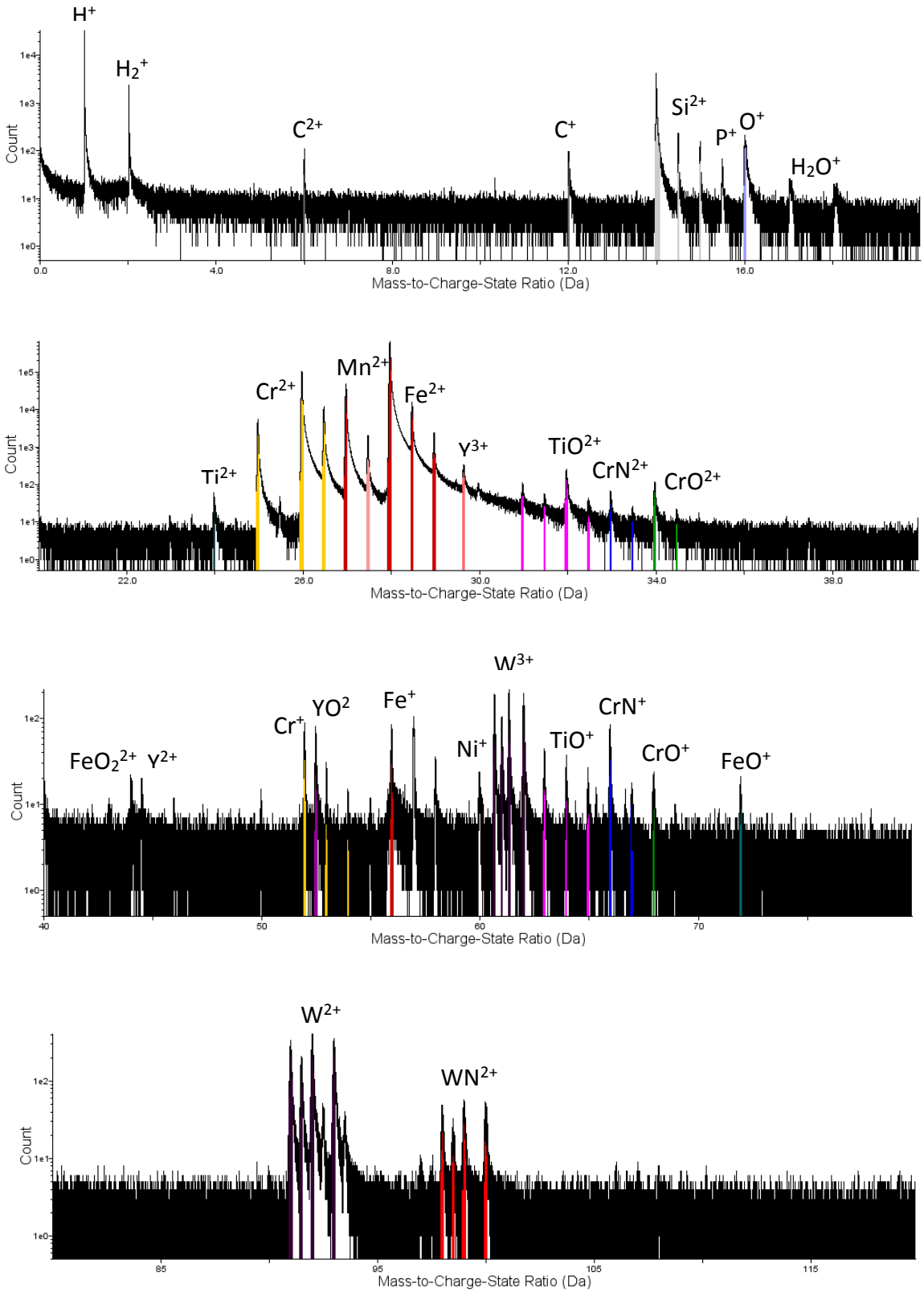


Figure 2.5 Mass spectrum labelled using the standard range file taken from a 50M ion Fe-14Cr-0.2Ti-3W-0.25Y_2O_3 dataset run using 0.3nJ laser pulsing at 50K. The particularly low background noise enables the identification of several additional minor peaks including a possible phosphorous and nickel peak. Note the abnormally high $^{57}Fe^+$ peak indicative of a possible convolution.

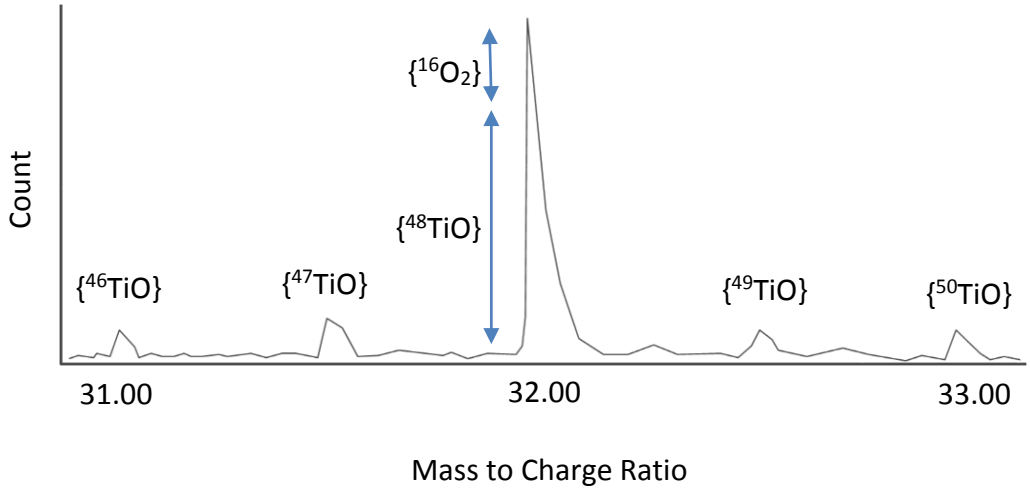


Figure 2.6 Schematic of convolved TiO and O_2 peaks between 31 and 33 amu.

Once the peak has been identified the upper and lower bounds of the mass to charge ratio thought to include those counts associated with the particular ion are determined. The method selected to determine this range directly affects compositional measurements and needs to account for both the sample background and the peak broadening effect that results from the slight variation in ion flight times caused by non-instantaneous ionisation of sample atoms [130]. No systematic rules or ranging algorithms are currently available and a degree of judgement must be exercised when setting a range for each peak depending on the material behaviour and the experimental circumstances.

Studies comparing simulated and experimental data conducted by Hudson, Smith and Gault have found manual ranging to compare favourably with automated methods and that ranges taken to some fraction of the full width half maximum performed similarly well at the expense of the effective detection efficiency [132]. Ranging the whole peak proved more variable, providing the most accurate compositional measurements for some species and the least accurate for others depending on the interaction between peak tails and the background.

In the following work all the mass spectra were analysed by hand using the peak widths at one tenth of their height to determine the range of mass to charge ratios associated with that peak and the ion or ions to which it corresponds. This provided

a repeatable and reliable measurement of the composition at the nominal detection efficiency of the instrument. A common set of ranges, stored in the range file shown in Appendix A, was applied to each mass spectrum for consistency and modified on a case by case basis using Appendix B and the available ranging tools in IVAS. For example in Figure 2.5 the spectrum exhibits particularly low background noise allowing several additional peaks outside the standard range file to be identified (including a possible nickel peak) although all contain under 100 counts.

Data quality is determined by the mass resolution and the signal to noise ratio particularly in those regions of the mass spectrum containing the principal species used for particle identification. One such region presented in Figure 2.7 shows the characteristic peaks associated with titanium oxide, a strongly clustering ion that can be easily used to isolate the oxide particles in reconstructed data. Both mass spectra shown in Figure 2.7 were taken from the same alloy run at 50K using 0.3nJ pulses at 200kHz. The peaks are easily identified in (a) and can be ranged appropriately. In (b) the mass resolution appears to be similar based upon the width of the major peak but the noise wholly obscures some of the minor peaks. Attempting to range these would include the noise in the reconstruction, impairing analysis and particle identification.

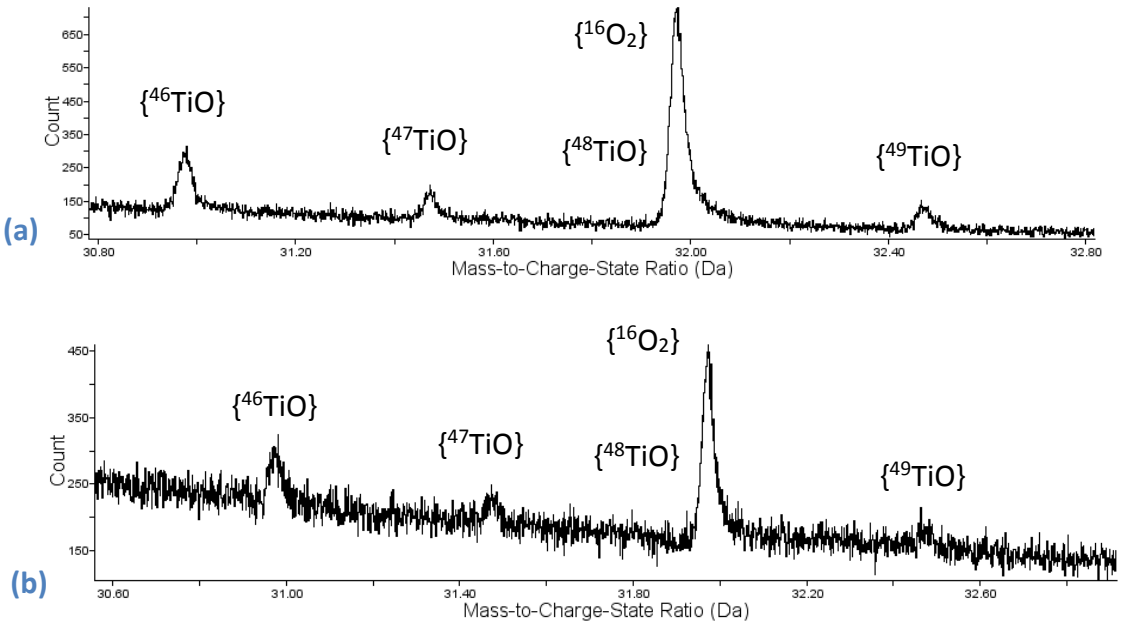


Figure 2.7 Mass spectra region showing characteristic TiO peaks from Fe-14Cr-0.2Ti-3W-0.25Y_2O_3 run at 50K, 200kHz and 0.3nJ pulse energy. (a) Low noise (b) High noise

All datasets undergo a background noise correction prior to analysis by fitting a simple power law curve to the background. Some samples are simply too noisy to be successfully characterised through a combination of especially poor tip geometry, heavy chamber contamination or electrode emission. Multiple datasets were recorded for each consolidation condition to provide a minimum number of particles from at least three high quality datasets for characterisation. In all cases those peaks associated with the major particle forming elements were found to be free from significant peak overlap.

2.2.5 3D Reconstruction

The reconstruction of the ranged dataset from the detector coordinates and time of flight data uses a simple point projection model developed by Bas to map the position of each atom [133]. The planar atomic coordinates are calculated from the detector hit coordinates and magnification η by Equation 2.2.

Equation 2.2 $$x = \frac{X_d}{\eta} \quad y = \frac{Y_d}{\eta}$$

If the sample were spherical the ion trajectories could be assumed to lie perpendicular to the sample surface but the body of the needle distorts the field and bends the ions towards to the detector reducing the magnification by some factor ξ. Expressed in Equation 2.3 the magnification η varies with the tip radius r flight path to the detector d and the image compression factor ξ.

Equation 2.3 $$\eta = \frac{d}{\xi r}$$

The ion flight path d and image compression factor ξ are both constant for a particular sample geometry but the tip radius r changes over the course of a run as material is removed from the tip. The radius must be recalculated for each ion from the relationship between r, sample voltage V, and the electric field F shown in Equation 2.4.

Equation 2.4 $$r = \frac{V}{k_f F}$$

The depth coordinates are calculated from the evaporation sequence of the ions from the sample. Bas assumes the sample surface area A_S and volume v can be related via the depth z according to Equation 2.5 and if the small angle approximation can be applied the sample area and detector area A_D are related via the magnification according to Equation 2.6.

Equation 2.5 $$\frac{dv}{dz} = A_S$$

Equation 2.6 $$A_S = \frac{A_D}{\eta^2}$$

These equations allow the depth coordinate to be determined using Equation 2.7 and a full spatial reconstruction to be performed if all the values are known. Unfortunately the detector efficiency Ω, image compression factor ξ and field factor k_f are generally unknown. Gault and Moody [134] suggest a variety of methods for improving the estimated values of each quantity but these rely upon capturing crystallographic features in the data which are difficult to identify in multicomponent systems like ODS alloys.

Equation 2.7 $$dz = \frac{\Omega d^2 k_f{}^2 F^2}{\xi V^2 A_D \eta^2}$$

To overcome these difficulties Williams performed a preliminary TEM characterisation on a number of ODS samples prior to APT analysis [71]. Comparative micrographs and atom maps like those presented in Figure 1.16 allowed the tip radius to be measured and the field term calculated from the evaporation voltage using Equation 2.4. Using a field factor provided by the manufacturer k_f the measurements suggested a lower evaporation field F for the material than that recommended by the IVAS software

[135] for iron based alloys but indicated that the particle dispersion had minimal influence on the evaporation behaviour of the material [61].

The spatial relationships between features like the grain boundaries shown in Figure 1.16 that are visible in both the micrograph and the atom map allowed Williams to select an appropriate image compression factor for each sample. Using the detector efficiency provided by the manufacturer, the three unknown quantities present in Equation 2.7 can be accounted for, provided each sample can be successfully characterised by TEM prior to APT. Unfortunately a combination of handling and atmospheric exposure significantly reduces the likelihood of a sample surviving the process and yielding a usefully large dataset.

To maximise the quantity of high quality data available for analysis, no prior tip characterisation was performed. Instead the reconstruction process was guided by a separate TEM characterisation of the oxide particles. From these direct observations, the reconstruction parameters could be adjusted where necessary to produce particles of the appropriate size and shape for each consolidation condition. Though superficially less rigorous, this approach made larger total volumes of material available for analysis, allowing particle densities and compositions to be calculated using the total number of ions in a dataset, which remains constant however the data are reconstructed.

2.2.6 Data Analysis Techniques

The maximum separation method developed by Hyde and English [136] was used to isolate the oxide particles in the reconstructed APT data. Their approach relies upon the simple assumption that two solute atoms in a particle are likely to be close together in the reconstructed dataset. How close together two solute atoms need to be in order for them to be included in the same particle is set by the maximum separation D_{max}. The application of the maximum separation criterion to each atom of the chosen particle forming solute identifies every cluster in the dataset.

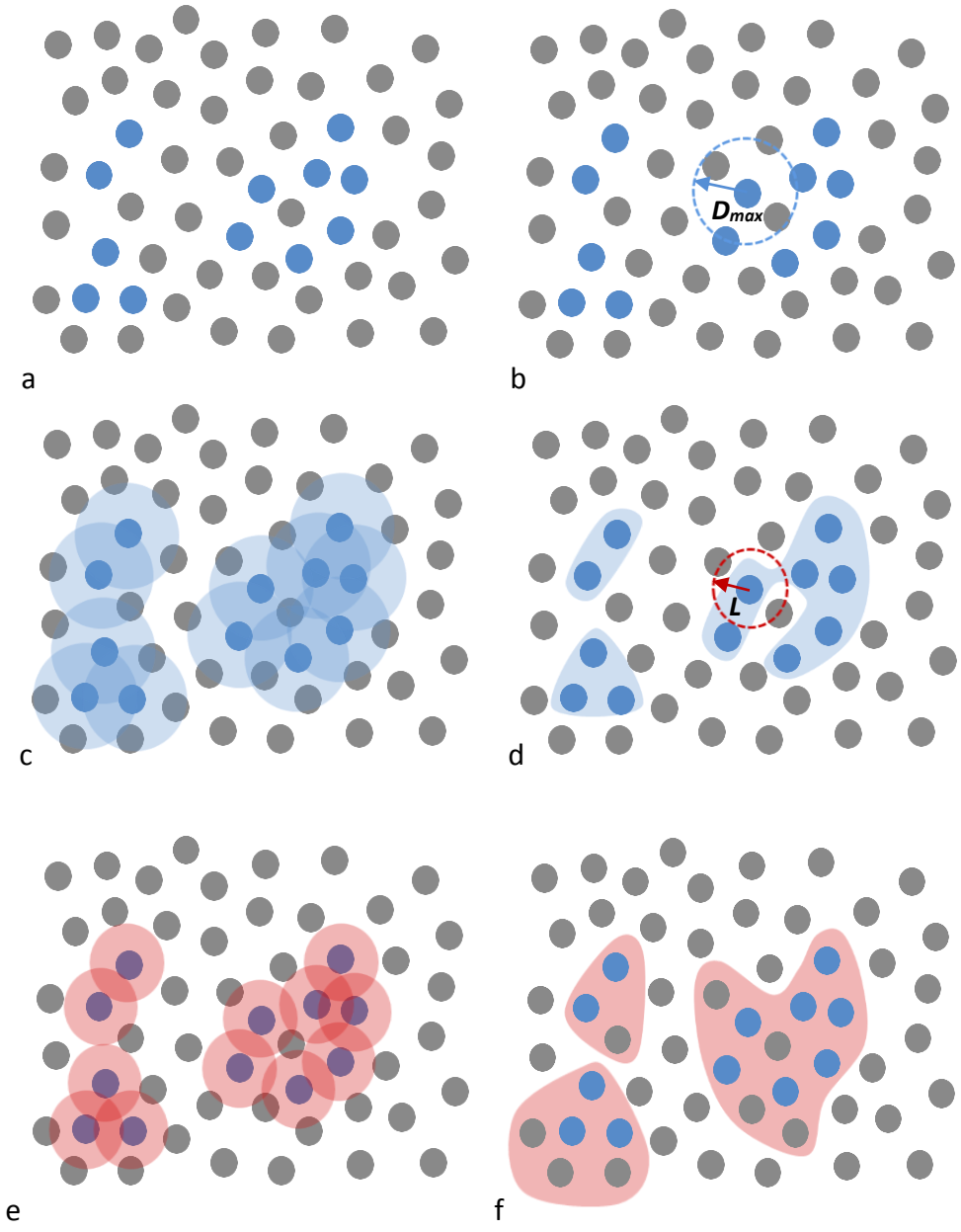


Figure 2.8 2D schematic showing the implementation of the maximum separation criterion on a binary alloy system (a) Solute atoms in blue cluster in a matrix (b) A sphere of radius D_{max} is applied to a solute atom. Every atom inside the sphere is assigned to the putative cluster. (c) The process is repeated for each solute atom in the dataset (d) Three clusters are isolated from the overlapping spheres provided $N_{min} < 3$ (e) All the atoms within some radius L of the solute atoms are included inside the cluster boundary (f) Three particles are identified in the dataset.

The process shown schematically in Figure 2.8 isolates clusters of the chosen solute ion in the dataset using an appropriate D_{max}. Some minimum number of associated ions N_{min} that constitute a cluster may be set to reduce the contribution of random associations between solute ions to the clustering statistics. The contribution made to the cluster composition from all the other ions present in the dataset is determined using an envelope parameter L. All ions within L of a solute ion are included in the cluster with L typically falling between 0.5 and 1.0 D_{max}.

The selection of a solute ion and the clustering parameters D_{max} N_{min} and L directly affects particle identification and characterisation in a dataset. Using the same values throughout an experimental campaign provides a superficial integrity to the results but this approach becomes unrealistic if significant changes are expected in particle characteristics between datasets. The difficulty in discriminating between genuine clusters and fluctuations in a random solute distribution become ever greater with increasing particle density and corresponding reductions in particle size. Compensating for what amounts to a changing signal to noise ratio requires some systematic alteration of the chosen clustering parameters.

One method proposed by Stephenson [137] uses the variations in the separation between local solute atoms to control cluster selection parameters in individual datasets, but the particle density and solute content of a typical ODS microstructure are considered to be unsuitable for the proper application of this technique. A variety of tools are natively available in the IVAS reconstruction software for studying the effects of each parameter on the clustering analysis. These were combined by Williams to rationalise parameter selection in [74] and their application to the ODS systems developed here is presented in Section 4.4.

2.3 Transmission Electron Microscopy

Bright field and high resolution methods were used to characterise the unimplanted ODS alloys in each consolidation condition. Samples were prepared by electropolishing using the method outlined in Section 2.3.1 below and the microscopy

performed with a JEOL 2100 operating at 200kV. Fresnel contrast methods were used to characterise the helium bubble population in the implanted alloys. Samples were prepared using the FIB lift out method to remove foils from the irradiated surfaces. The analysis was performed in a JEOL 2200 equipped with an omega energy filter operating at 200kV. In each region recorded under Fresnel contrast, energy filtered micrographs were taken and used to compute the local foil thickness.

2.3.1 Disk Sample Preparation Method

Wafers of alloy cut using an ISOMET 4000 precision saw and a cubic boron nitride blade were mechanically ground to a thickness of approximately 60µm using progressively finer silicon carbide paper to 4000 grit. 3.0mm disks were mechanically punched from the wafer and thinned using a Struers TenuPol and a 5% perchloric acid 95% methanol electrolyte solution at -40^{o}C. The process removes the mechanically deformed surface layers from the disks and produces an electron transparent region of pristine material for characterisation at the centre of the sample. At 60µm thick the disks caused some magnetic interference in the TEM column but thinner samples could not be reliably produced and periodic realignment of the electron optics was sufficient to alleviate the problem.

2.3.2 Lift Out Sample Preparation Method

TEM samples of the helium implanted alloys were prepared using a FIB, following the method outlined in [138]. A platinum layer 2µm wide and about 20µm long deposited on the implanted surface using a gas injection system and an appropriate beam current protects the subsurface material during the lift out process. Roughly cutting the surrounding material away to a depth of about 10µm on three side of the platinum, produces a 1µm thick sample for lift out, topped with 1µm of protective platinum.

Tilting the stage away from the ion beam allows the sample to be undercut producing a sample approximately 10µm deep and 20m long attached to the surrounding material at one end. The GIS and micromanipulator are positioned above the free end

and a layer of platinum deposited between the manipulator tip and the sample. When safely attached the sample is cut free, removed to the TEM grid and reattached using a third platinum deposition. If these stages are completed successfully, the manipulator can be cut away to produce a 1µm thick, 10µm wide sample of material under the protective platinum, containing the whole 3µm deep implanted layer.

Thinning the lift-out to electron transparency uses progressively lower ion beam currents to remove material parallel to the plane of the TEM grid, accounting for the ion beam tails by tilting the stage 1 to 2^{o} away from the beam. Reducing the accelerating voltage of the SEM column provides a rough metric for judging the thickness of the thinned region as it becomes transparent under 15kV electrons. When further thinning under 30kV gallium risks damaging the sample, reducing the accelerating voltage on the ion column and sputtering material from the thinned region at a 10^{o} to 15^{o} angle to the ion beam allows further thickness reductions to be achieved with the additional benefit of removing any amorphous material that may have formed on the sample surface under the 30kV beam.

2.3.3 Fresnel Contrast Microscopy

Fresnel contrast imaging exploits the electron-wave phase shift induced by the difference in potential between a bubble and the surrounding matrix. At focus no contrast can be seen but in under and over focused conditions the phase shift outlines the bubble periphery in a Fresnel fringe. For voids and low pressure bubbles below 5nm in diameter and with no associated strain field the technique offers the only method for generating contrast [139].

The sample is usually tilted well away from the Bragg condition for all reflections, to minimise diffraction contrast and a series of micrographs recorded at both under and over focus. Under these conditions voids and bubbles appear as light dots surrounded by a dark fringe when under focussed, and dark dots surrounded by a light fringe when over focussed. At 0.8µm to 1.0µm defocus, voids and bubbles down to 1nm are easily detected but care should be exercised when sizing voids from fringe measurements as discussed in Section 5.3 [139] [165].

2.3.4 Energy Filtered Transmission Electron Microscopy

EFTEM makes use of the characteristic energy losses in the inelastically scattered electrons transmitted through a sample to identify the elements present. The elastically scattered component of the signal, commonly referred to as the zero loss peak, provides a simple measure of sample thickness. The ratio between the elastic intensity isolated using an energy filter I_0 and the total intensity I_t of the transmitted beam yields the local sample thickness t via Equation 2.8, provided the mean free path λ of the incident electrons in the sample material is known [140].

Equation 2.8 $$t = \lambda \ln \frac{I_t}{I_0}$$

Malis and Egerton [141] developed a parametric relationship between the electron energy E_0, average energy loss E_m, a relativistic factor F and the collection semi-angle β of the instrument, for computing the mean free path λ in a sample material with some average atomic number Z. The assumptions made in the formulation of Equation 2.9 necessitate the use of a collection semi-angle below 15 mrad, set using the appropriate objective aperture.

Equation 2.9 $$\lambda = \frac{106F(E_0 / E_m)}{\ln(2\beta E_0 / E_m)}$$

Using an objective apertures to set the collection semi-angle improves the spatial resolution in EFTEM mapping but unavoidably excludes part of the inelastic signal. Removing the objective aperture allows the whole inelastic signal to be captured and used to produce the best possible estimate of the intensity ratio in Equation 2.8, but the collection semi-angle becomes too large for the proper application of Equation 2.9 [142].

To obtain the most precise measurement of $\frac{t}{\lambda}$ no objective apertures were used when recording the thickness maps of the helium implanted regions. Absolute thickness values were computed from a reference value of λ taken from a comprehensive study of λ variation conducted by Lakoubovskii and Mitsuishi [143]

2.4 Nanoindentation

Developed as a tool for measuring the mechanical properties of thin films by Pethica, nanoindentation applies and records the load and displacement of a diamond indenter tip at a sample surface [144]. Capable of measuring loads down to 1.0μN and displacements down to 0.2nm, modern indenter systems are commonly used to assess the mechanical properties of ion implanted materials.

2.4.1 Principle of Operation

The Agilent G200 Nanoindentation system used here relies on electromagnetic actuation and capacitive displacement measurement. The system applies either a load or displacement to the indenter tip once located at the sample surface and records a load displacement curve during indentation like that shown in Figure 2.9. Corrections for the supporting spring stiffness, frame stiffness and thermal drift are made to the measurements automatically but the sample mounting introduces another compliance term to the system.

A variety of methods for mounting implanted samples were compared by Hardie [92] [145] who found hot wax adhesives produced a predictable 10% reduction in the measured elastic modulus of a sample at 500nm indentation depths. Hot wax was therefore used to mount all the samples indented here.

2.4.2 Data Analysis

Indentation data were processed using the method developed by Oliver and Pharr [95] and the quantities identified in Figure 2.9. These include the peak load P_t ; the indentation depth at peak load h; the indentation depth on unloading h_r ; the indentation contact depth h_c ; and the unloading stiffness S. Both the reduced modulus E_r in Equation 2.10 and hardness H in Equation 2.11 require knowledge of the contact area A between the indenter tip and the sample surface.

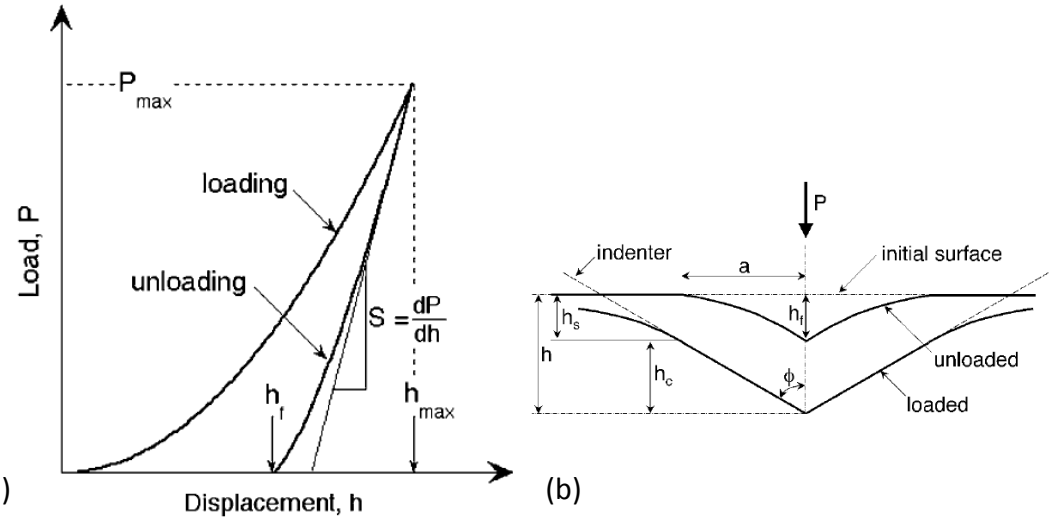


Figure 2.9 (a) Schematic of a typical load displacement curve from a nanoindentation test (b) Schematic section through an indentation showing quantities used in the analysis [95]

Equation 2.10 $$E_r = \frac{\sqrt{\pi}}{2}\frac{S}{\sqrt{A}}$$

Equation 2.11 $$H = \frac{P}{A}$$

In microhardness measurement the contact area needs to be measured following the indentation but direct measurement in nanoindentation would require repeated use of an SEM. Instead the contact area is calculated based on the indentation depth h_c and an area function $A(h_c)$ determined by the tip shape. Variations in the tip geometry are accounted for using a calibration material with a known indentation response following the method outlined by Oliver and Pharr [95].

Indents in fused silica were used to calibrate the tip before beginning each indent array. Taking the modulus E of the fused silica as 72GPa and the modulus E_i and Poisson's ratio v_i of the Berkovich diamond as 1141GPa and 0.07 the reduced modulus in fused silica E_r can be calculated using Equation 2.12. If the measured reduced modulus differed appreciably from this value a new area function was calculated for use in Equation 2.10 to correct for the changing tip geometry.

Equation 2.12 $$\frac{1}{E_r} = \frac{(1-v^2)}{E}\frac{(1-vi^2)}{E_i}$$

Equation 2.13 $$A(h_c) = 24.5h_c^{\ 2}$$

The area function for a perfect Berkovich contact is shown in Equation 2.13. Additional terms are added to compensate for tip deformity and blunting. Once a satisfactory area function has been constructed, the contact depth h_c is calculated via Equation 2.14 from the depth at peak load h and the surface displacement at the contact perimeter h_s. This is calculated in turn from Sneddon's force displacement relationship shown in Equation 2.15, using a geometric constant ε appropriate to the indenter tip and the stiffness S taken from the load displacement curve. All of these processes are automated by modern indentation software packages, allowing large numbers of indentation experiments to be conducted relatively quickly.

Equation 2.14 $$h_c = h - h_s$$

Equation 2.15 $$h_s = \varepsilon \frac{P_{\max}}{S}$$

2.4.3 Continuous Stiffness Measurement

The necessary use of the contact stiffness S computed from the unloading portion of the load displacement curve in the computation of both hardness and modulus only allows measurements of these quantities to be recorded at the maximum indentation depth. To more usefully measure hardness and modulus as a function of depth the indentation would have to be repeatedly loaded and unloaded at set depth increments. To avoid this time consuming process, Oliver and Pharr developed a dynamic method termed continuous stiffness measurement (CSM) [146].

CSM imposes a sinusoidal oscillation on the force applied to the indenter tip and continuously monitors the displacement, computing the contact stiffness from the phase or amplitude change between the two signals, accounting for the response of the whole system using a simple spring dashpot model of the indenter. CSM mode was used to record all the nanoindentation data presented in Section 6.

2.4.4 Pile Up and Sink In

The iteration and selection of an appropriate area function for the tip when indenting fused silica is typically automated and easily conducted prior to sample indentation but deformation of the sample surface around the indenter complicates matters. Even for a perfect Berkovich tip geometry, pile-up and sink-in of the sample material at the indent site changes the area function in a manner unique to the material under analysis.

If material pile-up or sink-in around the tip is suspected an SEM or AFM survey of the indentation site is necessary to account for the difference in the contact area. Pile-up causes particular problems because the additional contact area can produce a significant overestimate of the hardness and modulus, replicating the effects of radiation induced hardening in implanted samples.

Oliver and Pharr found the yield stress to modulus ratio and the work hardening behaviour to be the major factors in predicting pile-up [145] [166]. Soft alloys with little or no capacity for work hardening are likely to pile-up but any significant work hardening should constrain the upward flow of material around the indent. Being both natively hard and capable of further work hardening ODS systems are unlikely to undergo pile-up [147].

2.5 Electron Backscattered Diffraction

Electron backscattered diffraction (EBSD) implemented in the SEM uses the Kikuchi patterns produced on a phosphor screen positioned inside the vacuum chamber to identify the crystallographic orientation of a region of the sample microstructure under the electron spot [140]. The patterns are recorded on a CCD and automatically indexed as the spot moves over the sample producing a map of the microstructural texture.

Pattern quality figures, phase identifies and inverse pole figures are recorded simultaneously and map the sample crystallography at a resolution limited by the spot size, step size and scan area [140]. The EBSD performed here on a TESCAN MIRA FEG SEM used the AZTEC EBSD software to record maps using 20, 50 and 80nm spots and 50 to 100nm step sizes to capture the local microstructure around indents and on a larger scale over 100 micron regions.

3 Production and Characterisation of a Model ODS Alloy

3.1 Summary

Before beginning a full implantation campaign with a set of variable controlled alloys, a production study using a model Fe-14Cr-0.25Y_2O_3 (wt%) ODS system was undertaken to validate the proposed manufacturing methods. These methods included the powder metallurgy and mechanical alloying processes under development by M. Gorley and H. Zhang at the University of Oxford and the hot consolidation of the powder at the University of Birmingham.

Initial attempts using elemental powders mechanically alloyed in a stainless steel vessel and consolidated under uniaxial pressure proved unsatisfactory. The low consolidation density and poor iron chromium mixing were addressed using a hot isostatic press (HIP) to consolidate a pre-alloyed iron chromium powder supplied by Aubert Duval. Further changes to the production parameters, including an increase in the alloying time and a change in milling vessel composition, were made following a preliminary characterisation of the product using a combination of TEM and APT.

3.2 Alloy Production

All the powder metallurgy work undertaken prior to the production of consolidated material was completed by M. Gorley and H. Zhang. This work is briefly summarised here in Sections 3.2.1 and 3.2.2.

Initial attempts to mechanically alloy pure elements produced an uneven iron and chromium distribution in the product visible in the backscattered signal of the SEM [148]. The inhomogeneity persisted even when the elemental powders were processed for extended period of up to 100 hours, causing atmospheric ingress and vessel erosion to become significant sources of contamination in the product [148].

Consolidation of the mechanically alloyed powder in a 50MPa uniaxial press proved similarly problematic, producing an essentially unconsolidated sintered powder prone

to fracture during subsequent sample preparation. An illustrative SEM micrograph of a fracture surface produced during my preparation of 3.0mm TEM disks from these early specimens and taken with the assistance of E. Grieveson is shown in Figure 3.1.

To remedy these difficulties pre-alloyed powders were used, removing the need for mechanically alloying the iron to the chromium. The processed powder was then delivered to Bodycote Ltd for hot isostatic pressing (HIP). These methods are outlined in Sections 3.2.1, 3.2.2 and 3.2.3 below.

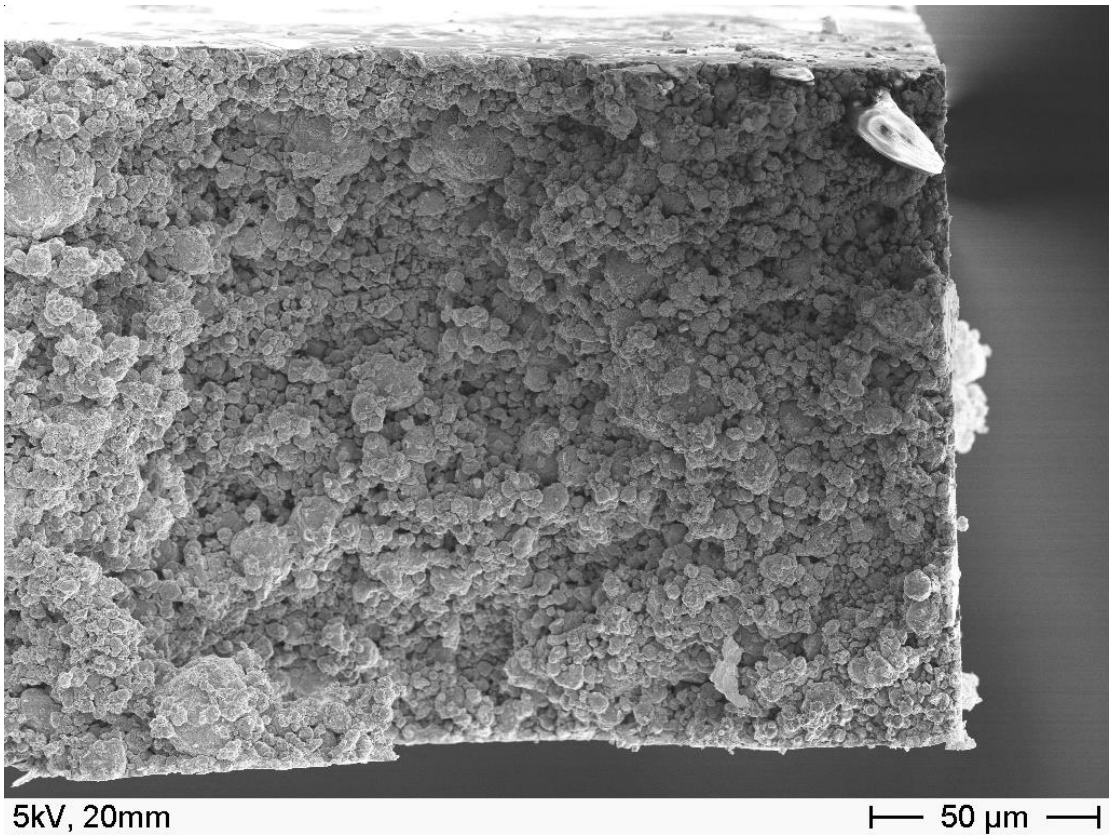


Figure 3.1 Unconsolidated powder particles on a fracture surface in a sample of Fe-14Cr-0.25Y2O3 powder subject to uniaxial hot press at 50MPa and 1100°C.

3.2.1 Powder Metallurgy

Table 3.1 shows the chemical composition of the pre-alloyed Fe-14Cr (wt%) gas atomised powder provided by Aubert Duval, showing significant silicon and manganese impurities. The gas atomization processes produce spherical powder particles like the one shown in Figure 3.2. These were sieved to remove particles larger than 150µm and handled in an inert 99.999% argon atmosphere throughout processing to reduce surface oxidation.

Elemental Composition											
	Fe	**Si**	**Mn**	**S**	**Cr**	**Ni**	**Mo**	**Co**	**N**	**O**	**C**
(wt%)	85.279	0.281	0.194	0.003	14.130	0.020	0.005	0.008	0.010	0.052	0.004
(at%)	84.032	0.552	0.194	0.005	14.941	0.019	0.003	0.007	0.039	0.179	0.018

Table 3.1 Chemical analysis of pre-alloyed Fe-14Cr powder provided by Aubert Duval

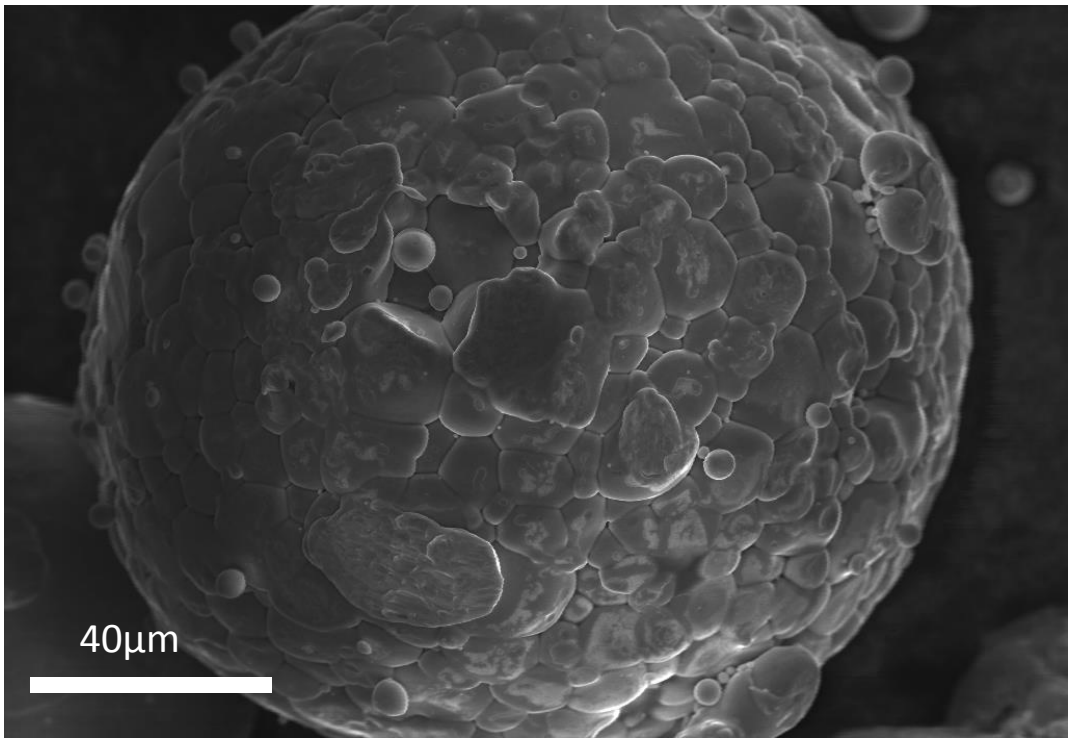


Figure 3.2 SEM micrograph showing a pre-alloyed Fe – 14Cr powder particle [148]

3.2.2 Mechanical Alloying

High energy Fritsch Pulverisette planetary ball mills were used to mechanically alloy the Fe-14Cr (wt%) powder to $0.25Y_2O_3$ (wt%) under a 99.999% argon atmosphere. The milling vessel and milling balls were fabricated from an Fe-18Cr-9Ni-2Mn-1Si stainless steel. A 250rpm milling speed, 24 hours milling time and 10:1 ball to powder weight ratio were chosen to produce powder particles <100µm as shown in Figure 3.3. X-ray diffraction studies of these powders conducted by Gorley [148], show the complete integration of the yttrium oxide into the ferritic microstructure of the particles.

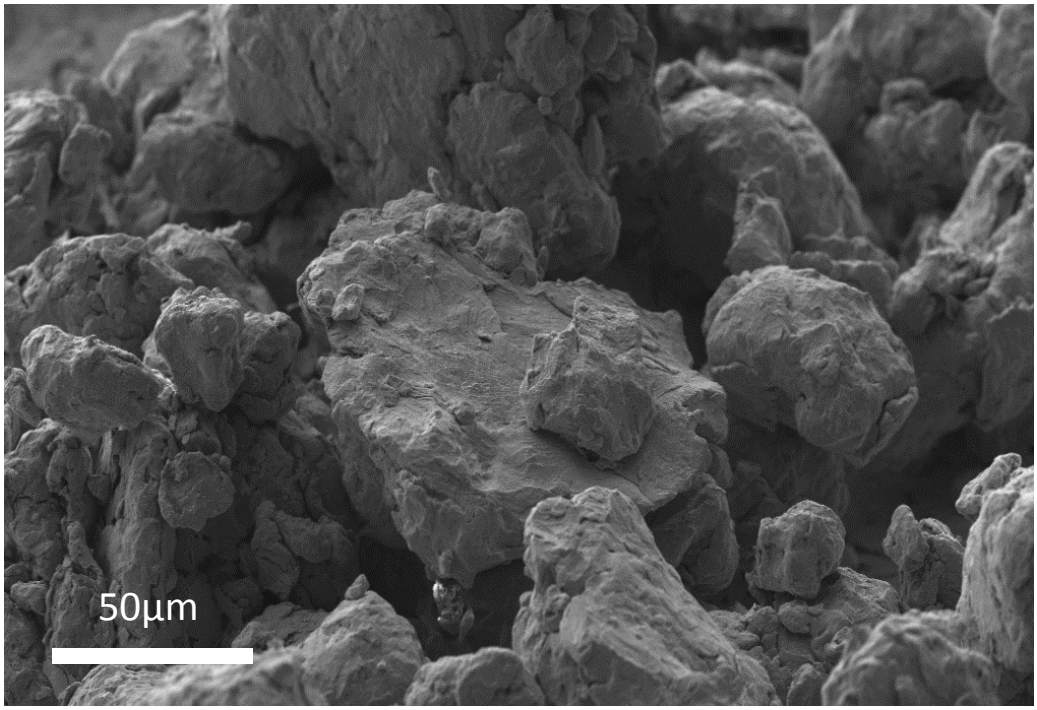


Figure 3.3 SEM micrograph showing the mechanically alloyed Fe-14Cr-0.25Y_2O_3 (wt%) powder particles [147].

3.2.3 Consolidation

The milled powders were placed in mild steel cans as shown in Figure 3.4 and sealed for transportation under argon. The canned powder was degassed for up to 8 hours at 400°C to remove trapped argon before the cans were crimped prior to hot isostatic pressing. The initial consolidation of the model Fe-14Cr-0.25 Y_2O_3 alloy made use of a standard HIP cycle offered by Bodycote heating at 3°C per minute to 1120°C and 103MPa with a dwell time of approximately 4 hours as shown in Figure 3.5.



Figure 3.4 Mild steel can during fabrication

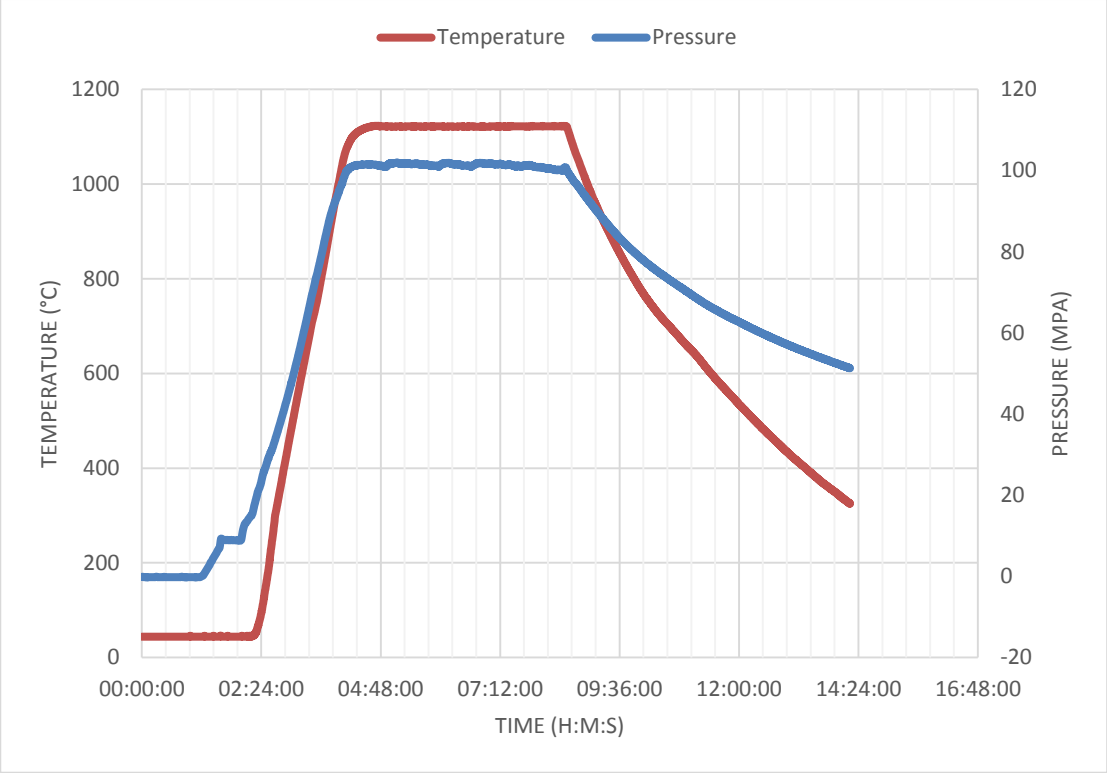


Figure 3.5 Time temperature pressure profiles for the HIP cycle used in the consolidation of model Fe-14Cr-0.25Y_2O_3 samples.

No further thermal or mechanical treatments were performed on the consolidated alloy, in an effort to limit the number of potential variables in the analysis. Bulk samples were prepared using a precision saw and a cubic boron nitride blade following the methods outlined in Section 2.3.1.

3.3 Characterisation

3.3.1 TEM

TEM samples were prepared from the consolidated alloy by FIB lift out and the microscopy performed at 297kV using a JEOL 3000F. The bright field micrographs in

Figure 3.6 show the ferritic microstructure populated by 5nm to 30nm oxide particles and some large carbides. The number of coarse (>10nm) particles present in the sample conforms to expectations for a model ODS system free from titanium or vanadium additions associated with particle refinement as discussed by Ukai and Larson [62] [63]. The absence of these elements may also explain the lack of any visible core shell arrangement like that observed by Hsiung [80].

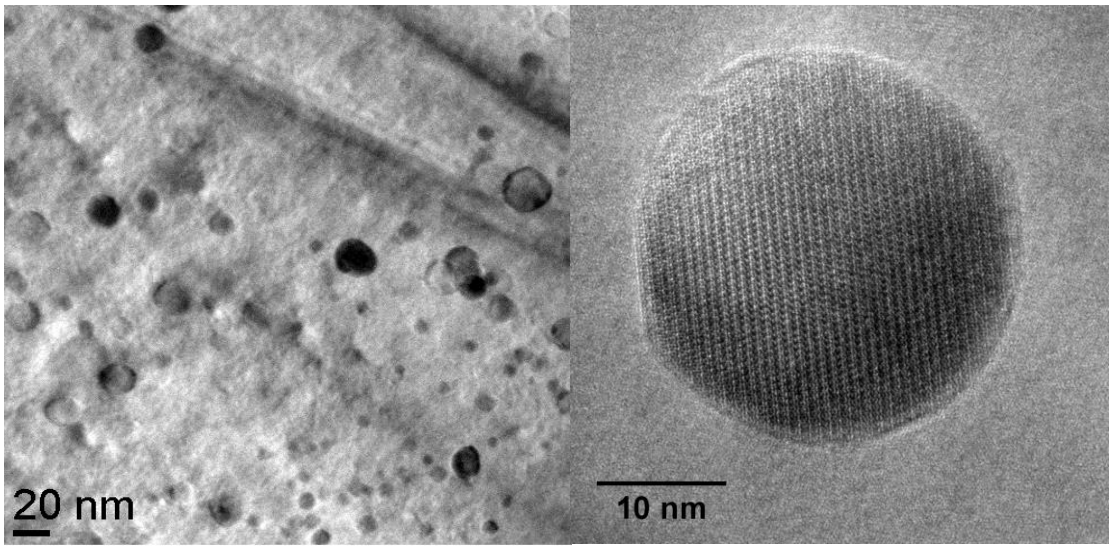


Figure 3.6 Bright field TEM micrographs showing nanoparticles from 30 nm to 5nm in diameter. Note that although some Fresnel effects do appear visible the lattice is consistent up to the particle boundary which shows no sign of a shell structure.

3.3.2 STEM

The bimodal grain size distribution in the alloy becomes apparent in the low magnification high angle annular dark field (HAADF) scanning TEM (STEM) micrographs presented in Figure 3.7. These show the oxide particles present in both the large and small grained regions of the sample and significant grain boundary decoration similar to that seen in MA 957 by Miller in Figure 1.12.

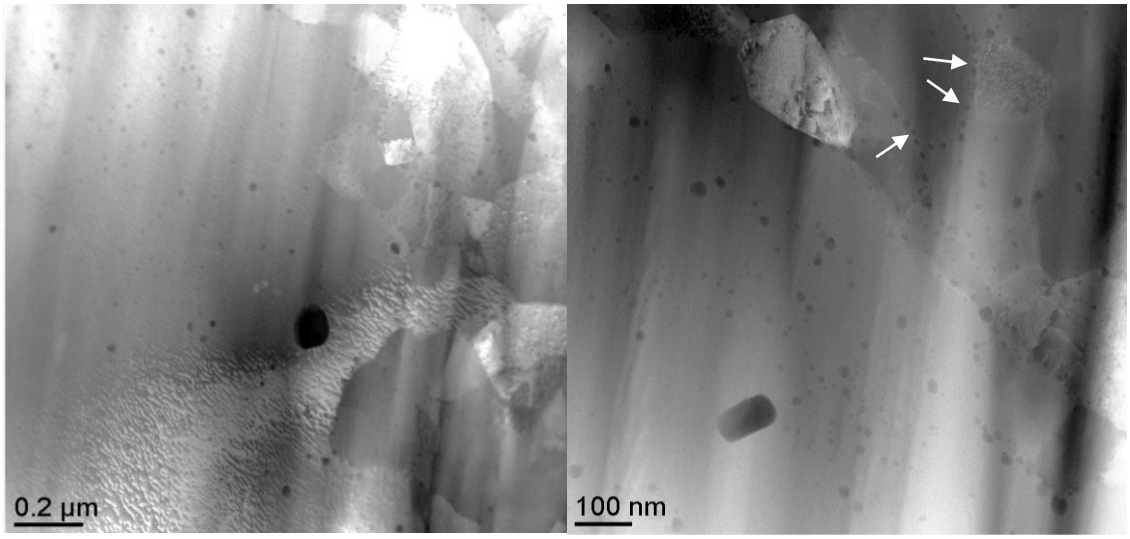


Figure 3.7 STEM HAADF micrographs taken using a 0.6nm probe showing extensive nanoparticle grain boundary decoration (as indicated) and a bimodal grain size distribution

3.3.3 Spatially Resolved EDX

A bright field micrograph taken of a 30nm particle in Figure 3.8 shows a bubble feature present at the particle boundary. The feature is indicated on a HREM micrograph of the same particle shown in Figure 3.8. A STEM EDX line profile taken through the particle and the bubble produced the plots shown in Figure 3.9 using the iron, chromium, silicon, argon and oxygen Kα and yttrium L lines. The plots show an yttrium based nanoparticle, possibly an yttrium silicate oxide, accompanied by an argon bubble incorporated during the manufacturing process attached to the particle boundary.

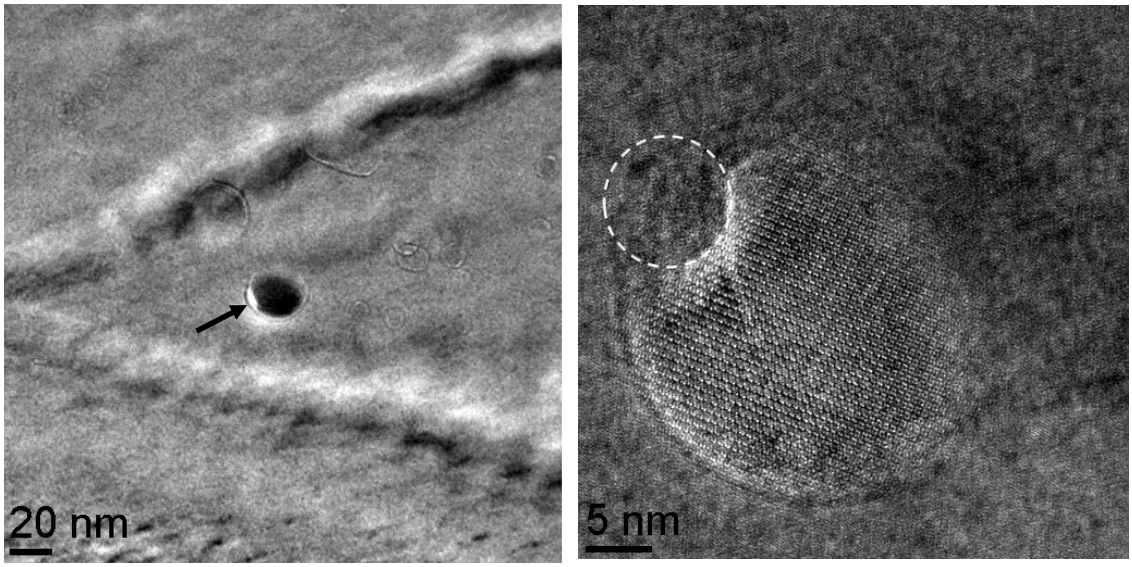


Figure 3.8 Bright field and HRTEM micrographs taken from a 30nm particle showing an argon bubble at the particle boundary indicated in each micrograph.

The copper Kα lines originating from the sample holder were ignored and no nickel lines indicative of contamination from the milling pot were identified in the EDX spectrum. No core shell structures like those shown in Figure 1.18 and Figure 1.19 are apparent in either the HRTEM micrographs in Figure 3.8 or the EDX plots in Figure 3.9. However, the 2.0nm step size used in recording the EDX spectra when combined with the effects of beam broadening would likely obscure any 1.0nm thick shell structures, such as those identified by Klimenkov [78].

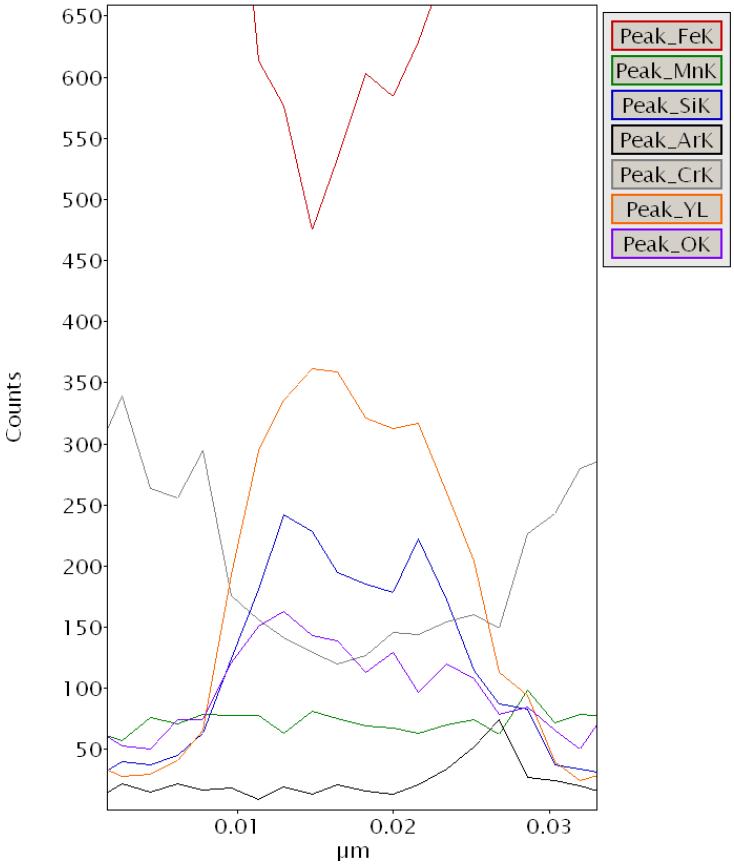
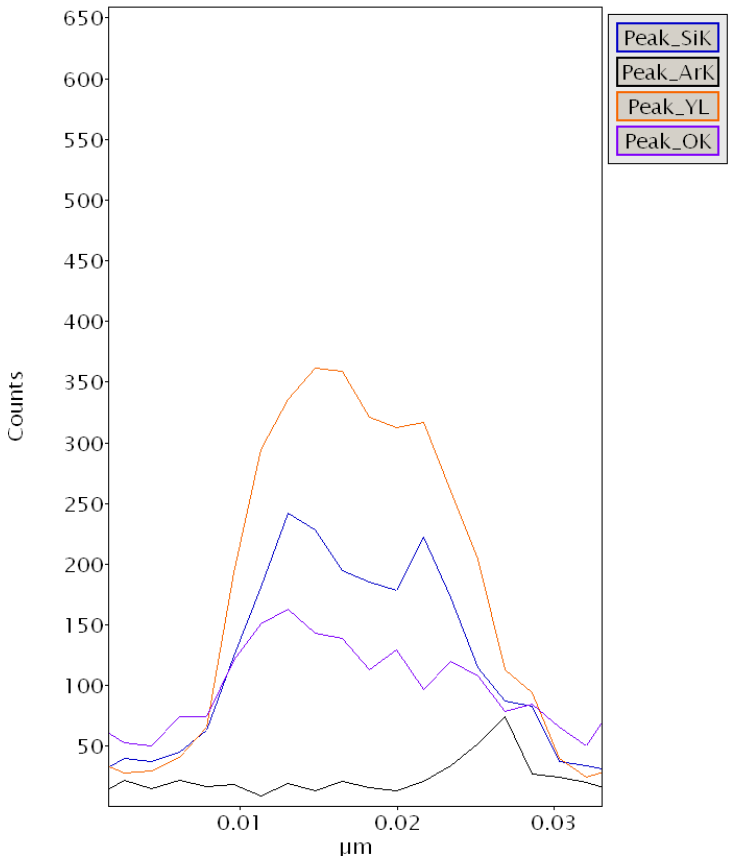


Figure 3.9

(a) EDX line profile through oxide particle and associated argon bubble showing Fe and Cr depletion and Y Si O enrichment



(b) EDX line profile showing only those elements present in the particle including the Ar signal at the particle boundary.

3.3.4 APT

Three atom probe data sets between 10 and 20 million ions in size were recorded from the Fe-14Cr-0.25 Y_2O_3 model alloy using samples prepared and analysed following the methods outlined in Section 2.2. The bulk composition of each dataset is shown in Table 3.2 alongside the chemical analysis of the pre-alloyed Fe-14Cr powder provided by Aubert Duval in at%. A section of the mass spectrum showing yttrium, nickel and titanium oxide peaks and a corresponding atom map of these ions is shown for each dataset in Figure 3.10 and Figure 3.11

	Elemental Composition (at%)									
	Fe	**Si**	**Mn**	**Ti**	**Cr**	**Ni**	**Y**	**N**	**O**	**C**
Sample (a)	84.7	0.5	0.2	0.1	14.1	0.1	0.1	0.0	0.2	0.0
Sample (b)	84.1	0.5	0.2	0.1	14.7	0.1	0.1	0.0	0.2	0.0
Sample (c)	85.6	0.4	0.2	0.0	13.5	0.1	0.0	0.0	0.0	0.0
Average	84.8	0.5	0.2	0.1	14.1	0.1	0.1	0.0	0.1	0.0
Stan Dev	0.8	0.1	0.0	0.0	0.6	0.0	0.0	0.0	0.1	0.0
Powder	84.032	0.552	0.194	-	14.941	0.019	-	0.039	0.179	0.018

Table 3.2 Bulk compositions from three samples (a)-(c) of the Fe-14Cr-0.25Y_2O_3 model alloy

Datasets (a) (b) and (c) match the powder composition recorded in Table 3.2 in iron, chromium, silicon and manganese content. Mechanically alloying 0.25Y_2O_3 (wt%) to the powder makes 0.1Y (at%) available to the consolidated alloy. Datasets (a) and (b) both contain approximately 0.1Y (at%), showing identifiable yttrium peaks in Figure 3.10. The yttrium partitions to a population of small (<5nm) particles shown in the atom maps presented in Figure 3.11.

Figure 3.10 also shows characteristic titanium oxide peaks present in datasets (a) and (b). These partition to the same particle population, indicating a substantial titanium addition occurred either during the gas atomisation process or through the incorporation of residual titanium-containing powders during mechanical alloying.

Dataset (c) shows no comparable particle population and no yttrium or titanium peaks are present in Figure 3.10, suggesting very little yttrium remains dispersed in the alloy following consolidation. The composition of dataset (c) thus provides a reasonable proxy for the composition of the iron-chromium matrix.

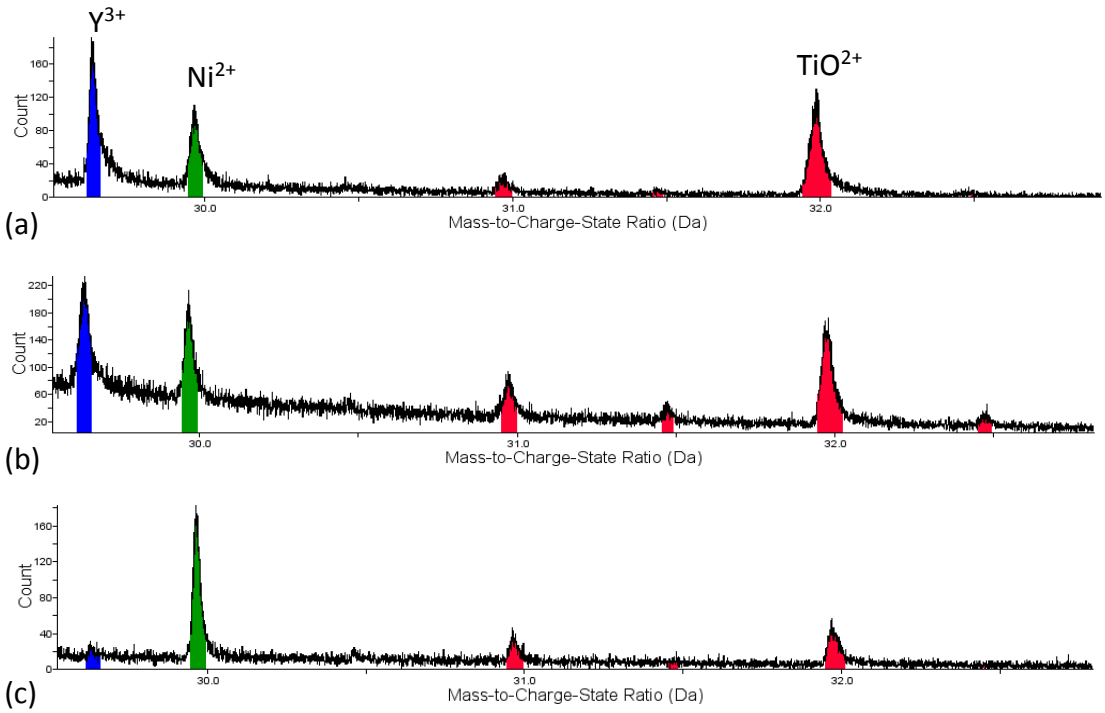
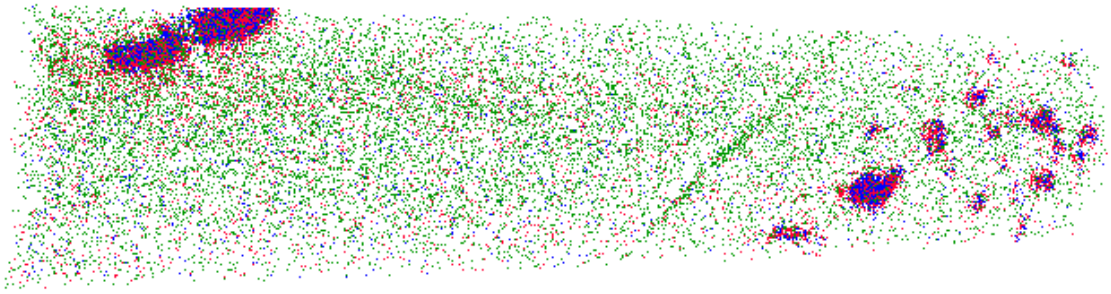


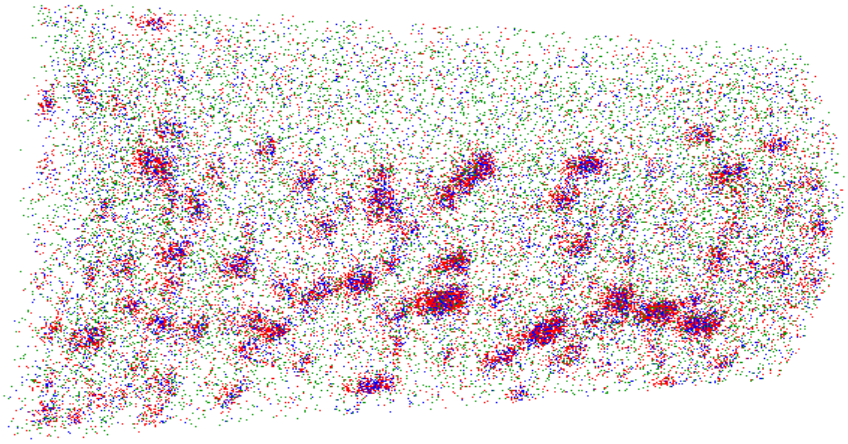
Figure 3.10 Mass spectra showing Ni (green) Y (blue) and TiO (red) in three samples of the Fe-14Cr-0.25Y_2O_3 model alloy

A Ni^{2+} peak present in all three datasets shown in Figure 3.10, indicates the presence of further contamination. Significant overlap occurs between the major nickel and minor iron peaks but if only those peaks associated with Ni^{60} and free from convolution with other ions are ranged, the Ni content of the consolidated alloy exceeds that of the pre-alloyed powder by a factor of 5. This suggests that significant erosion and incorporation of the Fe-18Cr-9Ni-2Mn-1Si stainless steel milling pot and balls occurred during the mechanical alloying stage discussed in Section 3.2.2.

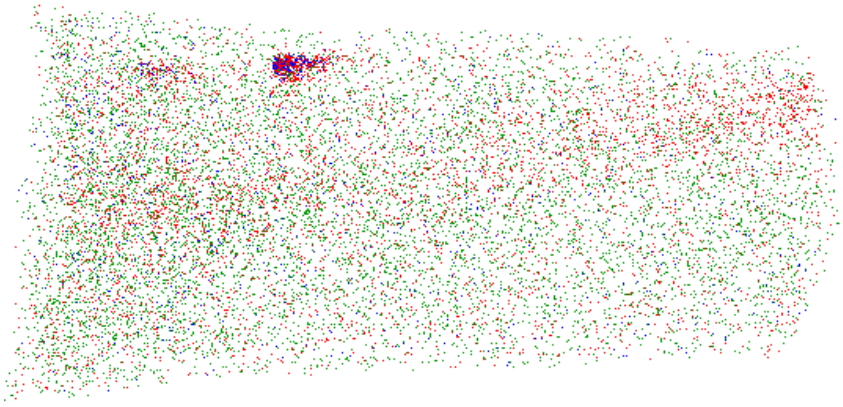
The nickel distribution can be seen in Figure 3.11 for each dataset. In all cases it appears dispersed throughout the analysis volume and shows no propensity to partition to the particles. Some nickel segregation does occur at the grain boundary seen in Figure 3.11(a). An analysis conducted using 1D cylindrical concentration profiles taken through the boundary, sampling the concentration of each ion every 0.5nm, was used to produce the Gibbsian interfacial excesses for chromium, silicon, manganese and nickel shown in Table 3.3.



(a)



(b)



(c) 50nm

Figure 3.11 Atom maps showing Ni (green) Y (blue) and TiO (red) in three samples of the Fe-14Cr-0.25Y_2O_3 model alloy containing approximately 42 million ranged ions in total.

	Γ (atoms/nm²)			
	Cr	**Si**	**Mn**	**Ni**
Sample Volume 1	15.6	2.1	0.2	0.2
Sample Volume 2	19.7	2.0	0.4	0.4
Sample Volume 3	18.0	1.9	0.3	0.2
AVERAGE	17.7. ± 2.1	2.0 ± 0.1	0.3 ± 0.0	0.3 ± 0.0

Table 3.3 Gibbsian interfacial excesses (Γ) of Cr Mn Si and Ni computed from the APT dataset shown above using a cylindrical sample volume positioned at three different locations on the grain boundary in the Fe-14Cr-0.25Y_2O_3 alloy.

The Gibbsian interfacial excess Γ quantifies the additional solute present at a grain boundary, providing a simple and direct method for comparing solute segregation [149] [150]. It is easily calculated from APT data using Equation 3.1 by approximating the grain boundary area A to the cross section of the cylindrical sample volume and computing the excess solute n by numerically integrating under a 1D concentration profile taken along the volume. This method, shown schematically in Figure 3.12, assumes that the step size used to perform the integration exceeds the voxel size of dataset and that the boundary shows minimal curvature inside the volume.

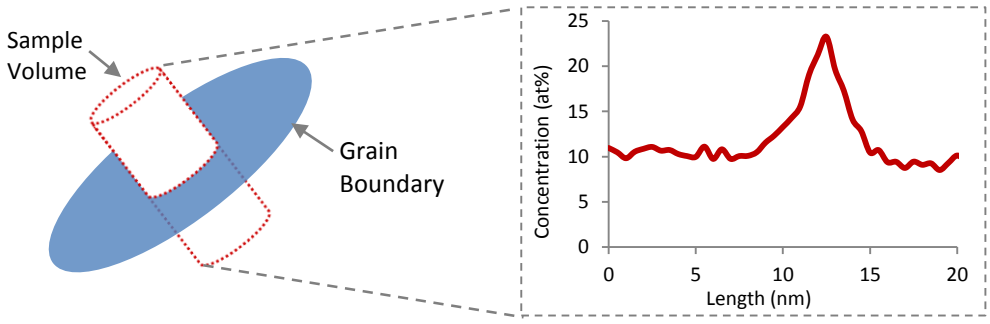


Figure 3.12 Schematic showing a 1D concentration profile taken along a cylindrical sample volume through a grain boundary like that shown in Fig 3.11 (a)

Equation 3.1 $$\Gamma_i = \frac{n_i}{A}$$

The full width of the Cr peak was used to set the limits of the numerical integration in each case and a standard error computed using three separate sample volumes taken at different positions along the boundary as shown in Table 3.3. The interfacial excesses of the chromium, silicon, manganese and nickel indicate the boundaries are accommodating to solute elements but the main particle forming species show no segregation and no particles are present at the boundary.

3.4 Discussion

The manufacturing route outlined in Section 3.2 successfully produced a fully dense model alloy and a population of yttrium based oxide particles dispersed through a microstructure featuring the bimodal grain size distribution characteristic of ODS systems. Large particles between 10nm and 30nm are evident in both the large (>1µm) and small (<200nm) grains in the TEM micrographs presented in Figure 3.6, 3.7 and 3.8. This suggests that an even distribution of the particle forming elements occurred during mechanically alloying.

3.4.1 Particle Characterisation Using Complementary TEM/APT Techniques

Yttrium, silicon and oxygen are identified as the primary particle forming elements from the EDX line profiles taken through the large, 30 nm particle shown in Figure 3.8 but titanium oxide and nickel are identified in the atom probe mass spectra shown in Figure 3.10. Here the titanium and yttrium are both present at a concentration of 0.1 (at%) and partition to the population of small (<5nm) particles shown in Figure 3.11. In a section of the EDX spectrum taken from the line profile through the large particle (Figure 3.13), the yttrium Kα and Kβ peaks are both evident, but no titanium or nickel signals are recorded.

Though dependent upon measurements taken from only one large particle these data indicate the presence of two distinct particle dispersions consistent with the particle refinement effects attributed to titanium by Ukai and Larson [62] [63]. One comprises large precipitates (possibly yttrium silicate oxides), associated with grain boundaries. The other is made up of small yttrium-titanium particles more typical of a YWT system; none of which show any association with the grain boundary present in Figure 3.11. The uneven distribution of these small particles through the total sample volume makes it difficult to calculate a valid number density for the dispersion, and the titanium contamination undermines any treatment of the material as a simple model alloy.

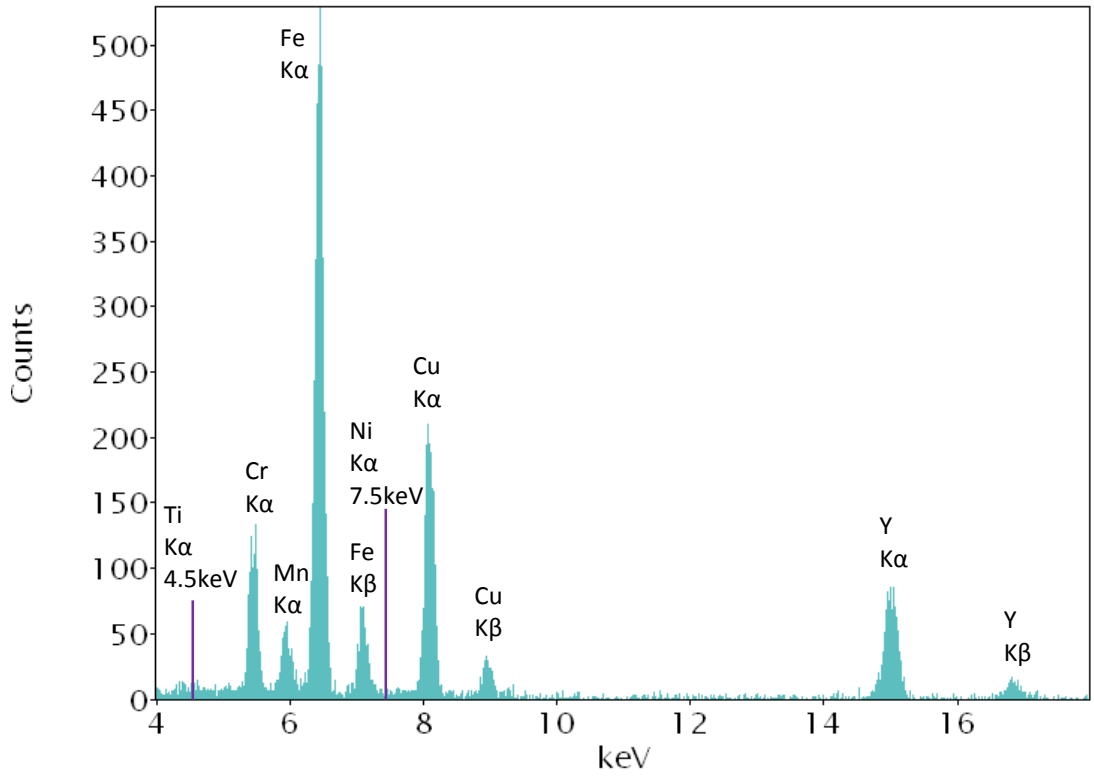


Figure 3.13 EDX Spectrum extracted from the particle shown in Figure 3.8 showing Fe Cu Cr Y peaks and the Kα peak positions for Ti and Ni

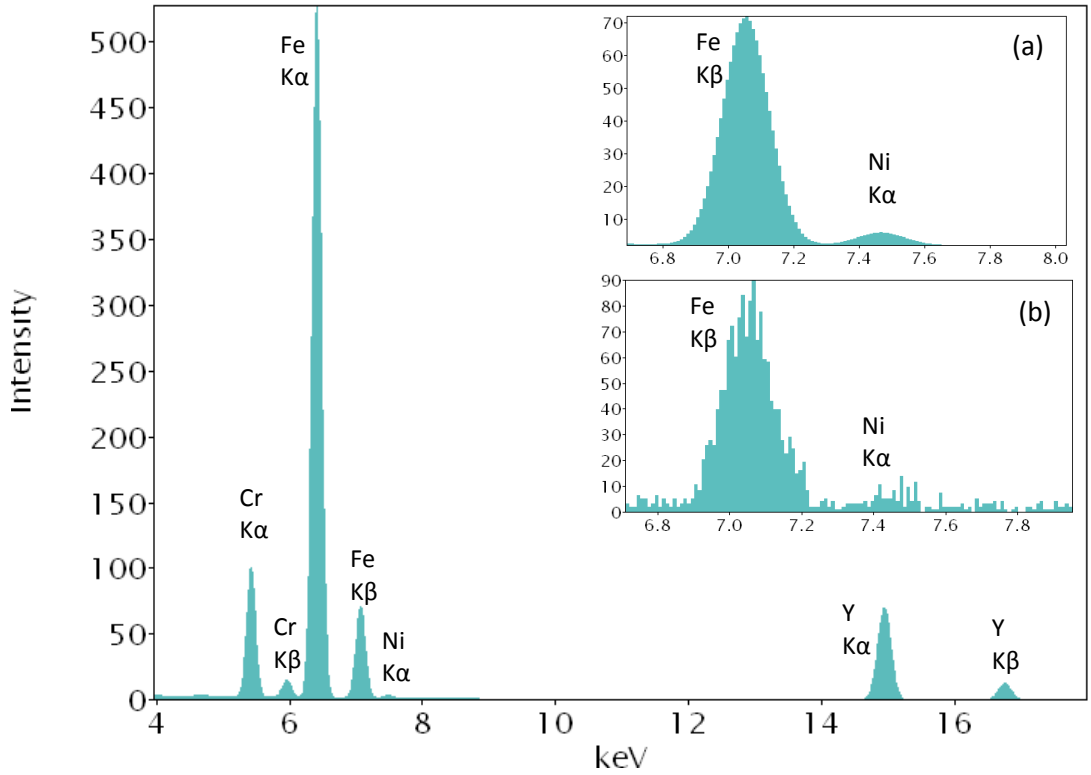


Figure 3.14 Simulated EDX spectrum for a simplified Fe-30Cr-20Y-0.5Ni (at%) system. (a) shows the Ni peak produced at 7.5keV. In (b) this peak is obscured with the addition of Poisson noise.

3.4.2 Vessel Composition and Powder Contamination

The presence of titanium poses no problems for the production of YWT alloys for the implantation study but the nickel content of the model alloy indicates that significant erosion and incorporation of the milling vessel steel occurred during mechanical alloying. A simulated EDX spectrum, produced using the DTSA software package [151] and presented in Figure 3.14, reproduced the main peaks at the appropriate intensities recorded in Figure 3.13 using a simplified Fe-30Cr-20Y system. Adding 0.1Ni (at%) produced a detectable Ni Kα peak at 7.5keV in the simulation but the signal to noise ratio remained poor up to 0.5Ni (at%) as shown in Figure 3.14.

Increasing the duration of the mechanical alloying process, from 24 to 60 hours, to improve the homogeneity of the consolidated alloy in line with the neutron diffraction studies on yttrium dissolution reported by Zhang and Gorley in [152], increases the potential for contamination from the vessel. To address this problem, all subsequent powder processing makes use of a bespoke Fe-1.6Cr-0.25Mn-0.3Si AISI 52100 chromium steel vessel, limiting the available contaminants to those already present in the pre-alloyed powder.

3.4.3 Argon Trapping at Particle Boundaries

The argon bubble trapped at the particle boundary in Figure 3.8 demonstrates the gas trapping potential of the particle dispersion. The arrangement closely resembles the micrographs recorded by Klimenkov in [46] and [153] showing large argon bubbles trapped at particle boundaries in electropolished TEM samples of a Fe-9Cr-1.1W-0.45Mn-0.2V-0.14Ta-0.3Ti-0.3Y_2O_3 ODS alloy.

Klimenkov calculates atomic densities for argon bubbles of various sizes from the signal intensities of EDX spectra. These were calibrated using the titanium signal recorded from the adjacent particle and weighted using the Cliff-Lorimer method, assuming that the particle is spherical and that it adopts a $Y_2Ti_2O_7$ structure.

The densities were converted to gas pressures using the Van der Waals equation applied to the consolidation temperature of the alloy, producing results in good agreement with the equilibrium pressure model. However, the lack of a standard for calculating the Cliff-Lorimer k-factors, and the assumptions regarding particle geometry, likely introduce much larger errors than are included in the calculated pressures.

Applying these assumptions to the 5nm argon bubble shown in Figure 3.8 provides estimates for atomic density and pressure at 300K of 15 nm^{-3} and 200MPa ± 50MPa. The successful identification of these features at these high pressures validates use of the FIB lift out method for the study of trapped gas bubbles and demonstrates their stability in thin foils exposed to an ion beam during sample preparation.

3.5 Summary

A nominal model alloy Fe-14Cr-0.5Si-0.2Mn-0.2Ni-0.1Ti-0.3Y_2O_3 made using pre-alloyed Fe-14Cr powders and consolidated at 1120^{o}C and 103MPa supports a minimum of two particle compositions in the oxide particle dispersion. One is characterised by large yttrium oxide based (>10nm) precipitates and the other, (being more characteristic of YWT alloy formulations), comprising small (<5nm) yttrium titanium particles. At the length scales accessible using APT the particle dispersion appears inhomogeneous, meriting an increase in the duration of mechanical alloying in line with the neutron diffraction data presented by Gorley and Zhang [152].

The microstructure exhibits what appears to be a bimodal grain size distribution, although a full statistical characterisation of grain size is limited by both the small sample area visible in the TEM and the lack of alternative techniques capable of resolving the smallest grains. Significant precipitate decoration is visible at grain boundaries enriched in chromium, silicon, manganese and nickel. The difficulty in detecting the nickel contributed by vessel erosion in the TEM, demonstrates the necessity of using multiple independent techniques to perform a reliable characterisation. To improve control over the alloy compositions, especially when using longer alloying times, all subsequent production used nickel-free AISI 52100 chromium steel vessels and milling balls.

4 Characterisation of a YWT ODS System Processed Using Systematically Varying Consolidation Conditions

4.1 Summary

Having substantiated the processing route, a set of Fe-14Cr-3W-0.2Ti-0.25Y_2O_3 ODS alloys were fabricated using the methods outlined in Section 3 with the aim of producing controlled material for subsequent characterisation. These were chemically assayed and successfully consolidated at 950^{o}C, 1050^{o}C and 1150^{o}C in an attempt to reproduce the reduction in particle density with temperature noted by Alinger [58], enabling a subsequent study of the effects of particle density on helium sequestration.

Preliminary TEM characterisation verified the successful production of three particle dispersions, each having a regular shape and size distribution. The average particle size varied from 1.1nm to 1.6nm with increasing temperature. Like the model alloy characterised in Section 3, the system exhibited a bimodal grain size distribution at all three consolidation temperatures. No correlation between the grain size and the particle dispersion was apparent.

A full APT characterisation was performed for each HIP temperature. A particle analysis was completed using the maximum separation method [136], with cluster selection parameters chosen using a combination of TEM data and the Kolli and Seidman method [154]. This allowed the particle number density in each consolidation to be evaluated. These were found to be in good agreement with those reported by Alinger in a comparable system [14] [58] but the use of APT in this work, instead of SANS, provided additional insights into the chemistry of the particle dispersion.

Apart from a few large manganese-titanium oxides the particles adopt a $Y_2Ti_3O_5$ stoichiometry that fits none of the known stable oxide chemistries. Thermal aging at 1150^{o}C causes a shift to a $YTiO_2$ stoichiometry and a corresponding loss of chromium. It is proposed that the transformation from metastable cluster to pyrochlore oxide observed by Ribis and DeCarlan [76] occurs in the system studied here. The atom probe data indicates a possible correlation between the loss of the chromium shell and the transition to the more thermodynamically favourable pyrochlore oxide.

4.2 Materials and Methods

A Fe-14Cr-3W-0.4Ti (wt%) powder composition was selected for the production of a YWT alloy to match the formulation studied by Odette and Alinger [58]. However, the chemical analysis provided by Aubert Duval in Table 4.1, shows 0.2Ti (wt%) in the received material. The powder was mechanically alloyed to powdered $0.25Y_2O_3$ (wt%) using the methods outlined in Section 3.2.2 under the revised processing conditions provided in Section 3.5.

	Elemental Composition											
	Fe	**Si**	**Mn**	**Cr**	**Ni**	**Mo**	**Co**	**Ti**	**N**	**W**	**O**	**C**
(wt%)	82.09	0.17	0.35	14.04	0.02	0.00	0.01	0.24	0.01	3.03	0.01	0.01
(at%)	82.76	0.34	0.36	15.19	0.02	0.00	0.01	0.27	0.04	0.93	0.03	0.04

Table 4.1 Chemical analysis of pre-alloyed Fe-14Cr-0.2Ti-3W powder provided by Aubert Duval

The alloyed Fe-14Cr-3W-0.2Ti-$0.25Y_2O_3$ powder and a reference Fe-14Cr-3W-0.2Ti powder were prepared for consolidation at 150 MPa as outlined in Section 3.2.3. The HIP temperature was ramped at 3°C/min and held at the consolidation point for a 4 hour dwell period. Samples were consolidated at 850°C, 950°C, 1050°C and 1150°C as shown in Table 4.2 but those processed at 850°C failed to produce a dense solid and were not studied further.

Pre-alloyed (wt%)	**Mechanically alloyed (wt%)**	**Processing conditions**			
Fe-14Cr-0.2Ti-3W	-	150MPa 1150°C 4hr	150MPa 1050°C 4hr	150MPa 950°C 4hr	150MPa 850°C 4hr
Fe-14Cr-0.2Ti-3W	$0.25Y_2O_3$				

Table 4.2 Summary of alloy composition and consolidation conditions

Samples of the successfully consolidated alloys were submitted for chemical analysis to London Scandinavian Metals Analytical Services to provide an independent measurement of composition prior to characterisation. These measurements were produced using X-ray fluorescence techniques and inert gas fusion methods where necessary. The data are summarised for the Fe-14Cr-3W-0.2Ti reference system in Table 4.3 and the ODS Fe-14Cr-3W-0.2Ti-0.25Y_2O_3 system in Table 4.4.

	Elemental Composition ± 0.05												
	Fe	**Al**	**Si**	**Mn**	**Cr**	**Ni**	**Mo**	**Co**	**Ti**	**N_{GF}**	**W**	**O_{GF}**	**C_{GF}**
(wt%)	82.81	0.17	0.15	0.35	13.06	<0.05	<0.05	<0.05	0.21	0.03	2.65	0.09	0.11
(at%)	82.70	0.35	0.30	0.35	14.00	<0.05	<0.05	<0.05	0.24	0.12	0.80	0.32	0.52

Table 4.3 Chemical analysis of consolidated Fe-14Cr-0.2Ti-3W provided by London Scandinavian. (X_{GF} denotes gas fusion)

	Elemental Composition ± 0.05												
	Fe	**Al**	**Si**	**Mn**	**Cr**	**Ni**	**Mo**	**Co**	**Ti**	**N_{GF}**	**W**	**O_{GF}**	**C_{GF}**
(wt%)	82.21	0.11	0.18	0.33	13.34	<0.05	<0.05	<0.05	0.21	0.20	2.66	0.28	0.09
(at%)	81.39	0.23	0.36	0.33	14.17	<0.05	<0.05	<0.05	0.24	0.79	0.80	0.97	0.42

Table 4.4 Chemical analysis of consolidated Fe-14Cr-0.2Ti-3W-0.25Y_2O_3 provided by London Scandinavian. (X_{GF} denotes gas fusion)

Both alloys show minimal nickel, molybdenum and cobalt content supporting the steps taken to address the incorporation of vessel materials outlined in Section 3.4.2. Silicon and manganese are constant from powder to consolidation with silicon showing a modest reduction from the values recorded in the model alloy analysed in Section 3. No likely sources of the 0.23Al (at%) could be identified in the production or analysis methods, suggesting that the contamination occurs during gas atomisation.

The oxygen content of both systems would indicate the incorporation of significant quantities of atmospheric oxygen during production in addition to the 0.18 (at%) provided by 0.25Y_2O_3 (wt%) but the LECO gas fusion methods used for oxygen quantification by London Scandinavian necessarily expose powdered alloy to the atmosphere potentially inflating both the oxygen and nitrogen values shown in Table 4.3 and Table 4.4. Y was not checked as the addition of Y was controlled at the alloying stage.

4.3 TEM Characterisation

Samples of the consolidated alloys were prepared for TEM characterisation following the methods outlined in Section 2.3 and imaged using a JEOL 2100 TEM at the University of Liverpool with the assistance of Dr Karl Dawson. Figure 4.1(a)-(d) catalogues the microstructure in the Fe-14Cr-3W-0.2Ti-0.25Y_2O_3 alloy consolidated at 1150^{o}C. The sample presents a bimodal equiaxed grain size distribution apparent in Figure 4.1 (a). The grain size varies between 20 and 200nm in the fine grained regions but much larger grains are present, some over a micron wide.

The oxide particles are dispersed through the wider microstructure shown in Figure 4.1 (b) at very high densities and appear to be evenly distributed through both the coarse and fine grained regions like those shown in Figure 4.1 (c) and (d) . The particles visible in Figure 4.1 (d) are regular in shape and size showing no evidence of the bimodal particle size distribution evident in the model alloy. Large oxide particles and carbides over 100nm in size are present but form a small proportion of the overall population and there is little evidence of the pronounced grain boundary decoration that is apparent in the model alloy shown in Figure 3.7.

Similar trends in the grain size distribution and particle dispersion are apparent in the samples consolidated at 1050^{o}C and 950^{o}C as shown in Figure 4.2 and Figure 4.3 with the coarse grains being particularly apparent in Figure 4.3(a). The particle distribution in these large grains is shown in Figure 4.3(b), demonstrating that a consistent and apparently uniform distribution of the oxide particles forms throughout the microstructure at all three consolidation temperatures. Unfortunately variations in sample thickness and the lack of an analytical capability prevented quantitative measurements of particle number densities being taken from these micrographs.

As in the model alloy there are no core-shell structures apparent in the HRTEM micrographs recorded in Figure 4.4 showing 2 to 3nm particle from both the 1150^{o}C and 950^{o}C alloys. The size of these particles compared to those shown in Figure 3.8 makes it difficult to reliably interpret the crystallography and infer a structure but the micrographs do provide a reliable means of validating subsequent APT reconstruction from measurement of the particle size distribution.

The distribution and average particle sizes for each consolidation temperature are shown in Figure 4.5 based on a minimum sample size of 50 particles. The particles were measured by hand using line measurement tools in the ImageJ software package. The average radius increase from 1.0 to 1.6nm indicates modest coarsening from 950°C to 1150°C. This is consistent with a significant change in particle number density and is in good agreement with the SANS measurements presented by Odette [14] and Alinger [58][64] in a comparable Fe-14Cr-3W-0.4Ti-0.25Y_2O_3 system.

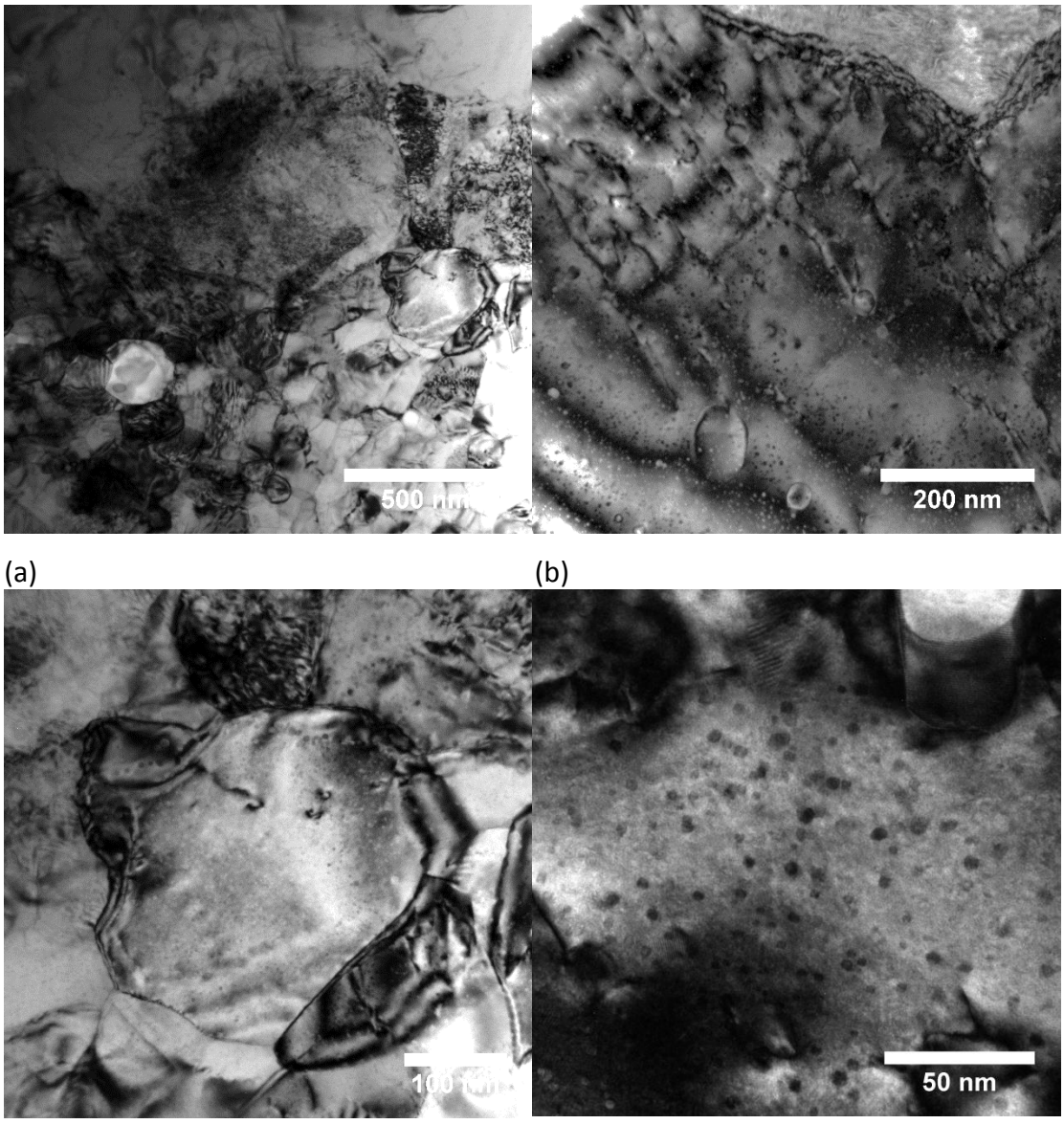
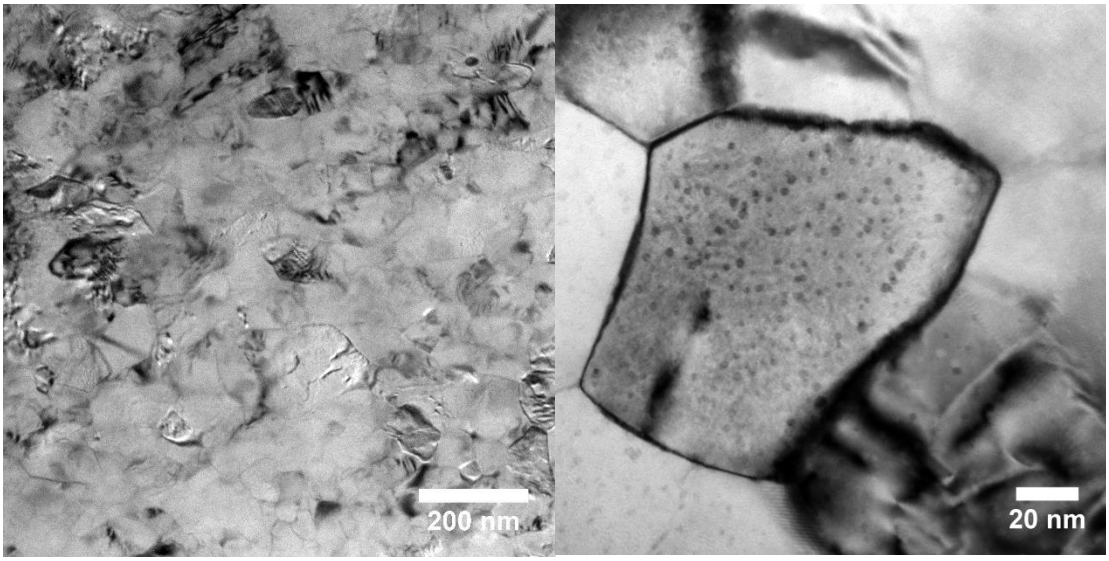
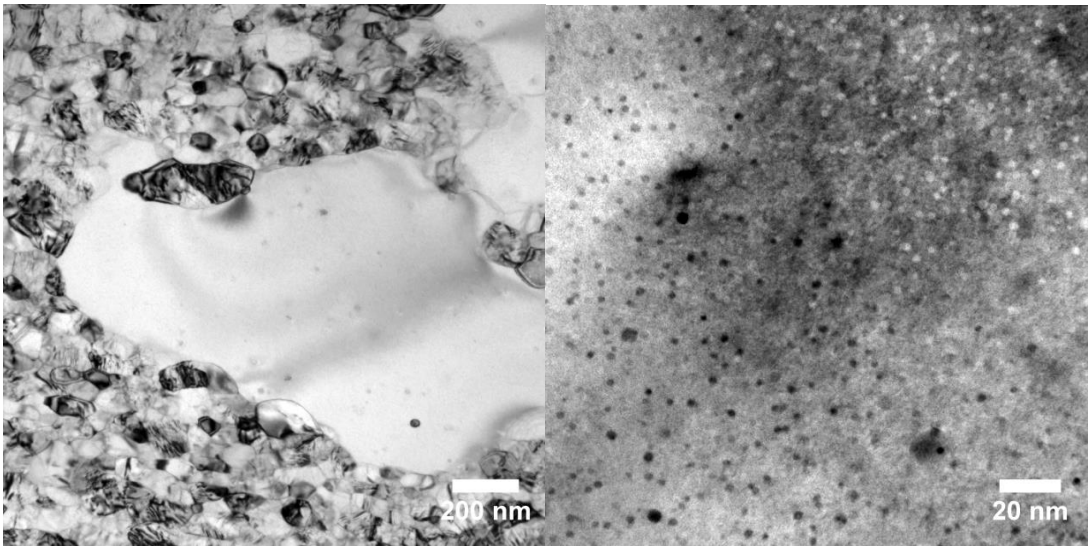


Figure 4.1 14YWT 1150°C Bright field TEM micrographs (a) Wider microstructure showing coarse and fine grained regions some presenting a dense dislocation network (b) A dense particle dispersion in a coarse grained region (c) A dense particle dispersion in a fine grained region (d) Particle dispersion in a single 100nm grain used in establishing an average particle size



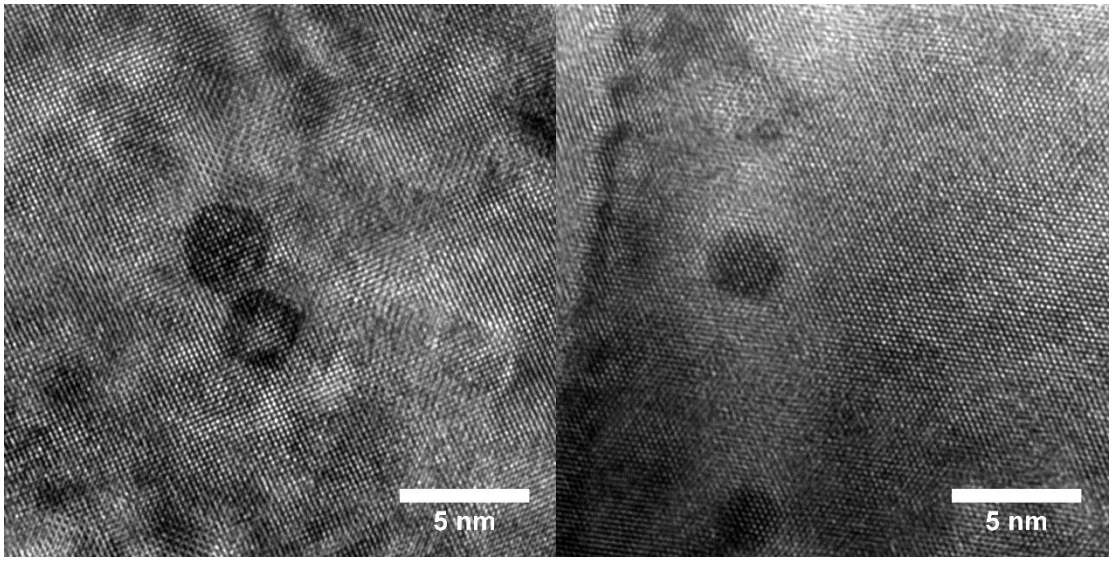
(a) (b)

Figure 4.2 14YWT 1050°C Bright field TEM micrographs (a) Wider microstructure showing a fine grained region (b) A dense particle dispersion in a fine grained region



(a) (b)

Figure 4.3 14YWT 950°C Bright field TEM micrographs (a) Wider microstructure showing coarse and fine grained regions (b) A dense particle dispersion in the coarse grain shown in (a)



(a) (b)

Figure 4.4 14YWT HRTEM micrographs recorded with the assistance of Dr Karl Dawson showing particles in material consolidated at (a) 1150°C (b) 950°C

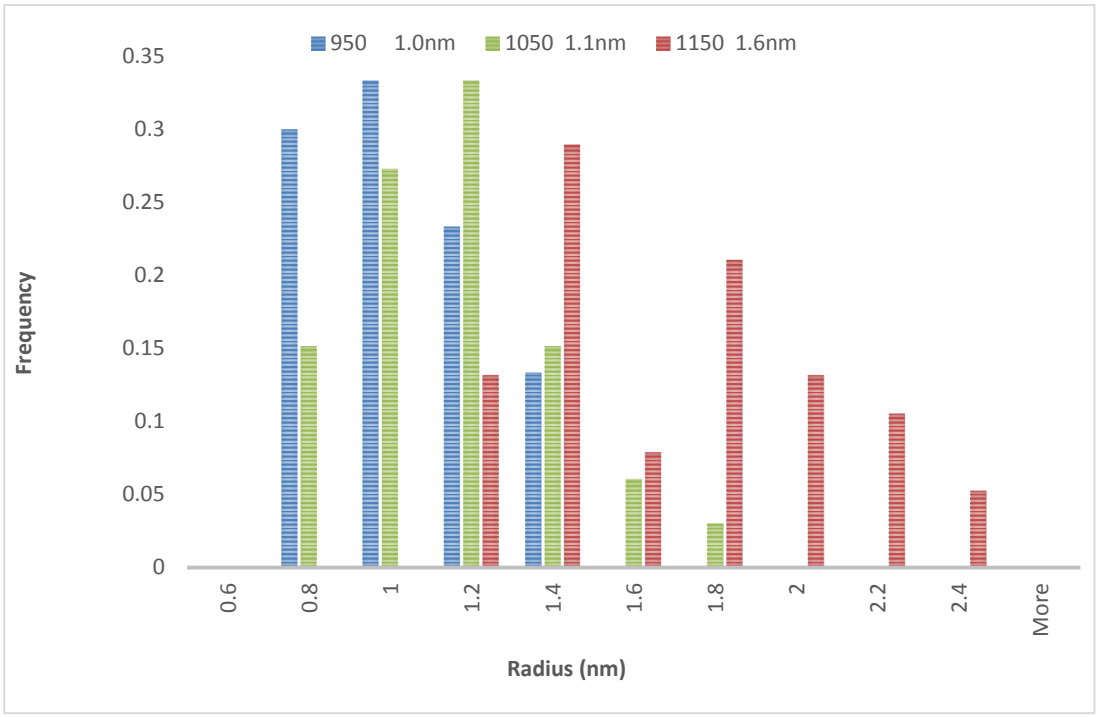


Figure 4.5 Particle size distributions and average particle sizes for each consolidation condition recorded from TEM data using a minimum of 50 particles for each temperature.

4.4 APT Characterisation

An in depth atom probe characterisation including a particle analysis was performed for samples from each consolidation condition using a minimum of 600 clusters taken from datasets between twenty and fifty million ions in size. Samples were prepared using the electropolishing methods presented in 2.2.2 and run under the analysis conditions presented in Section 2.2.3. A particle characterisation was performed for each reconstructed dataset found to be of sufficient quality using the maximum separation method outlined in Section 2.2.6. The methods used to find appropriate maximum separation parameters are developed in Sections 4.4.1 to 4.4.4 below.

4.4.1 Solute Selection

In ODS alloys a number of different solutes show clustering behaviour in the reconstructed data, but using all of these in the maximum separation method can impair the isolation of genuine clusters from the dispersion of solutes, particularly if some have significant matrix concentrations. One approach to selecting which solutes to use applies binomial grid based frequency distribution techniques to the dataset, which is divided up into voxels containing a constant total number of ions n_b [130]. The analysis measures the frequency with which voxels containing n ions of the chosen solute occur in the dataset and compares it with the expected binomial frequency distribution that would occur if the solute were randomly distributed.

The binomial distribution $f_b(n)$ and experimental distribution e(n) can be plotted and compared for each solute, with any significant difference in the two indicating a departure from a random spatial distribution in that particular solute. This departure can be quantified using X^2 statistics [130] since the expression shown in Equation 4.1 approximately follows the X^2 probability distribution with n_b degrees of freedom. The approximate X_e^2 statistics enable significance testing and provide useful insights into the spatial distribution of a particular solute. Unfortunately X_e^2 values show some dependence on the size of the dataset becoming ever more likely to indicate probable structure in a random distribution in larger datasets.

To correct the analysis for dataset size, X_e^2 is normalised by the total number of voxels N using a Pearson coefficient μ as shown in Equation 4.2. Values of μ lie between 0 and 1 with random solute distributions returning 0 and perfect associations returning 1. The Pearson coefficient does depend on the voxel size, which must remain constant if different solute distributions are to be compared [130]. No simple criterion exists for selecting how many ions to use per voxel, but voxels containing between 50 and 1000 ions are generally appropriate for the majority of solute distributions [130].

The Pearson coefficient provides a method for qualitatively assessing the departure from randomness in a solute distribution but the values are open to misinterpretation if solutes at radically different concentrations are compared. The coefficients shown in Table 4.5, computed using 200 and 1000 ion voxels for each of the major cluster forming species, indicate significant structure in the titanium oxide and yttrium distributions and a minimal departure from randomness in the yttrium oxide.

The bulk concentrations of titanium oxide and yttrium ions shown in Table 4.5 are comparable at all three temperatures making the comparison straightforward. Yttrium oxide ions appear at far lower concentrations and although they are very likely to be associated with the particles, their low concentration produces an apparently random distribution. In practice therefore the Pearson coefficient provides a good qualitative indication of which solutes are most suitable for use with the maximum separation method. Given the consistently high coefficients and concentrations recorded for titanium oxide, it was used to perform the cluster search in all cases.

Equation 4.1 $$X_e^{\,2} = \sum_{n}^{n_b} \frac{(e(n) - f_b(n))^2}{f_b(n)}$$

Equation 4.2 $$\mu = \sqrt{\frac{X_e^{\,2}}{N + X_e^{\,2}}}$$

	μ (200 ions per voxel)				μ (1000 ions per voxel)				Concentration (at%)			
Temp (°C)	**TiO**	**Y**	**O**	**YO**	**TiO**	**Y**	**O**	**YO**	**TiO**	**Y**	**O**	**YO**
950	0.49	0.36	0.14	0.08	0.63	0.41	0.26	0.13	0.14	0.09	0.07	0.02
1050	0.88	0.59	0.37	0.14	0.81	0.66	0.49	0.28	0.19	0.09	0.07	0.01
1150	0.83	0.41	0.44	0.12	0.89	0.45	0.65	0.15	0.23	0.09	0.07	0.01

Table 4.5 Pearson coefficients μ and bulk concentrations computed for each principal cluster forming ion in each consolidation condition indicating the degree of randomness in the spatial distributions using 200 and 1000 ions per voxel

4.4.2 D_{max} and N_{min} Selection

An analysis conducted by Hyde [155], using simulated atom probe data, showed that the cluster selection parameters D_{max} and N_{min} employed in the maximum separation method outlined in Section 2.4.2 are interdependent and strongly influence the characteristics of the identified clusters. However, he found that optimised selection parameters are capable of accurately characterising both the size and number density of particles in simulated and real data. If a particle population is to be properly characterised a reliable method of choosing these parameters to fit the particulars of each dataset is therefore required.

A variety of different methods have been proposed for performing the parameter selection. Some, like the approach advocated by Stephenson [137] are computationally intensive or involve prior knowledge of the sample crystallography. The approach outlined by Kolli and Seidman [154] however, can be directly implemented in IVAS and has been used successfully by Williams to isolate particle dispersions of various sizes, densities and chemistries at each processing stage for YWT based ODS steels [74].

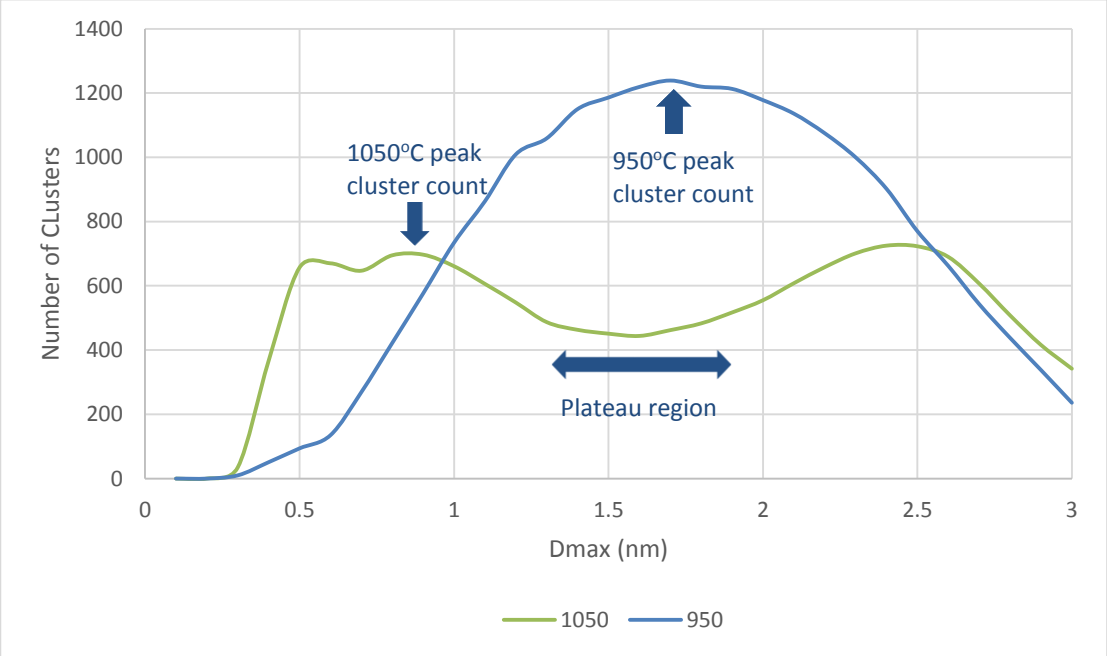


Figure 4.6 Variation in the number of clusters identified by the maximum separation method with D_{max} for an N_{min} of 6 in material consolidated at 950°C and 1050°C showing the typical plateau region and the peak cluster counts at 0.9nm and 1.7nm

Kolli and Seidman proposed plotting the number of clusters as a function of D_{max} for different values of N_{min}, producing curves like those shown in Figure 4.6. The curves typically plateau in some range of D_{max} values, below which large numbers of clusters are produced when particles are broken up and above which random fluctuations in the solute concentration are erroneously included in the count. Within this range, variations in D_{max} cause minimal variation in the cluster count, producing the plateau region and indicating that the selection parameters have successfully isolated the particles. At very large D_{max} values the method no longer functions at all, as individual particles are amalgamated into clumps and the number of identified clusters falls.

Figure 4.6 shows the variation in the cluster count with D_{max} for an N_{min} of 6 in two forty million ion datasets, one consolidated at 1050^{o}C the other at 950^{o}C. Figure 4.7 shows atom maps of these two dataset, using the particle-forming titanium oxide and yttrium ions to reveal the clustering in a 10 million ion subset of the data. The clusters isolated by the maximum separation method are shown alongside these atom maps in Figure 4.7, for D_{max} values of 0.9 and 1.7nm. These values were chosen from Figure 4.6 to isolate the maximum number of clusters in each consolidation and illustrate the application of the Kolli Seidman method to a real dataset.

At a D_{max} of 0.9nm, 700 clusters are isolated in the 1050^{o}C consolidation. Many are formed artificially when the individual particles shown in Figure 4.7(a) are divided into small clusters as shown in Figure 4.7(b). In the 950^{o}C consolidation, 580 clusters are identified at a D_{max} of 0.9nm. These appear to be discrete and correspond closely to those particles visible in Figure 4.7(d). These particles are isolated even at very small D_{max} values, removing the initial peak in the cluster count seen for the 1050^{o}C consolidation in Figure 4.6.

In the D_{max} range from 1.2 to 2.0nm the number of clusters isolated from the 1050^{o}C consolidation shows little variation. At 1.7nm the 460 clusters shown in Figure 4.7 (c) are isolated from the atom map shown in Figure 4.7 (a). In the 950^{o}C consolidation the cluster count reaches a maximum at 1.7nm and shows no comparable plateau in Figure 4.6. The inclusion of random solute fluctuations increases the count to 1200

clusters at a D_{max} of 1.7nm, doubling the apparent particle number density in the 950°C consolidation as is evident from Figure 4.7(f).

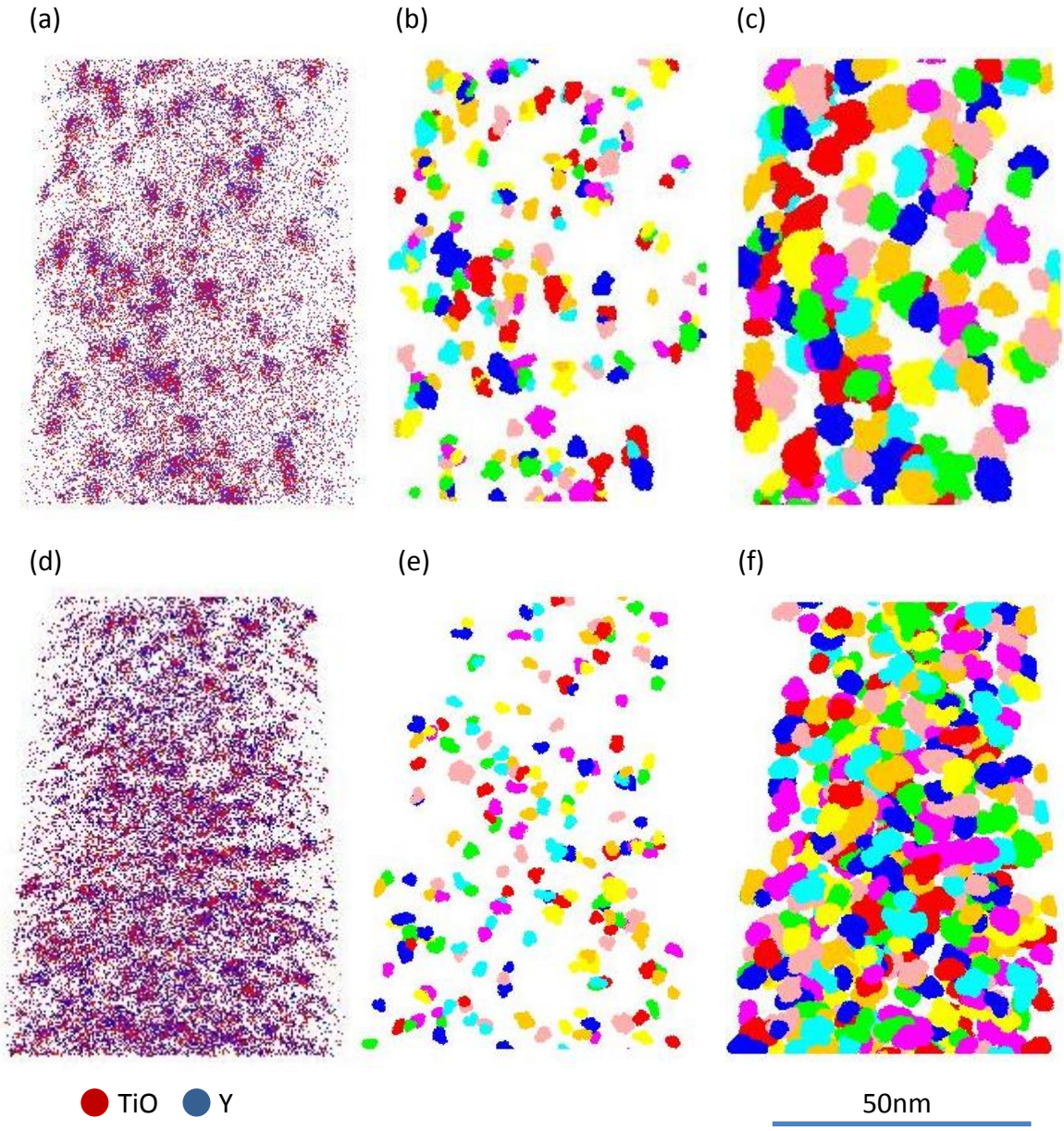


Figure 4.7 (a) Atom map showing the major particle forming ions (titanium oxide and yttrium) in a sample consolidated at 1050°C. (b) Clusters identified using a D_{max} of 0.9nm. (c) Clusters identified using a D_{max} of 1.7nm.

(d) Atom map showing the major particle forming ions (titanium oxide and yttrium oxide) in a sample consolidated at 950°C. (e) Clusters identified using a D_{max} of 0.9nm. (f) Clusters identified using a D_{max} of 1.7nm.

Note the presence of large particles identified as collections of small clusters in (b) and particle amalgamations in (f).

It is clear that if the two datasets presented in Figures 4.6 and 4.7 are to be properly characterised different selection parameters are required in each case. The denser dispersions of smaller particles formed at lower processing temperatures are particularly susceptible to the inclusion of random clusters, which consequently shows continuous variation with changing D_{max} values. By contrast, populations of larger particles at lower densities are more easily isolated using a D_{max} selected from the stable range of values identified using plots like those shown in Figure 4.6. The extent of this range varies with N_{min} as is evident if several D_{max} curves taken for different N_{min} are plotted together in Figure 4.8.

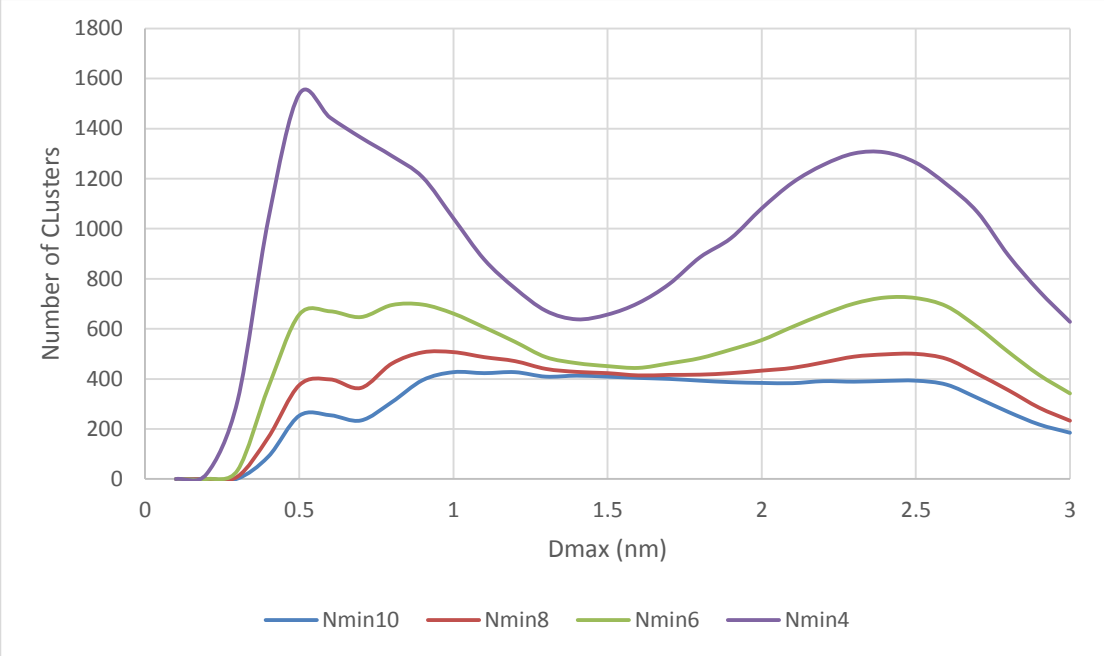


Figure 4.8 Variation in the cluster count with D_{max} for the 1050°C consolidation for different values of N_{min}

These curves show the effect of varying the chosen N_{min} on the cluster count in the 1050°C consolidation. Above an N_{min} of 6 and a D_{max} of 1 the counts begin to converge towards 400 clusters, identifying the optimum selection parameters for this particular dataset. In cases where significant random clustering prevents convergence as in the 950°C consolidation an alternative approach is required that accounts for this problem.

The number of random clusters liable to be detected in a particular dataset at various D_{max} values can be conservatively estimated by mass randomising the data and repeating the cluster search. This process randomly swaps the mass to charge ratios of all the ions in the reconstruction, removing any correlation between spatial and chemical information in the dataset. Figure 4.9 compares the cluster count in the 950°C consolidation presented in Figure 4.6 and Figure 4.7, with the count taken following mass randomisation of the dataset. This shows significant numbers of random clusters forming above a D_{max} of 1.0nm, although it is an overestimate of the numbers likely to form in the actual dataset, since all the solute ions present (including those associated with the particles) are made available for clustering following mass randomisation.

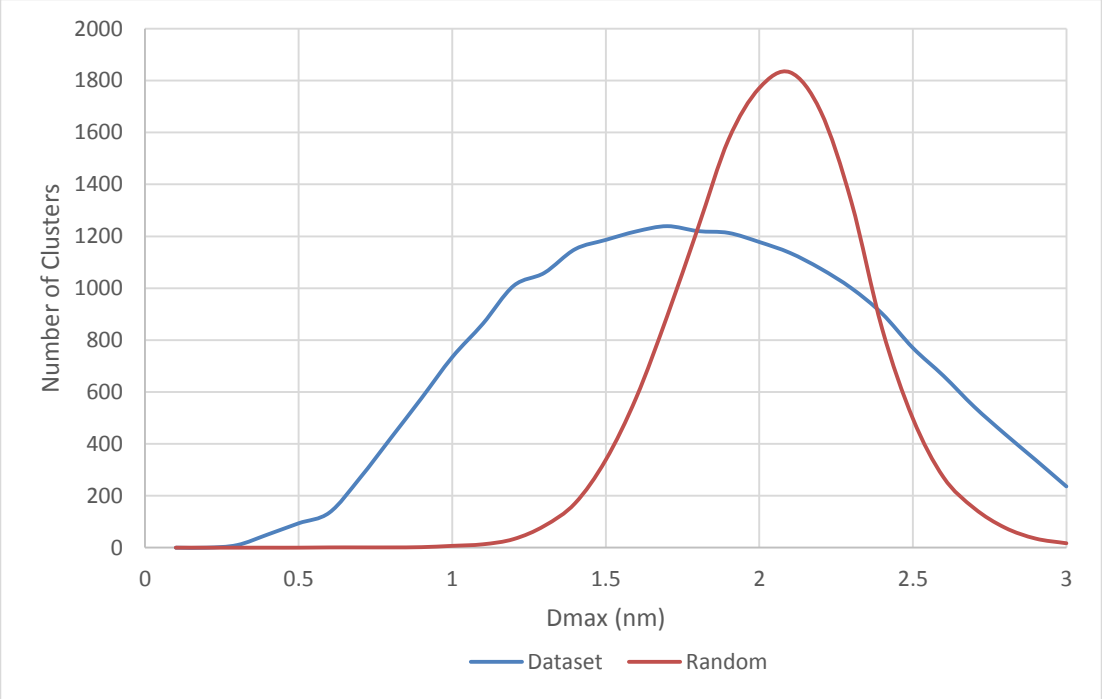


Figure 4.9 Variation in the cluster count with D_{max} for the 950°C consolidation overlaid with the cluster count following mass randomisation of the same dataset for an N_{min} of 6.

In [74] Williams proposed subtracting the number of random clusters N_{random} from the number of clusters identified in the original dataset N_{real} and normalising the result by N_{real}. A plot of this function for the 950°C dataset, shown in Figure 4.10, allows the effects of varying the chosen D_{max} to be compared for different values of N_{min} in those datasets where high matrix solute concentrations (typical of low temperature consolidations) obscure the convergence behaviour shown in Figure 4.8.

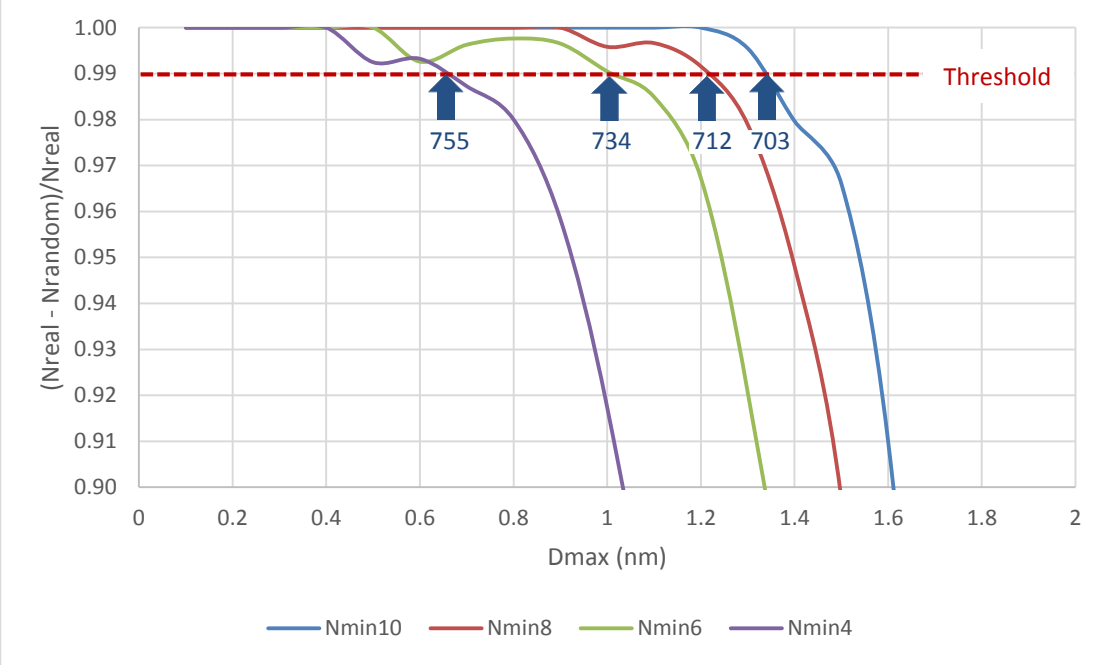


Figure 4.10 Variation in the cluster count with D_{max} following the subtraction of the random contribution and normalisation for the 950°C consolidation at different values of N_{min}. N_{real} values at the 0.99 threshold are shown.

The departure of the normalised cluster count from 1.00 in Figure 4.10 indicates the inclusion of random clusters with increasing D_{max}. The D_{max} value at departure (defined using some threshold value of the normalised cluster count) visibly increases with N_{min}. Williams uses a conservative threshold of 99% shown in Figure 4.10 and suggests selecting the largest D_{max} above this threshold for the smallest possible N_{min} to maximise the number of genuine clusters that are recorded.

This approach discards the minimum number of clusters based upon N_{min} but necessarily limits D_{max}. It also ignores the convergence that occurs in the total number of clusters identified at the threshold with increasing N_{min}, as shown on Figure 4.10. This behaviour illustrates the interdependence of the two selection criteria discussed by Hyde [136]. It results from the larger D_{max} values that become accessible at the larger N_{min} values allowing larger clusters to form, compensating for the more restrictive choice of N_{min}.

In an attempt to broaden the evidential basis for the N_{min} selection, an alternative estimate was made based on the particle size distributions taken from the TEM shown in Figure 4.5. This requires an assumed particle structure and chemistry from which the atomic densities of each element in the particle can be obtained. The smallest particles observed under HRTEM then provide a direct estimate for the minimum particle size. By accounting for the detection efficiency of the atom probe the minimum number of ions of any one particle forming element that the smallest particle will produce when field ionised can be estimated. No particles smaller than 1.0nm were observed in any of the micrographs taken from the 950^{o}C consolidation. If these particles adopt a $Y_2Ti_2O_7$ structure as widely believed [14], they can be expected to yield clusters containing six titanium oxide ions when reconstructed.

In the example shown in Figure 4.10, setting N_{min} to 6 makes D_{max} values up to 1.0nm accessible, which satisfactorily isolates clusters from the titanium oxide dispersion in the 950^{o}C consolidation, as shown in Figure 4.7. Consequently an N_{min} of 6 was used for an initial analysis in each 950^{o}C reconstruction, with a D_{max} chosen to ensure 99% of those clusters isolated from the data correspond to the genuine particle dispersion. At higher consolidation temperatures, convergence behaviour like that seen in Figure 4.8 simplified the selection process appreciably and allowed cluster isolation to be performed reliably over a relatively wide range of N_{min} and D_{max} values.

4.4.3 L Selection

The envelop distance L illustrated in Figure 2.8 is usually set within 0.5 - 1.0 D_{max} since too small an envelope can produce holes in the clusters but too large an envelope risks counting ions sitting between two clusters in close proximity as belonging to both. The size of the envelope determines how many ions (other than those identified as the clustering solute) are to be included as part of a cluster. This directly impacts on the cluster composition but has no effect on the particle identification process and the resultant number density.

Given the substantial trajectory aberrations known to be associated with the oxide particles in ODS systems, large numbers of spurious ions are likely to be included in the clusters regardless of the extent of the envelop parameter. The contribution of aberrated material from the matrix to the clusters is addressed by a subsequent matrix correction step outlined in Section 4.4.4 below. This process can also account for the addition of a shell of matrix material caused by the use of the envelope parameter which would otherwise necessitate a separate erosion process [61]. On this basis L was set to D_{max} in all cases to ensure each cluster is fully encompassed.

4.4.4 Matrix Correction

The matrix correction method developed by Williams, addresses the incorporation of surrounding matrix material into a particle on reconstruction as a result of the trajectory aberrations discussed in Section 1.6.3. The correction assumes the particles contain no iron and that matrix atoms are introduced into the particle uniformly by any aberration [61]. In practice this is unlikely given the different mass to charge ratios associated with the various alloy components, heavier ions being less susceptible to sudden changes in field compared to lighter more highly charged species.

Compensating for these behaviours on reconstruction would likely require a model of the field conditions at each particle and although attempts to quantify the aberrations using experimental data are underway, at present the matrix is assumed to behave uniformly [156]. A fraction of all the solute ions partitioned to the clusters is therefore removed in direct proportion to the aberrant iron content. The assumption that the particles contain no iron to begin with is supported by EDX spectra taken from

particles that have been chemically extracted from the ferritic matrix. In the case of the extractions performed by Dawson on ODM401 (Fe-14Cr-0.85Ti-0.3Mo-0.2Y_2O_3) [158] these spectra are corroborated by HREM micrographs that show particles in the ferritic matrix adopting a pyrochlore structure commensurate with the yttrium titanium chemistry identified in the EDX.

4.4.5 Particle Number Density Variation with Consolidation Temperature

Once cluster selection parameters had been identified for each dataset using the methods outlined above, a particle number density could be calculated for each consolidation condition. Using a minimum of 600 clusters in each case, particle number densities were computed using Equation 4.3 based on dataset volumes calculated from a weighted iron/chromium atomic number density Ω and the total number of ions in the dataset N modified by the atom probe detection efficiency ξ.

Equation 4.3 $$No.\ Density = \frac{N_c \xi}{N\Omega}$$

The variation in the average particle density in the Fe-14Cr-3W-0.2Ti-0.25Y_2O_3 system with consolidation temperature is shown in Figure 4.11, with error bars showing the overall spread in the measurements from different datasets. These data are presented alongside the measurements taken from the Fe-14Cr-3W-0.4Ti-0.25Y_2O_3 system by Alinger [14] at UC Santa Barbara using small angle neutron scattering (SANS) for comparison.

Particle size measured by taking the average radius of gyration of the clusters identified in the ATP data is also shown for comparison. Sizing from APT is generally more subjective than TEM methods and though in good agreement with the TEM for the 950^oC and 1150^oC consolidations reported in Section 4.3, the average radius estimated for the 1050^oC consolidation appears anomalously large. A further discussion of sizing methodology in APT is made in Section 4.4.10 where no supporting TEM data are available.

The Oxford and Santa Barbara alloys shared common processing methods and consolidation conditions but differ in titanium content. The apparent variation in the

particle number density therefore indicates the potentially significant impact of titanium content on particle formation. Any further analysis would require all processing variables be accounted for and compared in the two studies which extends beyond the scope of this analysis.

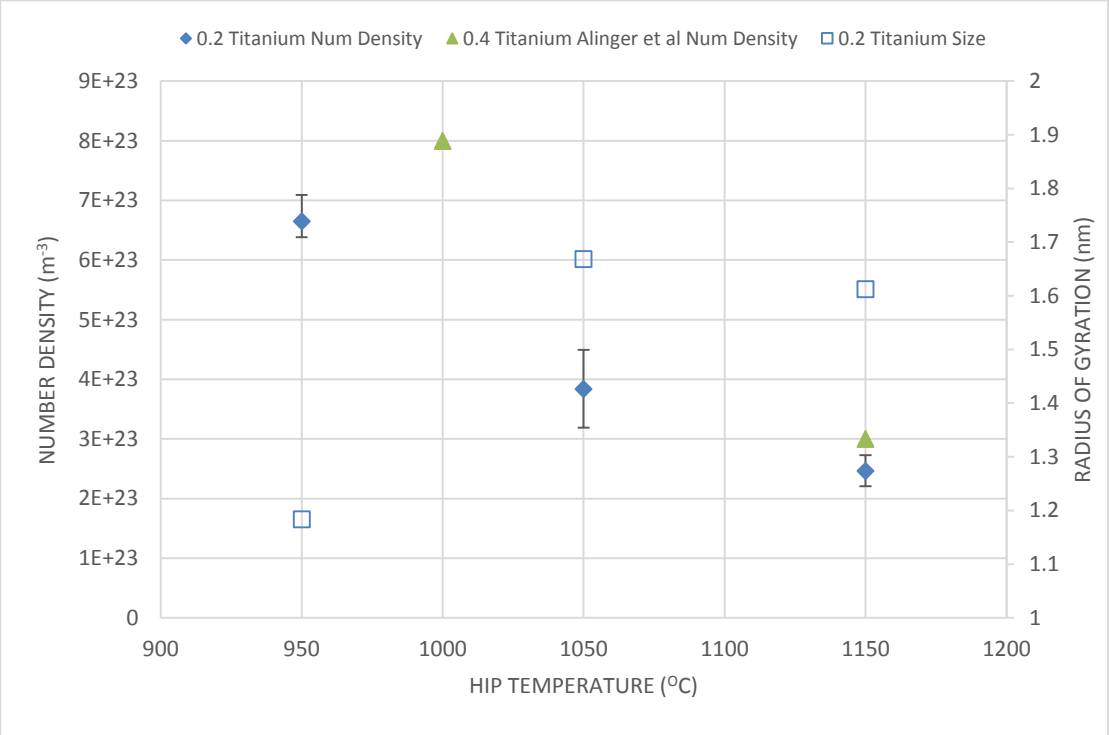


Figure 4.11 Variation in cluster number density and size with HIP temperature as measured by APT in the Fe-14Cr-3W-0.2Ti-0.25Y_2O_3 system. SANS data taken by Alinger [14] in the Fe-14Cr-3W-0.4Ti-0.25Y_2O_3 system is provided for comparison.

Figure 4.11 shows the Fe-14Cr-3W-0.2Ti-0.25Y_2O_3 (wt%) system supports an average particle number density of 2.5×10^{23} m^{-3} when consolidated at 1150°C, comparable to the densities reported by Alinger in the Fe-14Cr-3W-0.4Ti-0.25Y_2O_3 (wt%) system. These measurements also match those reported using both APT and TEM in other YWT systems consolidated at 1150°C including MA957 [157] and ODM401 [158].

Both the 0.2Ti and 0.4Ti compositions show the same trend in Figure 4.11; a substantial drop in particle density with increasing consolidation temperature. The Fe-14Cr-3W-0.2Ti-0.25Y_2O_3 (wt%) system shows a significantly smaller density reduction by comparison with the 0.4Ti (wt%) alloy, falling from 7×10^{23} m^{-3} at 950°C to 2×10^{23} m^{-3} at 1150°C. The density reduction can be directly observed in the APT data by mapping the major cluster-forming ions in datasets consolidated at each temperature as shown in Figure 4.12.

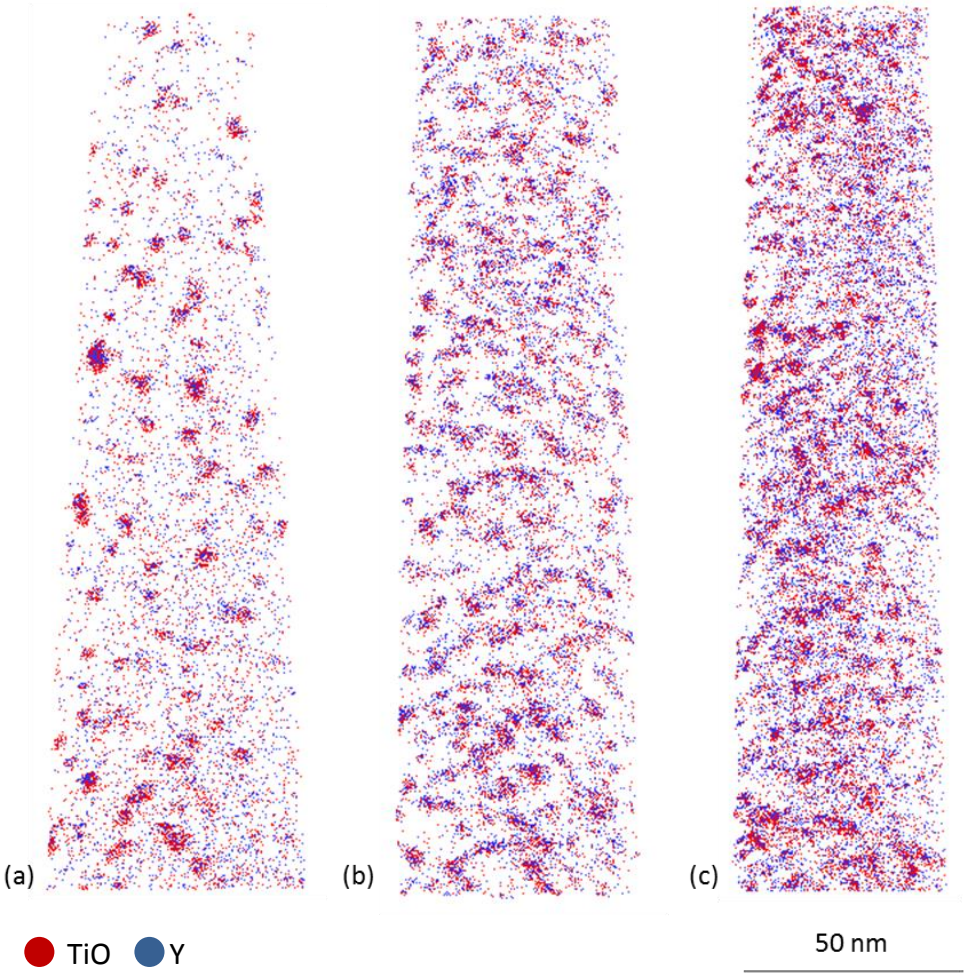


Figure 4.12 Particle density variation shown using atom maps of the major titanium oxide and yttrium particle-forming ions in samples consolidated at (a) 1150 °C (b) 1050°C (c) 950 °C

4.4.6 Alloy Chemistry Variation with Consolidation Temperature

Table 4.6 shows the bulk compositions measured by APT for each consolidation temperature, alongside the nominal composition for the system. The measurements are computed from the total number of ions of each element identified in a dataset, averaged over three datasets, using a minimum of 80 million ions in total to calculate the average composition.

The matrix compositions shown in Table 4.6 are computed in the same way, following the removal of all those ions identified as part of the cluster distribution by the maximum separation method. An electron probe microanalysis (EPMA) carried out by Gorley, shown in Table 4.6 along with the chemical analysis shown in Table 4.4 provide

an independent measurement of the nominal composition in the consolidated alloy. These are broadly consistent with the bulk APT compositions, except for the higher concentrations of oxygen and nitrogen identified in Table 4.4. These are likely to have been inflated by atmospheric exposure during the chemical analysis.

The 0.2 (at%) Al identified in Table 4.4 is absent from the bulk APT measurements. A peak corresponding to Al^{2+} does appear in some datasets but at concentrations <0.005(at%). Coarse aluminium oxides like those present in the aluminium containing alloys (MA956 and PM2000) discussed in Section 1.6.1 and located outside the APT volumes sampled in Table 4.6, may be responsible for the aluminium content reported in Table 4.4. Alternatively aluminium contamination might have occurred during the chemical analysis though no details concerning the analysis procedure are available.

Within error the bulk compositions from APT are broadly consistent. The oxygen content shows a modest reduction between corresponding bulk and matrix compositions that increases with processing temperature, indicative of oxygen migration from the matrix to the particles. This is attributed to the formation of large (>30nm) grain boundary oxides by Williams, which are discussed in more detail in Sections 4.4.8 and 4.4.9.

(at%)	Nom	EPMA	APT Bulk Composition			APT Matrix Composition		
			1150°C	1050°C	950°C	1150°C	1050°C	950°C
Cr	15.2	14.5	12.2 ± 1.41	13.9 ± 0.34	13.2 ± 0.24	12.0 ± 1.0	13.7 ± 0.3	13.0 ± 0.2
Fe	83.3	84.0	85.9 ± 1.85	84.2 ± 0.63	84.9 ± 0.24	86.3 ± 1.1	84.7 ± 0.4	85.2 ± 0.2
Y	0.1	0.1	0.1 ± 0.01	0.1 ± 0.02	0.1 ± 0.01	0.1 ± 0.0	0.0 ± 0.0	0.1 ± 0.0
O	0.2	-	0.3 ± 0.09	0.2 ± 0.11	0.2 ± 0.02	0.1 ± 0.0	0.1 ± 0.0	0.2 ± 0.0
Si	-	-	0.5 ± 0.07	0.4 ± 0.01	0.4 ± 0.01	0.4 ± 0.0	0.4 ± 0.0	0.4 ± 0.0
Mn	-	0.4	0.3 ± 0.05	0.3 ± 0.08	0.3 ± 0.01	0.2 ± 0.0	0.3 ± 0.0	0.3 ± 0.0
C	-	-	0.0 ± 0.01	0.0 ± 0.03	0.0 ± 0.01	0.0 ± 0.0	0.0 ± 0.0	0.0 ± 0.0
Ti	0.4	0.3	0.2 ± 0.11	0.1 ± 0.06	0.1 ± 0.01	0.1 ± 0.0	0.1 ± 0.0	0.1 ± 0.0
W	0.9	0.8	0.5 ± 0.05	0.6 ± 0.09	0.6 ± 0.01	0.5 ± 0.0	0.6 ± 0.1	0.6 ± 0.0
N	-	-	0.1 ± 0.07	0.2 ± 0.07	0.1 ± 0.01	0.1 ± 0.0	0.1 ± 0.0	0.1 ± 0.0

Table 4.6 Average bulk and matrix compositions measured using APT for each consolidation condition. A nominal composition is provided for reference alongside independent EPMA measurements taken by Gorley [147].

4.4.7 Particle Chemistry Variation with Consolidation Temperature

The average cluster composition produced by the maximum separation method for each consolidation condition is shown in Table 4.7, both before and after matrix correction. The average composition is taken using all the clusters identified in all the available datasets for a particular consolidation with a standard error. Those precipitates that noticeably depart from the typical oxide particle characteristics in composition or size are excluded from the data shown in Table 4.7. These are the subject of a separate analysis presented in Section 4.4.8.

In all three consolidation conditions the clusters isolated by the maximum separation method are primarily iron and chromium. Following the matrix correction an yttrium, oxygen and titanium stoichiometry emerges with minor silicon and nitrogen components; but the clusters still contain large amounts of chromium even after the matrix correction has been applied. A modest reduction in this chromium content occurs with increasing consolidation temperature but in general the particle compositions are stable across the range of consolidation temperatures.

	APT Cluster Composition (at %)			APT Matrix Corrected Cluster Composition (at%)		
	1150°C	**1050°C**	**950°C**	**1150°C**	**1050°C**	**950°C**
Cr	15.3 ± 0.1	16.8 ± 0.1	17.4 ± 0.1	51.3 ± 0.8	55.7 ± 0.9	58.7 ± 1.2
Fe	79.3 ± 0.1	78.4 ± 0.1	77.3 ± 0.1	0.0 ± 0.0	0.0 ± 0.0	0.0 ± 0.0
Y	0.6 ± 0.1	0.6 ± 0.1	0.6 ± 0.1	7.5 ± 0.7	7.3 ± 0.8	6.1 ± 1.3
O	1.7 ± 0.1	1.3 ± 0.1	1.4 ± 0.1	18.8 ± 0.7	16.5 ± 0.8	15.2 ± 1.3
Si	0.8 ± 0.1	0.6 ± 0.0	0.7 ± 0.1	4.7 ± 0.9	4.2 ± 0.8	3.7 ± 1.5
Mn	0.3 ± 0.1	0.3 ± 0.0	0.4 ± 0.1	0.8 ± 1.0	0.7 ± 1.1	1.0 ± 1.5
C	0.1 ± 0.1	0.1 ± 0.1	0.2 ± 0.1	1.6 ± 0.8	1.7 ± 0.8	1.6 ± 1.4
Ti	1.0 ± 0.1	0.8 ± 0.1	0.9 ± 0.1	12.0 ± 0.7	10.0 ± 0.8	10.6 ± 1.2
W	0.4 ± 0.0	0.6 ± 0.0	0.7 ± 0.2	-0.8 ± 2.0	-0.1 ± 2.5	0.2 ± 3.2
N	0.5 ± 0.1	0.4 ± 0.0	0.4 ± 0.1	4.1 ± 0.7	4.0 ± 0.7	2.9 ± 1.0

Table 4.7 Average cluster compositions for each consolidation temperature calculated from a minimum of 600 clusters. The compositions are shown for the APT raw data and following the matrix correction.

APT Matrix Corrected Y:Ti:O Cluster Ratios (at%)			
	1150°C	**1050°C**	**950°C**
Y	19.5 ± 1.8	21.6 ± 2.3	19.1 ± 3.9
Ti	31.3 ± 1.8	29.5 ± 2.3	33.2 ± 3.7
O	49.2 ± 1.7	48.9 ± 2.5	47.7 ± 3.9

Table 4.8 Average Y:Ti:O ratios in the matrix corrected cluster composition for each consolidation condition

The Y:Ti:O ratios presented in Table 4.8 maintain a constant 2:3:5 stoichiometry within experimental error for each consolidation condition. This differs appreciably from the 1:2:3 stoichiometry reported by Williams for a 14YWT system consolidated at 1150°C but shares the same 1:1 metal to oxygen ratio. The significance of this chemistry and the effects of subsequent thermal treatments are discussed further in Sections 4.4.10 and 4.5

4.4.8 Titanium-Manganese Precipitates

Large 20 to 50 nm precipitates included by the maximum separation method in the wider cluster population were omitted from the compositional analysis performed in Section 4.4.7. These were removed for a separate characterisation of their composition and properties and proved in all cases to contain high concentrations of manganese, titanium, silicon and oxygen. One particular dataset taken from an 1150^{o}C consolidation contained three separate examples of these large particles, which are easily seen in the atom maps shown in Figure 4.13.

The yttrium, titanium oxide and chromium oxide atom maps in Figure 4.13 show the general cluster population dispersed throughout the dataset. The large precipitates are evident in all save the yttrium and tungsten maps in Figure 4.13 but appear to have two distinct phases, one enriched in silicon, titanium and oxygen and the other in chromium, oxygen and manganese. The precipitates are particularly evident in the titanium map and increased the bulk concentration of metallic titanium in this dataset to 0.1 (at%). This is in contrast to the wider oxide cluster population that typically contributes 0.01 (at%) metallic titanium to the bulk, with the majority of the titanium present evaporating as titanium oxide as shown in Figure 4.13.

The average composition of the three large precipitates is shown in Table 4.9. Their size makes them relatively immune from aberrations and the compositions are presented without any form of matrix correction but this treatment ignores the obvious internal structure evident from Figure 4.13. Separate compositions are provided in Table 4.9 for the titanium and manganese phases identified in Figure 4.13 using 5 (at%) manganese and 5 (at%) titanium isoconcentration surfaces shown in Figure 4.14.

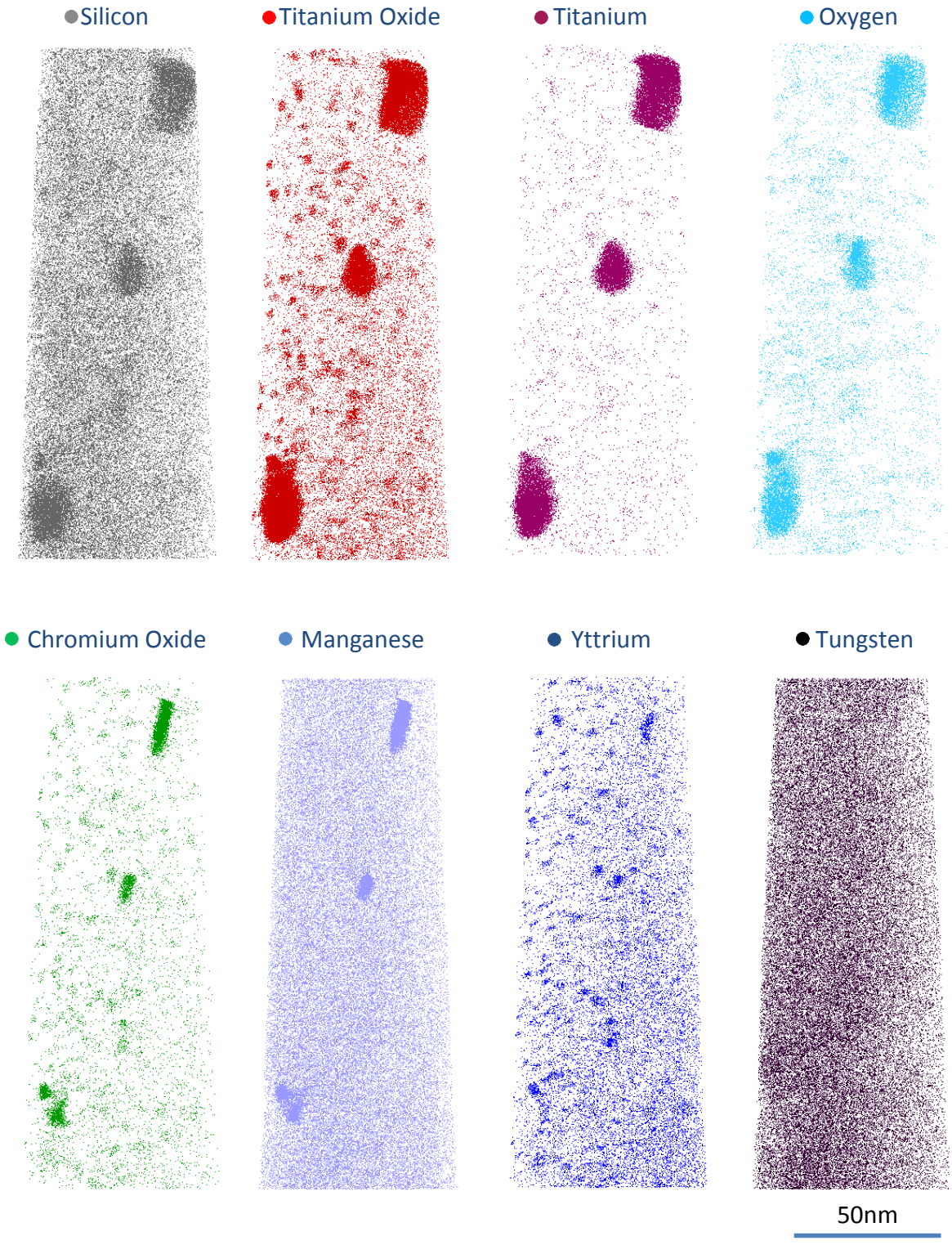


Figure 4.13 Atom maps of the major solute ions recorded from an 1150°C consolidation showing oxide particle clustering in the yttrium titanium oxide and chromium oxide ions and large precipitates in the silicon, manganese, oxygen and titanium ions.

Taking the compositions from Table 4.9, the 5 (at%) manganese isoconcentration surfaces enclose four Fe-21Cr-10Mn-13Ti-18O inclusions associated with three Fe-18Cr-9Si-26Ti-19O (at%) precipitates enclosed by 5 (at%) titanium isoconcentration surfaces. These compositions would indicate the presence of substoichiometric oxide phases and although no manganese oxide peaks are present, significant quantities of both chromium oxide and titanium oxide ions are recorded and appear in Figure 4.13.

Multiple detection events and evaporation between pulses were considered and discounted as a source of oxygen loss by Williams in a study of the evaporation behaviour of bulk oxides [61]. Nevertheless, these factors may be responsible for suppressing the detection of oxygen ions in the precipitates, given their different chemistry and ionisation behaviour. TiO^+ and O_2^+ peak convolution can be discounted by the presence of minor TiO^+ isotopes as shown in Section 2.2.4 but there is a possibility that the O^+ peak conceals O_2^{2+} ions. Although no other O_2 peaks are visible in the dataset, if the majority of the O^+ peak were O_2^{2+} this would account for the apparently substoichiometric composition in both these two phases and the oxide particles.

The close spatial association between the two phases shows no correlation with orientation inside the dataset, suggesting the spatial relationship is genuine and not the result of an evaporation artefact. The size and orientation of the largest precipitate shown in Figure 4.15 allowed a 1D cylindrical concentration profile to be taken through the titanium containing phase in the direction of evaporation, sampling the concentration of each ion every 1.0nm.

Sampling interfaces perpendicular to the evaporation direction reduces the homogenising influence of aberrations on particle boundaries, allowing shell structures to be resolved like those shown in the chromium map in Figure 1.17. The concentration profile presented here in Figure 4.15 shows a similar structure in the titanium containing precipitate. The chromium concentration increases from the matrix concentration of approximately 15% in the vicinity of the precipitate to 30% at the precipitate boundary with the symmetry of the profile offering further evidence that the feature is a genuine structure and not an evaporation artefact.

	Precipitate Composition (at%)		
	Maximum Separation	Isoconcentration 5% Titanium	Isoconcentration 5% Manganese
Cr	19.15 ± 1.2	18.1 ± 1.1	20.8 ± 0.6
Fe	44.98 ± 5.4	23.5 ± 2.6	31.6 ± 6.4
Y	0.30 ± 0.0	0.2 ± 0.0	0.7 ± 0.1
O	13.01 ± 1.6	19.3 ± 2.2	17.9 ± 2.7
Si	5.50 ± 0.8	9.0 ± 0.3	2.3 ± 0.3
Mn	3.04 ± 1.2	1.5 ± 0.5	9.7 ± 1.3
C	0.02 ± 0.0	0.0 ± 0.0	0.0 ± 0.0
Ti	11.70 ± 0.6	26.1 ± 1.5	13.4 ± 2.8
W	0.54 ± 0.1	0.3 ± 0.1	0.7 ± 0.2
N	1.76 ± 0.2	2.0 ± 0.2	2.9 ± 0.1

Table 4.9 Average composition for the three large precipitates visible in the atom maps shown in Figure 4.14. The composition produced by the maximum separation method is compared to the compositions taken from those regions identified in Figure 4.14 using 5% titanium and 5% manganese isoconcentration surfaces.

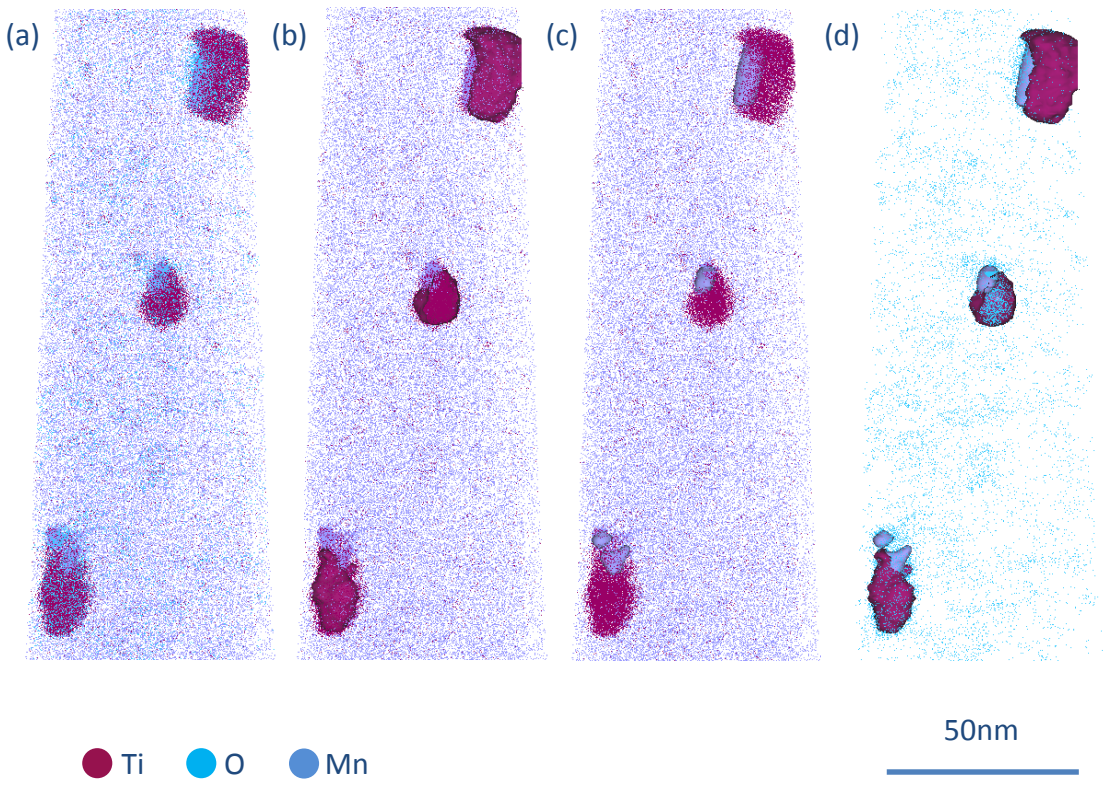


Figure 4.14 (a) Atom maps of oxygen manganese and titanium ions in an 1150°C consolidation showing three large oxygen rich precipitates with distinct titanium and manganese rich regions isolated using isoconcentration surfaces (b) 5% titanium (c) 5% manganese (d) composite with oxygen map

The absence of a chromium-depleted region corresponding to the enrichment around the precipitate like that shown in Figure 1.19 suggests the operation of an alternative formation mechanism to the low temperature chromium diffusion process proposed by Klimenkov in [78]. Two possibilities include either formation by chromium rejection to the shell during precipitation or segregation during consolidation at sufficiently high temperatures such that chromium can diffuse from the matrix to compensate for any local depletion caused by the formation of the precipitate shell.

The precipitates show no association with the wider cluster distribution and unlike the large oxides identified by Williams, show no association with grain boundaries either, though it is conceivable that these precipitates formed at grain boundaries which subsequently moved. Similar manganese chromium oxide precipitates were identified by Klimenkov in a batch of ODS Eurofer subjected to extensive thermo-mechanical treatment following consolidation [159]. These were characterised using analytical TEM and two phases were identified using a combination of EELS and EDX. These were a manganese-chromium-vanadium oxide precipitate and an yttrium oxide inclusion in a vanadium shell at the precipitate boundary.

Klimenkov finds lines of these precipitates up to 10µm long in the Eurofer and attributes the poor impact performance in the alloy to the formation of these features. The configuration of the three precipitates in Figure 4.14 would suggest the possibility of similar formations existing here and although the analysed volume is too small to say for sure these precipitates are clearly forming independently of the subsequent thermo-mechanical treatment.

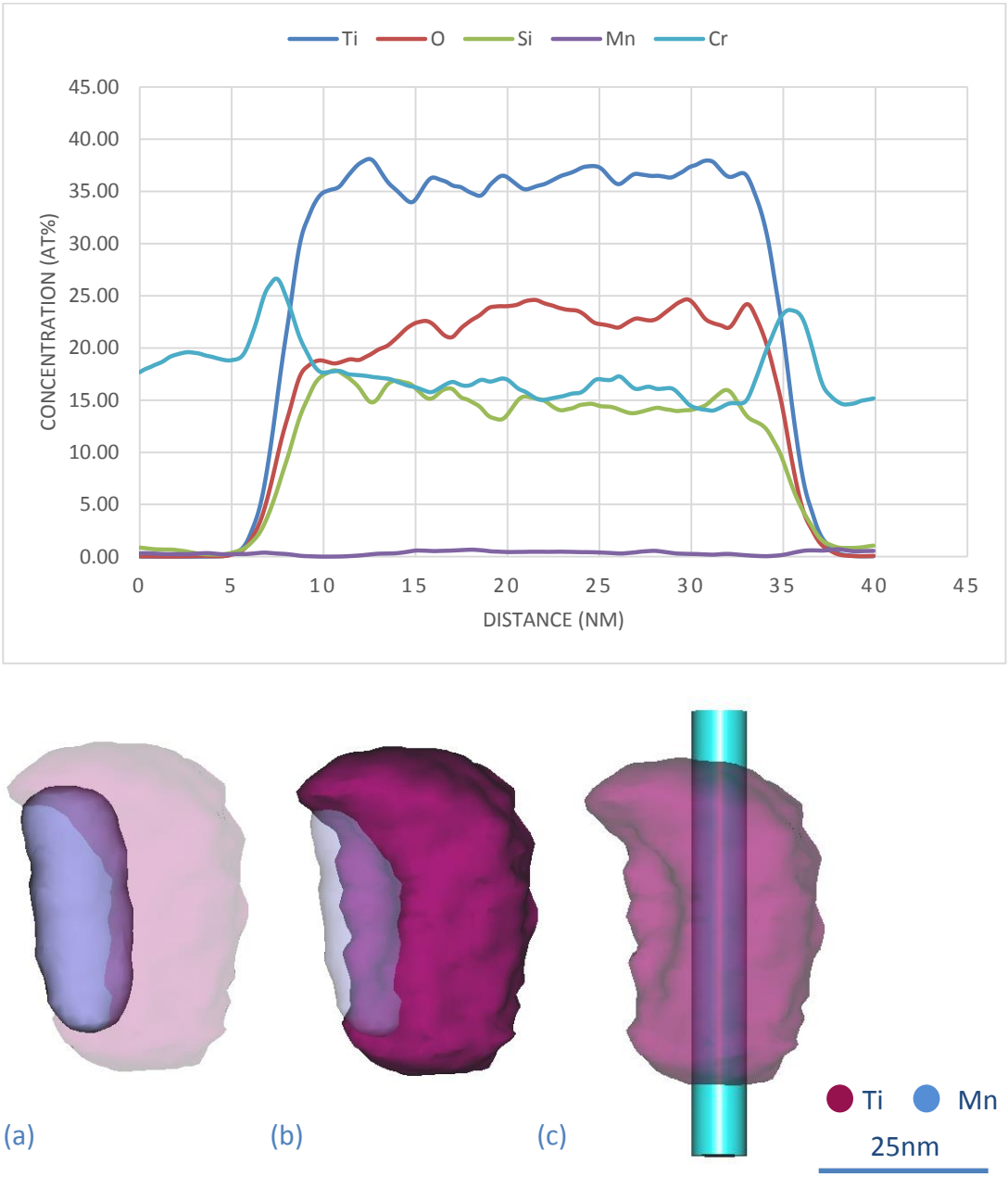


Figure 4.15 Isoconcentration surfaces showing (a) the manganese phase and (b) the titanium phase accompanied by a 1D concentration profile taken through the titanium phase in the direction of evaporation using the cylindrical sample volume shown in (c). By sampling every 1.0nm the profile successfully resolves a chromium shell above and below the precipitate.

4.4.9 Grain Boundary Analysis

A grain boundary was successfully identified in an atom probe reconstruction for each consolidation condition, using the visible segregation of various solute elements. The boundaries shown in Figure 4.16 are easily visible in the tungsten and tungsten nitride atom maps. These are presented alongside the titanium oxide and yttrium maps showing the local cluster formation in the vicinity of these boundaries.

Local magnification effects and associated density fluctuations may give a misleading impression of solute segregation in an atom map, but as discussed in Section 3.3.4 the Gibbsian interfacial excess provides a reliable method for assessing the levels of enrichment or depletion in concentration profile taken through the boundary. Average Gibbsian excesses are shown for the main segregating elements in Table 4.10. Chromium, silicon and tungsten contribute comparable excesses to the boundaries in the 950^{o}C and 1150^{o}C consolidations.

The boundary in the 1050^{o}C conditions shows a more modest enrichment in chromium, silicon and tungsten but here the boundary partitions the dataset as shown in Figure 4.14, separating a particle dispersion at 4.5x10^{23}m^{-3} from an apparently particle free grain. The chemistry of this region reflects the average matrix chemistry of the 1050^{o}C consolidation, with the associated absence of yttrium and titanium ions. This is the only region of particle free material located using the atom probe and indicates the continued presence of local deficiencies in the distribution of the particle forming elements even in material fabricated using pre-alloyed powder.

The grain boundary particles in the 950^{o}C consolidation show no differences in size or chemistry from the wider particle population, but in the 1050^{o}C and 1150^{o}C consolidations the boundary particles are significantly larger compared to those in the grain interior. The disparity is visible in the titanium oxide and yttrium ion maps shown in Figure 4.16 and assuming that the titanium oxide ion content of a cluster scales with volume, a grain boundary particle in the 1050^{o}C and 1150^{o}C consolidations is on

average approximately three times the size of a particle in the wider dataset, in contrast to those in the 950°C consolidation.

None of the datasets show any evidence of other large (>15nm) grain boundary oxides like those identified by Williams [61]. Given the evident capacity of the boundaries to accommodate solute atoms (as demonstrated by the excesses shown in Table 4.10) and the size of the grain boundary particles at higher consolidation temperatures, it seems likely that thermally driven grain boundary diffusion of particle forming solute occurs in these systems.

	Γ (atoms/nm^2)		
	1150°C HIP	**1050°C HIP**	**950°C HIP**
Cr	23.6 ± 1.6	15.7 ± 2.1	22.8 ± 1.0
Si	2.2 ± 0.4	1.2 ± 0.5	2.5 ± 0.2
Mn	0.5 ± 0.2	0.6 ± 0.2	0.6 ± 0.1
C	0.3 ± 0.0	0.1 ± 0.1	0.1 ± 0.0
W	9.2 ± 0.7	4.3 ± 0.7	6.5 ± 0.3

Table 4.10 Average Gibbsian interfacial excess (Γ) of Cr Mn Si C and W at randomly oriented grain boundaries in the Fe-14Cr-0.2Ti-3.0W-0.25Y_2O_3 system at each consolidation temperature.

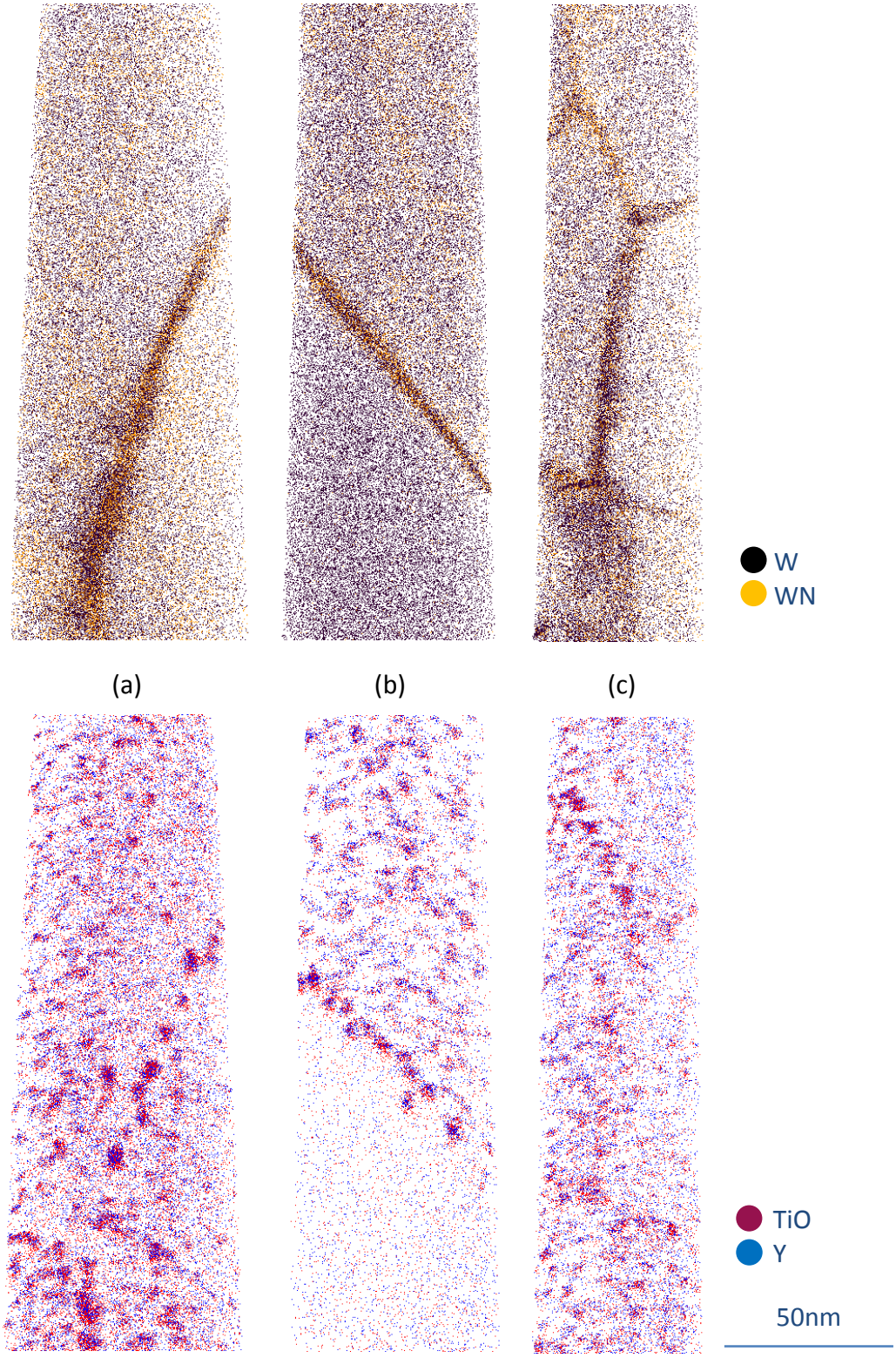


Figure 4.16 Grain boundaries visible in tungsten and tungsten nitride atom maps in (a) 1150°C (b) 1050°C (c) 950°C consolidations and corresponding atom maps showing the local titanium oxide and yttrium clustering.

4.4.10 Thermal Stability

Alinger found MA957 alloys showed minimal coarsening behaviour in the particle population and in the microstructure when aged at 1150^{o}C, suggesting that the processing temperature must be exceeded if significant changes are to be observed [58]. To validate these findings for lower consolidation temperatures, the 950^{o}C consolidation was subject to short term thermal aging at 1150^{o}C. This provided an additional benefit in allowing material consolidated at 1150^{o}C to be compared to material aged at 1150^{o}C following low temperature consolidation.

Atom probe match-stick samples of the 950^{o}C material were annealed in high vacuum (< 10^{-6} Torr) at 1150^{o}C in alumina crucibles prior to electropolishing. Samples were aged for a four hour period, corresponding to the dwell time used in the 1150^{o}C HIP consolidation. Extended aging periods of ten and one hundred hours were completed but the one hundred hour samples responded poorly to electropolishing and no viable atom probe tips were produced from these samples. The crucibles were also found to have turned a pale green, indicating significant chromium evaporation occurred in the course of the experiment. Despite these difficulties, at least two datasets greater than 30 million ions were recorded from each of the shorter, four and ten hour, annealing periods.

The effect of the aging process is immediately apparent in the atom maps presented in Figure 4.17, which show a noticeable reduction in cluster density and a corresponding increase in cluster size. The absence of any TEM data for the annealed samples necessitates a reliance upon the atom probe data for size information. A variety of sizing methods can be used including total ion count and spatial extent but the radius of gyration is used here. When computed using all the solute atoms prior to matrix correction it is in good agreement with the TEM data available for the 950^{o}C consolidation and can be readily calculated for each cluster.

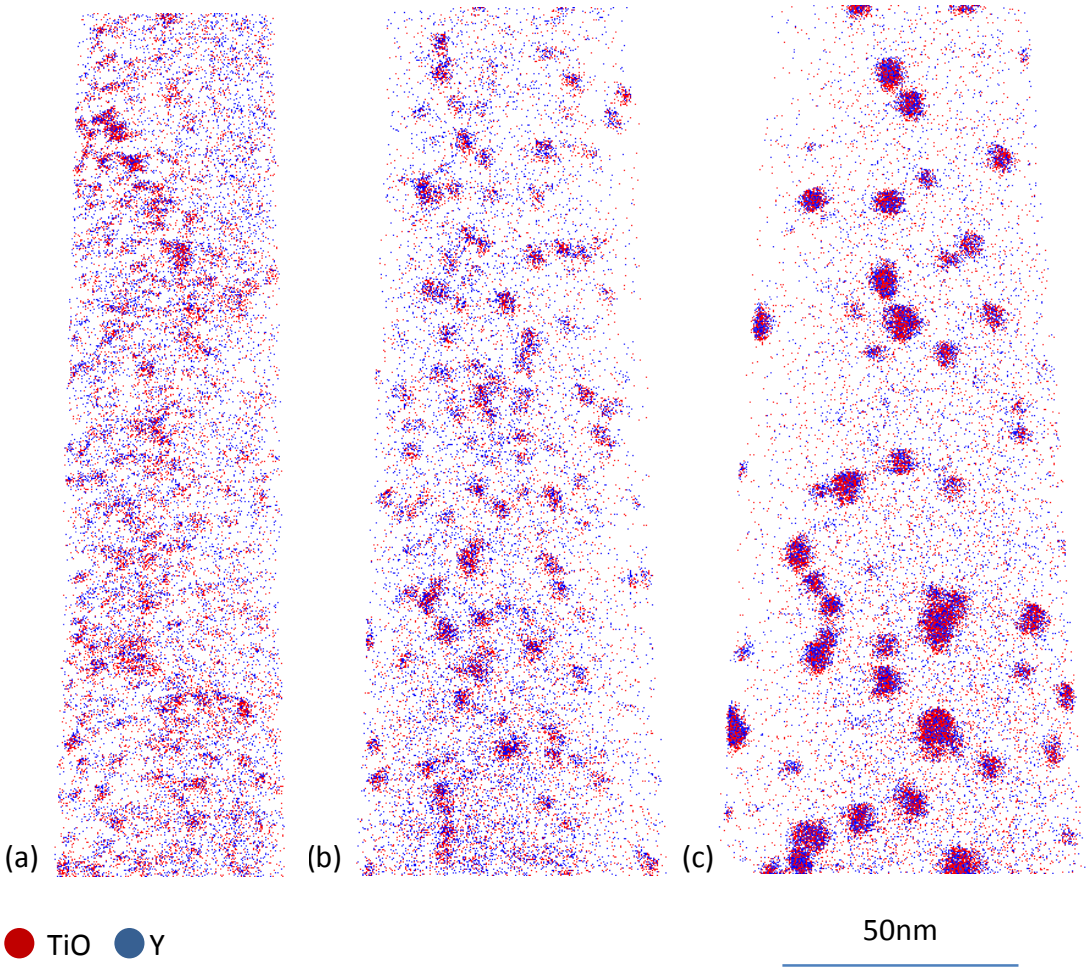


Figure 4.17 Particle density variation shown using atom maps of the major titanium oxide and yttrium particle forming ions in samples consolidated at 950 °C and subject to (a) 0 hours (b) 4 hours and (c) 10 hours of vacuum annealing at 1150°C

Cluster size and number density variation with annealing time are shown in Figure 4.18, while the corresponding size distributions for each aging period are shown Figure 4.19. The number density falls from 7×10^{23} m^{-3} as recorded from the 950°C consolidation to 2×10^{23} m^{-3} following a 4 hour anneal and the average radius of gyration increases from 1.2nm to 1.6nm. These values exactly match those recorded for the 1150°C consolidation, providing evidence that cluster development occurs by a classical thermally driven coarsening mechanism.

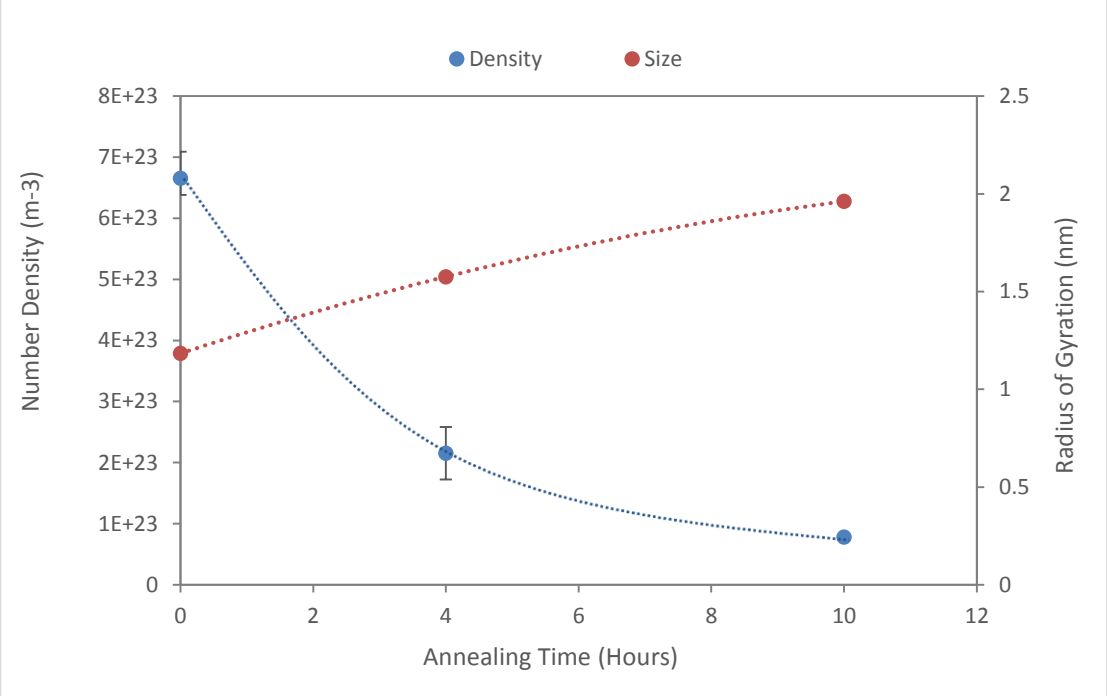


Figure 4.18 Variation in cluster number density and size in the Fe-14Cr-3W-0.2Ti-0.25Y_2O_3 system consolidated at 950°C and annealed at 1150°C for up to ten hours

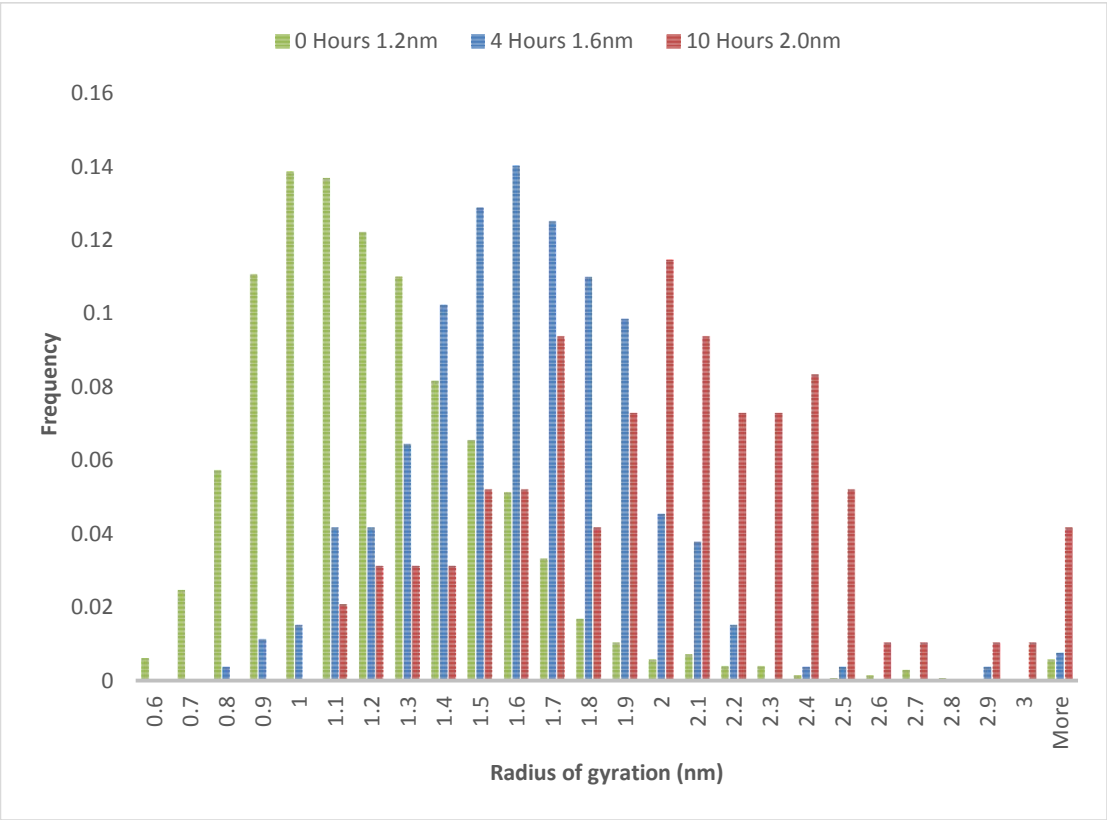


Figure 4.19 Cluster size distributions and average cluster sizes calculated using atom probe dataset from the Fe-14Cr-3W-0.2Ti-0.25Y_2O_3 system consolidated at 950°C and annealed at 1150°C for up to ten hours

Annealing for ten hours causes a further reduction in cluster density from 2×10^{23} m^{-3} to 8×10^{22} m^{-3} and an increase in average cluster size from 1.6 to 2.0 nm, suggesting significant changes can occur in the particle population when aging at the consolidation temperature, even for short periods of time. The changes in size and density shown in Figure 4.18 are however inconsistent with an overall conservation of particle forming material. The particle volume fraction decreases from 0.45% to 0.35% at 4 hours and to 0.25% at 10 hours, possibly indicating a loss of cluster forming species to large oxides like those shown in Figure 4.13, although a change in cluster composition could also be responsible.

Average bulk and matrix compositions are shown in Table 4.11 for the 950°C consolidation in the as-HIPed condition and following four and ten hour annealing periods at 1150°C. These compositions and the associated errors were calculated in the same way as those presented in Table 4.6 for the different consolidation conditions and like the compositions shown in Table 4.11 are broadly consistent showing only moderate variation with annealing time.

The matrix chromium content following the four hour anneal shows a modest increase potentially correlated with a corresponding reduction in the particle chromium content as discussed in more detail in Section 4.5 below. More generally a reduction in the matrix yttrium, titanium and oxygen content is indicative of particle growth via partitioning of solute to the clusters from the matrix.

	APT Bulk Composition (at%)			APT Matrix Composition (at%)		
	0 Hours	**4 Hours**	**10 Hours**	**0 Hours**	**4 Hours**	**10 Hours**
Cr	13.2 ± 0.2	14.6 ± 0.2	12.9 ± 0.0	13.0 ± 0.2	14.5 ± 0.2	12.9 ± 0.0
Fe	84.9 ± 0.2	83.5 ± 0.2	85.3 ± 0.0	85.2 ± 0.2	83.8 ± 0.1	85.6 ± 0.0
Y	0.1 ± 0.0	0.1 ± 0.0	0.1 ± 0.0	0.1 ± 0.0	0.0 ± 0.0	0.0 ± 0.0
O	0.2 ± 0.0	0.2 ± 0.0	0.2 ± 0.0	0.2 ± 0.0	0.1 ± 0.0	0.1 ± 0.0
Si	0.4 ± 0.0	0.4 ± 0.0	0.5 ± 0.0	0.4 ± 0.0	0.4 ± 0.0	0.5 ± 0.0
Mn	0.3 ± 0.0	0.3 ± 0.0	0.1 ± 0.0	0.3 ± 0.0	0.3 ± 0.0	0.1 ± 0.0
C	0.0 ± 0.0	0.0 ± 0.0	0.0 ± 0.0	0.0 ± 0.0	0.0 ± 0.0	0.0 ± 0.0
Ti	0.1 ± 0.0	0.1 ± 0.0	0.0 ± 0.0	0.1 ± 0.0	0.0 ± 0.0	0.0 ± 0.0
W	0.6 ± 0.0	0.7 ± 0.0	0.7 ± 0.0	0.6 ± 0.0	0.7 ± 0.0	0.7 ± 0.0
N	0.1 ± 0.0	0.0 ± 0.0	0.1 ± 0.0	0.1 ± 0.0	0.0 ± 0.0	0.0 ± 0.0

Table 4.11 Average bulk and matrix compositions in the 950°C consolidation following aging at 1150°C in vacuum.

Average cluster compositions for each annealing period are shown in Table 4.12, in both the uncorrected and matrix-corrected conditions. The compositions presented in Table 4.12, like those presented for the different consolidation temperatures in Table 4.7, show a significant chromium content even when matrix-corrected. However, the modest reduction in the proportion of chromium seen with increasing consolidation temperature is here more significant with annealing time.

The corrected chromium content falls by 20 (at%) following the four hour anneal and by another 10 (at%) following the ten hour anneal. By comparison the difference in chromium content between the 950^{o}C and 1150^{o}C consolidations shown in Table 4.7 is just 8 (at%). Such a significant chromium loss from the clusters particularly in the chromium-rich matrix of the four hour samples and the associated green colouration of the crucibles suggests chromium mobilised at 1150^{o}C is potentially moving out of the clusters and into the matrix to replenish chromium lost to evaporation.

Chromium evaporation was shown to occur in vacuum annealing experiments at 1000^{o}C in Fe-16Cr-12Ni-2.5Mo stainless steels by Smith and Hales [99]. EDX depletion profiles consistent with simple diffusion and surface transfer mediated losses extended up to 50µm from sample surfaces. In a HIP consolidation high pressures would supress evaporation and the steel can would maintain chromium partial pressures at the sample boundary. By contrast the large surface area to volume ratio of the atom probe match sticks are likely to contribute to significant bulk chromium loss during the vacuum annealing process.

Further compositional changes are evident in the yttrium, titanium and oxygen content of the clusters. Following annealing the Y:Ti:O ratio shifts noticeably from the 2:3:5 stoichiometry seen in the as consolidated alloy, to a 1:1:2 ratio as shown in Table 4.13. Williams found no changes occurred in a comparable YWT system annealed at 1200^{o}C for up to one hundred hours and although the shift in stoichiometry seen here preserves the ubiquitous 1:1 metal to oxygen ratio these findings differ significantly from those presented by Williams [61].

	APT Cluster Composition (at %)			APT Matrix Corrected Cluster Composition (at%)		
	0 Hours	4 Hours	10 Hours	0 Hours	4 Hours	10 Hours
Cr	17.4 ± 0.1	16.2 ± 0.0	14.7 ± 0.0	58.7 ± 1.2	38.5 ± 1.1	28.5 ± 0.5
Fe	77.3 ± 0.1	78.3 ± 0.0	75.2 ± 0.0	0.0 ± 0.0	0.0 ± 0.0	0.0 ± 0.0
Y	0.6 ± 0.1	0.9 ± 0.0	2.1 ± 0.0	6.1 ± 1.3	13.8 ± 0.5	16.9 ± 0.2
O	1.4 ± 0.1	1.8 ± 0.1	4.2 ± 0.1	15.2 ± 1.3	27.0 ± 0.6	33.6 ± 0.3
Si	0.7 ± 0.1	0.6 ± 0.0	0.6 ± 0.0	3.7 ± 1.5	2.5 ± 1.1	1.3 ± 0.5
Mn	0.4 ± 0.1	0.4 ± 0.0	0.2 ± 0.0	1.0 ± 1.5	1.9 ± 0.7	0.7 ± 0.3
C	0.2 ± 0.1	0.1 ± 0.0	0.2 ± 0.0	1.6 ± 1.4	1.6 ± 0.5	2.0 ± 0.2
Ti	0.9 ± 0.1	0.9 ± 0.0	2.1 ± 0.1	10.6 ± 1.2	13.4 ± 0.5	16.2 ± 0.2
W	0.7 ± 0.2	0.7 ± 0.0	0.6 ± 0.0	0.2 ± 3.2	-0.7 ± 2.7	-0.8 ± 0.0
N	0.4 ± 0.1	0.1 ± 0.0	0.2 ± 0.0	2.9 ± 1.0	2.1 ± 0.4	1.7 ± 0.1

Table 4.12 Average cluster compositions in the 950°C consolidation following aging at 1150°C in vacuum

	APT Matrix Corrected Y:Ti:O Ratio (at%)				
	1150°C	1050°C	950°C	950°C 4 Hours at 1150°C	950°C 10 Hours at 1150°C
Y	19.5 ± 1.8	21.6 ± 2.3	19.1 ± 3.9	25.4 ± 1.0	25.3 ± 0.3
Ti	31.3 ± 1.8	29.5 ± 2.3	33.2 ± 3.7	24.7 ± 0.9	24.3 ± 0.3
O	49.2 ± 1.7	48.9 ± 2.5	47.7 ± 3.9	49.9 ± 1.1	50.3 ± 0.4
Y:Ti:O	2:3:5			1:1:2	

Table 4.13 Average Y:Ti:O ratios in the matrix corrected cluster composition for each consolidation condition and in samples from the 950°C consolidation subject to 4 hour and 10 hour vacuum annealing at 1150°C showing a shift in stoichiometry between the consolidated and anneal material.

4.5 Discussion

The Fe-14Cr-0.2Ti-3W-0.25Y_2O_3 system was successfully consolidated at 1150°C, 1050°C and 950°C, producing fully dense alloys, free from nickel contamination. The microstructures show a bimodal grain size distribution at all consolidation temperatures and an apparently uniform distribution of 1.0 to 3.0nm oxide particles. The uniformity of the particle distribution is supported by EPMA data taken by Gorley, showing constant yttrium and titanium concentration profiles in material consolidated at 1150°C [148].

These findings demonstrate the efficacy of the mechanical alloying process in producing a uniform dispersion of particle-forming solute, ruling out local particle deficiencies as a potential cause for the bimodal grain size distribution. Evidently there are some particle free regions, possibly even entire particle free grains, as shown by the atom map in Figure 4.16(b). However, transmission electron micrographs of the wider microstructure strongly indicate that no relationship exists between particle concentration and grain size.

The trend in particle density with consolidation temperature initially demonstrated by Alinger [58] was successfully reproduced here in a Fe-14Cr-0.2Ti-3W-0.25Y_2O_3 system, as shown in Figure 4.11. The reduction in cluster density with increasing consolidation temperature, as measured by APT, is substantially less pronounced compared to that observed by Alinger using SANS. Given that titanium concentration constitutes the only significant difference between these two alloys this suggests a possible role for titanium in influencing coarsening behaviour.

However, these indications run contrary to the outcome of a comparison between titanium-free and titanium-containing alloys made by Williams in [160] which found no evidence that titanium plays any role in particle coarsening. As noted in Section 4.4.5, any firmer conclusions regarding the role of titanium would require further details of the Santa Barbara alloys and their reproduction at Oxford before a direct comparison could be made.

The use of APT rather than SANS in producing these data provides useful chemical information, establishing a consistent chromium content and a $Y_2Ti_3O_5$ cluster stoichiometry at all consolidation temperatures, as demonstrated in the radar plots of Figure 4.20. Combined with an apparently invariant matrix composition, this strongly indicates a classical coarsening process with particle nucleation completed, even at low consolidation temperatures.

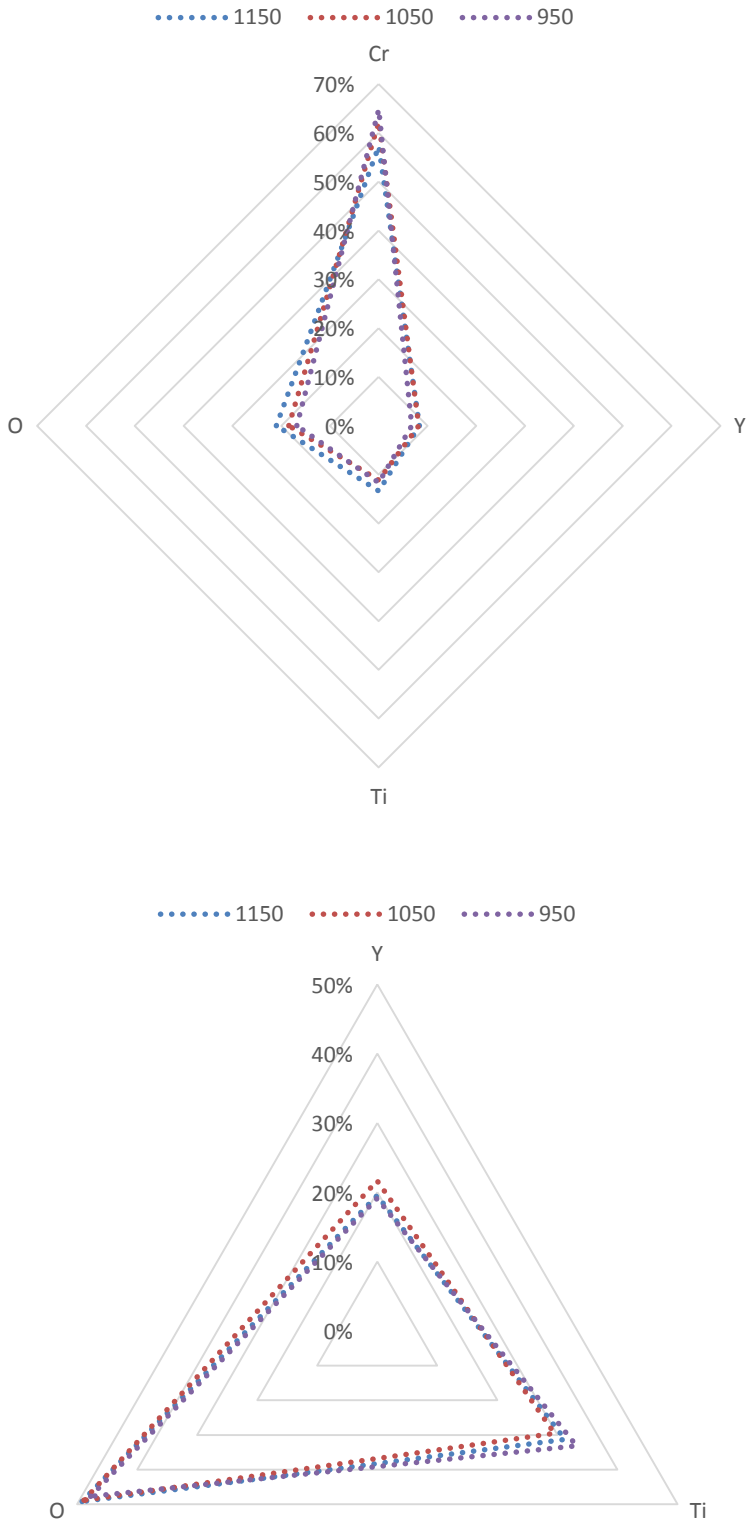


Figure 4.20 Radar plots showing chromium, yttrium, titanium and oxygen ratios following consolidation at 950°C, 1050°C and 1150°C.

The metal to oxygen ratio and substoichiometric oxide composition shown in Table 4.8 are common in APT analyses of YWT alloy systems, including those analysed by Alinger [14] and by Williams [61]. However, the $Y_2Ti_3O_5$ stoichiometry corresponds to none of the stable yttrium and titanium oxides shown in Table 4.14, although even the phases listed here are subject to some uncertainty regarding their stability over the range of processing temperatures used in these experiments.

Oxide	Metal Oxygen Ratio	Formation Enthalpy (kJ/mol)	Structure
TiO_2	1:2	944	Tetragonal
Ti_3O_5	3:5	2457	Monoclinic
Ti_2O_3	2:3	1522	Corundum
TiO	1:1	543	Rock Salt
Y_2O_3	2:3	1907	Cubic
Y_2TiO_5	3:5	372 [161]	Orthorhombic
$YTiO_3$	2:3	346 [159]	Perovskite
$Y_2Ti_2O_5$	4:5		Pyrochlore
$Y_2Ti_2O_7$	4:7	3874 [162]	Pyrochlore

Table 4.14 M:O ratios, formation enthalpies and structures for stable yttrium and titanium oxides (taken from [163] unless stated to the contrary.)

The absence of a thermodynamically stable oxide stoichiometry corresponding to the observed cluster chemistry, supports the arguments made by Ribis and DeCarlan, that the clusters occupy a metastable phase in a coherent orientation relationship with the matrix following consolidation and prior to coarsening during any subsequent thermal treatment [76]. The defective rock salt structure identified by Hirata [77] for particles of comparable size, provides a possible identity for a coherent phase, with a low interface energy, substoichiometric oxide composition and 1:1 metal to oxygen ratio.

On annealing at 1150^{o}C the cluster chemistry undergoes a shift, as clearly demonstrated in Figure 4.21. The metal oxygen ratio is maintained but the clusters adopt a new $YTiO_2$ stoichiometry. A minimum 1:1 Y:Ti ratio is evident in the stable oxide phases shown in Table 4.14 and in the Y_2O_3/TiO_2 phase diagram presented by Gong in [164], potentially indicating a thermodynamically motivated shift from a metastable phase to a stable oxide has occurred during the annealing process.

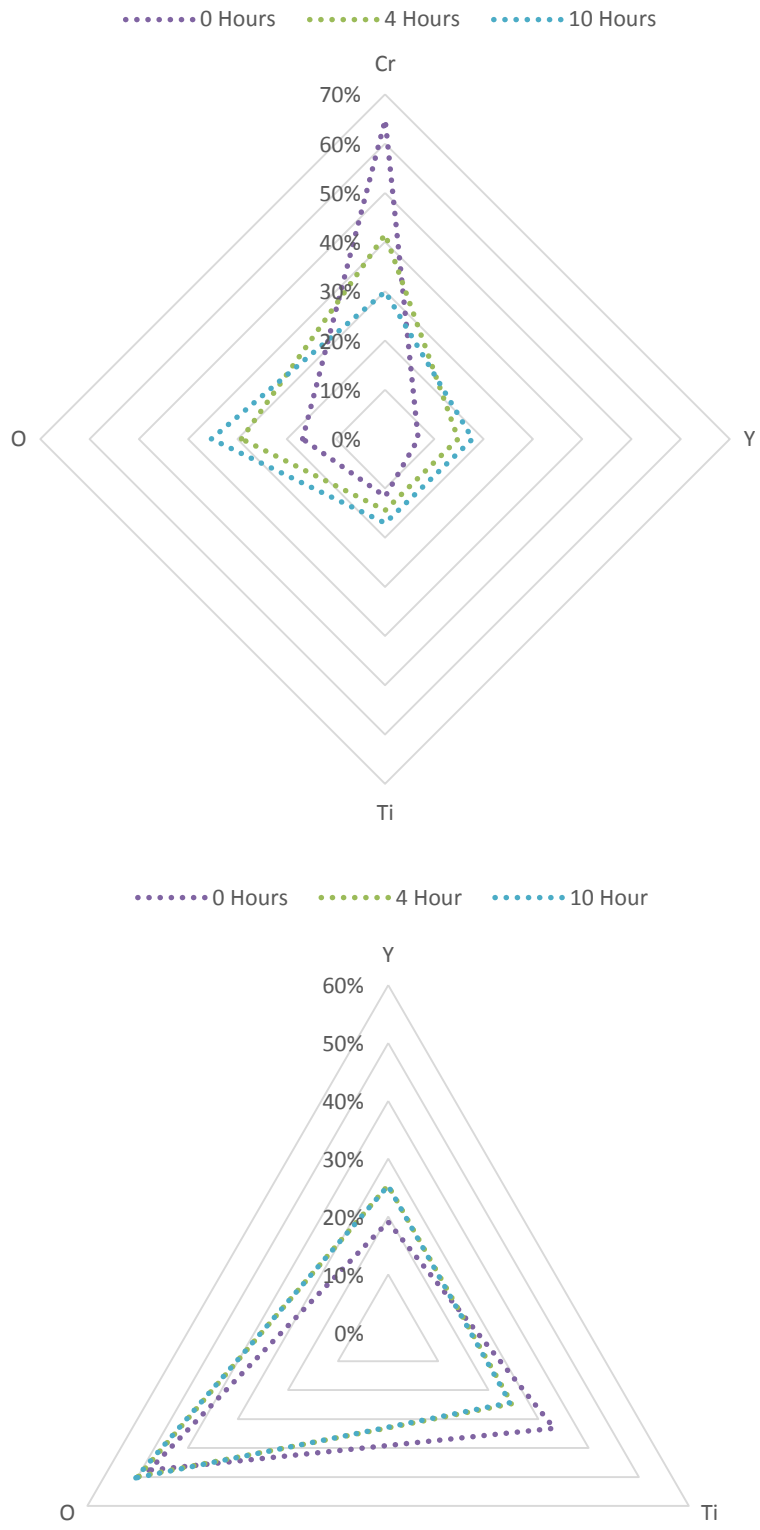


Figure 4.21 Radar plot showing chromium, yttrium, titanium and oxygen ratios following thermal ageing of the 950°C consolidation at 1150°C for 0 hours, 4 hours and 10 hours.

Given the exceptionally low diffusion coefficients for yttrium in α iron at typical consolidation temperatures quoted by Ribis [76] and the reduction in the matrix yttrium content seen in Table 4.11 indicating cluster growth, it seems likely that yttrium diffusivity constitutes the rate controlling factor in this process. If the factors suppressing oxygen detection discussed in Section 4.4.8 are responsible for a comparable loss of oxygen in the particle data, the shift in stoichiometry shown in Figure 4.21 may indicate the change from a metastable phase (potentially with the defective rock salt structure proposed by Hirata [77]) to the stable pyrochlore oxide recorded by Ribis and DeCarlan [76].

Ribis and DeCarlan [76] annealed material initially consolidated at 1150^{o}C at 1300^{o}C for one hour. If the change from metastable aggregates to stable oxide they observed in the TEM corresponds to the change in particle chemistry shown in Figure 4.21 it would demonstrate that a conversion from the metastable phase to a stable oxide took place at 1150^{o}C. In this case the persistence of the presumed metastable $Y_2Ti_3O_5$ stoichiometry in the 1150^{o}C consolidation used by Ribis and DeCarlan becomes an outstanding question, along with the possible significance of the reduction in cluster chromium content.

The chromium loss is most noticeable following the four hour aging period, which produces clusters of approximately the same size as those identified in the 1150^{o}C consolidation. The difference in chromium content in clusters of comparable size thus removes any possibility of the loss arising as an aberration artefact. The colouration of the crucibles following the anneal and the observations reported by Smith and Hales in [99] certainly indicate significant chromium evaporation occurs and produces a depletion profile comparable to the scale of an atom probe match stick.

The evidence for the existence of a chromium shell around the particles beyond the large chromium content identified by the atom probe is circumstantial but compelling. The shell can be directly observed around the large titanium oxide precipitates in Figure 4.15 and appears around large yttrium oxide particles identified by Williams [61], Hatzoglou [68] and Klimenkov [78].

If exposure to vacuum at high temperature during the annealing process causes chromium to diffuse away from the particle boundaries to replenish a depleted matrix, the change in the local chemistry may contribute to the change in particle stoichiometry. This would explain why in the consolidation process where chromium partial pressures are maintained the change shown in Figure 4.21 is absent. However, further work would be required to examine this hypothesis.

5 Helium Implantation of a YWT ODS System with Varying Oxide Particle Number Densities

5.1 Summary

Helium implantation conditions were selected to produce gas concentrations in the alloys commensurate with those anticipated for first wall and blanket components in a fusion reactor at the end of their operational life [14]. The 300°C implantation temperature was initially chosen to compliment a dual (helium/self-ion) irradiation campaign at the JANNUS facility that would have correlated the helium injection with high levels of displacement damage. Unfortunately these experiments were postponed indefinitely and therefore no dual implantation data are available for comparison and the displacement damage accompanying the delivery of the helium for this study is much lower than would be expected in a first wall component.

Temperatures of 300°C are certainly more common in irradiation campaigns aiming to approximate fission plant operation and although most regimes for a fusion breeding blanket system exceed 300°C, the wide applications of ODS alloys as structural materials in fusion reactors ensure that low operational temperatures remain relevant for their development. Temperatures below 500°C also simplify experimental arrangements increasing the likelihood of successfully completing implants at multiple ion energies, using different systems, as was necessary here.

Multiple energies were used for the ion implant, to provide an even helium concentration profile over the topmost 3.0μm of each sample, enabling subsequent mechanical assessments to be conducted by nanoindentation. The total quantity of helium implanted was thus comparatively large and required delivery at high dose rates in order to complete the implant in the time available. Dose rate effects have been shown to have a significant effect on the irradiation response of iron alloys [145] and though treated as a fixed variable in the following study the potential influence of dose rate should always be considered in subsequent work.

Following implantation, a number of control studies designed to substantiate the use of Fresnel contrast methods in bubble imaging were conducted and are presented here in Section 5.4.1. Helium bubble densities were then computed for the oxide

dispersion strengthened and reference alloys, using image processing techniques and energy filtering methods outlined in Sections 5.3 and 5.4. When compared to the particle densities established by APT in Section 4.4.4 above, a strong correlation between particle and bubble densities becomes apparent.

Use of the JEOL 2200 and the omega filter were supported by Dr Judy Kim and the aberration corrected microscopy group at Oxford.

5.2 Helium Implantation

Samples of the Fe-14Cr-3W-0.2Ti-0.25Y_2O_3 ODS and Fe-14Cr-3W-0.2Ti (wt%) control alloy in each consolidation condition were prepared for implantation following the methods outlined in Section 2.1.1. The implantation energies and doses required to produce an average 2000 appm helium concentration in a 3.0µm layer were computed using the SRIM software as discussed in Section 2.1.2. These are shown in Table 5.1 and the corresponding helium concentration and damage profiles calculated using Equation 2.1 are shown in Figures 5.1 and 5.2.

Two accelerators were used to conduct the implantation with the highest energy ions implanted first. A general purpose implanter covering 0.2-2MeV delivered the majority of the helium and a low energy beam line was used to implant 0.1 and 0.05 MeV helium into the immediate surface of the samples. Both beam lines were configured for a dose rate of 10^{12} ions cm^{-2} s^{-1} at 300°C as discussed in Section 2.1.1.

Table 5.1 Helium ion implantation energies chosen to produce a 2000 appm helium ion concentration in the top 3.0µm of the ODS samples

Energy MeV	Dose (ions/cm²)
0.05	3.60E+15
0.1	1.50E+15
0.2	5.00E+15
0.3	1.00E+15
0.4	5.00E+15
0.6	5.00E+15
0.8	5.00E+15
1.0	5.00E+15
1.2	5.00E+15
1.4	5.00E+15
1.6	5.50E+15
1.8	6.00E+15
Average He Content (appm)	**1975**
Average Damage (DPA)	**0.31**

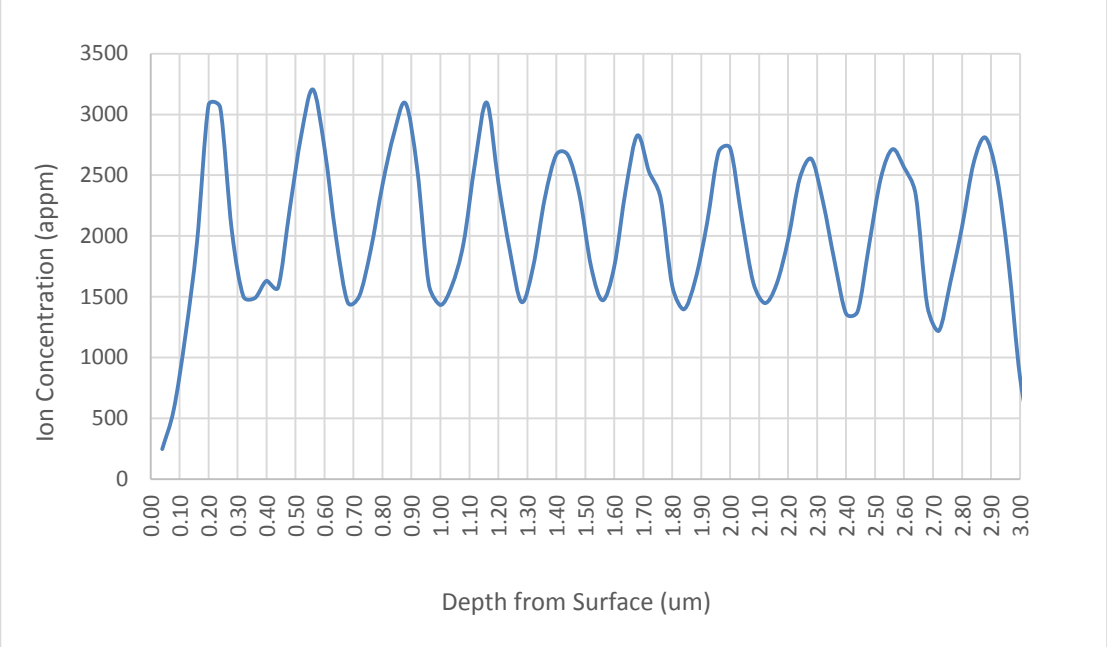


Figure 5.1 Helium ion concentration varying with depth in pure iron simulated using the SRIM software package for eleven different energies chosen to produce a 2000 appm helium ion concentration in the top 3µm of the ODS samples

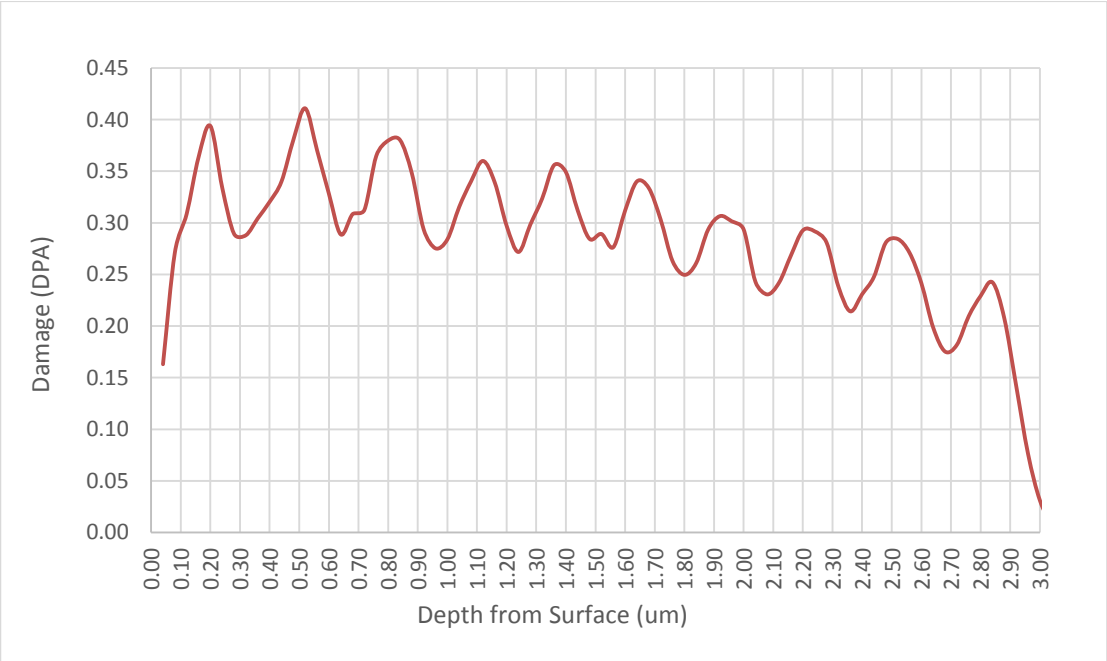


Figure 5.2 Damage varying with depth in pure iron simulated using the SRIM software package for eleven different energies chosen to produce a 2000 appm helium ion concentration in the top 3µm of the ODS samples

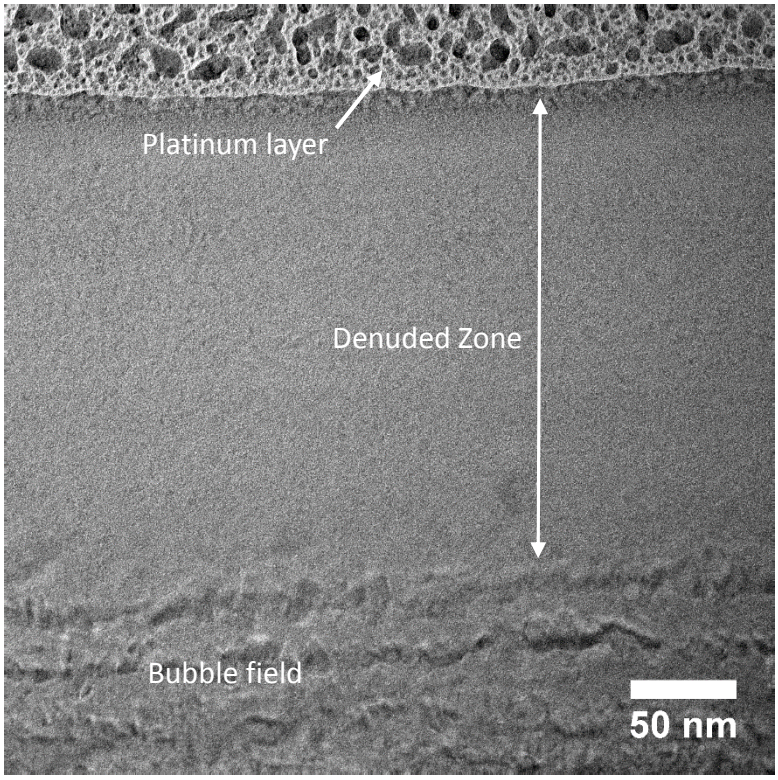
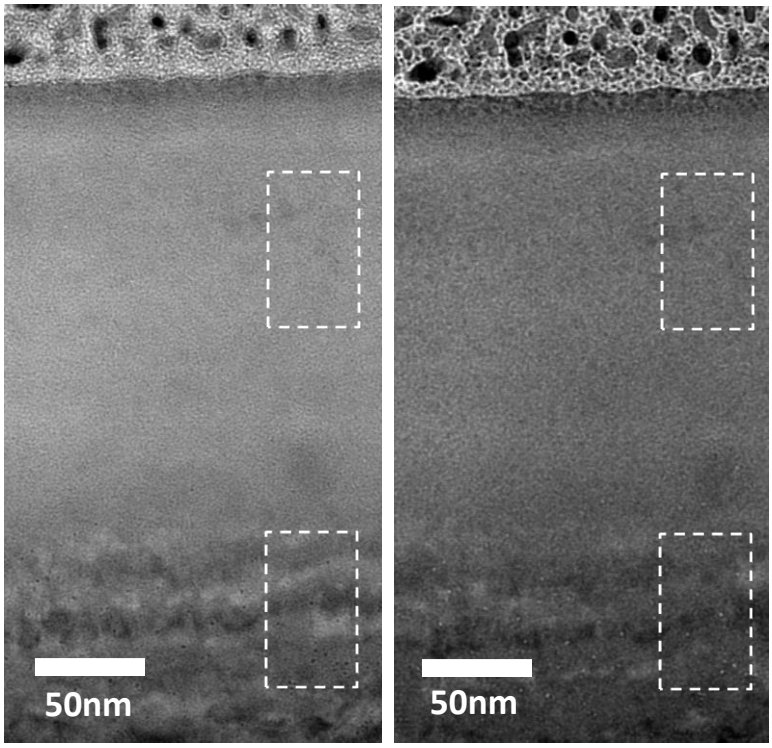


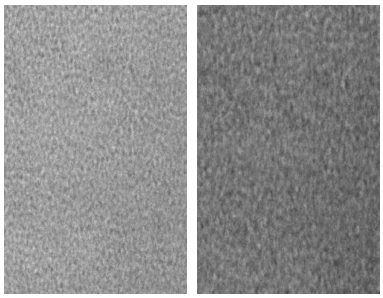
Figure 5.3 Micrographs of implanted Fe-14Cr-0.2Ti-3W showing the protective platinum layer applied in the FIB at the sample surface and the immediate subsurface region. At 1.0µm over and under focus a $3.6x10^{22}m^{-3}$ bubble field can be identified using white and black Fresnel fringes (arrows on insets). A 300nm wide denuded zone extends from the free surface.

1.0µm over focus

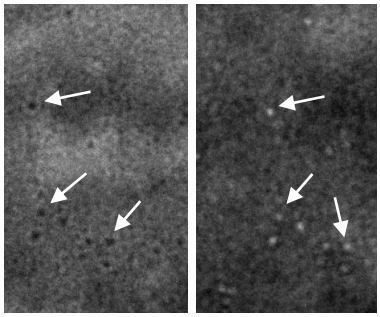
1.0µm under focus



Denuded zone



Bubble field at $3.6x10^{22}m^{-3}$



FIB lift-outs were used to access the implanted surfaces for characterisation with TEM. Samples were prepared following the methods outlined in Section 2.3.2. TEM micrographs showing the protective platinum layer deposited on the implanted surface of an Fe-14Cr-0.2Ti-3W sample consolidated at 1050^{o}C during the lift out procedure are presented in Figure 5.3. The bubble field becomes visible at an appropriate defocus as outlined in 2.3.3 and begins approximately 300nm below the sample surface.

A denuded zone, free from bubbles occupies the uppermost 300nm of the foil shown in Figure 5.3 and appears in all the implanted samples surveyed here. The presence of the denuded zone may result from the close proximity of a free surface during implantation but ion beam exposure during sample preparation may have exacerbated the problem, particularly in the reference alloys which lack the high sink densities associated with ODS materials.

5.3 Data Analysis and Image Processing

The micrographs recorded from the implanted samples were processed using the ImageJ software package. In Figure 5.4 micrographs taken from the implanted Fe-14Cr-0.2Ti-3W-0.25Y_2O_3 alloy consolidated at 950^{o}C are shown. At focus the local microstructure is apparent and at 1.0µm under and over focus the helium bubble population outlined by Fresnel fringes becomes visible. These micrographs were converted to 8 bit images for processing using a bandpass filter to isolate structures between 40 and 5 pixels in size. This effectively smooths the image and removes the local background for thresholding as shown in Figure 5.5.

Applying an edge finding analysis to the thresholded image allows the dark or bright spots corresponding to the helium bubbles to be identified, measured and counted. Residual diffraction contrast and amalgamated bubble features were identified based on their size and shape and removed from the collated data. A minimum feature size was set at 1.0nm, below which helium bubbles no longer produce reliable Fresnel contrast, according to the multislice simulations of inert gas bubbles conducted by Yao [165].

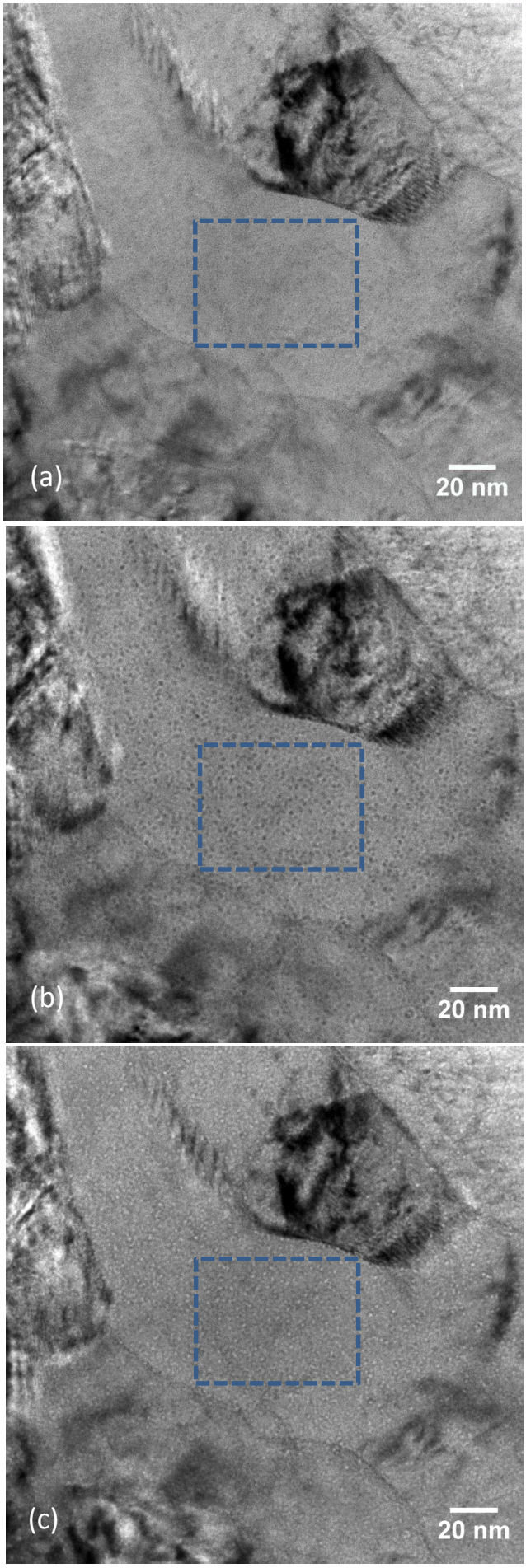


Figure 5.4 TEM micrographs 0.0µm and ±1.0µm defocus recorded from the same 180nm x 180nm area in a sample of the implanted Fe-14Cr-0.2Ti-3W-0.25Y_2O_3 consolidated at 950°C showing the bubble field outlined in Fresnel fringes and the local microstructure (a) 0.0µm (b) +1.0µm (c) -1.0µm

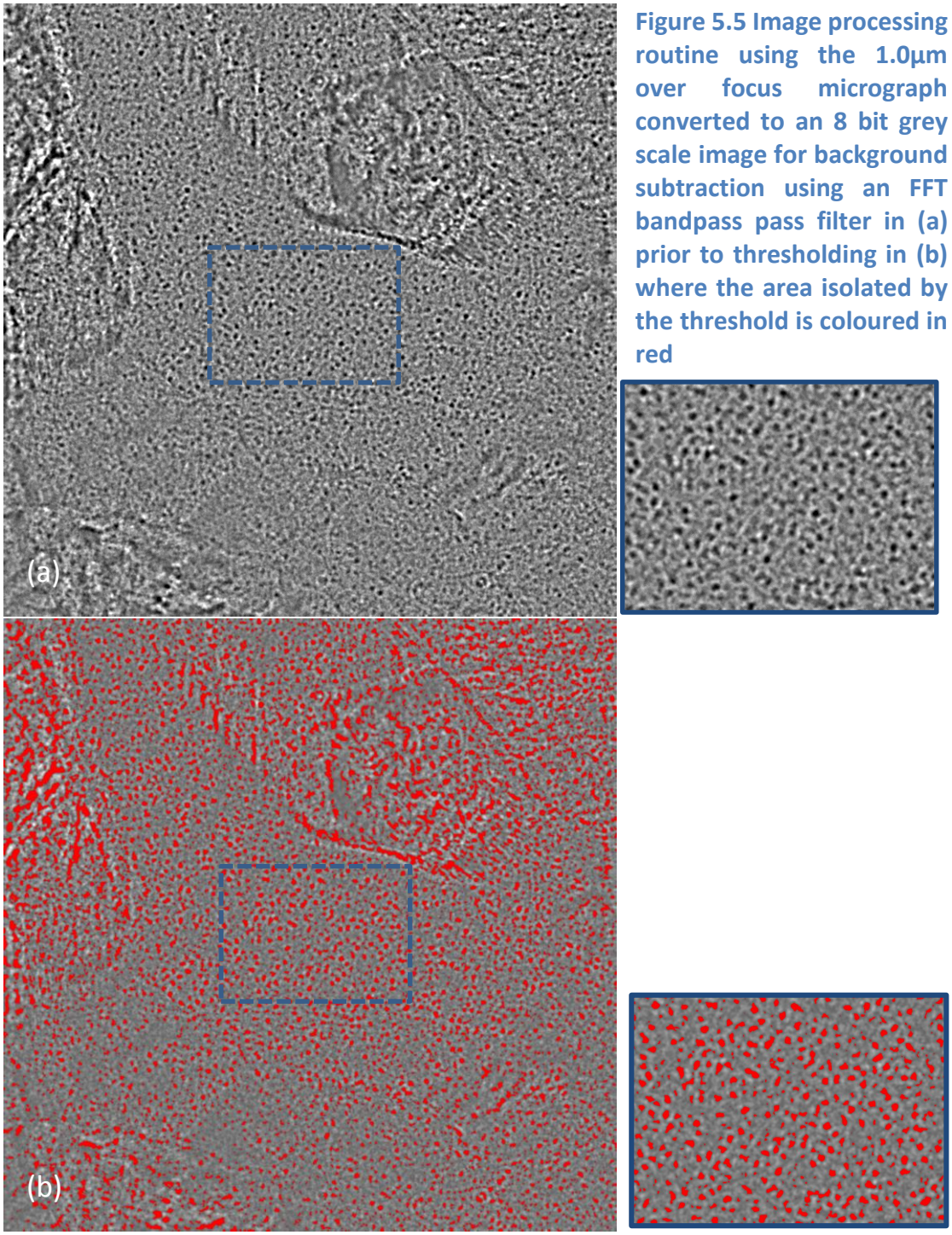


Figure 5.5 Image processing routine using the 1.0µm over focus micrograph converted to an 8 bit grey scale image for background subtraction using an FFT bandpass pass filter in (a) prior to thresholding in (b) where the area isolated by the threshold is coloured in red

The selection of a threshold from the 256 available grayscale values in an 8 bit image necessarily required some judgement, particularly in the 950^{o}C consolidations where very high bubble densities were found to be particularly prone to amalgamation. Using the over focused micrographs and threshold values of 100 ± 5, bubbles were successfully isolated with minimal amalgamation in all cases. This approach proved to be more reliable than manual counting methods and allowed an appropriate uncertainty to be systematically assigned to the average bubble density for each alloy.

When selecting a region of the implanted microstructure for mapping, a set of through focus micrographs were recorded under conventional bright field conditions. Grains well away from the Bragg condition were typically chosen to minimise diffraction contrast and provide a smooth background for subsequent processing. Once a satisfactory focal series had been recorded the region was thickness mapped following the procedure outlined in Figure 5.6.

On the JEOL 2200 200kV system used here, the Omega filter provides an in-column energy filtering capability that allows the primary imaging CCD to record the filtered micrographs, removing any need for realignment of the primary electron optics. Having recorded the total electron intensity when taking the conventional bright field images, the filter is activated and used to select the zero loss peak intensity. This produces an image of the implanted microstructure using only the elastically scattered electrons.

A thickness map is produced as a function of the mean free path λ by taking the ratio of these two images according to Equation 2.8. Removing objective apertures from the column and recording the entire signal allows the most accurate intensity ratio to be recorded, as discussed in Section 2.3.4. A reference value for λ was used to compute the average sample thickness and therefore the volume and bubble density from the average intensity in the thickness map.

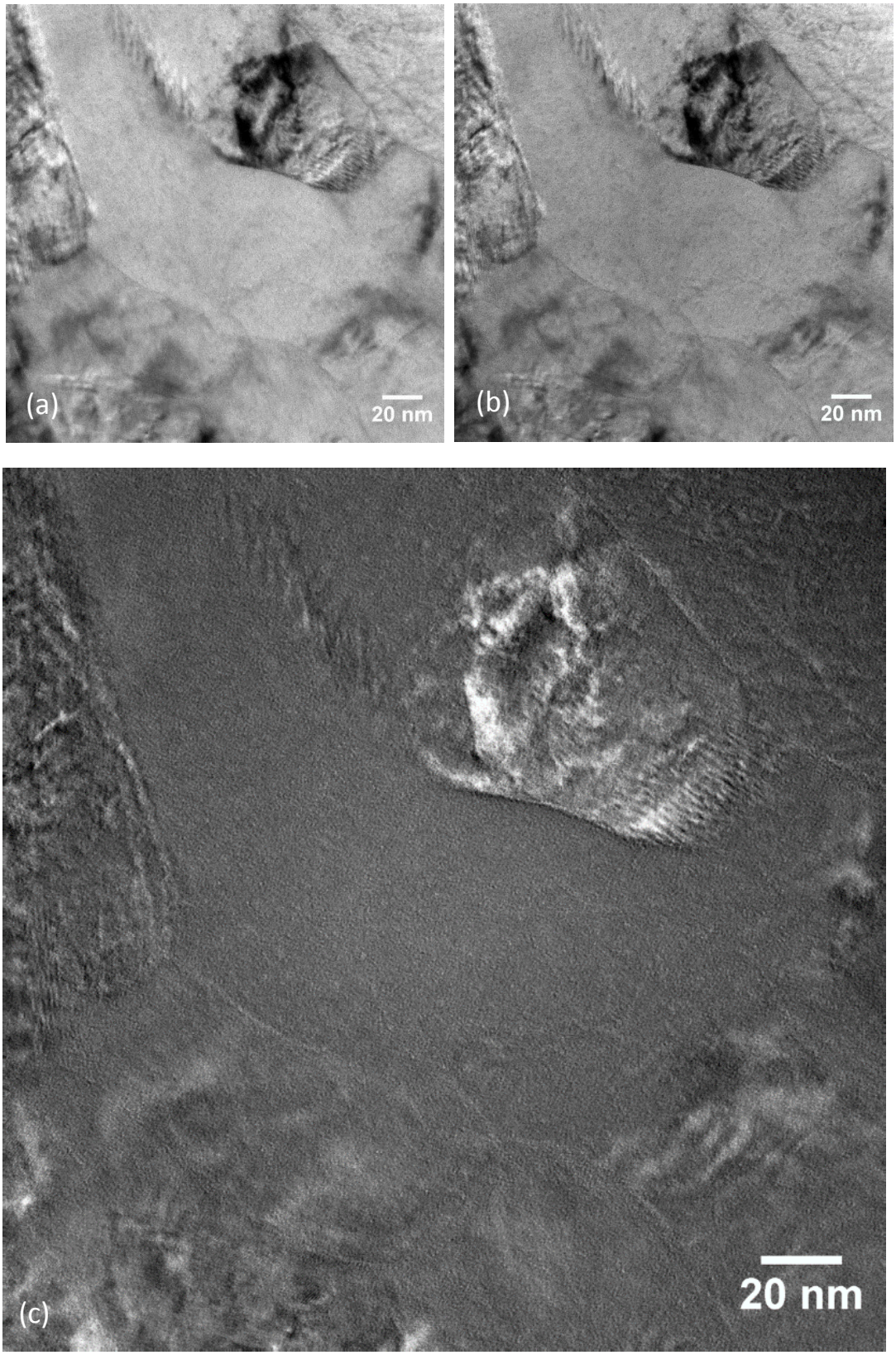


Figure 5.6 Using Equation 2.8 the thickness mapping process takes the ratio of (a) the elastic electron intensity and (b) the total unfiltered electron intensity to produce (c) a thickness map as a function of the mean free electron path.

5.4 Bubble Densities

5.4.1 Experimental Control – Implanted and Unimplanted Samples

A number of features are known to produce Fresnel fringes in ODS alloys imaged at an appreciable defocus. These include the oxide particles which were deliberately imaged at large defocusses by Hsiung [80] and voids or surface pits that might form during sample preparation [139]. These are of particular concern since a void would be indistinguishable from a bubble unless significant lattice strain were present, while a pit would produce bubble-like contrast, requiring sophisticated stereo imaging procedures to detect.

To provide the necessary confidence in the Fresnel imaging method a control study was performed using an unimplanted sample of the Fe-14Cr0.2Ti-3W-0.25Y_2O_3 alloy consolidated at 1150^{o}C. This was prepared in the same way as the implanted specimens and imaged under the same conditions. The through focus series recorded from this sample is presented in Figure 5.7 alongside a series taken from an implanted sample of the same alloy. As is evident from these micrographs the unimplanted control shows none of the Fresnel features that are evident in the implanted sample.

5.4.2 Implanted Alloys

Having satisfactorily demonstrated that the Fresnel contrast methods employed to survey the bubble population are free from sample preparation artefacts, samples of the implanted Fe-14Cr0.2Ti-3W-0.25Y_2O_3 alloy and the reference Fe-14Cr0.2Ti-3W alloy consolidated at 1150^{o}C were prepared and characterised. The micrographs from each sample are presented in Figure 5.8 and show a significant difference in the degree of bubble formation.

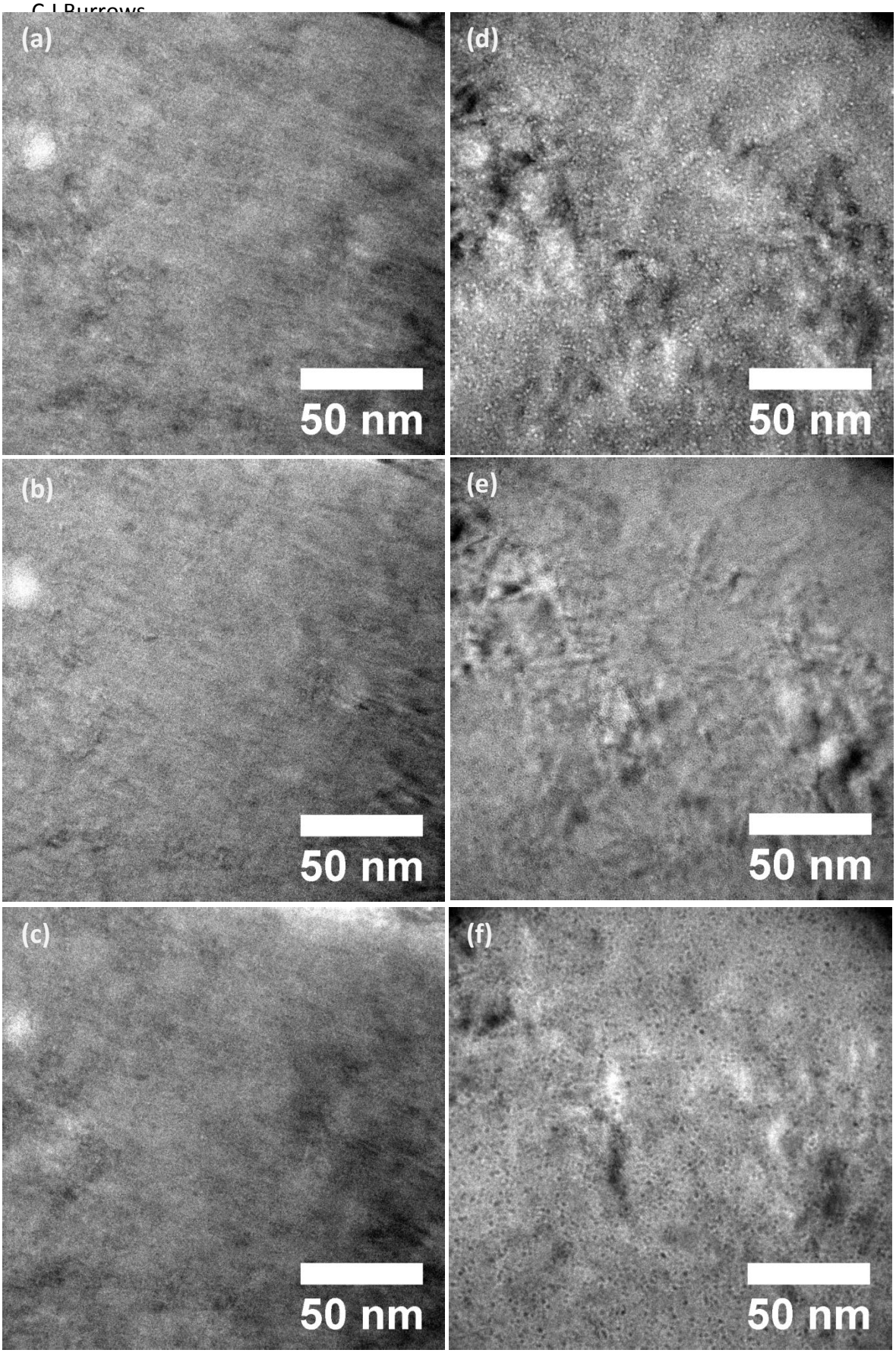


Figure 5.7 Experimental control for the 1150°C Fe-14Cr-0.2Ti-3W-0.25Y_2O_3 in the unimplanted condition at (a) -1.0µm (b) 0.0 µm and (c) +1.0 µm focus and in the implanted condition at (d) -1.0µm (e) 0.0 µm and (f) +1.0 µm focus

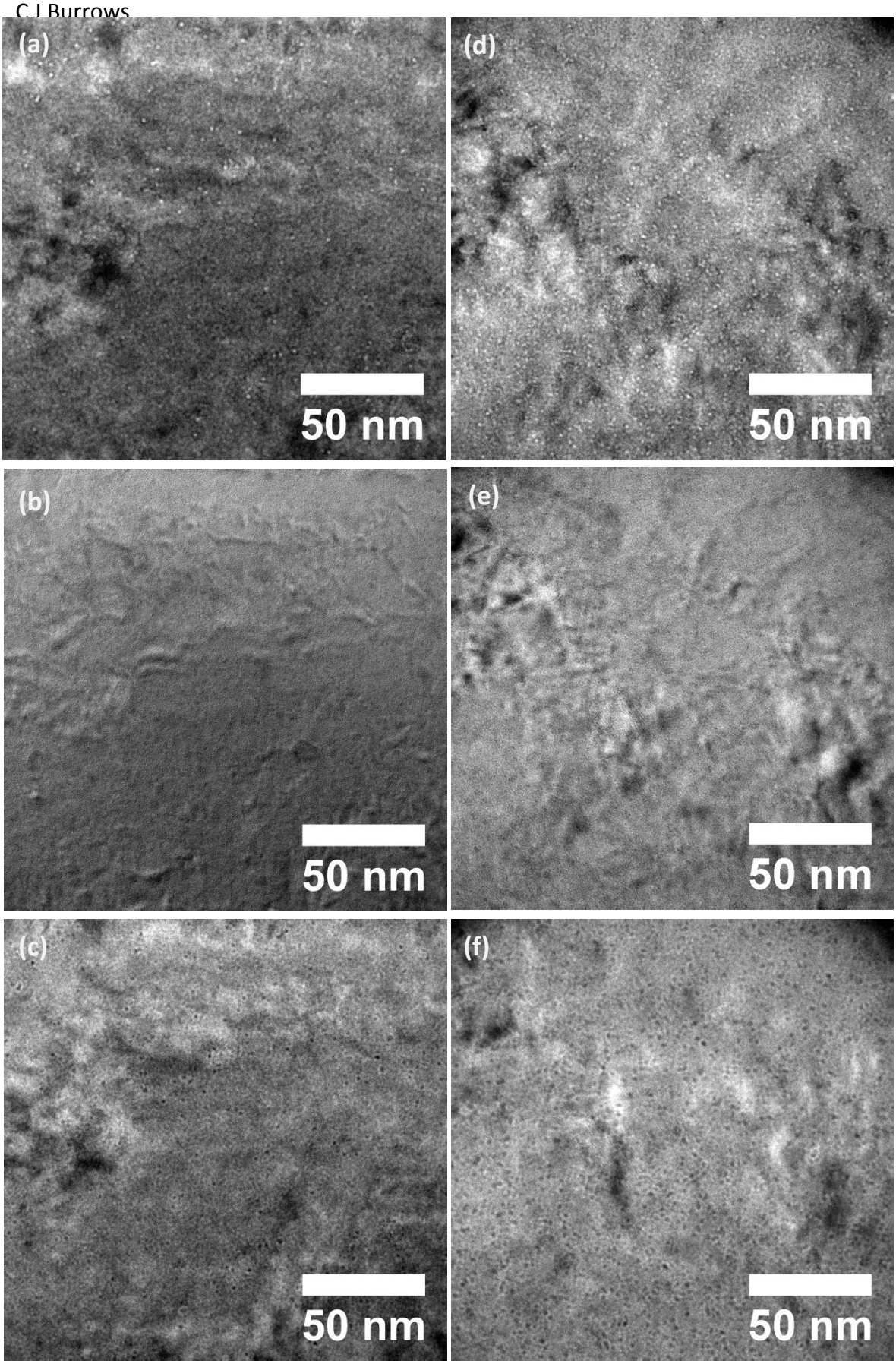


Figure 5.8 Experimental control comparing the 1150°C Fe-14Cr-0.2Ti-3W in the implanted condition at (a) -1.0µm (b) 0.0 µm and (c) +1.0 µm focus and the 1150°C Fe-14Cr-0.2Ti-3W-0.25Y_2O_3 in the implanted condition at (a) -1.0µm (b) 0.0 µm and (c) +1.0 µm focus

At $3.6\times10^{22}m^{-3}$ the bubble density in the reference alloy is substantially lower than that found in the ODS system which at $1.4\times10^{23}m^{-3}$ is comparable in magnitude to the average oxide particle density found in the 1150°C consolidations (Table 5.2). The bubbles are of a similar size in both samples, possibly indicating some helium losses occurred in the reference alloy. These might be attributed to local grain boundaries or to the proximity of the free surfaces produced during sample preparation, which in an alloy lacking the sink densities associated with oxide dispersion strengthening might exert a greater influence over the retained helium content of the sample.

The significance of bubble size and the difficulties inherent in estimating retained helium content using equations of state like those presented in Section 1.2 are discussed in Section 5.5 below. The bubble densities in the Fe-14Cr0.2Ti-3W-0.25Y_2O_3 alloy are presented in Table 5.2 for each consolidation temperature. The uncertainty in these measurements particularly those taken from the 950°C consolidation are large but the trend remains quite striking as is evident from Figure 5.9.

In all three consolidation conditions the bubble and particle number densities are comparable, rising from $1.4\times10^{23}m^{-3}$ in the 1150°C consolidation to $8.2\times10^{23}m^{-3}$ in the 950°C consolidation. The correlation provides good evidence for gas trapping at the particles and demonstrates that a measure of control can be exercised over the gas accumulation process via the oxide particle dispersion by varying the consolidation temperature.

Composition (wt%)	**Fe-14Cr-3W-0.2Ti-0.25Y_2O_3**			**Fe-14Cr-3W-0.2Ti**
Consolidation Temperature (°C)	**1150°C**	**1050°C**	**950°C**	**1150°C**
Bubble Number Density (10^{23} m^{-3})	1.4 ± 0.6	3.2 ± 1.2	8.2 ± 2.3	0.4 ± 0.1
Particle Number Density (10^{23} m^{-3})	2.5 ± 0.3	3.8 ± 0.7	6.7 ± 0.4	NA ± NA

Table 5.2 A summary of the particle number densities as determined by APT and the bubble number densities as determined by TEM in the ODS system at each consolidation temperature and in the reference alloy at 1150°C

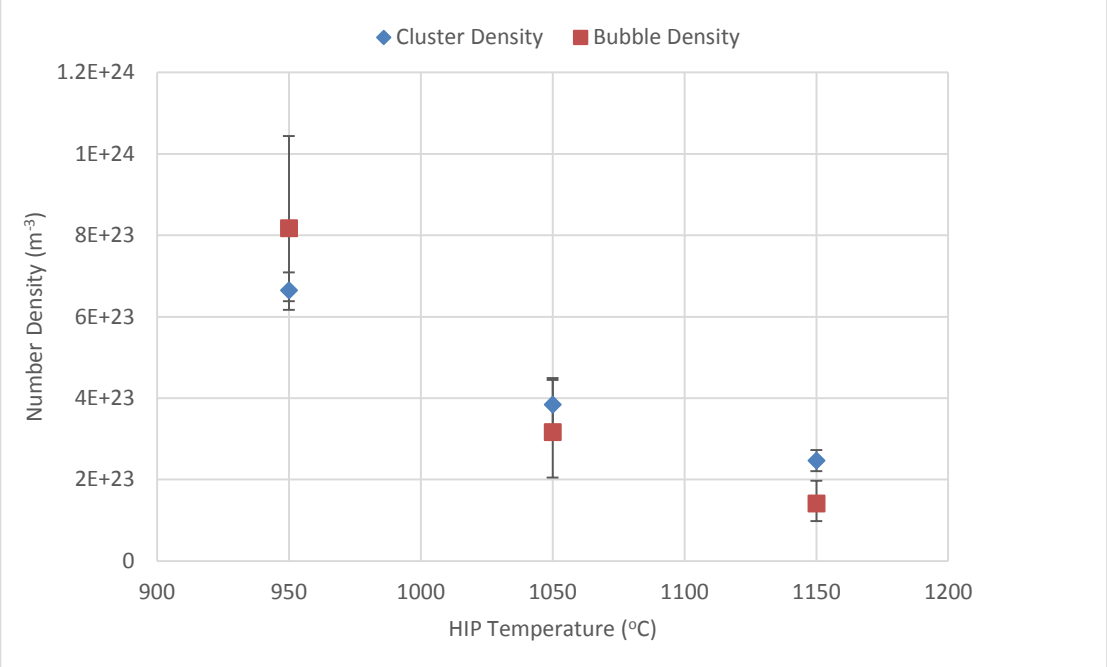


Figure 5.9 Variation in particle and bubble number densities with consolidation temperature

5.5 Discussion

The four fold increase in helium bubble density in the ODS, compared to the reference alloy in the 1150°C consolidation, validates the useful role particle trapping plays in sequestering helium gas. Similarly, the close correlation between particle and bubble densities strongly indicates that the oxide particle dispersion is by far the dominant factor in controlling the gas accumulation process.

The consolidation conditions might potentially influence the availability of other trapping sites, particularly dislocations and carbides, depending on the extent of microstructural pinning and any subsequent heat treatments, but deconvolving these effects from those of the coarsening particle dispersion is likely to be difficult. The reference alloys would provide some opportunity to elucidate these effects but their coarse microstructure offers a less than perfect analogue of a particle free oxide dispersion strengthened system.

All the bubbles in the surveyed samples were found to be small and produced Fresnel fringes between 1.0nm to 2.0nm in diameter, comparable to those produced by Ryazanov at 300^{o}C in ODS Eurofer, as shown in Figure 1.35. Yao found the ratio of the fringe diameter to the bubble diameter to lie between 0.8 and 0.9 for bubbles in these size ranges when imaged under a 200keV beam but expressed some concern regarding the large uncertainties associated with fringes smaller than 2.0nm.

Bubbles in the 1150^{o}C consolidation produced fringes that on average reached 1.4nm in diameter, falling to 1.2nm in the 1050^{o}C consolidation. Contrary to expectations the average fringe diameter increased again in those samples surveyed from the 950^{o}C consolidation to 1.5nm. The amalgamation and distortion of the extremely dense bubble population during image processing, most likely accounts for this size increase but taken together these various factors make it very difficult to assign sizes to the bubbles with greater than 1.0nm precision.

These difficulties in turn make quantification of the helium content by this method very imprecise, quite apart from the various assumptions that must be made in the application of an equation of state. Of these, modelling the bubbles as spherical thin walled pressure vessels, in equilibrium with an iron matrix, is perhaps the most significant simplification. In reality, bubbles have been seen to take on faceted shapes, which when trapped at the boundary of an oxide particle present a far more complicated free surface energy balance than that assumed by any of the models detailed in Section 1.2.

The Mills Liebenberg and Bronson (MLB) model presented in Equation 1.14 was used to produce the density and pressures for helium bubbles of different sizes shown in Table 5.3. The atomic densities calculated for the trapped helium, allow the gaseous content of the implanted samples to be estimated from the bubble sizes and number densities recorded in Section 5.4.2. These are shown in Table 5.4 and are compared to the concentrations delivered during the implantation. Additional estimates are provided for comparison from EUROFER and MA957, using data reported by Ryazanov [120], Yamamoto [109] and Odette [14].

Radius (nm)	Volume (cm^3/mole)	Helium density (atoms/cm^3)	Pressure (GPa)
0.5	5.0	1.2E+23	7.7
0.6	5.3	1.1E+23	6.4
0.7	5.5	1.1E+23	5.5
0.8	5.8	1.0E+23	4.8
0.9	6.0	1.0E+23	4.3
1.0	6.2	9.7E+22	3.9
1.5	7.1	8.5E+22	2.6
2.0	7.9	7.7E+22	1.9

Table 5.3 Helium states computed for bubbles of varying sizes using the Mills Liebenberg and Bronson Equation of State shown in Equation 1.14

	Implantation Temp (°C)	Injected He (appm)	Damage (dpa)	Bubble No Density (m^{-3})	Radius (nm)	He density (atoms/cm^3)	MLB He (appm)
EUROFER [120]	300	1000	0.23	4.0E+23	1.0	9.7E+22	1918
EUROFER [120]	500	1000	0.23	3.5E+23	2.0	7.7E+22	10598
EUROFER [109]	300	89	3.9	3.6E+23	0.5	1.2E+23	270
EUROFER [109]	400	82	3.9	1.2E+22	1.5	8.5E+22	169
EUROFER [109]	500	372	9	1.5E+22	2.0	7.7E+22	454
MA957 [109]	500	380	9	3.0E+23	0.5	1.2E+23	225
1150°C	300	2000	0.3	1.4E+23	1.0	9.7E+22	671
1050°C	300	2000	0.3	3.2E+23	1.0	9.7E+22	1534
950°C	300	2000	0.3	8.2E+23	1.0	9.7E+22	3932

Table 5.4 Implantation conditions, bubble properties and helium concentrations calculated using the MLB model in Eurofer MA957 and each of the three consolidations assuming a bubble radius of 1.0nm. Injected helium concentrations are provided for comparison.

The MLB helium concentrations shown in Table 5.4 were calculated for each consolidation assuming 1.0nm bubbles at the number densities recorded in Table 5.2. The calculated concentrations are seen to approach the implanted concentration to one order of magnitude. The implantation data provided by Odette and Yamamoto for neutron irradiated samples of MA957 and ODS Eurofer also match the calculated concentrations shown in Table 5.4 [109].

The different levels of displacement damage sustained by each of the sample sets and the different dose rates inherent to neutron irradiation and ion implantation appear to have had little impact on the accuracy of the calculated helium concentration. The one major discrepancy apparent in Table 5.4, occurs in the 500^{o}C 1000appm implant conducted by Ryazanov [120]. If in equilibrium with the ferritic matrix, the large bubbles that populate these samples and which are shown in Figure 1.35 correspond to a 10000appm helium content.

The unusual nature of the implantation conducted by Ryazanov, in an attempt to produce uniform gas concentrations through macroscopic tensile specimens, may have contributed to such an excess of large bubbles but these bubbles may simply no longer satisfy the assumptions made in the MLB model. The bubbles at the particle boundaries in Figure 1.35 are flattened and distorted by the particles and given that their inflation occurred at approximately constant density are unlikely to have remained as pressure stabilised bubbles transitioning instead to low pressure voids.

The lack of a systematic temperature variation in the study conducted here hampers the development of any further conclusions regarding the accuracy of the MLB model but the difficulties inherent in correlating injected and retained gas are apparent. Alternative quantification methods might offer some insight for future studies.

6 Micromechanical Response To Helium Implantation

6.1 Summary

Following helium implantation the oxide particle dispersion appeared to successfully sequester the accumulated gas in a dense dispersion of high pressure bubbles. The close correlation between the particle and bubble densities provides good evidence for the direct association between bubbles and particles. This indicates a significant potential for mitigating the detrimental effects of gas build up on the mechanical performance of the consolidated alloy.

With the assistance of C. Hardie, nanoindentation methods were used to access the mechanical properties of the implanted layer in the manner discussed in Section 2.4, using the Agilent G200 indenter at the Culham Centre for Fusion Energy (CCFE). Average hardness values were obtained for each alloy prior to helium implantation. These showed a substantial hardening effect produced by the addition of yttrium oxide to the base alloy along with a large spread in the oxide dispersion strengthened hardness measurements.

SEM assays of the indent arrays were used to eliminate pile-up and sink-in at the indentation sites as potential sources of the spread. Instead the wide variation in hardness was found to be correlated with the grain size of the microstructure. The difference in grain size distribution between the oxide dispersion strengthened and reference systems are apparent from the band contrast maps, presented in Figure 6.1.

Having accounted for any anomalous surface deformations, the bimodal grain size, initially identified in the TEM micrographs of Section 4.3, was identified as the most likely source of the large variation in the hardness data. Quoting average grain sizes from maps like those in Figure 6.1 is difficult, since the oxide dispersion strengthened microstructure is only partially resolved, even when using the smallest step and spot sizes. Nevertheless, grains between 100 and 200nm in width are clearly visible in Figures 4.1 to 4.3.

Shallow indentation arrays, located on comparative EBSD maps of the 1150°C consolidation, were used to establish a firm correlation between hardness and grain size. This allowed the grain size and particle hardening effects to be effectively deconvolved and used to establish reliable estimates of the implantation and particle hardening. From these figures, reported below in Table 6.2, the suppression of helium hardening in particle reinforced alloys becomes apparent. Furthermore estimates for the obstacle strength of the particles themselves, can be made from the dispersed barrier model of hardening.

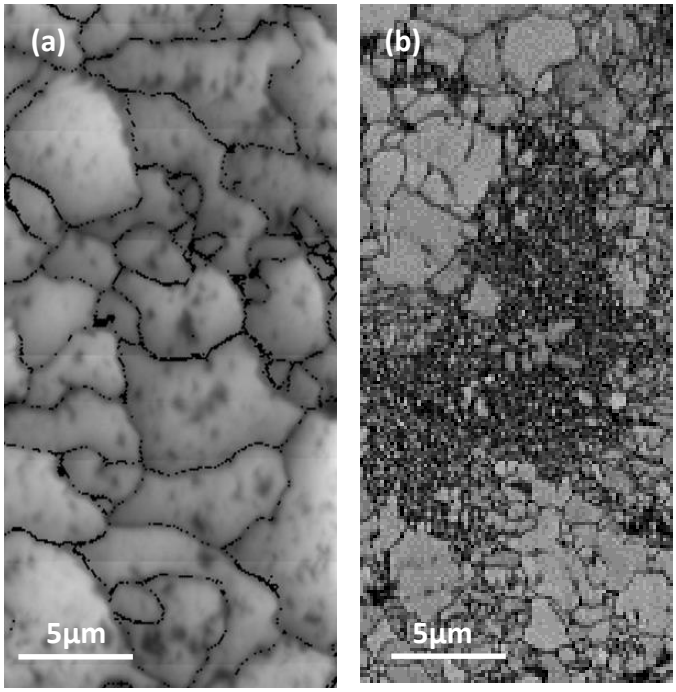


Figure 6.1 EBSD Band contrast maps taken from (a) Reference alloy [148] (b) ODS alloy consolidated at 1150°C showing the notable differences between the microstructure particularly the bimodal grain size distribution in the ODS system

6.2 Hardness Measurements

Four by four arrays of 2000nm deep indents were used to measure the hardness in each alloy for each consolidation condition in both the unimplanted state and following the implantation outlined in Section 5.2. The indentations were carried out using a new Berkovich diamond tip in the manner outlined in Section 2.4. The variation in hardness with depth averaged over the whole indent array is shown in Figure 6.2 for the unimplanted materials. The expected difference in hardness between the oxide dispersion strengthened and reference alloys is immediately apparent.

A modest variation in the hardness of the reference material likely occurs as a result of microstructural coarsening in the samples consolidated above 1000°C. In the ODS a number of factors likely contribute to the variation in hardness, including the different particle number densities. These effects are inevitably convolved with other microstructural differences, such as the bimodal grains size distribution observed in Figures 6.2 to 6.4, complicating any attempt to apply a simple Hall-Petch interpretation to the data.

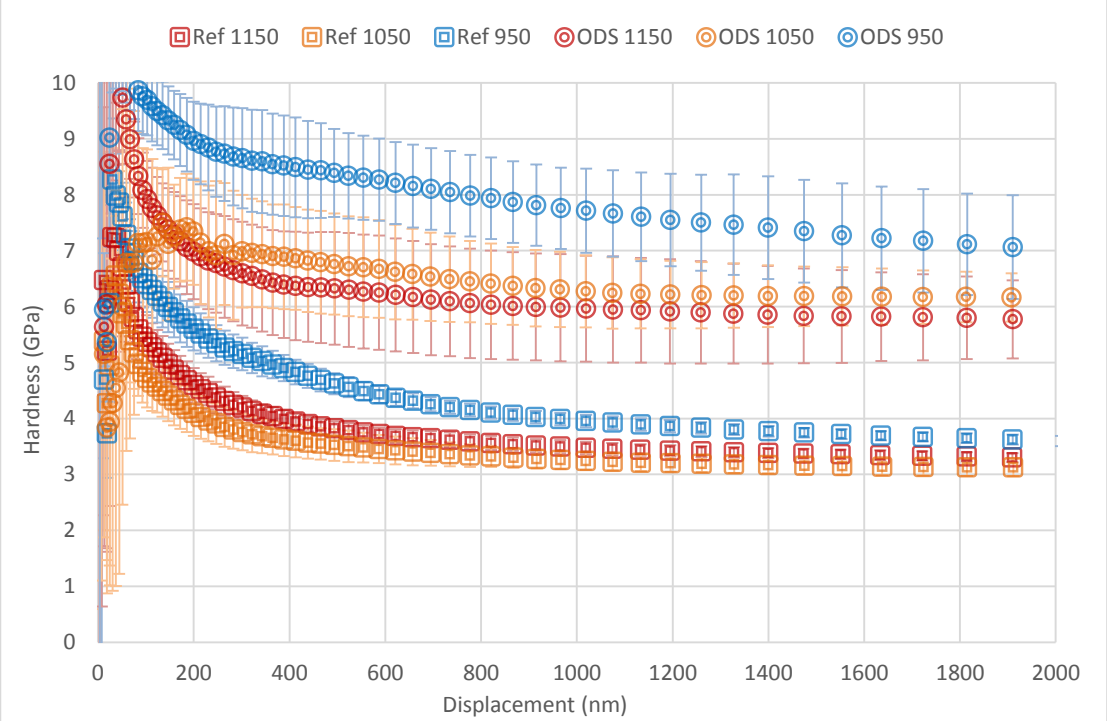


Figure 6.2 Average hardness with indentation depth recorded from an array of 16 indents for unimplanted ODS and reference alloys at each consolidation temperature. Note the difference in hardness between the ODS and reference alloys and the significant scatter in the ODS data.

The hardening effects of the helium are evident in the upper 500nm of the material, beyond which the plastic zone around the indenter tip moves out of the implanted layer and into the unimplanted material below. The effect of the helium addition on the reference alloys is shown in Figure 6.3. At a depth of 500nm all three consolidations have moved to approximately the same hardness. This indicates that in the absence of a systematic variation in sink densities, helium bubbles are forming at comparable densities, introducing the same number of new of barriers to dislocation motion in each consolidation and dominating all other effects in the implanted layer.

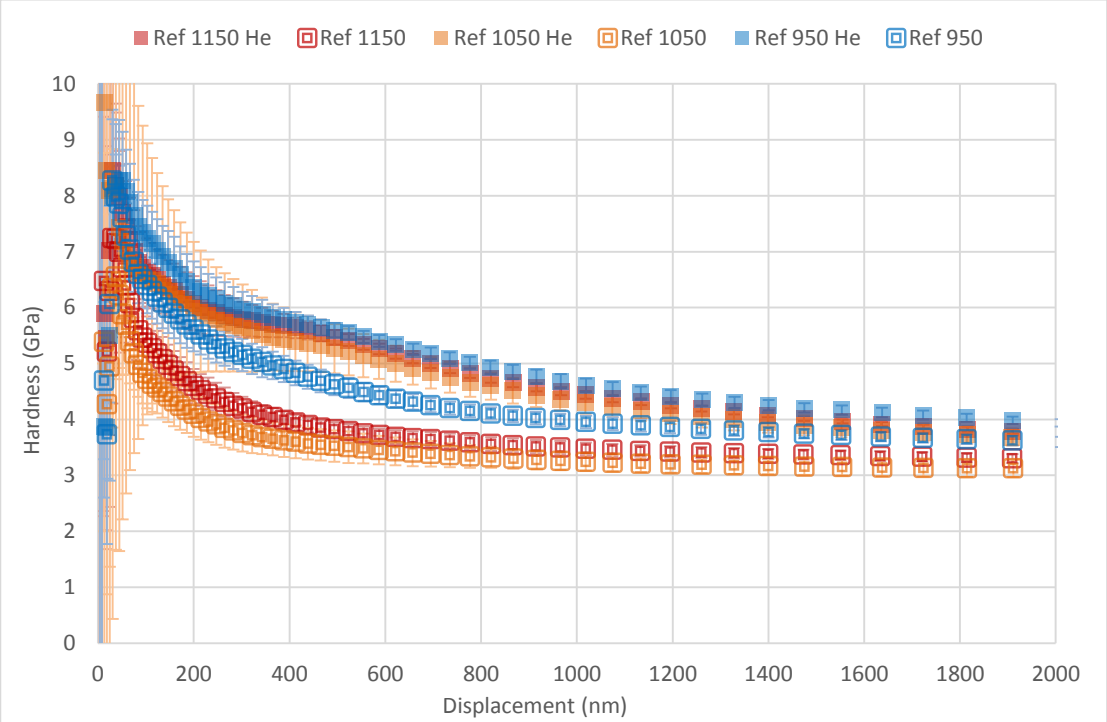


Figure 6.3 Average hardness with indentation depth recorded from an array of 16 indents for unimplanted and implanted reference alloys at each consolidation temperature showing all three implanted samples hardening to the same degree

In comparison the helium implantation caused a more modest increase in the average hardness of the oxide dispersion strengthened alloys shown in Figure 6.4. At 500nm from the surface the average indentation hardness increases with helium addition by approximately 0.5GPa in the 1150°C consolidation and 0.4GPa in the 1050°C consolidation.

The oxide particles appear to be functioning as anticipated, trapping the helium and suppressing the formation of any new barriers to dislocation motion but contrary to expectations the implanted 950°C consolidation shows a drop in hardness of 0.4GPa. Softening with helium injection was unanticipated and runs counter to the wider assumptions concerning the effects of transmutant helium accumulation. However, interpreting these findings is hampered by the significant scatter present in the ODS hardness data the origins of which are now considered.

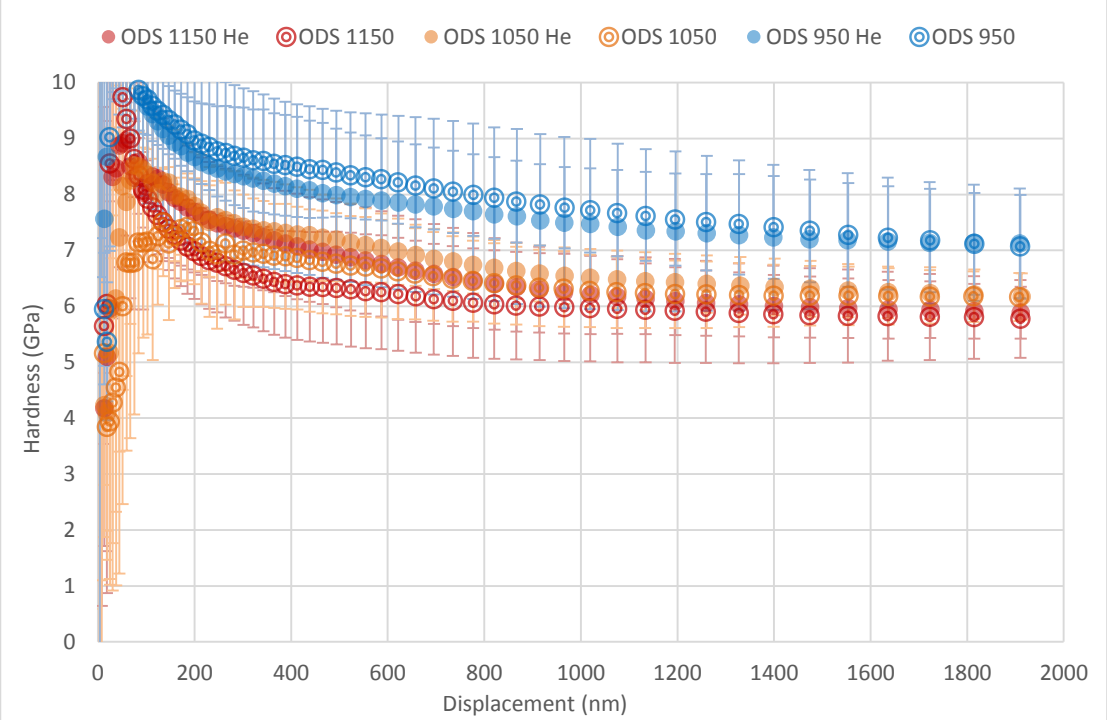


Figure 6.4 Average hardness with indentation depth recorded from an array of 16 indents for unimplanted and implanted ODS alloys at each consolidation temperature showing minimal change in hardness with the introduction of 2000appm helium

6.3 Hardness and Microstructure in Oxide Dispersion Strengthening Alloys

The error bars in Figures 6.2, 6.3 and 6.4 show the standard deviation in the average indentation hardness. These are substantially larger in the oxide dispersion strengthened alloys than the reference alloys. In an attempt to understand their origin and by extension the reliability of the apparent hardening and softening effects seen in Figure 6.4, the hardness variations with depth were plotted separately for each indent. Figures 6.5 to 6.8 show separate profiles for each indent in the 950°C and 1150°C ODS consolidations in both the implanted and unimplanted conditions.

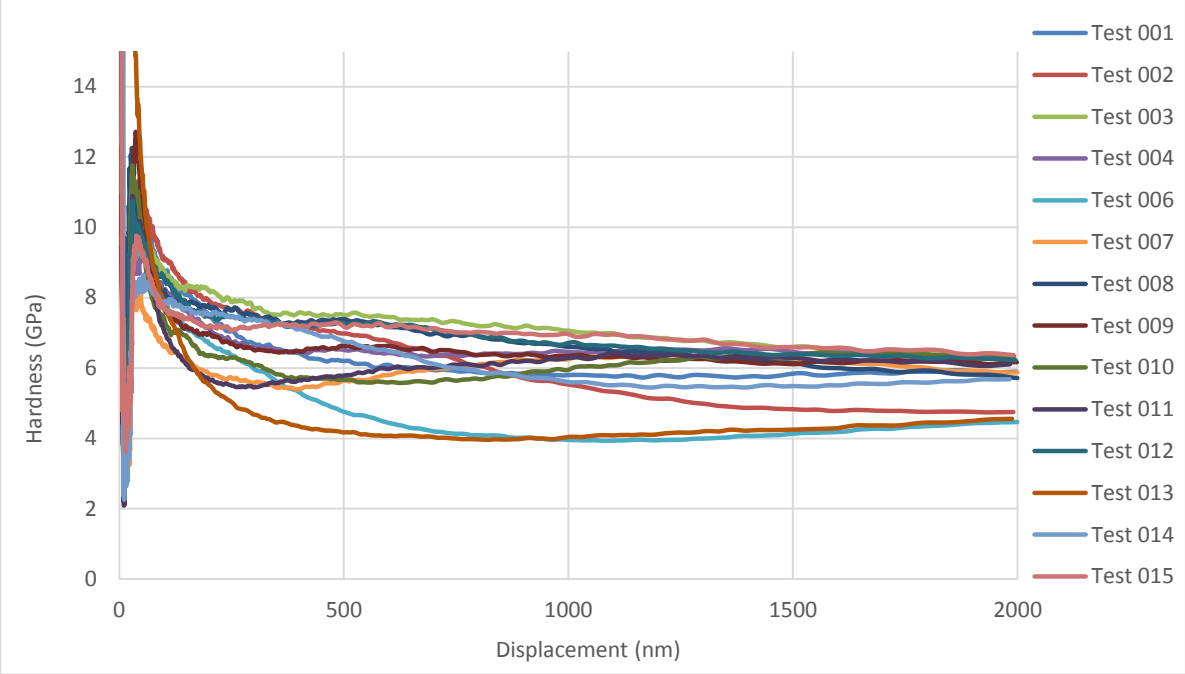


Figure 6.5 Hardness variation with depth as recorded from each indent in the unimplanted 1150°C ODS

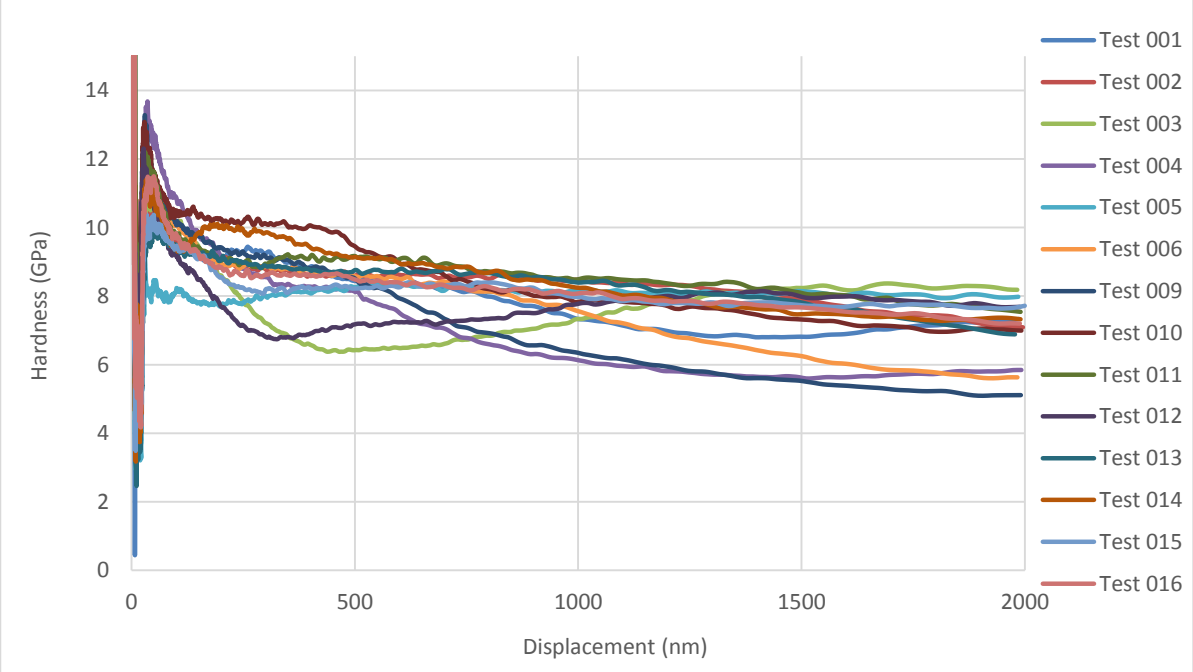


Figure 6.6 Hardness variation with depth as recorded from each indent in the unimplanted 950°C ODS

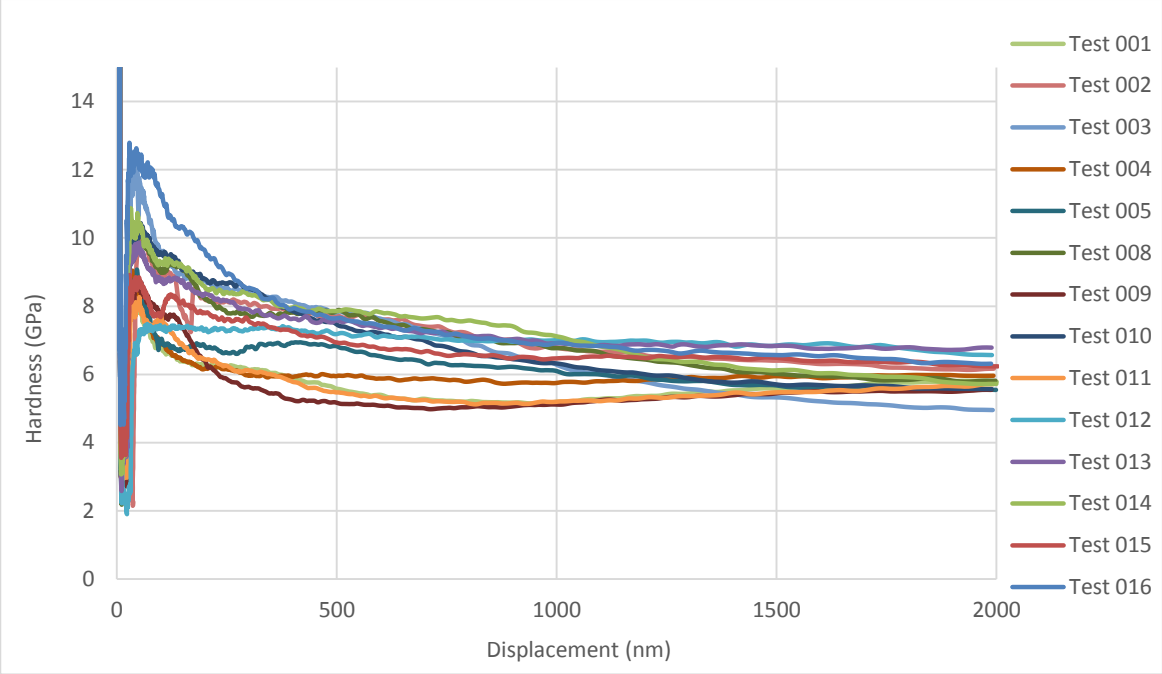


Figure 6.7 Hardness variation with depth as recorded from each indent in the implanted 1150°C ODS

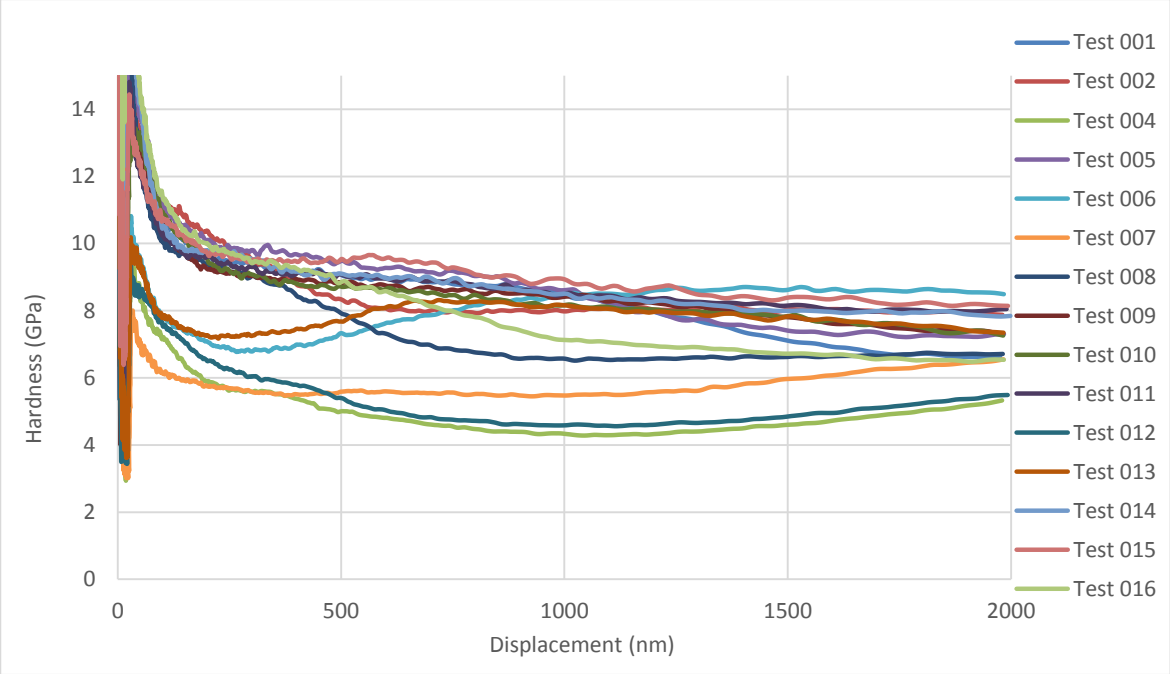


Figure 6.8 Hardness variation with depth as recorded from each indent in the implanted 950°C ODS

In each of these plots there appears to be a systematic spread in the indentation harness of the alloys. For example, indents 006 and 013 in Figure 6.5 and 004 and 012 in Figure 6.8 apparently sampled a consistently softer material. Based on the TEM and APT data presented in Sections 4.3 and 4.4, the number density and character of the particle dispersions can be assumed to be broadly consistent on the scale of a 2000nm deep indent. These variations in hardness are therefore indicative of some other inconsistency in the wider microstructure, provided the indentation data are reliable.

6.3.1 SEM Characterisation

As discussed in Section 2.4.4 the deformation of the sample material around the indenter tip causes significant complications when computing an indentation hardness. Sink-in and pile-up of the material surrounding the indent changes the contact area between the tip and surface, introducing appreciable errors in mechanical property measurements that are made assuming an area function calculated using Equation 2.13.

Oliver and Pharr [166] found surface deformation effects to be largely dependent upon two factors; the elastic modulus to yield stress ratio and the work hardening coefficient of the material. Consequently soft alloys with a minimal capacity for work hardening can be expected to show significant surface deformation [145]. By contrast, as noted in Section 2.4.4, these criteria make pile-up and sink-in quite unlikely in oxide dispersion strengthened alloys.

However, the circumstances of the implantation also need to be considered as pile-up and sink-in can become more prominent in thin layers of material deposited on an underlying substrate [166]. In hard coatings on a soft material the plastic deformation can occur in the substrate or, if the substrate is appreciably harder, the deformation may be confined to the coating. In the implanted samples the behaviour of the unimplanted alloy under the helium bearing layer may therefore influence how the surface behaves at the indentation site [167].

Given these complications and the significant pile-up recorded by Hardie [145] using SEM and AFM techniques in implanted Fe-Cr alloys , the indent arrays in the implanted samples were surveyed by SEM for evidence of pile-up or sink-in. Pile-up is of particular concern here since, as noted in Section 2.4.4, the actual contact area at the indent becomes larger than that computed from the area function. This leads to an overestimate in the measured hardness that mimics irradiation hardening.

Figure 6.9 shows two typical indents from the arrays in the implanted surfaces of the oxide dispersion strengthened and reference alloys consolidated at 1050^{o}C. Neither show any significant evidence of pile-up or sink-in though some surface wrinkling can be seen on one side of the indent impression in the reference alloy. No superficial correlations between the shape of the indents and the spread in the hardness measurements were evident, which again suggests an underlying microstructural reason for the variations in hardness.

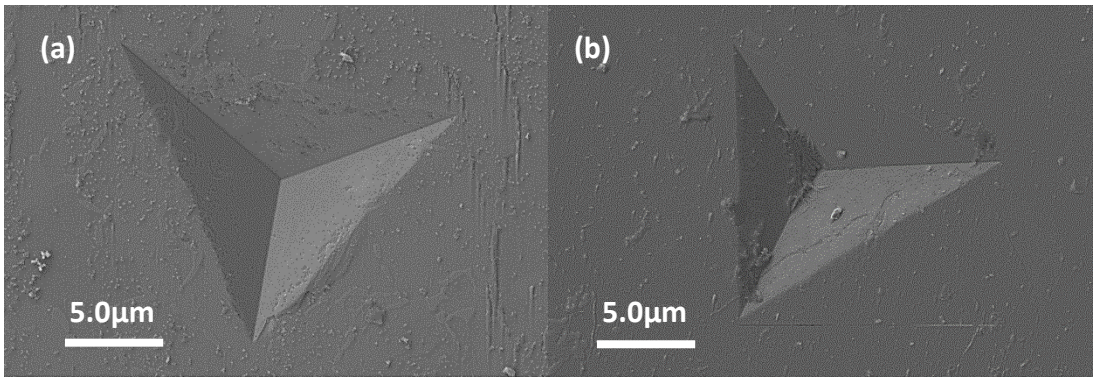


Figure 6.9 SEM micrographs of 2000nm deep indents from the implanted 1050^{o}C consolidation in (a) reference alloy and (b) ODS alloy showing no appreciable evidence of pile-up or sink-in

To further establish the validity of the measurements recorded from the implanted alloys, arrays of 500nm deep indents were applied to the same samples from the 1050^{o}C consolidation. These allowed the behaviour of the surface to be checked at the depth from which the hardness measurements were taken and at which the effects of the irradiation hardening were most evident from Figures 6.3 and 6.4. Two typical indents are presented in Figure 6.10 showing little evidence of the extensive pile-up observed by Hardie in irradiated Fe-Cr systems [145]

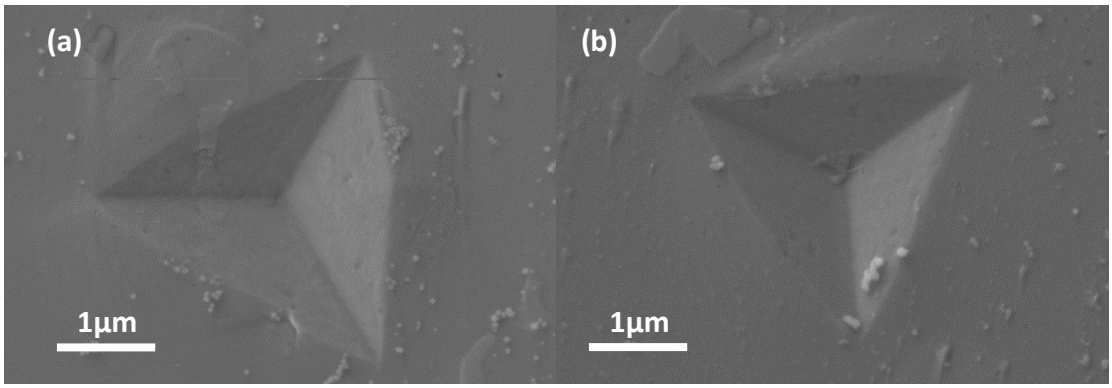


Figure 6.10 SEM micrographs of 500nm deep indents from the implanted 1050°C consolidation in (a) the reference alloy showing some surface uplift along the right hand edge of the impression and (b) the ODS alloy showing minimal surface uplift along the edges of the impression.

6.3.2 EBSD Characterisation

The micrographs presented in Figures 6.9 and 6.10 demonstrate that the implanted samples are largely free from any surface anomalies that might have significantly influenced the indentation hardness measurement. This allows the hardening observed in the reference alloy to be directly attributed to the implanted helium and suggests a genuine microstructural origin for the spread in indentation hardness discussed in Section 6.3.1. Contrary to initial expectations however, significant pile-up was observed around some indents in the unimplanted ODS alloys.

SEM micrographs of indent 006 in the unimplanted ODS consolidated at 1150°C are presented in Figure 6. 11. These clearly show material piled up along one edge of the indenter impression but as can be seen from Figure 6.5, indent 006 recorded a much *lower* hardness compared to the average for the unimplanted 1150°C alloy. This is contrary to what one might expect from an indent with significant pile-up. Indent 012 shown in Figure 6.13 exhibits a similar uplift in the surface along one edge of the indent but here the hardness exceeded the average by 0.8GPa.

It therefore seems likely, based on the lack of any correlation between the hardness measurements and the modest amount of pile-up present in the unimplanted alloy, that surface anomalies have minimal influence on the data and can be safely ignored in any further analysis. Instead, genuine microstructural differences between indent sites can be sought, the bimodal grain size distribution being perhaps the most obvious.

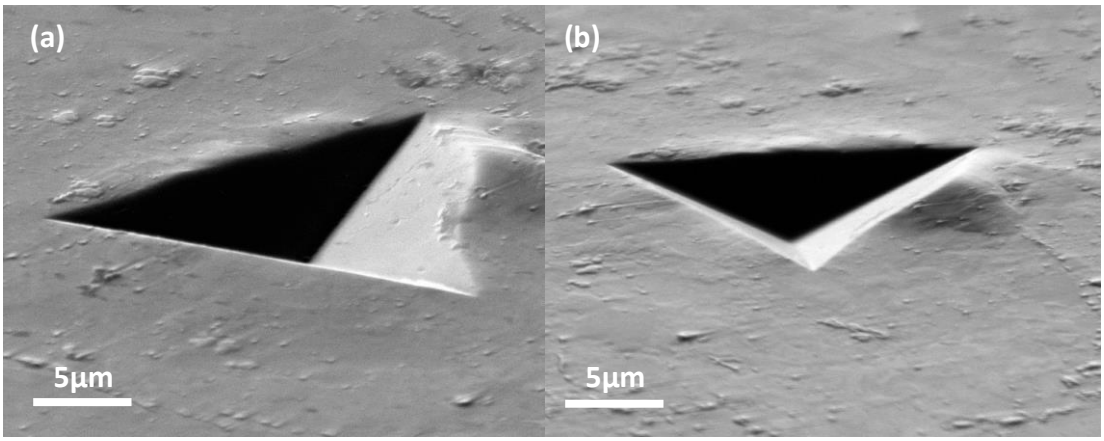


Figure 6. 11 SEM micrographs of indent 006 in the unimplanted 1150°C ODS showing pile-up at one edge of the indent

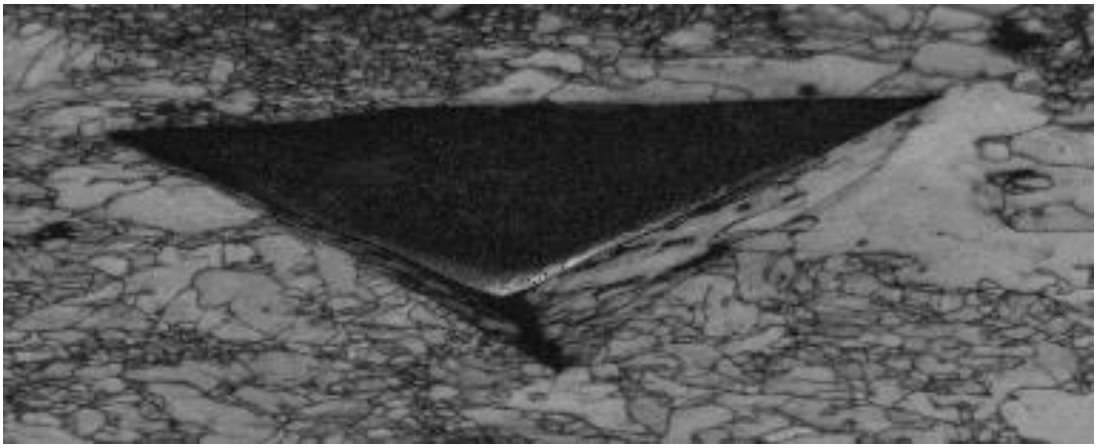


Figure 6.12 Band contrast map taken from Figure 6. 11 (b) showing the local microstructure around indent 006 and the large grain associated with the pile up at the indent periphery.

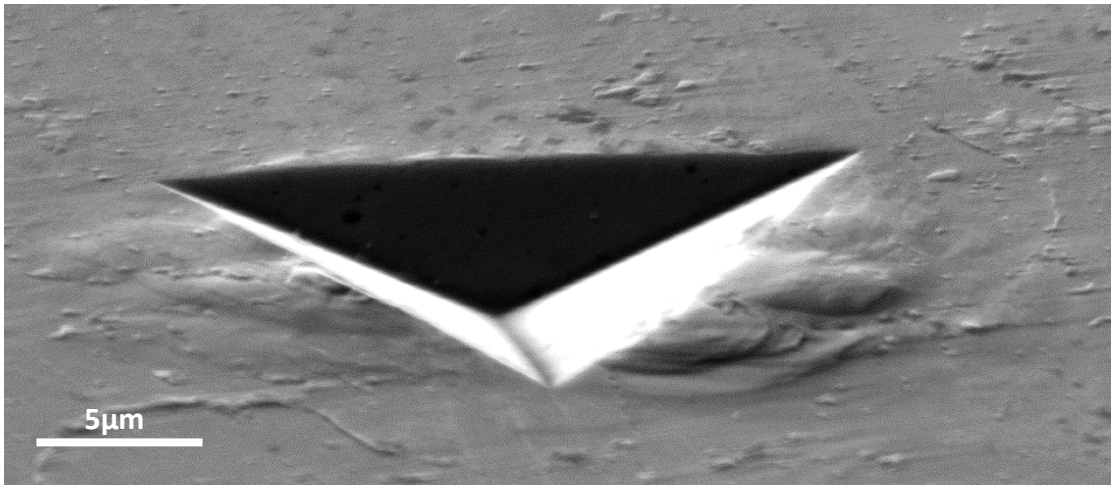


Figure 6.13 SEM micrographs of indent 012 in the unimplanted 1150°C ODS showing pile-up at one edge of the indent

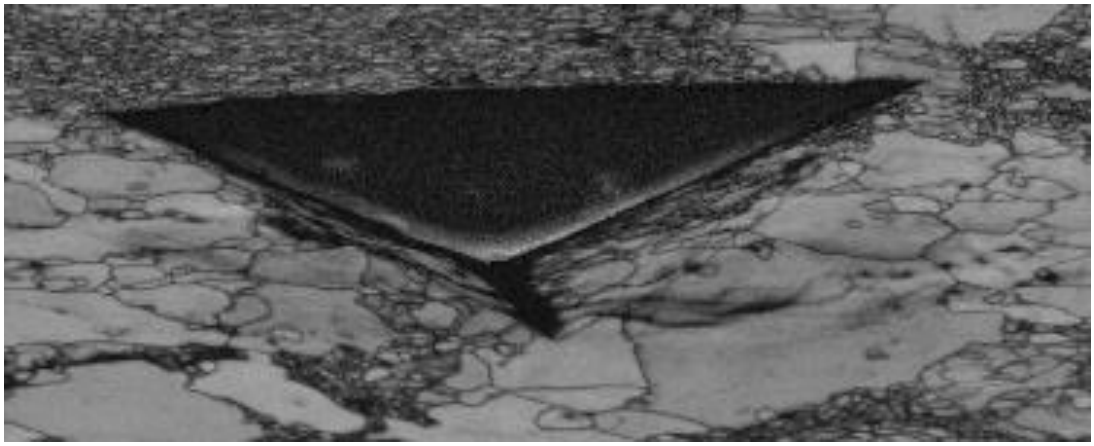


Figure 6.14 Band contrast map taken from Figure 6.13 showing the local microstructure around indent 012 and the large grain associated with the pile up at the indent periphery.

The electron backscatter diffraction (EBSD) techniques outlined in Section 2.5 provide a reliable method for assessing the microstructure on the scale of the nanoindentation arrays shown here. Figures 6.12 and 6.14 show Kikuchi band contrast maps recorded from the indent impressions in Figures 6. 11 and 6.13 using a 15kV beam and a 100nm step size. The local grain structure, and particularly the bimodal grain size distribution is very apparent from these Figures, which sample a far larger area than that shown in the TEM micrographs presented in Section 4.3.

On inspecting these micrographs, it is clear that the piled up material around the indents is associated with larger grains and in Figure 6.13 even conforms to the local grain structure to some extent. It seems likely that if the large grains are softer than the fine gained material those indents that record a significantly lower hardness may simply have sampled a larger grained region of the microstructure. By extension, those indents that show a sudden change in hardness at some depth, like indent 003 in Figure 6.6, are most probably the result of the plastic zone around the indenter tip moving out of a large grain and into a region of harder, fine grained material.

In an attempt to remove such effects and substantiate the difference in indentation hardness between regions with differing grain sizes, an array of 72, 300nm deep indents, was applied to the unimplanted 1150^{o}C ODS alloy. These were sufficiently shallow such that the plastic zone around each indent would be unlikely to cover regions with significantly varying grain sizes, allowing hardness measurements from very specific areas to be compared.

Figure 6.15 shows a band contrast map of the region adjacent to the original indent site prior to the application of the new array. Mapped using a 50nm step size, the bimodal grain size distribution becomes clear even over these large length scales. Following indentation a section of the same area was remapped (Figure 6.16) to enable particular indents to be easily located on Figure 6.15 and a judgement made concerning the local grain size of each.

Plotting indents 030 031 and 032 in Figure 6.17 shows the difference in hardness between large and small grained regions of the alloy explicitly. The fine grained microstructure, visible in Figure 6.15 at indent 030, abuts a large grained region sampled by indent 031 and the two sites differ in hardness by a factor of 2. Moving out of the large grains to indent 032, sees a return to the higher hardness values of indent 030.

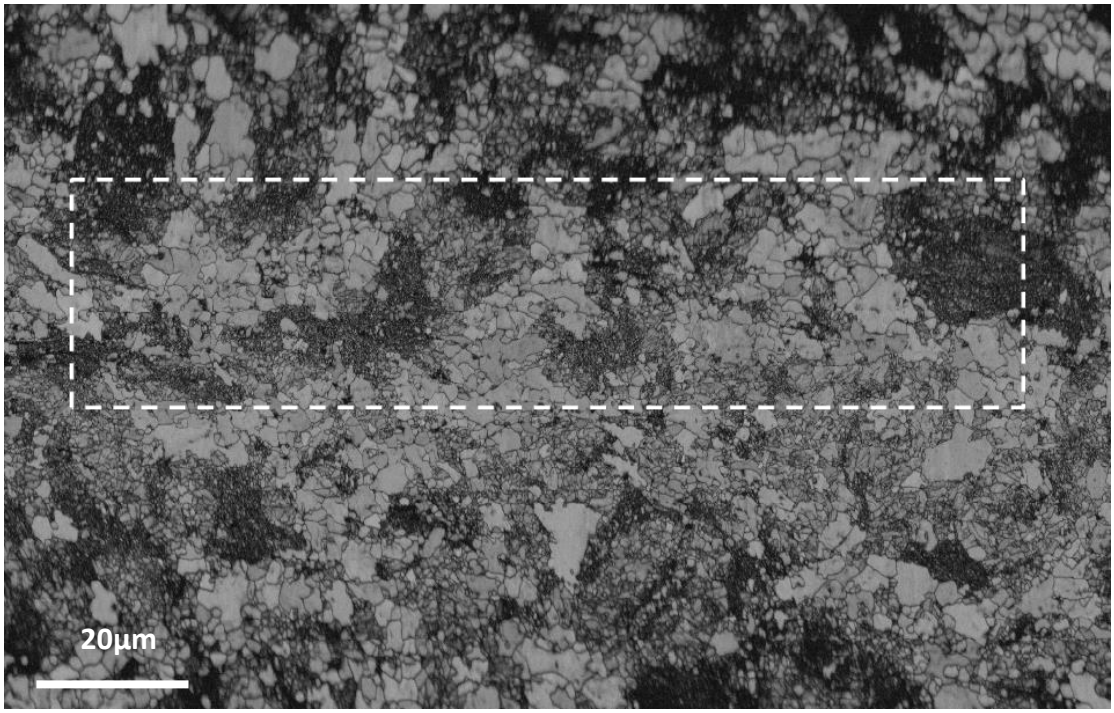


Figure 6.15 Band contrast map taken from the surface of the unimplanted ODS 1150°C consolidation prior to indentation showing the long range microstructure of the alloy and the region mapped below in Figure 6.16.

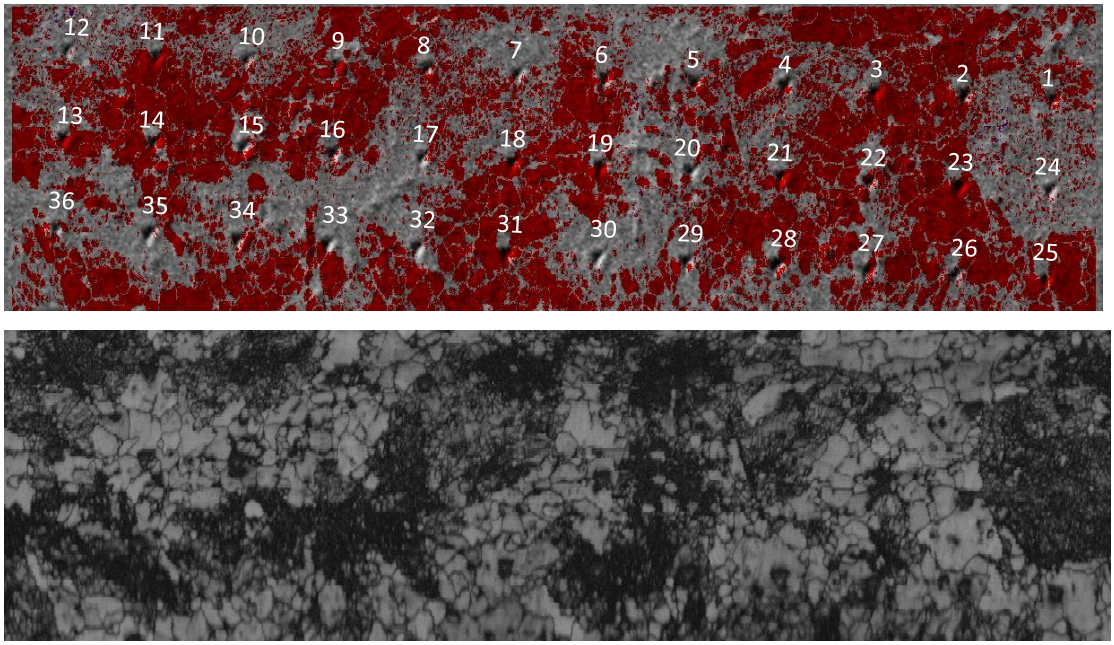


Figure 6.16 Section of Figure 6.15 remapped following indentation showing EBSD solutions in red overlaid on the SEM micrograph of the numbered indentation sites accompanied by the corresponding band contrast image recorded using a 100nm step size.

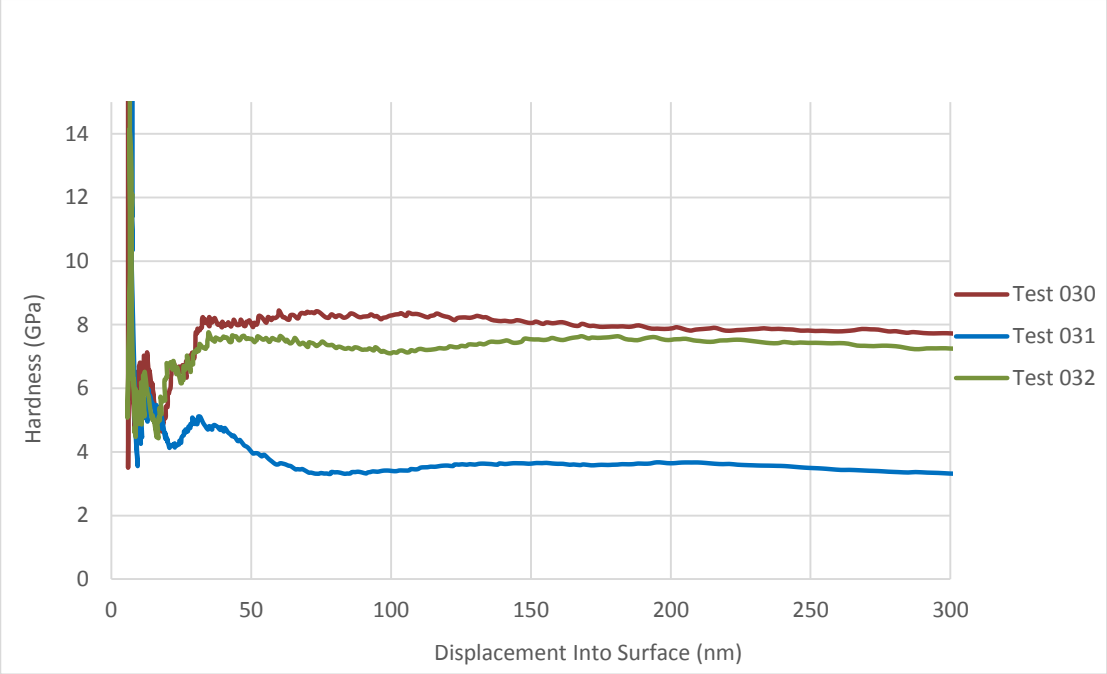


Figure 6.17 Hardness variation with depth as recorded from indents 030 031 and 032 in the region of the unimplanted 1150°C ODS mapped in Figure 6.16. The plots show a predictable hardness variation as the indenter moves from a fine grained region (030) to a large grained region (031) and back to a fine grained region (032).

6.4 Discussion

Evidently the introduction of yttrium oxide causes a significant change in the microstructure of the base alloy producing the bimodal grain size distribution evident in Figure 6.1. The average indentation hardness of each alloy in the implanted and unimplanted condition is summarised in Table 6.1 alongside the hardening caused by yttrium oxide addition and helium implantation.

Oxide dispersion strengthening hardens the base alloy by 2.0 to 4.0GPa but functions effectively in supressing further hardening with helium implantation. By contrast the reference alloys all show significant hardening on implantation, moving to the same average hardness at 500nm in Figure 6.3. This behaviour would indicate that the irradiation hardening overcomes initial differences in hardness resulting from the different processing temperatures.

Unimplanted	Consolidation Temp (°C)	Hardness at 500nm (GPa)	Y_2O_3 Hardening (GPa)
Reference	950	4.6±0.2	-
Reference	1050	3.5±0.3	-
Reference	1150	3.8±0.1	-
ODS	950	8.4±0.8	3.8
ODS	1050	6.8±0.9	3.2
ODS	1150	6.3±1.0	2.5

Implanted	Consolidation Temp (°C)	Hardness at 500nm (GPa)	Helium Hardening (GPa)
Reference	950	5.6±0.1	1.0
Reference	1050	5.3±0.4	1.7
Reference	1150	5.5±0.1	1.6
ODS	950	8.0±1.5	-0.4
ODS	1050	7.2±0.7	0.4
ODS	1150	6.9±0.9	0.6

Table 6.1 Summary of the average indentation hardness data for each consolidation in the implanted and unimplanted conditions including the hardening caused by the introduction of yttrium oxide and helium injection.

The data are relatively free from the sorts of indentation anomalies reported by Hardie in implanted iron chromium systems [145] but in the ODS alloys hardening effects attributed to grain size variation are superimposed upon the wider oxide dispersion hardening of the alloy. However, the spread in the indentation data, shown in Figures 6.5 to 6.8 enables the two effects to be effectively deconvolved.

By correlating the microstructure with particular indentation sites in Figure 6.16 and demonstrating variation in hardness with grain size in the 1150°C ODS alloy, the spread in the averaged hardness data seen in Figures 6.5 to 6.8 can be confidently attributed to the bimodal grain size distribution. The lower hardness values recorded from each ODS sample are therefore likely to provide an indication of the hardness of a large grained microstructure like that seen in the reference alloys subject to particle strengthening alone.

Taking these lower hardness values, presented in Table 6.2, allows the degree of particle and helium hardening to be determined while effectively controlling for grain size. The hardness scales approximately in proportion to the particle density in the unimplanted alloy, while helium produces modest hardening in the 1050 °C and 1150°C consolidation as noted above. On the other hand the softening in the 950 °C now becomes even more apparent.

Unimplanted	Consolidation Temp (°C)	Lower Bound Hardness at 500nm (GPa)	Particle Hardening (GPa)
ODS	950	7.6	3.0
ODS	1050	5.9	2.3
ODS	1150	5.3	1.5

Implanted	Consolidation Temp (°C)	Lower Bound Hardness at 500nm (GPa)	Helium Hardening (GPa)
ODS	950	6.5	-1.1
ODS	1050	6.4	0.6
ODS	1150	6.0	0.7

Table 6.2 Lower bound indentation hardness data for each ODS consolidation in the implanted and unimplanted conditions including the hardening caused by the introduction of a particle dispersion and helium injection.

The change in hardness values recorded in Table 6.2, when combined with the particle sizes and densities taken from the TEM and APT datasets presented in Sections 4.3 and 4.4, provide a means of quantifying the mechanical properties of the oxide particles using a dispersed barrier hardening model presented in Equation 6.1. The model relates the change in the yield stress of the material σ_y to the number density N and size d of an array of obstacles via the obstacle strength α (a constant between zero and one), Burgers vector b, shear modulus μ and the Taylor factor M (shown to be 3.06 for both FCC and BCC lattices by Stoller and Zinckle [168]).

Equation 6.1 $\Delta\sigma_y = \alpha M \mu b \sqrt{Nd}$

Applying this model to the data shown in Table 6.2 necessarily assumes that the indentation hardness can be related to yield stress. In microhardness measurement, empirical relationships exist for ferritic steels, according to which dividing hardness values by 3.03 provides an estimate of the macroscopic yield stress [169] [145]. Making such an assumption, the hardness values recorded in Table 6.2 were used to calculate the oxide particle obstacle strength α for each consolidation temperature as shown in Table 6.3.

Unimplanted	Consolidation Temp (°C)	Particle No Density N (10^{23} m^{-3})	Particle Size d (nm)	Particle α
ODS	950	6.7 ± 0.4	1.0	0.60
ODS	1050	3.8 ± 0.7	1.1	0.60
ODS	1150	2.5 ± 0.3	1.6	0.39

Table 6.3 Dispersed barrier obstacle strength of the oxide particles at each consolidation temperature computed using Equation 6.1

The α term in Equation 6.1 represents the strength of a specific barrier in terms of the Orowan hardening model, with a perfectly hard barrier having an α value of one. Such perfectly hard barriers provide strengthening by dislocation bowing. At lower α values, like those computed for the oxide particles and shown in Table 6.3, hardening is provided by a variety of mechanisms. These include particle shearing, which if repeated, with the movement of successive dislocations, can results in the complete separation of the particle into two parts. This effect could be confirmed using sufficiently high resolution TEM and would conclusively demonstrate the shearability of the particles inferred from these data.

7 Conclusions and Future Work

7.1 Characterisation of a YWT ODS System Under Systematically Varying Consolidation Conditions

An oxide dispersion strengthened Fe-14Cr-0.2Ti-3W-0.25Y_2O_3 alloy and a corresponding Fe-14Cr-0.2Ti-3W reference alloy, were fabricated and consolidated at 1150^{o}C 1050^{o}C and 950^{o}C. This provided a systematically varying population of oxide particles for study with appropriate experimental controls. The main conclusions are as follows:

7.1.1 Conclusions

- The bimodal grain size distribution appears to be unrelated to the particle dispersion. This is contrary to the suggestions made by Hoelzer [14], that local deficiencies in particle forming materials, produce particle free regions liable to coarsen during consolidation. The TEM micrographs showing dense particle dispersions throughout both large and fine grained regions here are also supported by EPMA conducted on the Oxford alloys by Gorley [148].
- The variation in HIP temperature produced a variation in particle size and density in the Fe-14Cr-0.2Ti-3W-0.25Y_2O_3 alloy. The particle dispersion coarsened from 6.7x10^{23}m^{-3} at 950^{o}C to 2.5x10^{23}m^{-3} at 1150^{o}C with a corresponding increase in size from 1.0nm to 1.6nm. The trend was comparable to that seen by Alinger [14] in a Fe-14Cr-0.4Ti-3W-0.25Y_2O_3 system using SANS, but less pronounced.
- Each consolidation showed a remarkable consistency in particle chemistry but no known stable oxide phases were found that corresponded to the recorded $Y_2Ti_3O_5$ stoichiometry. The particles adopted a $YTiO_2$ stoichiometry following vacuum annealing of the 950^{o}C consolidation at 1150^{o}C which is a far more plausible chemistry for a stable oxide and indicative of a transition from metastable cluster to stable oxide particle. These findings are in good agreement with those of Ribis and DeCarlan [76], Hirata [77] and Williams [61].

7.1.2 Future Work

- Confirmation of the uniform distribution of the oxide particle population could be made by atom probe tomography, using site specific focussed ion beam sample preparation methods.
- The complex particle chemistry remains to be fully understood. A variety of characterisation methods are available but all suffer from limitations, particularly when attempting to quantify the oxygen content of the oxide particles, which remains a key issue for understanding the formation mechanisms and behaviour. Combined energy filtered TEM and APT techniques might offer a solution, if sufficient numbers of clusters can be characterised.
- The chromium content of the particles poses similar difficulties. Nevertheless the potential significance of chromium in understanding particle formation and evolution at temperatures is evident from the annealing studies completed here. The difference in cluster chemistry between the four hour 1150^{o}C consolidation and the four hour 1150^{o}C anneal remains to be explained in the context of Ribis and DeCarlan [76] and Williams [61] proposals.

7.2 Helium Implantation of a YWT ODS System with Varying Oxide Particle Number Densities

The oxide dispersion strengthened alloys and the corresponding reference alloys produced at each consolidation temperature were implanted with 2000 appm helium over a depth of 3.0µm at 300^{o}C. TEM samples, prepared using a focussed ion beam system, were used to assess the accumulation of helium gas in the microstructure and to study the effect of the varying particle densities on the bubbles. The main conclusions are as follows:

7.2.1 Conclusions

- Control studies comparing the implanted and unimplanted ODS alloys validated the use of the commonly used Fresnel contrast methods in assaying the helium gas bubble population of an implanted TEM sample.
- The implanted ODS alloy demonstrated a fourfold improvement in gas retention capacity over the reference alloy in the 1150^{o}C consolidation. Both alloys supported bubbles of comparable size, indicating significant helium losses occurred from the reference alloy.
- The bubble and particle densities in the implanted ODS alloys show a strong correlation. This indicates that a direct association exists between the helium bubbles and the oxide particles, and that the gas accumulation process can be directly controlled via the particle dispersion by varying the consolidation temperature of an ODS system.

7.2.2 Future Work

- Accurate quantification of the helium content following implantation would provide experimental verification of the equations of state proposed in Section 1.2. Pressure measurements for individual bubbles, while possible using sensitive electron energy loss (EELS) methods, are subject to very large uncertainties [111].
- Alternatively thermal helium desorption (THD) methods, though usually qualitative might be used quantitatively, if appropriate control samples were available for comparison against experimental quantities. These measurements would have the additional benefit of providing information on the sink strengths associated with the various trapping sites [170].
- No attempts were made to study the effect of implantation temperature here. Ryazanov demonstrated the significant increase in bubble size that occurs with temperature for the same concentration of implanted helium, departing from the predictions of the MLB model. Further implantations at 500^{o}C and 800^{o}C would both provide insight into the limitations of the MLB model and its underlying assumptions.

7.3 Micromechanical Response To Helium Implantation

The oxide dispersion strengthened alloys and the corresponding reference alloys, produced at each consolidation temperature, were indented in the implanted and unimplanted condition. The indentation sites were subsequently checked for anomalies and the local microstructures surveyed using EBSD band contrast mapping. The main conclusions are as follows:

7.3.1 Conclusions

- The addition of yttrium oxide to the base alloy increases the average indentation hardness of the material via a combination of precipitate hardening and grain refinement. The particle hardening can be measured in large grained regions of the microstructure and increases in proportion to particle number density. Based on the dispersed barrier model the particles present imperfectly hard shearable obstacles to dislocation motion.
- The introduction of 2000appm helium produces a new array of such obstacles in the reference alloys, increasing the indentation hardness in each to 5.5GPa. In the ODS the correlation between bubble and particle densities suggests that the colocation of the two features produces no new barriers to dislocation motion. Indeed the helium implantation produces only minimal hardening in the 1150^{o}C and 1050 ^{o}C consolidations.
- The softening apparent in the 950^{o}C consolidation becomes even more apparent when the particle and grain hardening effects are isolated from one another. Complete envelopment of the particles in the helium bubbles may be responsible. This seems particularly likely given that the 1.0nm average particle size in the 950^{o}C consolidation. Envelopment would effectively remove the particles from the system replacing a hard barrier with a bubble giving rise to a significant softening effect.

7.3.2 Future Work

- The shearable character of the particles could be checked using HRTEM. Samples of strained alloys, possibly taken from an indentation site using lift out methods, should contain sheared particles visible when viewed parallel to the glide plane. In-situ straining methods could conceivably be used to capture the shearing process occurring with the passage of dislocation lines through a chosen particle.
- All of the indentation experiments were performed using material in the consolidated state. Another set of experiments, using annealed alloys, would provide some insight into any possible effects the change in particle chemistry seen in the atom probe might have on the hardness. Since any change from a metastable phase to a stable oxide stoichiometry seems likely to alter the crystallographic relationship between particle and matrix, a significant hardening effect might be expected, if it were not for the reduction in particle density associated with thermal aging. Deconvolving these two effects might be achieved by a simple comparison between the 1150^{o}C consolidation and the 1150^{o}C anneal. The particle dispersions in both alloys are of a comparable number density, differing only in their stoichiometry and presumably their structure.
- The potential cause of the softening seen in the implanted 950^{o}C alloy merits further investigation. TEM and HRTEM may provide some insight into the relationship between the small particles produced at this consolidation temperature and the helium bubbles, but the appearance of a fully enveloped oxide particle may be indistinguishable from a free bubble in the ferritic matrix.

8 Appendix A

Mass ranges stored in common range file:

Ion	Mass to Charge Ratio			Ion	Mass to Charge Ratio		
Cr	25.93	-	26.00	TiO	31.94	-	32.00
Cr	24.94	-	25.00	TiO	31.46	-	31.49
Cr	26.44	-	26.49	TiO	30.95	-	31.00
Fe	27.92	-	27.99	TiO	32.45	-	32.49
Fe	26.93	-	26.99	W	90.92	-	91.06
Fe	28.44	-	28.49	W	91.42	-	91.55
Fe	28.95	-	28.99	W	91.93	-	92.06
Y	29.62	-	29.66	W	92.93	-	93.06
YO	52.42	-	52.49	W	60.61	-	60.70
O	15.97	-	16.02	W	60.96	-	61.02
CrO	67.91	-	67.97	W	61.28	-	61.37
CrO	33.94	-	33.99	W	61.95	-	62.03
CrO	34.46	-	34.48	WN	97.92	-	98.05
Si	13.97	-	14.07	WN	98.44	-	98.53
Si	14.48	-	14.50	WN	98.92	-	99.07
Si	14.98	-	15.00	WN	99.92	-	100.06
CrN	65.91	-	66.00	Cr	51.91	-	52.00
CrN	32.96	-	32.99	Cr	52.91	-	52.98
CrN	33.46	-	33.48	Cr	53.91	-	53.97
CrN	66.92	-	66.97	Fe	55.85	-	56.05
FeO	71.91	-	71.97	TiO	62.90	-	63.00
Mn	27.44	-	27.50	TiO	63.91	-	64.00
C	11.99	-	12.01	TiO	64.90	-	64.99
Ti	23.96	-	23.99	C	5.99	-	6.02

9 Appendix B

Mass to charge ratio table used in tailoring range file and identifying overlaps

	M			C			N			O			C_2			N_2			O_2		
	1+	2+	3+	12	12	12	14	14	14	16	16	16	24	24	24	28	28	28	32	32	32
Ti	46.00	23.00	15.33	58.00	29.00	19.33	60.00	30.00	20.00	62.00	31.00	20.67	70.00	35.00	23.33	74.00	37.00	24.67	78.00	39.00	26.00
Ti	47.00	23.50	15.67	59.00	29.50	19.67	61.00	30.50	20.33	63.00	31.50	21.00	71.00	35.50	23.67	75.00	37.50	25.00	79.00	39.50	26.33
Ti	48.00	24.00	16.00	60.00	30.00	20.00	62.00	31.00	20.67	64.00	32.00	21.33	72.00	36.00	24.00	76.00	38.00	25.33	80.00	40.00	26.67
Ti	49.00	24.50	16.33	61.00	30.50	20.33	63.00	31.50	21.00	65.00	32.50	21.67	73.00	36.50	24.33	77.00	38.50	25.67	81.00	40.50	27.00
Ti	50.00	25.00	16.67	62.00	31.00	20.67	64.00	32.00	21.33	66.00	33.00	22.00	74.00	37.00	24.67	78.00	39.00	26.00	82.00	41.00	27.33
Cr_2	104.00	52.00	34.67	116.00	58.00	38.67	118.00	59.00	39.33	120.00	60.00	40.00	128.00	64.00	42.67	132.00	66.00	44.00	136.00	68.00	45.33
Cr	52.00	26.00	17.33	64.00	32.00	21.33	66.00	33.00	22.00	68.00	34.00	22.67	76.00	38.00	25.33	80.00	40.00	26.67	84.00	42.00	28.00
Cr	53.00	26.50	17.67	65.00	32.50	21.67	67.00	33.50	22.33	69.00	34.50	23.00	77.00	38.50	25.67	81.00	40.50	27.00	85.00	42.50	28.33
Mn	55.00	27.50	18.33	67.00	33.50	22.33	69.00	34.50	23.00	71.00	35.50	23.67	79.00	39.50	26.33	83.00	41.50	27.67	87.00	43.50	29.00
Fe	54.00	27.00	18.00	66.00	33.00	22.00	68.00	34.00	22.67	70.00	35.00	23.33	78.00	39.00	26.00	82.00	41.00	27.33	86.00	43.00	28.67
Fe	56.00	28.00	18.67	68.00	34.00	22.67	70.00	35.00	23.33	72.00	36.00	24.00	80.00	40.00	26.67	84.00	42.00	28.00	88.00	44.00	29.33
Fe	57.00	28.50	19.00	69.00	34.50	23.00	71.00	35.50	23.67	73.00	36.50	24.33	81.00	40.50	27.00	85.00	42.50	28.33	89.00	44.50	29.67
Fe	58.00	29.00	19.33	70.00	35.00	23.33	72.00	36.00	24.00	74.00	37.00	24.67	82.00	41.00	27.33	86.00	43.00	28.67	90.00	45.00	30.00
Fe_2	112.00	56.00	37.33	124.00	62.00	41.33	126.00	63.00	42.00	128.00	64.00	42.67	136.00	68.00	45.33	140.00	70.00	46.67	144.00	72.00	48.00
Y	89.00	44.50	29.67	101.00	50.50	33.67	103.00	51.50	34.33	105.00	52.50	35.00	113.00	56.50	37.67	117.00	58.50	39.00	121.00	60.50	40.33
Y_2	178.00	89.00	59.33	190.00	95.00	63.33	192.00	96.00	64.00	194.00	97.00	64.67	202.00	101.00	67.33	206.00	103.00	68.67	210.00	105.00	70.00
W	182.00	91.00	60.67	194.00	97.00	64.67	196.00	98.00	65.33	198.00	99.00	66.00	206.00	103.00	68.67	210.00	105.00	70.00	214.00	107.00	71.33
W	183.00	91.50	61.00	195.00	97.50	65.00	197.00	98.50	65.67	199.00	99.50	66.33	207.00	103.50	69.00	211.00	105.50	70.33	215.00	107.50	71.67
W	184.00	92.00	61.33	196.00	98.00	65.33	198.00	99.00	66.00	200.00	100.00	66.67	208.00	104.00	69.33	212.00	106.00	70.67	216.00	108.00	72.00
W	186.00	93.00	62.00	198.00	99.00	66.00	200.00	100.00	66.67	202.00	101.00	67.33	210.00	105.00	70.00	214.00	107.00	71.33	218.00	109.00	72.67

1 D. M. Duffy 'Fusion power: a challenge for materials science' *Phil Trans Roy Soc A* Volume 368 Page 3315 to 3328 (2010)

2 J. Boutard, A. Alamo, R. Lindau and M. Rieth 'Fissile core and Tritium-Breeding Blanket: structural materials and their requirements' *C. R. Physique* Volume 9 Page 287 to 302 (2008)

3 N. Baluc, K. Abe, J.L. Boutard, V.M. Chernov, E. Diegele, S. Jitsukawa, A. Kimura, R.L. Klueh, A. Kohyama, R.J. Kurtz, R. Lässer, H. Matsui, A. Möslang, T. Muroga, G.R. Odette, M.Q. Tran, B. van der Schaaf, Y. Wu, J. Yu and S.J. Zinkle 'Status of R&D activities on materials for fusion power reactors' *Nuclear Fusion* Volume 47 Page 696 to 717 (2007)

4 B. Wadsworth 'Neutron interactions in matter and neutron damage' *University Of York Fusion Materials Workshop* (2010)

5 K. Ehrlich 'The development of structural materials for fusion reactors' *Philosophical Transactions of the Royal Society A* Volume 357 Page 595 to 623 (1999)

6 D. Stork 'Materials for DEMO' *University Of York Fusion Materials Workshop* (2010)

7 S, J, Zinkle and L. L. Snead 'Designing Radiation Resistance in Materials for Fusion Energy' *Annual Review of Materials Research* Volume 44 Pages 241 to 267 (2014)

8 G. S. Was 'Fundamentals of Radiation Materials Science' Springer (2007)

9 L. K. Mansur 'Mechanisms and kinetics of radiation effects in metals and alloys' *Kinetics of Nonhomogeneous Processes* Page 377 to 463 (1987)

10 L. K. Mansur 'Theory and experimental background on dimensional changes in irradiated alloys' *Journal of Nuclear Materials Volume* 216 Pages 97 to 123 (1994)

11 J. N. Al Hajji N. M. Ghoniem 'Nucleation of grain boundary cavities under the combined influence of helium and applied stress' *Acta Metall* Volume 35 Page 1067 to 1075 (1987)

12 G. Dobmann S.N. Korshunov, M. Kroening, Yu.V. Martynenko, I.D. Skorlupkin and A.S. Surkov 'Helium and radiation defect accumulation in metals under stress' V*acuum* Volume 82 Pages 856 to 866 (2008)

13 G. R. Odette 'On mechanisms controlling swelling in ferritic and martensitic alloys' *Journal of Nuclear Materials Volume* 155 Pages 921 to 927 (1988)

14 G. R. Odette, M. J. Alinger and B. D. Wirth 'Recent development in irradiation resistant steels' *Annual Review of Materials Research* Volume 38 Page 471 to 503 (2008)

15 R. E. Stoller and G. R. Odette 'Analytical solutions for helium bubble and critical radius parameters using a hard sphere equation of state' *Journal of Nuclear Materials Volume* 131 Pages 118 to 125 (1985)

16 R. E. Stoller and G. R. Odette 'A comparison of the relative importance of helium and vacancy accumulation in void nucleation' *Radiation induced changes in microstructure 13 international symposium* Page 358 to 370 (1987)

17 G. R. Odette and D. T. Hoelzer 'Irradiation tolerant nanostructured ferritic alloys: Transforming Helium from a liability to an asset.' *Materials for Nuclear Power* Page 84 to 92 (2010)

18 I. R. Brearley and D. A. MacInnes 'An improved equation of state for inert gases at high pressures' *Journal of Nuclear Materials* Volume 95 Pages 239 to 252 (1980)

19 R. L. Mills, D. H. Liebenberg and J. C. Bronson 'Equation of state and melting properties of ^{4}He from measurements to 20kbar' *Physical Review B* Volume 21 Number 11 Pages 5137 to 5148 (1980)

20 S. E. Donnelly 'The density and pressure of helium in bubbles in implanted metals: A critical review' *Radiation Effects* Volume 90 Pages 1 to 47 (1985)

21 D. A. Young, A. K. McMahan and M. Ross 'Equation of state and melting curve of helium to very high pressure' *Physical Review B* Volume 24 Number 9 Page 5119 to 5127 (1981)

22 H. Trinkhaus 'Proceeding of the International Conference on Helium in Metals' *Radiation Effects* Volume 78 Page 189 (1983)

23 W. G. Wolfer, B. B. Glasgow M. F. Wehner and H. Trinkaus 'Helium Equation of state for small cavities' *Journal Of Nuclear Materials* Volume 122 Pages 565 to 570 (1984)

24 G. R. Odette 'Modelling microstructural evolution in fusion reactor environments' *Journal of Nuclear Materials* Volume 133 Pages 127 to 133 (1985)

25 J. J. Sniegowski and W. G. Wolfer 'On the physical basis for the swelling resistance of ferritic steels' *Fusion Technology Institute* (1983)

26 H. J. Bergmann, V. Levy, C. Brown, R. J. C. Roger and K. Ehrlich 'Cladding and wrapper material development for fast breeder reactors for high performance' *Proc. Int. Conf. on Fast Reactors and Related Fuel Cycles* Volume 17 (1991)

27 L. K. Mansur 'Mechanisms of swelling suppression in cold-worked phosphorous modified Fe-Ni-Cr alloys' *Philos Mag* Volume 61 Page 733 to 749

28 P J Maziasz 'Overview of microstructural evolution in neutron irradiated austenitic stainless steels' *Journal Of Nuclear Materials* Volume 205 Page 118 to 145 (1993)

29 S. Ukai and T. Uwaba 'Swelling rate verses swelling correlation in 20% cold-worked 316 stainless steels' *Journal Of Nuclear Materials* Volume 317 Page 93 to 101 (1993)

30 G. R. Odette and R. E. Stoller 'A composite model of microstructural evolution in austenitic stainless steel under fast neutron irradiation' *Int Symp Influ Irradiat Mater Prop 13th* Pages 371 to 392 (1987)

31 R. Kasada A. Kimura, R. Kasada, K. Morishita, R. Sugano, A. Hasegawa, K. Abe, T. Yamamoto, H. Matsui, N. Yoshida, B.D. Wirth and T.D. Rubia 'High resistance to helium embrittlement in reduced activation martensitic steels' Journal Of Nuclear Materials Volume 307 Page 521 to 526 (2002)

32 N. Baluc, D.S. Gelles, S. Jitsukawa, A. Kimura, R.L. Klueh, G.R. Odette, B. van der Schaaf and Jinnan Yu 'Status of reduced activation ferritic martensitic steel development' *Journal of Nuclear Materials* Volume 367 Pages 33 to 41 (2007)

33 D. Maisonnier, I Cook, S. Pierre, B. Lorenzo, P. Luigi, G. Luciano, N. Prachai and P. Aldo 'DEMO and fusion power plant conceptual design studies in Europe' *Fusion Engineering Design* Volume 81 Page 1123 to 1130 920060

34 K. Tobita, S. Nishio, M. Enoeda, M. Sato, T. Isono, S. Sakurai, H. Nakamura, S. Sato, S. Suzuki, M. Ando, K. Ezato, T. Hayashi, T. Hayashi, T. Hirose, T. Inoue, Y. Kawamura, N. Koizumi, Y. Kudo, R. Kurihara, T. Kuroda, M. Matsukawa 'Design study of fusion DEMO plant at JAERI' *Fusion Engineering and Design* Volume 81 Page 1151 to 1158 (2006)

35 M.I. Solonin, V.M. Chernov, V.A. Gorokhov, A.G. Ioltukhovskiy, A.K. Shikov, A.I. Blokhin 'Present status and future prospect of the Russian program for fusion low activation materials' *Journal of Nuclear Materials* Volume 283 Page 1468 to 1472 (2000)

36 E. Lucon R. Chaouadi and M. Decréton 'Mechanical properties of European reference RAFM steel (EUROFER 97) before and after irradiation at 300^{o}C' *Journal Of Nuclear Materials* Volume 329 Pages 1078 to 1082 (2004)

37 R. L. Klueh and A. T, Nelson 'Ferritic/martensitic steels for next generation reactors' *Journal Of Nuclear Materials* Volume 371 Pages 37 to 52 (2007)

38 R. L. Klueh 'New nanoparticle strengthened ferritic martensitic steels by conventional thermal mechanical treatment' *Journal Of Nuclear Materials* Volume 367 Pages 48 to 53 (2007)

39 A. Möslang, K. Ehrlich, T.E. Shannon, M.J. Rennich, R.A. Jameson, T. Kondo, H. Katsuta, H. Maekawa, M. Martone and V. Teplyakov 'Suitability and feasibility of the international fusion materials irradiation facility (IFMIF) for fusion materials studies' *Nuclear Fusion* Volume 40 Page 619 to 627 (2000)

40 S. Ishino 'Implications of fundamental radiation damage studies in the research and development of materials for a fusion reactor' *Journal of Nuclear Materials* Volume 239 Page 24 to 33 (1996)

41 N. Hashimoto, R. L. Klueh and K. Shiba 'Pros and cons of nickel and boron doping to study helium effects in ferritic martensitic steels' *Journal of Nuclear Materials* Volume 307 Pages 222 to228 (2002)

42 T. Yamamoto, G.R. Odette, P. Miao, D.T. Hoelzer, J. Bentley, N. Hashimoto, H. Tanigawa and R.J. Kurtz 'The transport and fate of helium in nanostructured ferritic alloys at fusion relevant He/dpa ratios and dpa rates' *Journal of Nuclear Materials* Volume 367 Pages 399 to 410 (2007)

43 D. Jimenez-Rey, F Mota and R. Vita 'Simulation for evaluation of the multi ion irradiation laboratory of Technofusion Facility and its relevance for fusion application' *Journal of Nuclear Materials* Accepted for Publication (2011)

44 N. Marochov and P. J. Goodhew 'A comparison of the growth of helium and neon bubbles in nickel' *Journal of Nuclear Materials* Volume 158 Pages 81 to 86 (1988)

45 C. Zhang, J. S. Jang, Y. Yang, Y. Song, Y. Sun, H. D. Cho and Y Jin 'A study of the suppression of high temperature helium embrittlement in an oxide particle dispersion strengthened alloy' *Chinese Science Bulletin* Volume 53 Page 3416 to 3421 (2008)

46 M. Klimenkov 'Quantitative measurement of argon inside of nano sized bubbles in ODS steels' *Journal of Nuclear Materials* Volume 411 Pages 160 to 162 (2011)

47 J. J. Fisher 'Dispersion strengthened ferritic alloy for use in liquid metal fast breeder reactors' US Patent Number 4075010 (1978)

48 R. Kasada, N. Toda, K. Yutani, H. S. Cho, H. Kishimoto and A. Kimura 'Pre and post deformation microstructures of oxide dispersion strengthened ferritic steels' *Journal of Nuclear Materials* Volume 367 Pages 222 to 228 (2007)

49 M. K. Miller 'Nanometer scale precipitation in ferritic MA/ODS alloy MA957' *Journal of Nuclear Materials* Volume 329 Pages 338 to 341 (2004)

50 R.L. Klueh, J.P. Shingledecker, R.W. Swindeman and D.T. Hoelzer 'Oxide dispersion strengthened steels: A comparison of some commercial and experimental alloys' *Journal of Nuclear Materials* Volume 341 Pages 103 to 114 (2005)

51 H. Zhang 'Processing of ODS alloys' Presentation to MFFP University of Oxford (2011)

52 B. Fournier 'Mechanical behavior and damage of oxide dispersion strengthened ferritic steels' Presentation to MFFP University of Oxford (2011)

53 C. Capdevila and H. K. D. H. Bhadeshia 'Manufacturing and microstructural evolution of mechanically alloyed oxide dispersion strengthened superalloys' Advanced Engineering Materials Volume 3 Page 647 to 656 (2001)

54 N. J. Cunningham 'Determining Processing Variable Effects on Nano-Particle Distribution in Nanostructured Ferritic Alloys' Thesis Submitted to UC Santa Barbara from MEng Mechanical Engineering (2008)

55 C. Suryanarayana, E. Ivanov and V. V. Boldyrev 'The science and technology of mechanical alloying' *Materials Science and Engineering* Volume 304 Pages 151 to 158 (2001)

56 C. Suryanarayana 'Mechanical alloying and milling' *Progress in Materials Science* Volume 46 Page 1 to 184 (2001)

57 S. Yamashita, S. Watanabe, S. Ohnuki, H. Takahashi, N. Akasaka, S. Ukai 'Effect of mechanical alloying parameters on irradiation damage on oxide dispersion strengthened ferritic steels' *Journal Of Nuclear Materials* Volume 283 Page 647 to 651 (2000)

58 M. Alinger, G. R. Odette and D. T. Hoelzer 'The development and stability of Y - Ti - O nanoclusters in mechanically alloyed Fe - Cr based ferritic alloys' *Journal of Nuclear Materials* Volume 329 Page 382 to 386 (2004)

59 S. Ukai and M. Fujiwara 'Perspectives of ODS alloys application in nuclear environments' *Journal of Nuclear Materials* Volume 307 Page 749 to 757 (2002)

60 S. Ukai, S. Ohtsuka and M. Fujiwara 'Nano-mesoscopic structure control in 9Cr-ODS ferritic steels' *Energy Materials* Volume 2 Page 26 to 35 (2007)

61 C Williams 'Atomic scale characterisation of oxide dispersion strengthened steels for fusion applications' Doctoral Thesis university of Oxford (2011)

62 S. Ukai, M. Harada, H. Okada, M. Inoue, S. Nomura, S. Shikakura, K. Asabe, T. Nishida, M. Fujiwara 'Alloy design of oxide dispersion strengthened ferritic steel for long life FBR core materials' *Journal Of Nuclear Materials* Volume 204 Page 65 to 73 (1993)

63 D. J. Larson, P. J. Maziasz, I. S. Kim and K. Myahara 'Three dimensional atom probe observation of nanoscale titanium oxygen clustering in an oxide dispersion strengthened Fe-12Cr-3W-0.4Ti +Y2O3 ferritic alloy' *Scripta Materialia* Volume 44 Pages 359 to 364 (2001)

64 M. Alinger 'On the formation and stability of nanometre scale precipitates in ferritic alloys during processing and high temperature service' Doctoral Thesis UC Santa Barbara (2004)

65 M. Miller, K. F. Russell and D. T. Hoelzer 'Characterization of precipitates in MA/ODS ferritic alloys' *Journal Of Nuclear Materials* Volume 351 Page 261 to 268 (2006)

66 Correspondence with G. R. Odette of the Department of Mechanical Engineering UC Santa Barbara (2011)

67 E. Marquis 'Core/shell structures of oxide rich nanofeatures in oxide dispersion strengthened Fe-Cr alloys' *Applied Physics Letters* Volume 93 Number 181904 (2008)

68 C. Hatzoglou, B. Radiguey and P. Pareige 'Experimental artifacts occuring during atom probe tomography analysis of ODS steels' *20th Workshop on Fe Cr alloys* (2012)

69 S.V. Rogozhkin, A.A. Aleev, A.G. Zaluzhnyi, A.A. Nikitin, N.A. Iskandarov, P. Vladimirov, R. Lindau and A. Möslang 'Atom probe characterization of nano scaled features in irradiated ODS EUROFER steel' *Journal Of Nuclear Materials* Volume 409 Page 94 to 99 (2011)

70 M. P. Moody, B. Gault, L. T. Stephenson, R. K.W. Marceau, R. C. Powles, A. V. Ceguerra, A. J. Breen and S. P. Ringer 'Lattice rectification in atom probe

tomography: toward true three-dimensional atomic microscopy' *Microscopy and Microanalysis* Volume 17 Page 226 to 239 (2011)

71 C. Williams, E. A. Marquis, A. Cerezo and G. D. W. Smith 'Nanoscale characterization of ODS EUROFER 97 steel: An atom probe tomography study' *Journal of Nuclear Materials* Volume 400 Page 37 to 45 (2010)

72 K. Oka, S. Ohnuki, S. Yamashita, N. Akasaka, S. Ohtsuka and H. Tanigawa 'Structure of nano-size oxides in ODS steels and its stability under electron irradiation' *Materials Transactions* Volume 48 Pages 2563 to 2566 (2007)

73 C. Williams, P. Unifantowicz, N. Baluc, G. D.W. Smith and E. A. Marquis 'The formation and evolution of oxide particles in oxide dispersion strengthened ferritic steels during processing' *Acta Materialia* Volume 61 Page 2219 to 2235 (2013)

74 C. Williams, D. Haley, E. A. Marquis, G. D. W. Smith and M. Moody 'Defining clusters in APT reconstructions of ODS steels' *Ultramicroscopy* Volume 132 Pages 271 to 278 (2013)

75 C. Williams, E. A. Marquis and G. D. W. Smith 'Quantifying the composition of yttrium and oxygen rich nanoparticles in oxide dispersion strengthened steels' *Ultramicroscopy* Volume 125 Pages 10 to 17 (2013)

76 J. Ribis and Y. de Carlan 'Interfacial strained structure and orientation relationships of the nanosized oxide particles deduced from elasticity-driven morphology in oxide dispersion strengthened materials' *Acta Materialia* Volume 60 Page 238 to 252 (2012)

77 A. Hirata, T. Fujita, Y. R. Wen, J. H. Schneibel, C. T. Liu and M. W. Chen 'Atomic structure of nanocluster in oxide dispersion strengthened steels' Nature Materials volume 10 Pages 922 to 926 (2011)

78 M. Klimenkov, R. Lindau and A. Moslang 'New insight into the structure of ODS particles in the ODS EUROFER alloy' *Journal Of Nuclear Materials* Volume 386 Page 553 to 556 (2009)

79 S. Ukai, S. Ohtsuka, M Fujiwara, T Kaito and T. Narita 'Nanostructure control in ODS martensitic steels by means of selecting titanium and oxygen contents' *Journal of Physics and Chemistry of Solids* Volume 66 Page 571 to 575 (2004)

80 L. Hsiung, M. Fluss, S. Tumey, J. Kuntz, B. El-Dasher, M. Wall, B. Choi, A. Kimura, F. Willaime, Y. Serruys 'HRTEM study of oxide nanoparticles in K3-ODS ferritic steel developed for radiation tolerance' *Journal Of Nuclear Materials* Volume 409 Page 72 to 79 (2011)

81 S. Lozano-Perez, V. de Castro Bernal and R. J. Nicholls ‘Achieving subnanometre particle mapping with energy-filtered TEM’ Ultramicroscopy Volume 109 Page 1217 to 1228 (2009)

82 P.J. Thomas ‘An introduction to energy filtered transmission electron microscopy’ Topics in Catalysis Volume 21 Page 109 to 138 (2002)

83 A.G. Certain, K.G. Field, T.R. Allen, M.K. Miller, J. Bentley, J.T. Busby 'Response of nanoclusters in a 9Cr ODS steel to 1dpa 525^{o}C proton irradiation' *Journal of Nuclear Materials* Volume 407 Pages 2 to 9 (2010)

84 A. G. Certain S. Kuchibhatla, V. Shutthanandan, D.T. Hoelzer and T.R. Allen ‘Radiation stability of nanoclusters in nano-structured oxide dispersion strengthened (ODS) steels’ *Journal of Nuclear Materials* Volume 434 Pages 311 to 321 (2013)

85 J. Bentley and D. T. Hoelzer 'EFTEM and spectrum imaging of mechanically alloyed oxide dispersion strengthened 12YWT and 14YWT ferritic steels' *Microscopy and Microanalysis* Volume 10 Page 662 to 663 (2004)

86 M. C. Salstron 'A database and constitutive model for the static and creep strength of MA 957 from room temperature to 1000^{o}C' *Transactions ANS* (2008)

87 D. T. Hoelzer J. Bentley, M.A. Sokolov, M.K. Miller, G.R. Odette and M.J. Alinger' Influence of particle dispersions on the high temperature strength of ferritic alloys' *Journal of Nuclear Materials* Volume 367 Page 166 to 172 (2007)

88 M. Alinger et al 'Toughness and tensile fracture properties of MA 957: implications for the development of nanocomposite ferritic alloys' *Journal of Nuclear Materials* Volume 307 Page 484 to 489 (2002)

89 M. Klimiankou, R, Lindau and A. Moslang 'Direct correlation between morphology of $(FeCr)_{23}C_6$ precipitates and impact behaviour of ODS steels' *Journal of Nuclear Materials* Volume 367 Page 173 to 178 (2007)

90 M. A. Pouchon, J. Chen, R. Ghisleni, J. Michler and W. Hoffelner ’Characterization of Irradiation Damage of Ferritic ODS Alloys with Advanced Micro-Sample Methods’ *Experimental Mechanics* Volume 50 Pages 79 to 84 (2010)

91 P. Hosemann, E. Stergar, L. Peng, Y. Dai, S.A. Maloy, M.A. Pouchon, K. Shiba, D. Hamaguchi, H. Leitner ‘Macro and microscale mechanical testing and local electrode atom probe measurements of STIP irradiated F82H, Fe-8Cr ODS and Fe-8Cr-2W ODS’ *Journal of Nuclear Materials* Volume 417 Page 274 to 278 (2011)

92 C. D. Hardie and S. G. Roberts 'Nanoindentation of model Fe-Cr alloys with self-ion irradiation' *Journal of Nuclear Materials* Volume 433 Pages 174 to 179 (2013)

93 W. D. Nix and H. Gao 'Indentation size effects in crystalline materials: A law for strain gradient plasticity' Journal of Mechanics and Physics of Solids Volume 46 Page 411 to 425 (1998)

94 Y. Takayama, R. Kasada, Y. Sakamoto, K. Yabuuchi, A. Kimura, M. Ando, D. Hamaguchi, H. Tanigawa 'Nanoindentation hardness and its extrapolation to bulk-equivalent hardness of F82H steels after single and dual ion beam irradiation' *Journal of Nuclear Materials* Article in Press (2013)

95 W. C. Oliver and G. M. Pharr 'Measurement of hardness and elastic modulus by instrumented indentation: Advances in understanding and refinements to methodology' *Journal of Materials Research* Volume 19 Page 3 to 20 (2003)

96 C. Shin, S. Lim, H. Jin, P. Hosemann and J. Kwon 'Development and testing of microcompression for post irradiation characterisation of ODS steels' *Journal of Nuclear Materials* Volume 444 Pages 43 to 48 (2014)

97 M. K. Miller, D. T. Hoelzer, E. A. Kenik and K. F. Russell 'Stability of ferritic MA/ODS alloys at high temperature' Intermetallics Volume 13 Page 387 to 392 (2007)

98 P. Miao, G. R. Odette, T. Yamamoto, M. Alinger and D. Klingensmith 'Thermal stability of nanostructured ferritic alloy' *Journal of Nuclear Materials* Volume 377 Page 59 to 64 (2008)

99 A. F. Smith and R. Hales 'Chromium depletion from stainless steels during vacuum annealing' Materials and Corrosion Volume 28 Pages 405 to 409 (1976)

100 J. S. Lee, C. H. jang, I. S. Kim and A. Kimura 'Embrittlement and hardening during thermal aging of high Cr oxide dispersion strengthened alloys' *Journal of Nuclear Materials* Volume 367 Page 229 to 233 (2007)

101 S. Yamashita, N. Akasaka, S. Ukai and S. Ohnuki 'Microstructural development of a heavily neutron irradiated ODS ferritic steel (MA 957) at elevated temperature' *Journal of Nuclear Materials* Volume 367 Page 202 to 207 (2007)

102 H. Kishimoto, K. Yutani, R. Kasada, O. Hashitomi and A. Kimura 'Heavy ion irradiation effects on the morphology of complex oxide particles in oxide dispersion strengthened ferritic steels' Journal of Nuclear Materials Volume 367 Page 179 to 184 (2007)

103 Monnet P. Dubuisson, Y. Serruys, M.O. Ruault, O. Kaı¨tasov, B. Jouffrey 'Microstructural investigation of the stability under irradiation of oxide dispersion strengthened ferritic steels' *Journal of Nuclear Materials* Volume 335 Page 311 to 321 (2004)

104 D. S. Gelles 'Microstructural examination of commercial ferritic alloys at 200 dpa' *Journal of Nuclear Materials* Volume 233 Page 293 to 298 (1996)

105 J. Saito, T. Suda, S. Yamashita, S. Ohnuki, H. Takahashi, N. Akasaka, M. Nishida, and S. Ukai 'Void formation and microstructural development in oxide dispersion strengthened ferritic steels during electron irradiation' *Journal of Nuclear Materials* Volume 258 Page 1264 to 1268 (1998)

106 H. S. Cho, R. Kasada and A. Kimura 'Effects of neutron irradiation on the tensile properties of high Cr oxide dispersion strengthened ferritic steels' *Journal of Nuclear Materials* Volume 367 Page 239 to 243 (2007)

107 A. Alamo, J.L. Bertin, V.K. Shamardin and P. Wident 'Mechanical properties of 9Cr martensitic steels and ODS - FeCr alloys after neutron irradiation at 325oC up to 42 dpa.' *Journal of Nuclear Materials* Volume 367 Page 54 to 59 (2007)

108 M. B. Toloczko, D. S. Gelles, F. A. Garner, R. J. Kurtz and K. Abe 'Irradiation creep and swelling from 400 to 600^{o}C of the oxide dispersion strengthened ferritic alloy MA 957' *Journal of Nuclear Materials* Volume 329 Pages 352 to 355 (2004)

109 T. Yamamoto, G. R. Odette, H. Kishimoto, J Rensman and P. miao 'On the effects of irradiation on the yield stress changes and hardening and non-hardening embrittlement of 8 Cr tempered martensitic steels: compilation and analysis of existing data' *Journal of Nuclear Materials* Volume 356 Pages 27 to 49 (2006)

110 A. Hasegawa, M. Ejiri, S. Nogami, M. Ishiga, R. Kasada, A. Kimura, K. Abe, S. Jitsukawa 'Effects of helium on ductile brittle transition behaviour of reduced activation ferritic steels after high concentration helium implantation at high temperature' *Journal of Nuclear Materials* Volume 386 Pages 241 to 244 (2009)

111 S. Frechard M. Walls, M. Kociak, J.P. Chevalier, J. Henry, D. Gorse 'Study by EELS of helium bubbles in a martensitic steel' *Journal of Nuclear Materials* Volume 393 Pages 102 to 107 (2009)

112 H. Kishimoto, K. Yutani, R. Kasada, A. Kimura 'Helium cavity formation research on oxide dispersion strengthened (ODS) ferritic steels utilizing dual ion irradiation facilities' Fusion Engineering and Design Volume 81 Page 1045 to 1049 (2006)

113 K. Yatani H. Kishimoto, R. Kasada, A. Kimura 'Evaluation of Helium effects on the swelling behavior of oxide dispersion strengthened ferritic steels under ion irradiation' *Journal of Nuclear Materials* Volume 367 Pages 423 to 427 (2007)

114 G. R. Odette, P. Miao, D. J. Edwards, T. Yamamoto, R. J. Kurtz, H. Tanigawa 'Helium transport fate and management in nanostructured ferritic alloys: In situ helium implanter studies' *Journal of Nuclear Materials* (2011)

115 R. J. Kurtz, G. R. Odette, P. Miao, T. Yamamoto, D. S. Gelles and B. M. Oliver 'The transport and fate of helium in martensitic steels at fusion relevant He/dpa ratios and dpa rates' *Journal of Nuclear Materials* Volume 367 Pages 417 to 422 (2007)

116 G. R. Odette, P. Miao, D. J. Edwards, T. Yamamoto, R. J. Kurtz and H. Tanigawa 'A comparison of cavity formation in neutron irradiated nanostructured ferritic alloys and tempered martensitic steels at high He/dpa ratios' *Transactions ANS* Volume 98 Pages 41 to 43 (2008)

117 T. Yamamoto G. R. Odette, P. Miao, D. J. Edwards, R. J. Kurtz 'Helium effects on microstructural evolution in tempered martensitic steels: In situ helium implanter studies in HFIR' *Journal of Nuclear Materials* Volume 386 Pages 338 to 341 (2009)

118 P. D. Edmondson, C. M. Parish, Y. Zhang, A. Hallen and M. K. Miller 'Helium entrapment in a nanostructured ferritic alloy' *Scripta Materialia* Volume 65 Page 731 to 734 (2011)

119 P. D. Edmondson C. M. Parish, Y. Zhang, A. Hallen and M. K. Miller'Helium bubble distributions in a nanostructured ferritic alloy' *Journal of Nuclear Materials* Volume 434 Page 210 to 216 (2013)

120 A. I. Ryazanov O.K. Chugunov, S.M. Ivanov, S.T. Latushkin, R. Lindau, A. Möslang, A.A. Nikitina, K.E. Prikhodko, E.V. Semenov, V.N. Unezhev, P.V. Vladimirov 'Tensile properties and microstructure of helium implanted EUROFER ODS' ' *Journal of Nuclear Materials* Volume 442 Pages 153 to 157 (2013)

121 J. Henry, X. Averty, Y. Dai, J. P. Pizzanelli and J. J. Espinas 'Tensile properties of an ODS 14Cr alloy irradiated in a spallation environment ' *Journal of Nuclear Materials* Conference Publication (2008)

122 T. Yamamoto G. R. Odette, H. Kishimoto, J. Rensman and P. Miao 'On the effects of irradiation and helium on the yield stress changes and hardening and non-hardening embrittlement of 8Cr tempered martensistic steels: compilation and analysis of existing data' *Transactions ANS* (2008)

123 J.F. Ziegler, M.D. Ziegler and J.P. Biersack 'SRIM – The stopping and range of ions in matter' *Nuclear Instruments and Methods in Physics Research B: Beam Interactions with Materials and Atoms* Volume 268 Pages 1818 to 1823 (2010)

124 International Standard practice for measurement of mechanical properties during charged particle irradiations ESTM E821 – 96 (2009)

125 H. Maeda 'Accurate bond length determination by EXAFS method' *Journal of the physical society of Japan* Volume 56 Pages 2777 to 2787 (1987)

126 M. K. Miller and Y. Zhang 'Fabrication and characterisation of APT specimens from high dose heavy ion irradiated materials' *Ultramicroscopy* Volume 111 Pages 672 to 675 (2011)

127 V. Sabelova, V. Kršjak, J. Kuriplach, M. Petriska, V. Slugeň, J. Šimeg Veterníková 'Characterisation of helium implanted Fe-Cr alloys by means of positron annihilation methods' *Journal of Nuclear Materials* Accepted Manuscript (2013)

128 M. K. Miller and R. G. Forbes 'Atom probe tomography' *Materials Characterisation* Volume 60 Pages 461 to 469 (2009)

129 G. L. Kellogg and T. T. Tsong 'Pulsed laser induced atom probe mass spectrometry' *Ultramicroscopy* Volume 5 Pages 259 to 260 (1980)

130 B. Gault, M. Moody, J. Cairney and S. Ringer 'Atom Probe Microscopy' *Springer Series in Materials* Science (2012)

131 K. Oh-Ishi, C. L. Mendis, T. Ohkubo and K. Hono 'Effect of laser power and specimen temperature on atom probe analysis of magnesium alloys' *Ultramicroscopy* Volume 111 Pages 715 to 718 (1980)

132 D. Hidson, G. D. W. Smith and B. Gault 'Optimisation of mass ranging for atom probe microanalysis and application to the corrosion process in Zr alloys' *Ultramicroscopy* Volume 111 Pages 480 to 486 (2011)

133 P. Bas, A. Bostel, B. Deconihout and D. Blavette 'A general protocol for the reconstruction of 3D atom probe data' Applied Surface Science Pages Volume 87 Pages 298 to 304 (1995)

134 B. Gault, M. Moody, F. Geuser, G. Tsafnat, A. Fontaine, L. T. Stephenson, D. Haley and S. P. Ringer 'Advances in the calibration of atom probe tomographic reconstruction' *Journal of Applied Physics* Volume 105 (2009)

135 CAMECA 'IVAS Software and User Guide' *CAMECA* (2013)

136 J. M. Hyde and C. A. English 'An Analysis of the structure of irradiation induced Cu enriched clusters in low and high nickel welds' MRS 2000 Fall Meeting 650 (2000)

137 L. T. Stephenson, M. Moody, P. V. Liddicoat and S. P. Ringer 'New techniques for the analysis of fine scale clustering phenomena with atom probe tomography data APT' Microscopy and Microanalysis Volume 13 Page 448 (2007)

138 R. M. Langford and C. Clinton 'In situ lift out using a FIB-SEM system' *Micron* Volume 35 Page 607 to 611 (2004)

139 M. L. Jenkins and M. A. Kirk 'Characterisation of radiation damage by transmission electron microscopy' *Institute of Physics Publishing* (2001)

140 D. B. Williams and C. B. Carter 'Transmission Electron Microscopy: A Textbook for Materials Science' *Springer* (2009)

141 T. Malis, S. C. Cheng and R. F. Egerton 'EELS Log Ratio Technique for specimen thickness measurement in the TEM' Journal of Electron Microscopy Technique Volume 8 Page 193 to 200 (1988)

142 A. Maigne 'How to optimise you EELS experiments by adjusting the collection angle of your spectrometer' Gatan Online (2014)

143 K. Lakoubovskii and K. Mitsuishi 'Mean free path of inelastic electron scattering in elemental solids and oxides using transmission electron microscopy: Atomic number dependent oscillatory behaviour' *Physical Review B* Volume 77 (2008)

144 M. R. Van Landingham 'Review of instrumented indentation' *Journal of Research NIST* Volume 108 Pages 249 to 265 (2003)

145 C. Hardie 'Micro-mechanics of irradiated iron chromium alloys for fusion reactors' Doctoral Thesis University of Oxford (2013)

146 W. C. Oliver and G. M. Pharr 'An improved technique for determining hardness and elastic modulus using load and displacement sensing indentation experiments' *Journal of Materials Research* Volume 7 Page 1564 to 1583 (1992)

147 D. Preininger 'Modelling of the effect of precipitates on work-hardening, ductility and impact behaviour of ferritic–martensitic Cr steels' *Journal of Nuclear Materials* Volume 307 Pages 514 to 520 (2002)

148 M. Gorley 'Powder processing of oxide dispersion strengthened steels for advanced nuclear applications' Doctoral Thesis University of Oxford (2014)

149 R. Hu, G. D. W. Smith and E. A. Marquis 'Atom probe study of radiation induced grain boundary segregation/depletion in a Fe-12Cr alloy' *Progress in Nuclear Energy* Volume 57 Pages 14 to 19 (2012)

150 M. A. Marquis, S. Lozano-Perez and V. de Castro 'Effect of heavy ion irradiation on the grain boundary chemistry of an oxide dispersion strengthened Fe-12Cr alloy' Journal of Nuclear Materials Volume 417 Pages 257 to 261 (2011)

151 C. Fiori 'DTSA : EDX Simulation Software Package' *National Institute of Standards and Technology* (2015)

152 H. Zhang, M. Gorley, K. B. Chong, M. E. Fitzpatrick, S. G. Roberts and P. S. Grant 'An in situ powder neutron diffraction study of nano-precipitate formation during processing of oxide dispersion strengthened ferritic steels' *Journal of Alloys and Compounds* Volume 582 Pages 769 to 773 (2014)

153 M. Klimenkov, R. Lindau and A. Moslang 'Transmission electron microscopy study of Ar filled bubbles in steel' *Journal of Microscopy* Volume 237 Pages 497 to 500 (2010)

154 R. P. Kolli and D. N. Seidman 'Comparison of computational and morphological atom-probe tomography analyses for a multicomponent Fe-Cu Steel' *Microscopy and Microanalysis* (2007)

155 J. M. Hyde, E. A. Marquis, K. B. Wilford and T. J. Williams 'A sensitivity analysis of the maximum separation method for the characterisation of solute clusters' *Ultramicroscopy* Volume 111 Page 440 to 447 (2011)

156 N. J. Cunningham. P. Wells and G. R. Odette 'Recent Progress on Understanding and Quantifying Atom Probe Tomography Artefacts for High Evaporation Rate nm-scale Phases in Fe Based *Alloys' Fusion Reactor Materials Program DOE* Volume 51 Pages 9 to 21 (2011)

157 Y. Wu, E. M. Haney, N. J. Cunningham and G. R. Odette 'Transmission electron microscopy characterisation of the nanofeatures in a nanostructured ferritic alloy MA957' *Acta Materialia* Volume 60 Page 3456 to 3468 (2012)

158 K. Dawson and G. J. Tatlock 'Characterisation of nanosized oxides in ODM401 oxide dispersion strengthened steel' *Journal of Nuclear Materials* Volume 444 Pages 252 to 260 (2014)

159 M. Klimenkov, R. Lindau and A. Moslang 'TEM study of internal oxidation in an ODS Eurofer alloy' *Journal of Nuclear Materials* Volume 386 Page 557 to 560 (2009)

160 C. Williams, G. D. W. Smith and E. A. Marquis 'The effect of Ti on he coarsening behaviour of oxygen rich nanoparticles in oxide dispersion strengthened steels

after annealing at 1200°C' *Scripta Materialia* Volume 67 Pages 108 to 111 (2012)

161 R. Chinnappan 'Thermodynamic stability of oxide phases of Fe-Cr based ODS steels via quantum mechanical calculations' CALPHAD Computer Coupling of Phase Diagrams and Thermochemistry Volume 45 Pages 188 to 193 (2014)

162 K. B. Helean 'Formation enthalpies of rare earth titanate pyrochlores' Journal of Solid State Chemistry Volume 177 Pages 1858 to 1866 (2004)

163 W. Gale 'Smithells Metals Reference Book' 8th Edition Elsevier (2004)

164 W. Gong, D. Li, Z. Chen, F. Zheng, Y. Liu, Y. Du, B. Huang 'Phase Equilibria of the TiO2 Y2O3 system' *CALPHAD Computer Coupling of Phase Diagrams and Thermochemistry* Volume 33 Pages 624 to 627 (2009)

165 B. Yao, D. J. Edwards, R. J. Kurtz, G. R. Odette and T. Yamamoto 'Multislice simulation of transmission electron microscopy imaging of helium bubbles in Fe' *Journal of Electron Microscopy* Volume 0 Pages 1 to 8 (2012)

166 G.M. Pharr and W.C. Oliver 'Measurement of thin film mechanical properties using nanoindentation' *MRS Bulletin* Volume 17 Page 28 to 33 (1992)

167 T.Y. Tsui and G.M. Pharr 'Substrate effects on nanoindentation mechanical property measurement of soft films on hard substrates' Journal of Materials Research Volume 14 Pages 292 to 301 (1998)

168 R. E. Stoller and S. J. Zinkle 'On the relationship between uniaxial yield strength and resolved shear stress in polycrystalline materials' *Journal of Nuclear Materials* Volume 283 Pages 349 to 352 (2000)

169 J. T. Busby, M. C. Hash and G. S. Was 'The relationship between hardness and yield stress in irradiated austentic and ferritic stainless steels' *Journal of Nuclear Materials* Volume 336 Pages 267 to 278 (2005)

170 K. Heinola, T. Ahlgren, K. Nordlund, J. Keinonen 'Hydrogen interaction with point defects in tungsten' *Physical Review B* Volume 82 Page 094102 (2010)